Origin and transformations of the carbon produced in the upwelling system off Cape Blanc – Cape Verde Front (NW Africa): optical and isotopic characterization

Rubén Campanero Nieto

PhD Thesis – Tesis Doctoral

Programa Doctorado
Ciencias de la Tierra

Memoria de tesis doctoral presentada por el Graduado en Geología Rubén Campanero Nieto para optar al grado de doctor por la Universidad de Granada

En Granada, junio de 2023

Supervisado por:

Dr. Antonio Delgado Huertas
Dr. Xosé Antón Álvarez Salgado

Editor: Universidad de Granada. Tesis Doctorales
Autor: Rubén Campanero Nieto
ISBN: 978-84-1195-036-7
URI: https://hdl.handle.net/10481/84689

El doctorando / The *doctoral candidate* **Rubén Campanero Nieto** y los directores de la tesis / and the thesis supervisor/s: **Antonio Delgado Huertas y Xosé Antón Álvarez Salgado**

Garantizamos, al firmar esta tesis doctoral, que el trabajo ha sido realizado por el doctorando bajo la dirección de los directores de la tesis y hasta donde nuestro conocimiento alcanza, en la realización del trabajo, se han respetado los derechos de otros autores a ser citados, cuando se han utilizado sus resultados o publicaciones.

/

Guarantee, by signing this doctoral thesis, that the work has been done by the doctoral candidate under the direction of the thesis supervisor/s and, as far as our knowledge reaches, in the performance of the work, the rights of other authors to be cited (when their results or publications have been used) have been respected.

Lugar y fecha / Place and date:

Granada, 22 de junio de 2023

Director/es de la Tesis / *Thesis supervisor/s;* Doctorando / *Doctoral candidate*:

Antonio Delgado Huertas Xosé Antón Álvarez Salgado Rubén Campanero Nieto

Funding: This PhD thesis has been developed at the Departamento de Petrología y Geoquímica of the Instituto Andaluz de Ciencias de la Tierra (CSIC-UGR) in the group of Biogeoquímica de Isótopos Estables and at the Departamento de Oceanografía of the Instituto de Investigaciones Marinas (CSIC) in the Organic Geochemistry Lab. The research was funded by the Spanish National Science Plan research grant FLUXES (CTM2015-69392-C31, -C32 and -C33). Rubén Campanero Nieto was supported by a predoctoral fellowship FPI from the Spanish Ministry of Science and Innovation (BES-2016-076462) and a research contract funded by e-IMPACT project (PID2019-109084RB-C21 and –C22).

A mis padres

Agradecimientos

En primer lugar, agradecer a mis directores de tesis Antonio y Pepe. Antonio, gracias por darme la oportunidad de entrar a trabajar en el grupo de isótopos estables y por enseñarme tanto sobre esta técnica y la meticulosidad que supone. Y por descontado, por la oportunidad de vivir en Granada, que ha sido una muy grata experiencia. Pepe, gracias por enseñarme todo lo que he aprendido sobre la oceanografía, hasta entonces muy desconocida para mí. Ya siempre miraré al mar con otros ojos. Gracias por las innumerables reuniones telemáticas, por explicarme las cosas las veces que haga falta, siempre dispuesto para solucionar dudas y preguntas. Aunque me quedé con las ganas de pasar algún tiempo en Vigo, seguro que habrá más oportunidades.

Gracias a Francisca Martínez Ruíz (Paqui), que ha sido mi tutora en el programa de doctorado.

A Arsenio, por su infinita paciencia en el laboratorio de isótopos estables, por ayudarme a montar la línea del TOC, solucionar miles de problemas y enseñarme montones de cosas sobre el mantenimiento de los equipos. También agradecer a María y Vanesa, del grupo LGO por la cantidad ingente de análisis de muestras que han hecho de las campañas FLUXES y que se han utilizado para la elaboración de esta tesis.

A las tripulaciones del buque Sarmiento de Gamboa, en el que he tenido el privilegio de participar en cuatro campañas, y a todos los compañeros científicos que he conocido, de la ULPGC y otros lugares. Estas experiencias han sido alucinantes y las llevaré siempre en el recuerdo.

A mis queridos compañeros del IACT, Manu, Nicole, Claudia, Erwin, Bob, Álvaro, Javi, Adrián, Ceci, Alejandro, Dimitri, Marievi, Manolis, Ricardo, Pablo, Elsi, Adriana, y un largo etcétera de compañeros que han pasado por el instituto y hemos coincidido en algunos momentos a lo largo de estos años. Por supuesto también agradecer a Antonio y Meri por las charlas diarias y hacerme desconectar un poco del trabajo. Agradecimiento especial a Sara, mi compañera de faenas de tesis durante todos estos años. Por haber sido un apoyo fundamental, creo que mutuo, para sobrellevar los momentos difíciles, y por descontado por todos los buenos momentos, que han sido más. ¡Mucho ánimo que ya no te queda nada para terminar también!

También agradecer a mis amigos de Granada, Julia, Laura, Aitana, Anabel y a todos los integrantes del coro Gospel Molotov que me han hecho sentir siempre muy querido, por los viajes, las cervezas, los conciertos y los buenos ratos que hemos pasado.

Finalmente, agradecer a mi gente de Madrid, a mi grupo de “colegarios” y especialmente a mi familia, a mis padres y a mis hermanos, por su apoyo y sus visitas a lo largo de todos estos años que he vivido en Granada.

General Abstract

The aim of this PhD thesis is to address the role of dissolved and suspended organic matter in the carbon biogeochemistry of the Cape Verde Frontal Zone (CVFZ), situated at the southern edge of the NW Africa Eastern Boundary Upwelling Ecosystem (EBUE). This region, in front of Cape Blanc, is the scenario where the confluence between North and South Atlantic waters occurs, forming a thermohaline front (Cape Verde Front, CVF) with a high meso- and submeso-scale heterogeneity and physical-biogeochemical variability. In addition, the upwelling system along with the southward flow of the Canary Current creates a year-round giant filament associated to Cape Blanc (CBGF) that exports the organic matter produced in the Mauritanian coast to the open ocean for hundreds of kilometers. This PhD thesis is framed within the FLUXES project that encompasses two oceanographic surveys carried out during 2017 in the CVFZ, covering from the regional scale (FLUXES I cruise) to the meso- and submeso-scale (FLUXES II cruise). The distributions of dissolved organic carbon (DOC), suspended particulate organic carbon (POC), colored (CDOM) and fluorescent (FDOM) dissolved organic matter and δ^{13}C-DOC have been analyzed in epipelagic, mesopelagic and bathypelagic waters of the CVFZ.

Mesoscale structures such as meanders, eddies and fronts defined the variability of DOC, POC, CDOM and FDOM in the epipelagic layer, showing the tight coupling that exists between the physical and biogeochemical properties. Moreover, atmospheric inputs of Sahara dust in the area play an important role by entering both organic matter and lithogenic particles that controlled to some extend the local biogeochemistry. In the meso-and bathypelagic waters, water mass mixing and large-scale mineralization processes explain mainly the observed distribution, although some local generation of CDOM and the recalcitrant fraction of FDOM (humic-like substances) and degradation of the labile fraction of FDOM (protein-like substances) was observed. The contribution of DOC and suspended POC to the local oxygen demand was very low (3.6 ± 2.1% and 4.5 ± 0.7%, respectively) suggesting that the oxygen demand was mainly supported by the sinking POC fraction. The presence of vertical chimney-like structures of DOC are hypothesized to be transporting organic carbon from the surface waters to the deep ocean by processes of adsorption/desorption onto ballasting particles that can be either allochthonous (lithogenic particles from Sahara dust) or autochthonous (biogenic particles). In addition, a connection between the surface coastal productive waters and the deep ocean has been observed through a column of high particle density that connected with a bottom nepheloid layer (BNL) developed along the continental slope. An increment in the CDOM and FDOM in this BNL not accompanied by an increment in AOU suggested the dissolution of DOM from the sinking particles and/or resuspension of DOM from the anoxic sediments. The isotopic characterization of DOC helped to distinguish between the labile and recently produced organic carbon in the coastal surface waters containing the more enriched values, from the refractory DOC that was exported to the ocean interior with more depleted signatures. A wide range of δ^{13}C-DOC (from -29.4 to -21.3‰ (V-PDB)) compared to other areas have been found in the CVFZ, suggesting that additional carbon sources apart from primary production are present, probably associated with terrestrial inputs from the adjacent continent. The results presented in this thesis dissertation provide new insights into the biogeochemistry of the CVFZ, being one of the most productive ocean regions in the World that plays a fundamental role in regulating the carbon cycle, mainly through carbon sequestration by the biological pump.

Resumen General

El objetivo de esta tesis doctoral es abordar el papel de la materia orgánica disuelta y en suspensión en la biogeoquímica del carbono de la Zona Frontal de Cabo Verde (CVFZ), situada en el extremo sur del sistema de afloramiento costero del noroeste de África. Esta región, frente a Cabo Blanco, es el escenario donde se produce la confluencia entre las aguas del Atlántico Norte y Sur, formando un frente termohalino (Frente de Cabo Verde, CVF) con una elevada heterogeneidad y variabilidad físico-biogeoquímica a meso y submesoescala. Además, el sistema de afloramiento junto con la Corriente de Canarias crea durante un filamento gigante asociado a Cabo Blanco (CBGF) que está presente todo el año y que exporta gran cantidad de la materia orgánica producida en la costa de Mauritania hacia el océano abierto a lo largo de cientos de kilómetros. Esta tesis doctoral se enmarca dentro del proyecto FLUXES que engloba dos muestreos oceanográficos realizados durante 2017 en la CVFZ, abarcando desde la escala regional (crucero FLUXES I) hasta la meso y submesoescala (crucero FLUXES II). Se han analizado las distribuciones de carbono orgánico disuelto (DOC), carbono orgánico particulado en suspensión (POC), materia orgánica disuelta coloreada (CDOM) y fluorescente (FDOM) y la desviación isotópica del DOC (δ^{13}C-DOC) en aguas epipelágicas, mesopelágicas y batipelágicas de la CVFZ.

La variabilidad de DOC, POC, CDOM y FDOM en la capa epipelágica está definida por estructuras de mesoescala como meandros, remolinos y frentes, mostrando la estrecha relación que existe entre las propiedades físicas y biogeoquímicas. Además, los aportes atmosféricos de polvo del Sáhara en la zona desempeñan un papel importante al introducir tanto materia orgánica como partículas litogénicas que controlan en cierta medida la biogeoquímica local. En las aguas meso y batipelágicas, la mezcla de masas de agua y los procesos de mineralización a gran escala explican principalmente la distribución observada, aunque se ha observado cierta generación local de CDOM y de la fracción recalcitrante de FDOM (sustancias de tipo húmico) y degradación de la fracción lábil de FDOM (sustancias de tipo proteico). La contribución observada del DOC y del POC en suspensión a la demanda local de oxígeno es muy baja (3.6 ± 2.1% y 4.5 ± 0.7%, respectivamente), lo que sugiere que la demanda de oxígeno es soportada principalmente por la fracción de POC en sedimentación. Se plantea la hipótesis de que la presencia de estructuras verticales de DOC en forma de chimeneas transportan carbono orgánico desde las aguas superficiales hasta el océano profundo mediante procesos de adsorción/desorción en partículas de lastre que pueden ser alóctonas (partículas litogénicas del polvo del Sahara) o autóctonas (partículas biogénicas). Además, se ha observado una conexión entre las aguas productivas costeras superficiales y el océano profundo a través de una columna de alta densidad de partículas que conecta con una capa nefeloide de fondo (BNL) desarrollada a lo largo del talud continental. Los incrementos observados en la CDOM y la FDOM en esta BNL no están acompañados de un incremento de la utilización aparente de oxígeno (AOU) sugiriendo la disolución de DOM de las partículas en sedimentación o bien la resuspensión de DOM de los sedimentos anóxicos. La caracterización isotópica del DOC ha servido para distinguir entre el carbono orgánico lábil y recientemente producido en las aguas superficiales costeras, con desviaciones isotópicas más enriquecidas, del carbono orgánico refractario que es exportado al interior del océano y contiene valores más empobrecidos. En la CVFZ se ha encontrado un amplio rango de δ^{13}C-DOC (de -29.4 a -21.3‰ (V-PDB)) en comparación con otras zonas, lo que sugiere la presencia de fuentes adicionales de carbono aparte de la producción primaria, probablemente asociadas a aportes terrestres procedentes del continente adyacente. Los resultados presentados en esta tesis doctoral aportan un nuevo nivel de conocimiento en la biogeoquímica de la Zona Frontal de Cabo Verde, una de las regiones oceánicas más productivas del planeta que juega un papel fundamental en la regulación del ciclo del carbono principalmente a través del secuestro de carbono por parte de la bomba biológica.

Index

List of acronyms 1

Chapter 1: General Introduction.....3

Chapter 2: New insights on dissolved organic matter cycling in the Cape Verde Frontal Zone from its optically active fraction 33

Chapter 3: High-resolution variability of dissolved and suspended organic matter in the Cape Verde Frontal Zone 79

Chapter 4: Methodology for δ^{13}C-DOC analysis by WCO-IRMS 113

Chapter 5: Carbon isotopic signature of dissolved organic carbon (δ^{13}C-DOC) in the Cape Verde Frontal Zone (CVFZ).....133

Chapter 6: General discussion.....161

Chapter 7: Conclusions 173

References.....177

List of acronyms

AA: Antarctic Intermediate Water
AABW: Antarctic Bottom Water
AC: Azores Current
AOU: Apparent oxygen utilization
BNL: Bottom nepheloid layer
CBGF: Cape Blanc Giant Filament
CC: Canary Current
CDOM: Colored dissolved organic matter
CUC: Canary Upwelling Current
CVC: Cape Verde Current
CVF: Cape Verde Front
CVFZ: Cape Verde Frontal Zone
dbar: decibar
DCM: Deep Chlorophyll Maximum
DIC: Dissolved inorganic carbon
DOC: Dissolved organic carbon
DOM: Dissolved organic matter
EA: Elemental analyzer
EBUE: Eastern boundary upwelling ecosystem
EEM: Excitation-emission matrices
Em: Emission
ENACW: Eastern North Atlantic Central Water
Ex: Excitation
FDOM: Fluorescent dissolved organic matter
HMW: High molecular weight
HTO: High temperature oxidation
INL: Intermediate nepheloid layer
IRMS: Isotope Ratio Mass Spectrometer
ISOW: Iceland Scotland Overflow Water
KDa: Kilo Dalton
KHP: potassium phthalate
LMW: Low molecular weight
LNEADW: Lower North East Atlantic Deep Water
LSW: Labrador Sea Water
MC: Mauritanian Current
MMW: Madeira Mode Water
MW: Mediterranean Water
NACW: North Atlantic Central Water
NASG: North Atlantic Subtropical Gyre
NATG: North Atlantic Tropical Gyre
NEADW: North East Atlantic Deep Water
NEC: North Equatorial Current
NECC: North Equatorial Countercurrent
NDIR: non-dispersive infrared

nm: nanometer
NM: nautical miles
PARAFAC: Parallel factor analysis
Pg C: Peta grames of carbon (1 Pg C = 10^{15} g C)
pCO_2: partial pressure of CO_2
POC: Particulate organic carbon
POC_{susp}: Suspended POC
POC_{sink}: Sinking POC
POM: Particulate organic matter
POM_{susp}: Suspended POM
POM_{sink}: Sinking POM
PUC: Poleward Undercurrent
RDOC: Refractory dissolved organic carbon
RU: Raman units
S: Salinity
SACW: South Atlantic Central Water
SE: Standard error
SRDOC: Semi-refractory dissolved organic carbon
SLDOC: Semi-labil dissolved organic carbon
SPE: Solid phase extraction
SPMW: Subpolar Mode Water
TOC: Total organic carbon
UF: Ultra filtration
UNEADW: Upper North East Atlantic Deep Water
URDOC: Ultra-refractory dissolved organic carbon
UVO: Ultraviolet oxidation
VPDB: Vienna PeeDee Belemnite
WCO: Wet chemical oxidation
WT: Water type
µM: micro molar
Z: depth
θ: Potential temperature

Chapter 1: General Introduction

1.1 The Global Carbon Cycle

The global carbon cycle can be classified into two separated realms, depending on its size and turnover timescales. The first realm comprises the majority of the carbon existing on Earth and is accumulated in rocks and sediments forming the geological carbon reservoir, with turnover times of 10,000 years or more (Ciais et al., 2013; Keeling, 1972; Kempe, 1979). It is, therefore, a long-term carbon reservoir. The second realm, is negligible in size compared to the vast geological carbon reservoir, but conversely, is characterized by relatively rapid turnover times and with large exchange fluxes, becoming a short-term carbon reservoir. It includes the carbon contained in the atmosphere, on land in vegetation, soils and freshwaters, in the ocean and the surface ocean sediments (Ciais et al., 2013; Keeling, 1972; Kempe, 1979). Turnover times can range between a few years, for example in the atmosphere reservoir, to millennia in the ocean and soils or sediments pools.

The natural carbon exchange between the long-term and short-term realms is assumed to be nearly constant over time and relatively small (0.3 PgC y^{-1}; 1 Pg = 10^{15} gC), but since the Industrial Era, anthropogenic activities has created an imbalance between the two realms, transferring significant amounts of fossil carbon from the long-term to the short-term reservoirs, coming from the burning of fossil fuels (Ciais et al., 2013; Hansen et al., 2005). The exchange and fluxes of carbon within the different short-term pools are of major importance regarding the carbon cycling, creating a balance between reservoirs and regulating the Earth climate (Fig. 1.1). A large flux of carbon maintained at near steady-state is established between the atmosphere and terrestrial organic matter, removing CO_2 from the atmosphere by plant photosynthesis and back again by plant respiration and plant decomposition. Other large carbon flux exists between the atmosphere and the surface ocean through gas exchange. This connection plays a crucial role in the global carbon cycle and the climate system regulation since the ocean contain the largest carbon reservoir within the short-term domain, being two orders of magnitude larger than the carbon in the atmosphere and one order larger than the carbon contained in ocean sediments, land soils and permafrost (Friedlingstein et al., 2022; Sabine et al., 2004). The majority of the ocean carbon pool is in form of dissolved inorganic carbon (DIC), counting with 37,000 PgC (Holmen, 1992; Ridgwell & Arndt, 2015) and can be present as carbonic acid (dissolved CO_2 or $CO_{2(aq)}$), bicarbonate (HCO_3^-) and carbonate (CO_3^{2-}) ions, depending on ocean alkalinity and pH. The rapid exchange between the atmosphere and the surface ocean DIC has implications for the atmospheric CO_2 partial pressure (pCO_2) and therefore for the

climate equilibrium, where small adjustments in the surface DIC may drive to severe changes in the atmosphere (Ridgwell & Arndt, 2015). In addition, there is an organic carbon pool in the ocean, present mostly in dissolved form (DOC) counting with 640 PgC, that represents one of the largest pools of reduce carbon on Earth (Hansell et al., 2009).

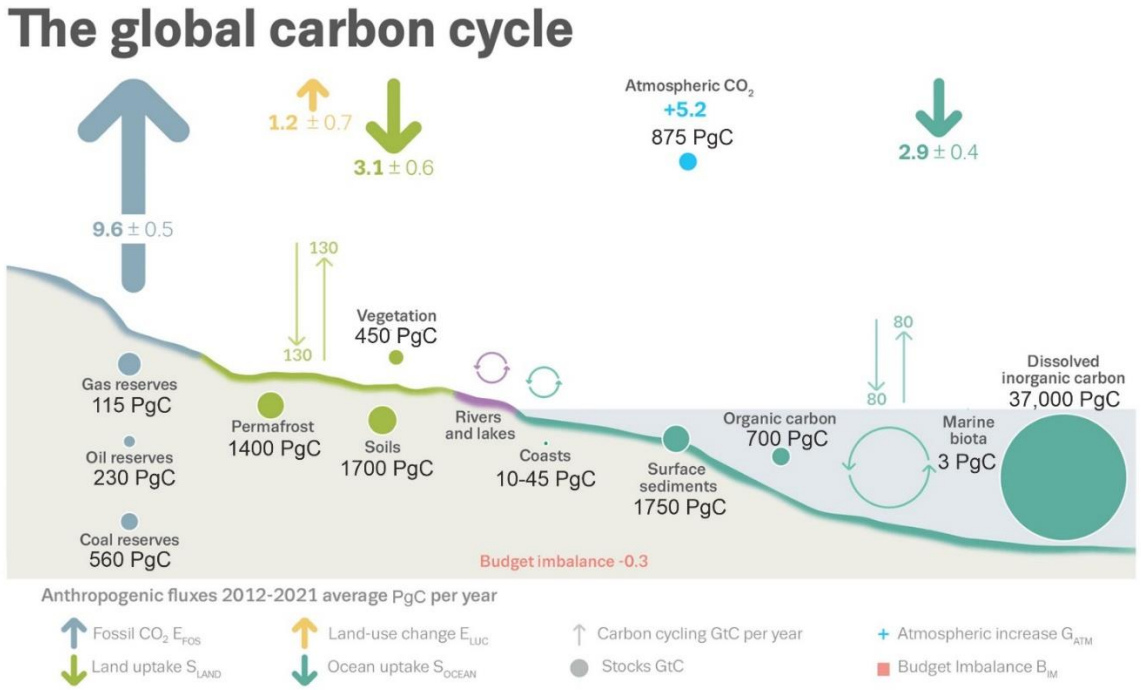

Figure 1.1: Schematic representation of the main carbon reservoirs and fluxes of the short-term realm. Fluxes are averages of the 2012-2021 decade expressed in PgC per year. Adapted from Friedlingstein et al. (2022).

Carbon is transported within the ocean by the so called 'carbon pumps', which transfers carbon typically from surface to deep ocean and can be classified into four different groups depending on its functioning: 1) the solubility pump; 2) the biological pump; 3) the carbonate pump; and 4) the microbial carbon pump (Fig. 1.2). A brief description of each pump is summarized as follows:

- **Solubility pump:** This carbon pump is responsible for the CO_2 sequestration from the atmosphere to the surface ocean by physical dissolution in seawater, that depends primarily on temperature, pressure and salinity (Teng et al., 1996; Weiss, 1974). At lower latitudes, where surface water is colder, the CO_2 dissolution is higher, and thus, carbon is transferred to deep ocean layers due to the downwelling of these cold, high-density and DIC-richer water bodies (Ridgwell & Arndt, 2015). Conversely, at lower latitudes, surface water is warmer and the CO_2 dissolution decrease.

- **Biological pump:** Also called ‘organic carbon’ or ‘organic matter’ pump. In brief, phytoplankton in the surface ocean take up CO_2, DIC and nutrients, and fix the carbon into organic material via photosynthesis. Once formed, most of the organic material is consumed and degraded back to CO_2 by zooplankton and bacteria within the first hundred meters, but a fraction survives to this degradation and is exported to the deep ocean where can be remineralized or accumulated in the sediments (De La Rocha, 2006).
- **Carbonate pump:** This pump comprises inorganic and biogenic production of calcium and magnesium carbonate ($CaCO_3$ and $MgCO_3$) at the ocean surface. It has been reported that as much of 50% of carbonate is dissolved within the water column as it sinks (Feely et al., 2004), with the remainder reaching the surface sediment. This carbon pump is controlled by the alkalinity of seawater that influences the speciation of dissolved carbon species (Ridgwell & Arndt, 2015).
- **Microbial carbon pump:** This pump consists primarily on the evolution of labile DOC into recalcitrant DOC by the microbial activity. This process was firstly proposed by Ogawa et al. (2001) and later developed and named as microbial pump by (Jiao et al., 2010). A considerable fraction (30-50%) of primary production in surface ocean is released as DOC (Biddanda & Benner, 1997; Ducklow et al., 1995) and only 1% of it is in form of labile DOC due to its rapid degradation by heterotrophs (Hansell, 2013). The microbial processing of organic matter transforms the low-concentrated labile carbon molecules into high-concentrated recalcitrant molecules (Jiao et al., 2010). The net production rate of this refractory DOC (RDOC) is relatively low (0.043 PgC y^{-1}; Hansell, 2013), but enough to maintain the RDOC inventory in the dark ocean counting with 630 ± 12 PgC of RDOC and >12 PgC of ultrarefractory DOC as black carbon (Hansell, 2013). The microbial carbon pump also contributes to release inorganic nutrients as nitrogen or phosphorous through the water column, contributing to the inorganic nutrient supply within the ocean circulation (Jiao et al., 2010).

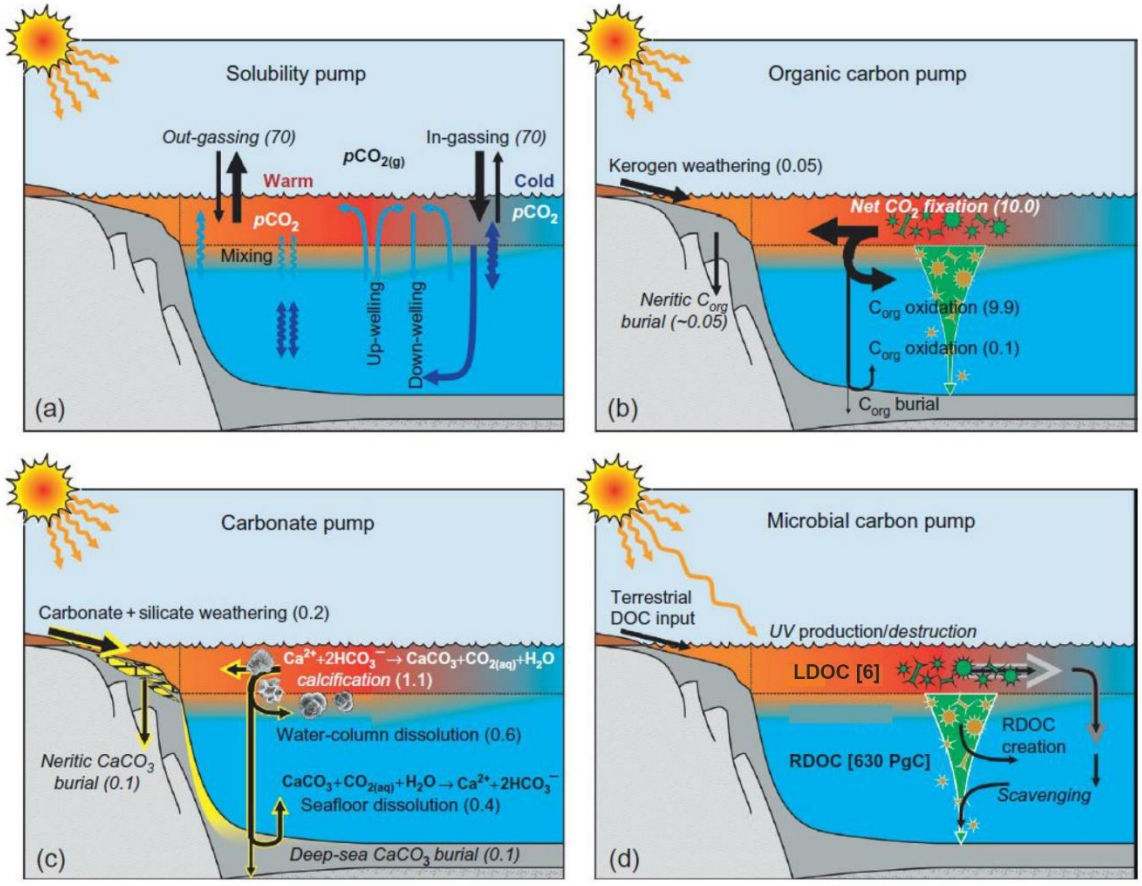

Figure 1.2: Schematic functioning of the four carbon pumps. a) solubility pump; b) biological pump or organic carbon pump; c) carbonate pump and d) microbial pump. LDOC, labile DOC; RDOC, refractory DOC. Carbon fluxes are shown in normal font and sinks in italics. Taken from Ridgwell and Arndt (2015).

1.2 What is dissolved organic matter?

Organic compounds are substances containing carbon and forming carbon-carbon and carbon-hydrogen covalent bonds. They are usually combined with other non-metal elements like oxygen, nitrogen, sulfur, phosphorous, halogens and others, forming organic molecules. Organic matter is originally formed by life, being the CO_2 the most important carbon source, using the sunlight as the primary energy source for the breakage of the C-O bond (Lechtenfeld et al., 2014; Redfield et al., 1963). In the marine environment, organic matter has been operationally defined as 'dissolved' (DOM) and 'particulate' (POM) organic matter, on the basis of the pore filter size used to separate both fractions, traditionally between 0.2-0.7 µm. In nature, there is a continuum of size, making therefore somewhat arbitrary this separation between dissolved and particulate. For consensus within the scientific community, the dissolved fraction is generally referred to as the marine organic matter that passes through a filter of 0.7 µm nominal pore size. Moreover, the dissolved fraction is not prone to sink, whereas the particulate fraction tends to form

aggregates and sink (Hedges, 2002). DOM is further classified into colloidal or high molecular weight (HMW; >1 KDa) and truly dissolved or low molecular weight (LMW; <1 KDa) (see Fig. 1.3).

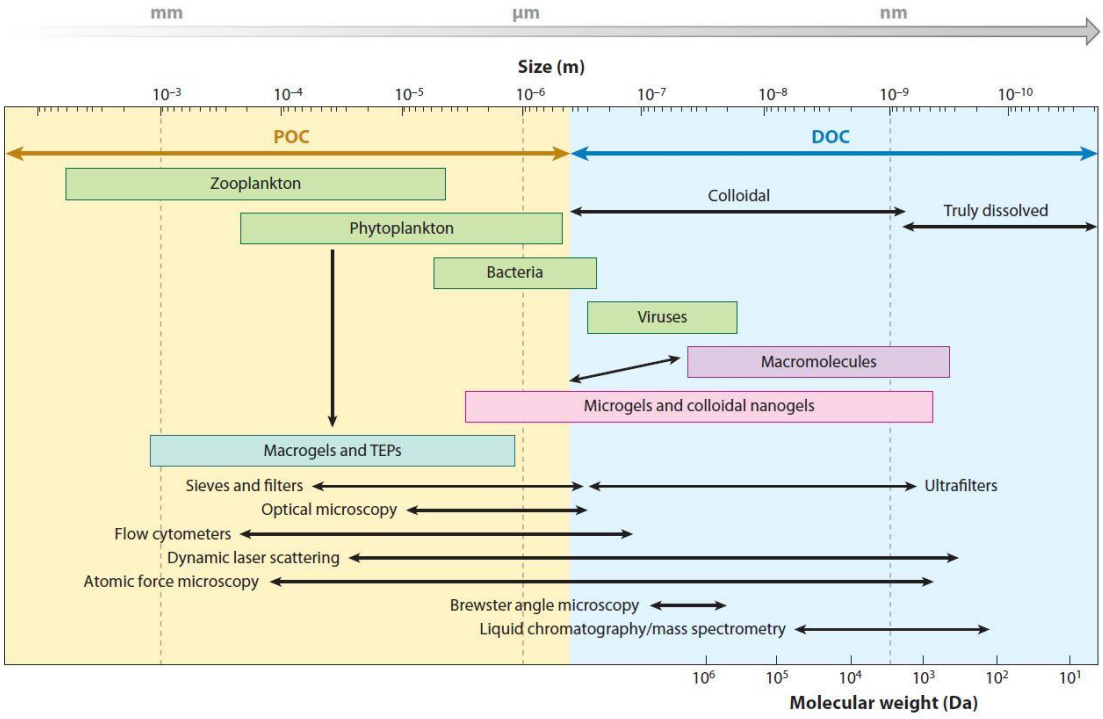

Figure 1.3: Scheme of the size scale classification of organic matter in the marine environment. Green boxes represent living organisms while blue and pink boxes represent non-living organic matter. Different techniques and procedures are indicated in the lower section. TEPs: transparent exopolymer particles. Taken from (Verdugo, 2011).

The DOM inventory consist of 662 PgC and is >200 times higher than the marine biomass (Hansell et al., 2009). It is mostly produced in the surface ocean by photosynthetic phytoplankton but additional DOM sources are atmospheric, fluvial and groundwater transport of organic matter from the continents, and also by organic matter release from the benthic boundary layer (Bauer & Bianchi, 2011; Burdige, 2007; Hansell, 2013; Jurado et al., 2008). Fresh organic matter supports the heterotrophic microbial populations and is of labile nature, being quickly respired back to CO_2 and surviving only from few hours to days (Hansell, 2013). A small fraction of the newly produced DOM escapes the rapid mineralization and is transformed into biologically resistant molecules, surviving and accumulating in the dark ocean from months to millennia, forming the inventory of dissolved organic carbon (DOC). Despite its large amount of carbon, the DOC concentration in the ocean is very low, usually ranging from 34 to 80 µmol L^{-1}, being higher in the surface ocean and progressively lower with depth (Hansell et al., 2009). Recalcitrant

DOC can be further classified based on its reactivity into semi-labil DOC (SLDOC), semi-refractory DOC (SRDOC), refractory DOC (RDOC) and ultra-refractory DOC (URDOC) (Hansell, 2013; Hansell et al., 2012). Each fraction plays different roles in the carbon cycle, for instance, labile DOC (LDOC) supports the microbial loop, SLDOC and SRDOC are the main fractions driving the biological pump, RDOC represents the 95% of the DOC pool and play the role of being the source or sink of carbon controlling paleoclimate variations. URDOC, smaller in size and globally distributed, may control the inventory of atmospheric CO_2 on geological timescales, linking therefore the biological and geological carbon cycles (Hansell, 2013; Jiao & Azam, 2011). In addition to the DOC reactivity classification, (Amon & Benner, 1996) presented a conceptual model of the size-reactivity continuum, updated later by Benner & Amon (2015), showing the evolution of DOM from larger to smaller size classes with increasing degradation (Fig. 1.4). As decomposition proceeds, the chemical complexity increase, the biological reactivity decreases and radiocarbon ages increase.

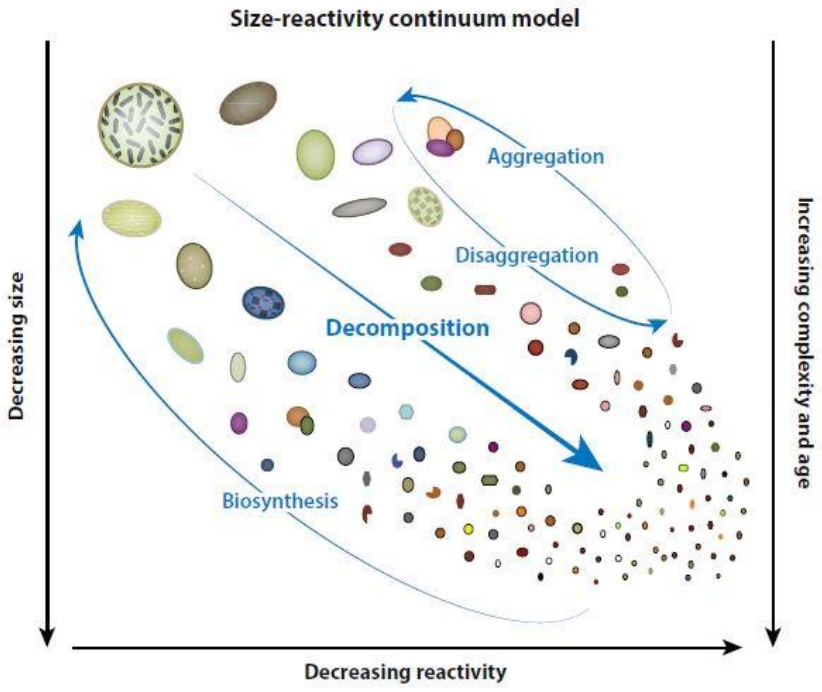

Figure 1.4: Conceptual model of the size-reactivity continuum indicating the evolution of organic carbon from larger to smaller size as decomposition increase. In the same way, the chemical complexity increase, the biological reactivity declines and the relative 14C age increase. Biosynthesis processes may recycle small molecules into larger size classes. Figure taken from Benner and Amon (2015).

The DOM inventory is balanced between sources and sinks maintaining constant its carbon amount. Heterotrophic prokaryotes are known as the main removal process of DOM in the ocean (Carlson & Hansell, 2015), through the transformation of DOM into POM (Azam et al., 1983; Pomeroy et al., 2007) and/or remineralization of DOM to its inorganic constituents (Ducklow et al., 1986; Goldman & Dennett, 2000). Regarding the removal of recalcitrant DOM, photo-oxidation has been proposed as the most important process once the recalcitrant DOM returns to the surface ocean (Dittmar, 2015), being degraded at a rate of 0.02 – 0.49 10^{15} g C y^{-1}, and therefore equilibrating the continental inputs of DOM by rivers, avoiding its accumulation (Stubbins et al., 2012). The long-term stability of DOM has been a subject of interest for the scientific community, and the question of why DOM accumulates in the ocean remains unambiguous and enigmatic. Recently, Baltar et al. (2021) proposed that refractory DOM should be operationally defined since there are various definitions and approaches to characterize RDOC, by explicitly stating how RDOC is defined and the analytical window used to measure it in an attempt to unify future studies. The average radiocarbon age of DOC is 3000-6000 years in the deep ocean (Bauer, 2002; Williams & Druffel, 1987), is accumulated under favorable environmental conditions for life, and therefore available for bacterial degradation, not like other major organic carbon reservoirs, that are locked in uninhabitable conditions, but still, seems to remain untouched for thousands of years (Dittmar, 2015). Another uncertain question would be related with why DOM eventually disappear after few thousand years and does not accumulate even longer if it survives to biological degradation. Three hypotheses were postulated to these questions, briefly summarized as follows (Dittmar, 2015):

- The environmental hypothesis indicates that DOM reactivity depends on the specific environmental conditions of each region or in different periods of the Earth history. In this sense, in oligotrophic areas, limitation of nutrients led to reduce primary production and the consequent heterotrophic bacterial consumption, favoring the accumulation of DOM molecules due to an absence of microbial activity.
- The intrinsic stability hypothesis connects the DOM reactivity with the molecular structure. RDOM and URDOM present a molecular structure that is difficult to be degraded by organisms that do not have any enzymatic pathway to decompose those molecules that persist and accumulate in the ocean. Biologically resistant molecules can be generated by biotic processes like the microbial processing or abiotic

processes like photodegradation (Hertkorn et al., 2006), thermogenic processes related with hydrothermal fluids (Dittmar & Koch, 2006) or terrestrial black carbon originated during fire events (Dittmar et al., 2012). Nevertheless, the molecular characterization of DOM remains largely undetermined, with only a few percent of deep DOM that has been molecularly identified (Dittmar & Paeng, 2009; Kaiser & Benner, 2009).

- The molecular diversity or dilution hypothesis is related with the low concentration of individual DOM compounds and the limited probability of encounter between heterotrophic bacteria and substrate (Arrieta et al., 2015; Dittmar, 2015). Under these low DOC concentrations of individual compounds, the energy demand of protein biosynthesis could exceed the energy gained from substrate utilization and therefore limiting the activity of bacterial consumers (LaRowe et al., 2012). This hypothesis implies that at enough DOM concentration, most molecules are potentially degradable, and that a dynamic steady-state exist between DOM inputs and outputs.

The reasons behind the long-term stability of DOM remains unknown, and probably a combination of these mechanisms explain the DOM dynamics and cycling, its accumulation and final fate in the deep ocean.

A small fraction of organic matter in the ocean is in particulate form. Marine biota represents only 3 PgC (Fig 1.1) and detritus of non-living organic matter about 20-30 PgC (Cauwet, 1981; Ciais et al., 2013; Pan et al., 2014). Particulate organic matter can be classified into suspended (POM_{susp}) and sinking (POM_{sink}) depending on its density. The suspended fraction is not prone to sink by gravity, instead its cycling depends on oceanic currents and other physical transport mechanisms as is the case of DOM. Conversely, the sinking fraction is settling from surface to deep waters at different settling rates, which can vary from tenths to hundreds of meters per day. These aggregates of organic matter are usually termed as ‘marine snow’ that is mainly formed by physical coagulation when individual particles encounter each other and stick together into aggregates higher than 0.5 mm (Iversen, 2023). Aggregates can also be made by fecal pellets, formed by egestion of the zooplankton leftovers. Ballast minerals (e.g., calcium carbonate, silicate and other lithogenic materials) play an important role on the sinking POM functioning, since the organic aggregates can be adsorbed into minerals favoring the settling velocity due to an increase in the particle density. The higher sinking rates implies less degradation of organic

matter, increasing the biological carbon pump efficiency (Armstrong et al., 2001). However, other studies reported that incorporation of lithogenic material into marine snow causes them to disaggregate lowering the average settling velocity of particles and reducing the biological carbon pump efficiency (Engel et al., 2009; Passow & De La Rocha, 2006).

1.3 Optical properties of DOM

Chromophoric or colored dissolved organic matter is a small fraction of DOM that interacts with solar radiation, absorbing light in the bands found at the Earth's surface, including the visible light (400-700 nm), the UVB (280-315 nm) and UVA (315-400 nm) (Nelson & Siegel, 2013). CDOM plays a major role controlling the light penetration in the surface ocean, influencing the phytoplankton and bacterial productivity since it absorbs harmful UV radiation (Fichot et al., 2008; Herndl et al., 1993; Nelson & Siegel, 2013). Quantification of CDOM in terms of its carbon concentration is not currently possible due to their chemical complexity that varies both in time and space, but the absorption coefficients of CDOM must correlate at some level with the quantity of chromophoric material that is present (Nelson & Siegel, 2013).

CDOM is ubiquitous in the marine environment, and natural marine waters show an exponential decay on its absorption spectra with increasing wavelength (λ) to undetectable levels at $\lambda > 600$ nm (Bricaud & Morel, 1981). The variability in the absorption spectra led to an assortment of indices used as tracers for photochemical and biological processes in the marine environment (Fig. 1.5). The most common indices employed are the absorption coefficients at specific wavelengths (Nelson et al., 2010), the absorption coefficient ratios (Engelhaupt et al., 2003) and spectral slopes (Helms et al., 2008; Twardowski et al., 2004). The absorption coefficients at specific wavelengths are used to quantify different CDOM fractions, whereas the coefficient ratios are indicative of the relative molecular weight and the spectral slopes provides information about the source, processing, molecular weight and chemistry of DOC (Engelhaupt et al., 2003; Helms et al., 2008; Lønborg & Álvarez-Salgado, 2014; Nelson et al., 2010).

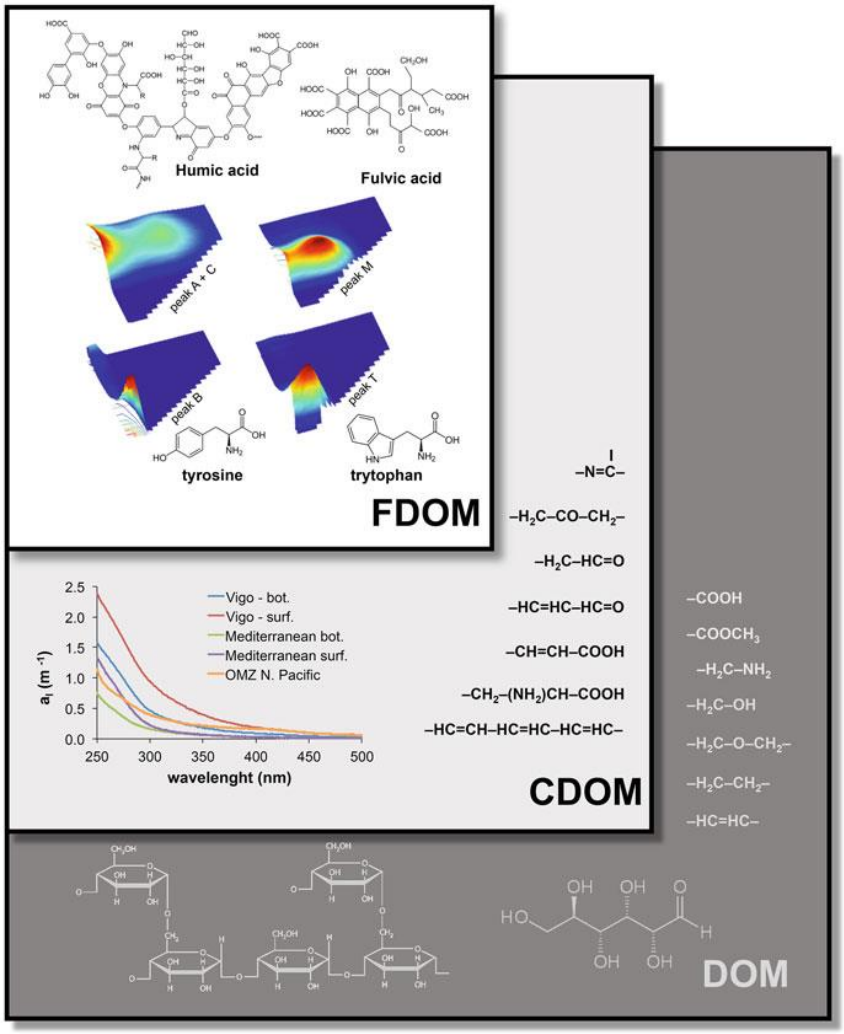

Figure 1.5: Bulk DOM, colored (CDOM) and fluorescent (FDOM) inventories of dissolved organic matter in the marine environment. Examples of transparent (λ<240 nm), colored (λ>240 nm) and fluorescent molecules are shown. Absorption coefficient spectra for different ocean regions, and excitation-emission matrices (EEMs) for different fluorophores are included. Taken from Álvarez-Salgado et al. (2023).

Distribution of CDOM in the oceans has been assessed by satellite estimates and by in situ field observations. Whereas satellite techniques only permit to characterize the surface ocean, in situ observations allows the characterization of the full water column. World Ocean patterns were reported by satellite observations (e.g. Bricaud & Morel, 1981; Nelson et al., 2010; Siegel et al., 2002), that reflect those obtained during in situ observations (e.g. Catalá et al., 2015; Kitidis et al., 2006; Swan et al., 2009). Lower values were reported in the subtropical gyres, where primary production is lower and photochemical degradation is higher. Conversely, the highest CDOM levels were found in subpolar oceans and upwelling regions, where primary production is higher and significant DOM inputs from the continents are present. In the open ocean, microbial processing is the major responsible for

new CDOM production (Rochelle-Newall & Fisher, 2002), whereas surface photobleaching plays the role of the main sink (Nelson et al., 1998; Swan et al., 2012).

A small fraction of the CDOM pool has the capacity to emit part of the absorbed radiation in the form of blue fluorescence constituting the fluorescent DOM (FDOM) pool (Fig. 1.5). Fluorescence occurs when molecules return from electronically excited state to ground state after first loosing energy to molecular vibration and internal conversion (Stedmon & Nelson, 2015). Excitation-emission matrices (EEMs) is the most common technique used for characterize DOM in terms of its composition and origin (Coble, 1996) that was first introduced by Weber (1961). It consists in a number of fluorescence emission scans at different excitation wavelengths that are compiled into a matrix. EEMs are commonly presented as the intensities of the individual excitation-emission pairs or peaks that are associated with specific compound classes (Coble, 2007).

Two types of DOM fluorescence signals or fluorophores are the most common in natural waters (Fig. 1.5): i) humic-like, with absorption maxima at > 300 nm and fluorescence emission in the visible range (> 400 nm); and ii) protein-like, with absorption maxima at < 300 nm and fluorescence emission in the UV region of the spectrum (< 400 nm) (Álvarez-Salgado et al., 2023; Coble, 1996). Humic-like fluorescence is related to aromatic humic substances of terrestrial and aquatic origins (Coble, 2007). These substances are complex by-products from organic matter decomposition containing aromatic rings and carboxylic substituents as the main components. They are classically divided into four main groups of individual excitation-emission peaks defined by Coble (1996) and Stedmon et al. (2003): peak A (Excitation (Ex)/Emission (Em) 250 nm/435 nm), peak C (Ex/Em 340 nm/440 nm), peak M (Ex/Em 320 nm/410 nm) and peak E (Ex/Em 450 nm/520 nm). Peak A is related to general humic-substances, peak C and M are related to terrestrial and marine humic-substances, respectively, and peak E is related to soil fulvic acids (Coble, 1996; Stedmon et al., 2003).

Conversely, the protein-like fluorescence is related to the aromatic amino acids phenylalanine (Ex/Em 260 nm/280 nm), tryptophan (peak T, Ex/Em 275 nm/340 nm) and tyrosine (peak B, Ex/Em 275 nm/310 nm) (Coble, 2007; Jørgensen et al., 2011). The protein-like fluorescence is used to trace the presence and abundance of proteins in natural marine waters since these aromatic amino acids are present in all proteins, with major presence of tryptophan and tyrosine over phenylalanine (Álvarez-Salgado et al., 2023;

Yamashita & Tanoue, 2003). Therefore, the study of the FDOM fraction is of valuable interest, providing information about terrestrial vs. marine origin and biological vs. photochemical transformations (Álvarez-Salgado et al., 2023).

The most widespread approach to process large EEM datasets is the parallel factor analysis (PARAFAC) (Stedmon & Bro, 2008). PARAFAC can decompose the overlapping fluorescence spectra into components that correspond to individual fluorophores (Fig. 1.6) (Murphy et al., 2013; Stedmon & Bro, 2008). Spectral fluorescence data are multi-way, i.e. more than two dimensions, in this case three-way of data, as the fluorescence of a sample depends on the wavelength of light absorbed (excitation) and the wavelength at which the fluorescence is observed (emission). The three-way dataset is decomposed by PARAFAC into a set of trilinear terms (a, b and c) fitting to Eq. 1 by minimizing the sum of squares of the residuals (e):

$$X_{ijk} = \sum_{f=1}^{F} a_{if} \cdot b_{if} \cdot c_{kf} + e_{ijk} \tag{1.1}$$

where i = 1, …, I represent the sample, j = 1, …, J represents λ_{Em}; k = 1, …, K represents λ_{Ex}; x_{ijk} represents the measured fluorescence intensity of sample i at λ_{Em} = j and λ_{Ex} = k; e_{ijk} represents the residual of the fitting; f = 1, …, F correspond to a PARAFAC component; and a_{if}, b_{if} and c_{kf} are the outputs of the model. a_{if} is the concentration of component f in sample i; b_{if} and c_{kf} are the normalized emission and excitation intensities of component f at λ_{Em} = j and λ_{Ex} = k by means that multiplying vectors b and c produces the EEM of component f. Summarizing the properties of the PARAFAC, 1) two components cannot have the same intensity or EEM; 2) the normalized excitation spectra of a component is invariant across emission wavelengths and vice versa; 3) fluorescence intensity of each component correlates linearly with concentration (Lambert-Beer law); and 4) total fluorescence intensity is due to the linear combination of the components so that quenching, interactions between fluorophores or changes in the electronic environment of the fluorophores are negligible (Álvarez-Salgado et al., 2023; Murphy et al., 2013; Stedmon & Bro, 2008).

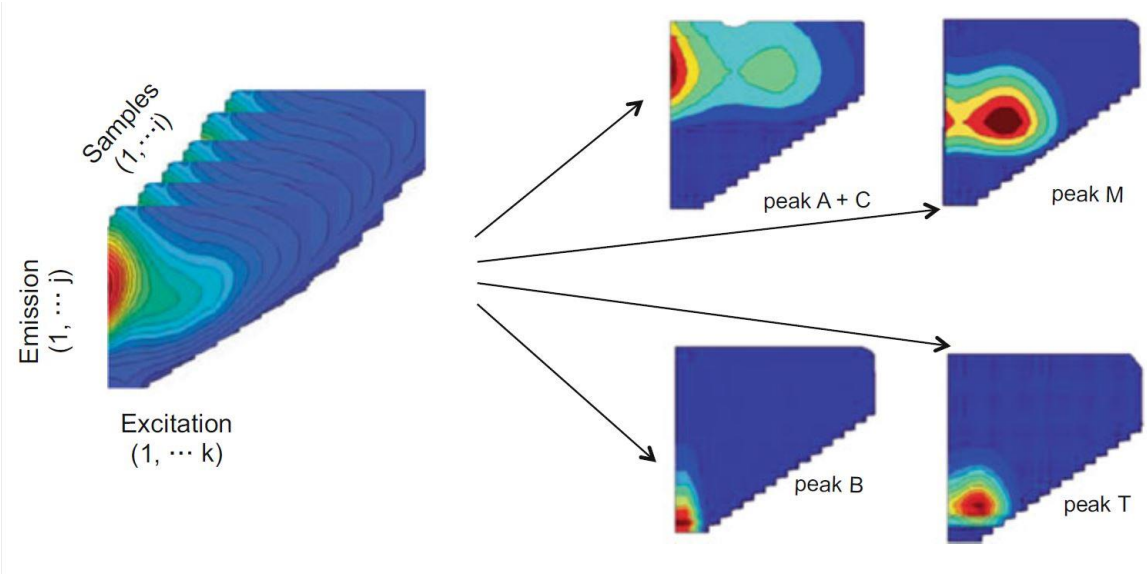

Figure 1.6: PARAFAC applied to an EEM dataset arranged in a multi-way (three-way) structure and decomposed into four PARAFAC components. Data from the Malaspina circumnavigation. Taken from Álvarez-Salgado et al. (2023).

The distribution of FDOM in the open ocean show in general terms lower concentrations of humic-like substances in surface waters due to photochemical degradation, which increase moderately with depth where these substances are produced by the microbial processing of organic matter (Jørgensen et al., 2014; Kinsey et al., 2018; Lønborg et al., 2009; Nieto-Cid et al., 2006). Regarding protein-like substances, opposite distribution was reported, with higher values at surface, where they are originated as by-products of photosynthetic activity, and decreasing with depth due to the rapid consumption by heterotrophic bacteria (Catalá et al., 2015; Jørgensen et al., 2011; Nelson & Gauglitz, 2016).

1.4 Isotopic characterization of DOC (δ^{13}C-DOC)

1.4.1 Principles of isotope geochemistry

Isotopes are atoms whose nuclei contain the same number of protons but a different number of neutrons. The term "isotopes" is derived from the Greek (meaning equal places) and indicates that isotopes occupy the same position in the periodic table. Isotopes can be divided into stable and unstable (radioactive) species. The latter have the property of emit energy in form of ionizing radiation in a process called radioactive decay. This process is unique for each radioisotope and is measured with a time period called half-life. On the contrary, stable isotopes have a negligible probability of natural decay and their half-life can be extremely large, even longer than the age of the Universe (Sharp, 2017).

There are 15 known isotopes of carbon, with atomic mass numbers ranging from 8 to 22 (Haynes, 2016), of which only ^{12}C and ^{13}C are stable. ^{14}C is a radioactive isotope with a half-life of 5730 ± 30 years (Godwin, 1962) and the remaining radioisotopes present half-lives too short (< 20 min; Haynes, 2016) that precludes any observation of their natural abundances in the environment (Beaupre, 2015). ^{12}C and ^{13}C isotopes comprise 98.93% and 1.07% of Earth's carbon inventory, respectively, and the chemical and physical effects that alter the natural abundances in the ratio $^{13}C/^{12}C$ are called 'fractionation processes' or 'isotope fractionation'. Isotopic fractionation is produced mainly by isotope exchange reactions (equilibrium isotope distribution) or by kinetic processes, which depends primarily on differences in reaction rates of isotopic molecules (Hoefs, 2021). Therefore, the extent of fractionation depends on the chemical, physical and biological processes at play, and it is sensitive to the conditions under which they occur (Beaupré, 2015).

The $^{13}C/^{12}C$ ratio (R) of a sample is commonly express in delta notation (δ), representing the perthousand (‰) deviation from the $^{13}C/^{12}C$ ratio of an internationally accepted material or standard known as PDB (Pee Dee Belemnite) in the case of carbon, following the equation:

$$\delta^{13}C = \left(\frac{R_{sample}}{R_{standard}} - 1\right) \cdot 1000 \qquad (1.2)$$

The formation of organic carbon occurs primarily by reduction of CO_2 during photosynthesis. The main isotope fractionation steps during biological carbon fixation are: 1) the preferential uptake of ^{12}C from CO_2 and intracellular diffusion of CO_2 and 2) the biosynthesis of cellular components (Degens et al., 1968b; Deuser et al., 1968; Hoefs, 2021). These statements suggest that fractionation depends on partial pressure of CO_2, where an unlimited amount of CO_2 available to a plant, the enzymatic fractionation will determine the difference between the original carbon source and the final bio product. On the contrary, whether CO_2 is a limiting factor, its diffusion into the cell will be slow, resulting in a smaller isotope fractionation (Farquhar et al., 1982: Hoefs, 2021). During photosynthesis, CO_2 is converted into two molecules of phosphoglycerate (PGA) by the enzyme ribulose-1,5-bisphosphate-carboxilase/oxygenase (RubisCO) in a process called carboxylation. Each PGA molecule contains three atoms of carbon, constituting the C3

photosynthetic pathway. The selectively removal of 'light' CO_2 (i.e., ^{12}C from ^{13}C) during carboxylation leads to the major carbon isotope fractionation in plants (Hoefs, 2021; Park & Epstein, 1960; Sharp, 2017). Two other photosynthetic pathways (C4 and Crassulacean Acid Metabolism, CAM) evolved in hot and arid areas minimizing photorespiration, which is a benefit under conditions of low pCO_2. This results in a lower isotope fractionation since all the available CO_2 is taken into the cell (Hatch & Slack, 1966).

1.4.2 Photosynthesis in aquatic systems

Aquatic photosynthetic organisms derive their carbon from the dissolved inorganic carbon (DIC) pool. Some studies have evaluated the processes by which phytoplankton assimilates inorganic carbon during photosynthesis and whether different organisms preferentially take dissolved CO_2 (CO_{2aq}) or bicarbonate (HCO_3^-) (Burkhardt et al., 1999; Degens et al., 1968a; Keller & Morel, 1999; Laws et al., 1997; Popp et al., 1998). There is an isotopic fractionation between both carbon species, with the CO_{2aq} resembling the atmospheric CO_2 composition (c.a. -8‰) and bicarbonate resembling the inorganic carbon composition in the ocean (c.a. 0‰) (Mook et al., 1974). Burkhardt et al. (1999) concluded that CO_2 flux into the cell constitutes a substantial portion of gross total carbon uptake in the species tested since their growing rates and isotope fractionation changed under different conditions of pCO_2. Those changes would not be expected if cells could take up only HCO_3^- directly from the medium. They also pointed out that changes in environmental conditions such as pCO_2, temperature, growth rates, cell size, light intensity or limiting nutrients affected the extent of fractionation, precluding a clear distinction between CO_{2aq} and HCO_3^- uptake. Other studies reported that some diatoms are able to assimilate HCO_3^- directly from the environment in the absence of the enzymatic reaction of carbonic anhydrase, which converts the HCO_3^- to CO_2 prior to enter the cell (Colman & Rotatore, 1995; Rotatore et al., 1995).

In summary, both CO_{2aq} and HCO_3^- are able to be assimilated by phytoplankton in marine waters depending on several biological and environmental conditions and one cannot distinguish between the inorganic carbon source in algal cells based on isotope data alone if they are not accompanied by additional information (Burkhardt et al., 1999; Keller & Morel, 1999; Laws et al., 1997). Then, the carbon isotopic composition of phytoplankton usually ranges between -18 and -31‰ (Boutton, 1991), depending on all the factors explained above. In addition, it is well known that ^{13}C is not uniformly distributed within

the plant, but varies between the different constituents like carbohydrates, proteins and lipids, being the latter considerably depleted relative to the other products of biosynthesis probably due to kinetic isotope effects (DeNiro & Epstein, 1977; Monson & Hayes, 1982). Nevertheless, marine plankton have been reported within an average isotopically heavier range (-20 to -24‰) than terrestrial plants (-25 to -30‰) (Boutton, 1991) even though both kind of organisms uses the C3 metabolic pathway (O'Leary, 1981). Some likely reasons for this could be due to a lower CO_2 diffusion into the cell in aquatic environments (O'Leary, 1981) or differences in the carbon source, where marine organisms are able to assimilate bicarbonate, with a heavier isotope composition relative to atmospheric CO_2 (Burkhardt et al., 1999; Keller & Morel, 1999; Marty & Planas, 2008). Adicionally, metabolic labeling and genome sequencing data suggest that green algae and diatoms may also perform C4 photosynthesis (Roberts et al., 2007; Xu et al., 2012).

1.4.3 Carbon isotopic composition of DOC (δ^{13}C-DOC)

The stable carbon isotope composition of DOC (δ^{13}C-DOC) depends on several factors such as the carbon source, the mechanisms by which that carbon was transformed and the environmental conditions in which those transformations occurred (Beaupré, 2015). Moreover, the bulk DOC isotopic ratio is an average of all the isotope ratios of the individual DOC compounds. This can be represented by a mass balance equation in which the bulk DOC isotope ratio (R_{bulk}) is the sum of the isotope ratio of each component (R_i) from $i = 1$ to n components, multiplied by their respective mole fractions of carbon atoms X_i, following the equation:

$$R_{bulk} = \sum_{i=1}^{n} R_i X_i \tag{1.3}$$

If the individual isotope ratios of the components are known, the mass balance equation can be used to calculate their relative proportions in the bulk DOC. However, in most cases, a significant overlap in the δ^{13}C exists between different carbon sources, making ambiguous the interpretation of the results (Beaupré, 2015).

The main carbon source of oceanic DOC comes from the primary producers at the surface layer (Álvarez-Salgado & Arístegui, 2015; Carlson & Hansell, 2015). However, other organic carbon sources are present in the DOC pool, originating in the ocean itself or from

terrestrial inputs (Follett et al., 2014). The continental sources include atmospheric deposition of black carbon from fossil fuels combustion and biomass burning (Kuhlbusch, 1998; Masiello & Druffel, 1998), and the continental runoff of organic carbon from C3 and C4 plants (McNichol & Aluwihare, 2007; Raymond & Bauer, 2001). Other sources described are the dissolution of sinking particulate organic carbon, the chemosynthetic organic matter from deep ocean hydrothermal vents (Lang et al., 2006; McCarthy et al., 2010) or the organic matter derived from oxidation of sedimentary methane (Pohlman et al., 2010). All these sources represent a wide range of $\delta^{13}C$ signatures with different cycling timescales (Beaupré & Druffel, 2009; Eglinton & Repeta, 2004; Griffith et al., 2012).

The degradation of DOC by heterotrophic bacteria has an imprint in the isotopic $\delta^{13}C$-DOC signature. Isotopic analysis of individual constituents of DOC have reported some differences on its $\delta^{13}C$. Labile compounds as carbohydrates and proteins presents higher $\delta^{13}C$ values compared to other constituents like lipids (Loh et al., 2004; Williams & Gordon, 1970). This means that in surface ocean productive waters where a higher proportion of labile DOC is present, a heavier $\delta^{13}C$ signature of total DOC is expected. Conversely, in subsurface and dark ocean waters where the most labile DOC has been degraded, depleted $\delta^{13}C$-DOC compounds remain, composed by a higher proportion of lipids and other depleted constituents conforming the low molecular weight fraction (Broek et al., 2020; Zigah et al., 2017).

1.5 The Cape Verde Frontal Zone

1.5.1 Oceanographic setting

There are four major Eastern Boundary Upwelling Ecosystems (EBUE's) in the World Ocean: California Current System (CalCS), Humboldt Current System (HumCS), Canary Current System (CanCS) and Benguela Current System (BenCS) (Bograd et al., 2023; Chavez & Messié, 2009) (Fig. 1.7). These areas are biologically productive regions that comprise only 1% of the world ocean in extension but represent up to 5% of the ocean global primary production (Behrenfeld & Falkowski, 1997; Carr, 2001), up to 20% of the global fisheries capture (Fréon et al., 2009; Pauly & Christensen, 1995), and around 40% of the carbon sequestration by the biological pump (Muller-Karger et al., 2005). Their high productivity is created by large-scale atmospheric pressure systems that favor along-shore and equatorward winds, which in combination with the Coriolis effect produce the

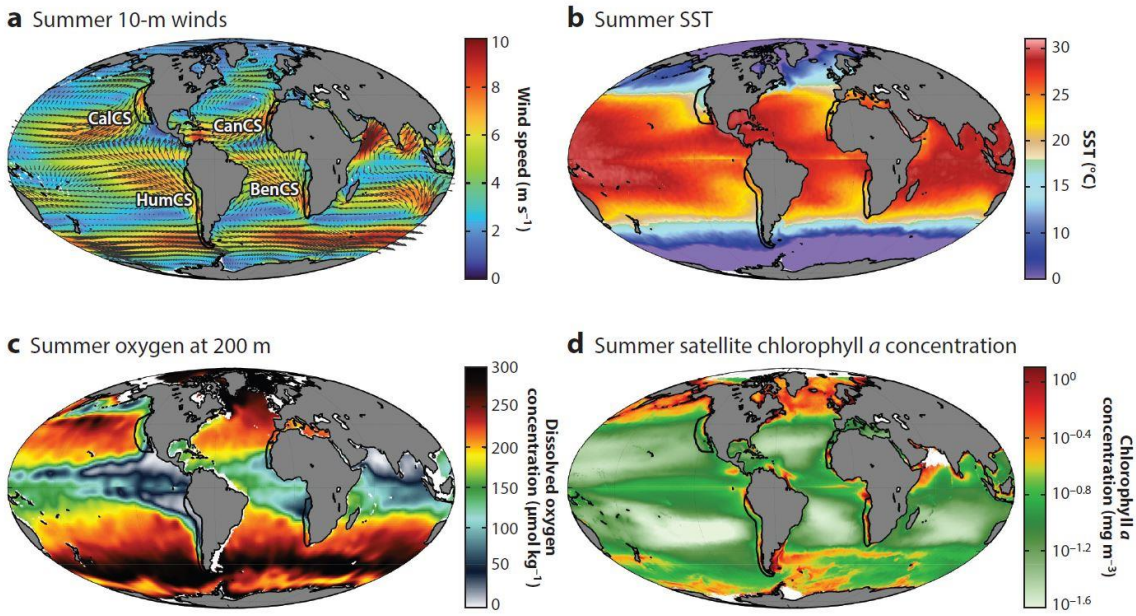

Figure 1.7: Global means on a) wind speed; b) Sea Surface Temperature (SST); c) dissolved oxygen concentration and d) clorophyll-a concentration during the summer period (June to August in the Northern Hemisphere and January to March in the Southern Hemisphere. The location of the four EBUEs is shown in black lines at the continental margins in each panel. Taken from Bograd et al. (2023)

advection of surface waters offshore and the subsequent upwelling of deeper, cold and nutrient-rich waters into the coastal photic zone, fueling the primary production in the form of phytoplankton blooms (García-Reyes et al., 2015).

The Cape Verde Frontal Zone (CVFZ), term that was first introduced by Zenk et al. (1991) to refer to an area situated within the CanCS, at the confluence of the North Atlantic subtropical and tropical gyres extending from Cape Blanc to Cape Verde Islands (17ºN - 21ºN). The frontal system is created by a wide northeast – southwest thermohaline front called the Cape Verde Front (CVF), formed by the meeting of the saltier, nutrient-poorer and oxygen-richer Eastern North Atlantic Central Water (ENACW) and the fresher, nutrient-richer and oxygen-poorer South Atlantic Central Water (SACW) **(**Fig. 1.8**)** (Burgoa et al., 2021; Pelegrí & Peña-Izquierdo, 2015b; Pérez-Rodríguez et al., 2001; Zenk et al., 1991). Barton (1987) was the first to describe the CVF, indicating maximum horizontal gradients in temperature and salinity but not in density, dominated by interleaving processes with double-diffusive intrusions (Burgoa et al., 2021; Klein & Tomczak, 1994; Martínez-Marrero et al., 2008; Pérez-Rodríguez et al., 2001). Moreover, a large number of structures at meso- and submesoscale (mesoscale: 10-100 km and weeks; submesoscale: 1-10 km and 1-10 days) such as eddies, meanders and intrusions make really

complex the physical processes controlling its formation and evolution (Burgoa, 2022) and therefore, the dynamics that drives the biogeochemical distribution and cycling.

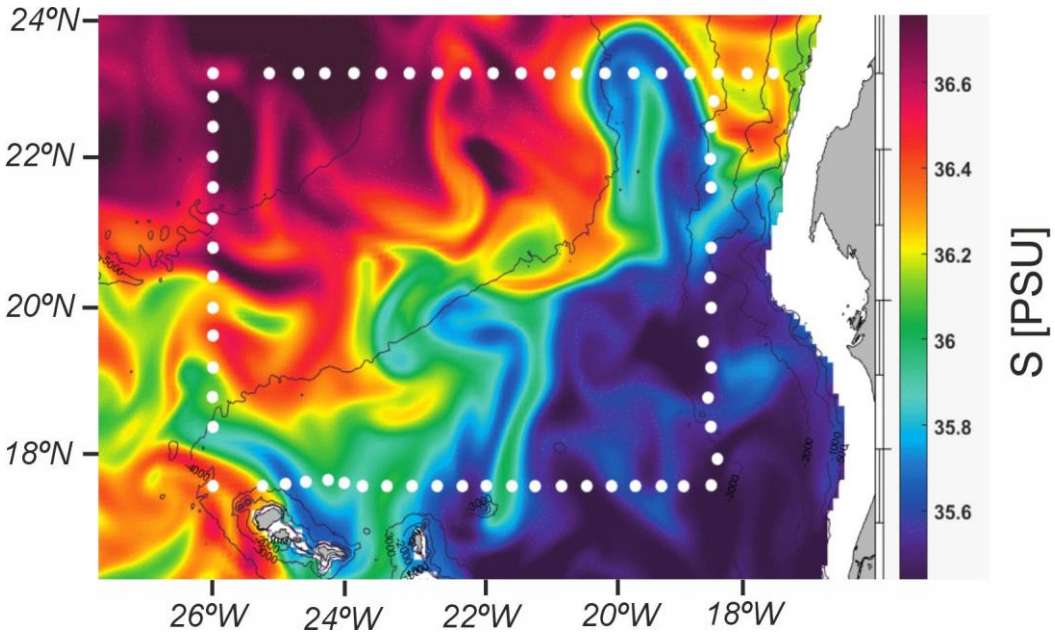

Figure 1.8. Salinity field at 150 m depth showing the encounter between the ENACW and SACW that creates the CVF. Reddish area represent the ENACW and the bluish area the SACW. PSU, practical salinity units. Obtained from Copernicus Marine Service (https://myocean.marine.copernicus.eu/).

1.5.2 Water masses in the CVFZ

Below the highly dynamic epipelagic layer (0 to 200 m depth), mesopelagic (200 to 1500 m depth) and bathypelagic (1500 m to bottom) waters are characterized by their richness in water masses of contrasting origin and biogeochemical history (Fig. 1.9). Central water masses are originated at the subtropical gyres of both hemispheres and spreads toward the equatorial regions (Pastor et al., 2015). They extend from approximately 100 to 700 m depth and are classified mainly into ENACW and SACW depending on its origin. ENACW originates in the North Atlantic subducting zone, reaching subsurface waters at lower latitudes through the thermocline circulation (Kawase & Sarmiento, 1985; Sarmiento et al., 1982). Conversely, SACW are formed at the subducting region of the South Atlantic subtropical gyre (Stramma & England, 1999). In turn, both ENACW and SACW are classified into different varieties depending on its thermohaline properties. NACW are subdivided into NACW of 15º and 12º, while SACW into 18º and 12º. Moreover, the Madeira Mode Water (MMW) is present in the area, originated at the Madeira region (Siedler et al., 1986).

The intermediate water masses are occupying the lower mesopelagic domain, approximately from 700 to 1500 m depth, consisted on the Subpolar Mode Water (SPMW), Mediterranean Water (MW) and Antarctic Intermediate Water (AA). The SPMW is other variety of the ENACW originated in the North Atlantic subducting zone (Boisséson et al., 2012; Pérez-Rodríguez et al., 2001). The MW is a very salty water mass originated from the mixing of the Mediterranean Overflow Water (MOW) from the Mediterranean Sea and entering the Atlantic through the Strait of Gibraltar and ENACW in the Gulf of Cadiz (Pérez-Rodríguez et al., 2001; Sánchez-Leal et al., 2017). The AA is formed in the Subantarctic Front, advected north to equatorial regions through the South Atlantic subtropical gyre (Suga & Talley, 1995).

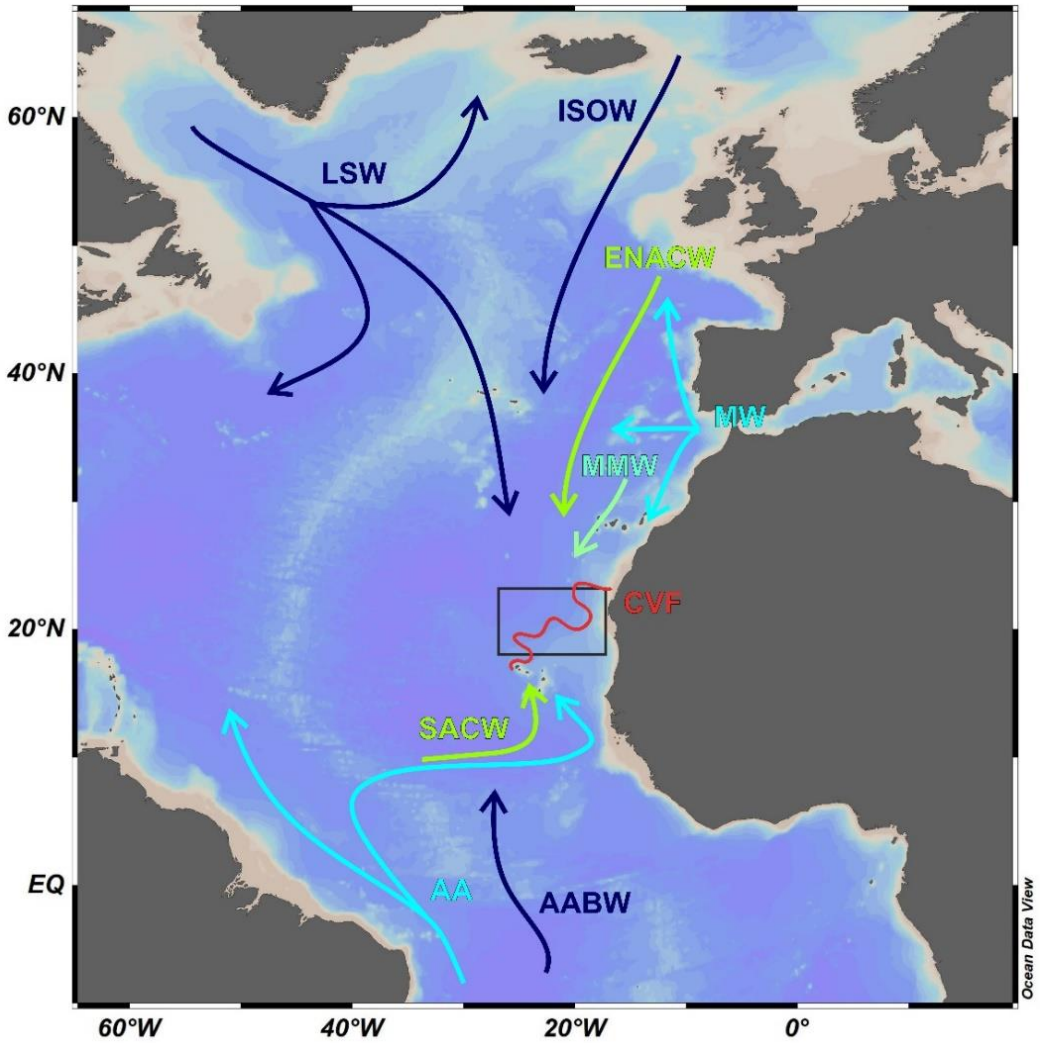

Figure 1.9: Schematic representation of the water masses origin that are present in the CVFZ. Green arrows indicate central water masses; light blue arrows indicate intermediate water masses and dark blue arrows indicates deep water masses. AABW and ISOW are primary water masses that form the NEADW (see main text for details). Adapted from Jerusalén-Lleó et al. (2023).

In the bathypelagic layer, three water masses arrive to the area, extending from 1500 m depth to bottom: Labrador Sea Water (LSW), from the Labrador Sea (Talley and McCartney, 1982) and two North East Atlantic Deep Water branches (NEADW), upper and lower, originally formed in the Northern North Atlantic but mixed with different proportions of Antarctic Bottom Water (AABW) and Iceland Scotland Overflow Water (ISOW) (Dickson & Brown, 1994; Fernández-Castro et al., 2019; Pastor et al., 2015; Valiente et al., 2022).

1.5.3 The boundary current system off NW Africa

The southeastern margin of the North Atlantic Subtropical Gyre (NASG) encompasses three major currents that flow predominantly southwards following an anticyclonic pathway: the Azores Current (AC); the Canary Current (CC), the Canary Upwelling Current (CUC) and the North Equatorial Current (NEC) (Stramma, 1984). Between the continental slope and the CUC, the Poleward Undercurrent (PUC) is flowing north, usually centered at 200-300 m depth (Barton, 1989). Extending from the Equator up to Cape Blanc (21ºN) and flowing in a cyclonic direction, the eastern margin of the North Atlantic Tropical Gyre (NATG) counts with the eastward North Equatorial Countercurrent (NECC), the Cape Verde Current (CVC) and the northward Mauritanian Current (MC). The confluence of the NASG and the NATG creates the CVF, where water is driven into offshore direction (Fig. 1.10) (Pelegrí & Peña-Izquierdo, 2015a). This convergence drives chlorophyll and nutrient-rich waters from the NATG and the coastal region into the southeastern margin of the NASG, maintaining a high rate of primary production that extends offshore by the presence of filaments (Gabric et al., 1993; Pastor et al., 2013). The upwelling system is functioning all year-round although is more intense during summer and fall (Pastor et al., 2008; Pelegrí & Peña-Izquierdo, 2015a).

1.5.4 Organic matter dynamics in the CVFZ

Apart from the CVF, the other major feature involved in the high dynamics of the CVFZ is the presence of the Cape Blanc Giant Filament (CBGF) (Fischer et al., 2009; Gabric et al., 1993; Helmke et al., 2005; Meunier et al., 2012; Nowald et al., 2015). Upwelled filaments are present along the NW African coast (Arístegui et al., 2009; Pelegrí et al., 2005), consisting on mesoscale structures associated to prominent capes that spread into the adjacent ocean from few hundred kilometers up to more than one thousand kilometer as in

the case of the CBGF (Álvarez-Salgado & Arístegui, 2015; Helmke et al., 2005; Meunier et al., 2012).

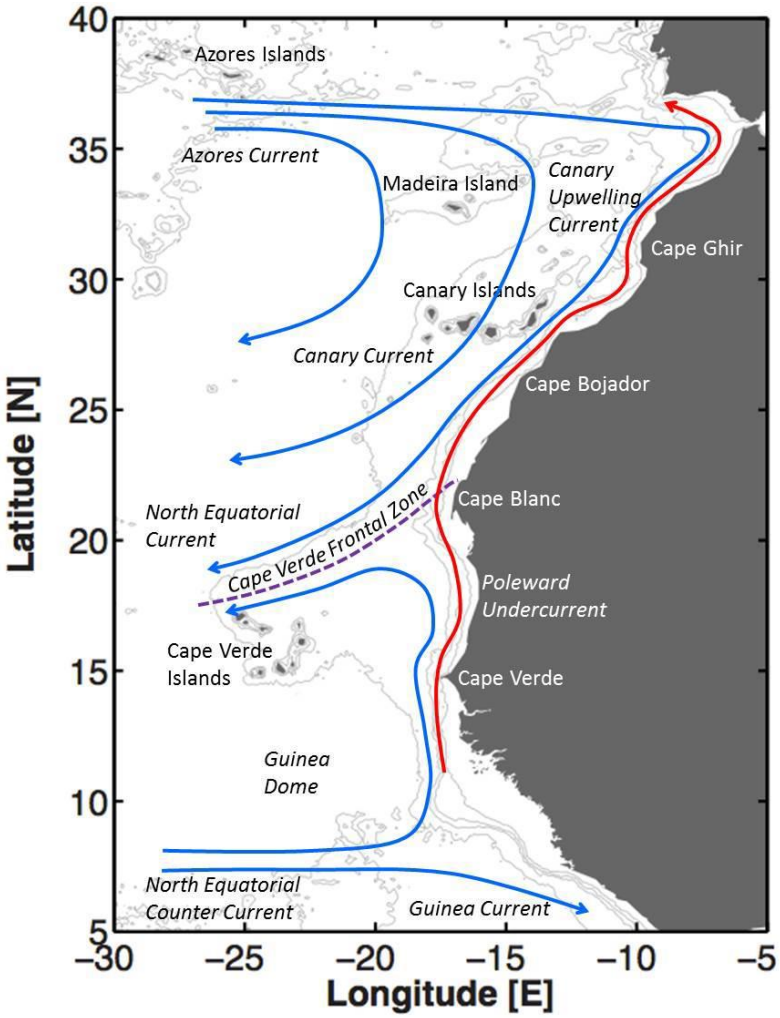

Figure 1.10. Scheme showing the main geographic features and oceanographic currents (in italics) along the Canary Current System. Taken from Pelegrí and Peña-Izquierdo (2015a).

Filaments play an important role regarding the lateral export of organic matter offshore as was reported in the pioneering studies of Van Camp et al. (1991) and Gabric et al. (1993), by means of sea surface temperature and ocean color satellite observations. They estimated that the CBGF could be responsible for the export of about 50% of the POM annual production in the area, implying that lateral export of suspended POM could exceed the vertical export of sinking POM. Nevertheless, these observations did not take into account the role of DOM, that was reported later for Canary Current filaments north of the CVFZ (García-Muñoz et al., 2004, 2005) as responsible of the export of about 33% of the freshly DOM produced in the shelf waters, a proportion much higher than that previously globally estimated by Hansell (2013) of <1% (Álvarez-Salgado & Arístegui, 2015).

The fate of the organic matter exported by the upwelled cold filaments remains uncertain. Observations with sediment traps concluded that part of the sinking POM is originated from the coastal waters (Fischer & Karakaş, 2009; Helmke et al., 2005; Neuer et al., 2002; Romero, 2002), suggesting that either the filament transports the sinking POC offshore or that suspended POM is aggregated forming sinking POM (Álvarez-Salgado & Arístegui, 2015). In addition, the adjacent Sahara dessert is a significant source of mineral particles entering the ocean by atmospheric deposition and producing a ballasting effect on both DOM and suspended POM by adsorption onto particles that increase the particle density and settling rates enhancing the biological carbon pump (Fischer et al., 2016; Iversen et al., 2010; van der Jagt et al., 2018). In addition, photochemical decomposition is also expected as a DOM sink and has been reported in the Cape Blanc area (Kitidis et al., 2014).

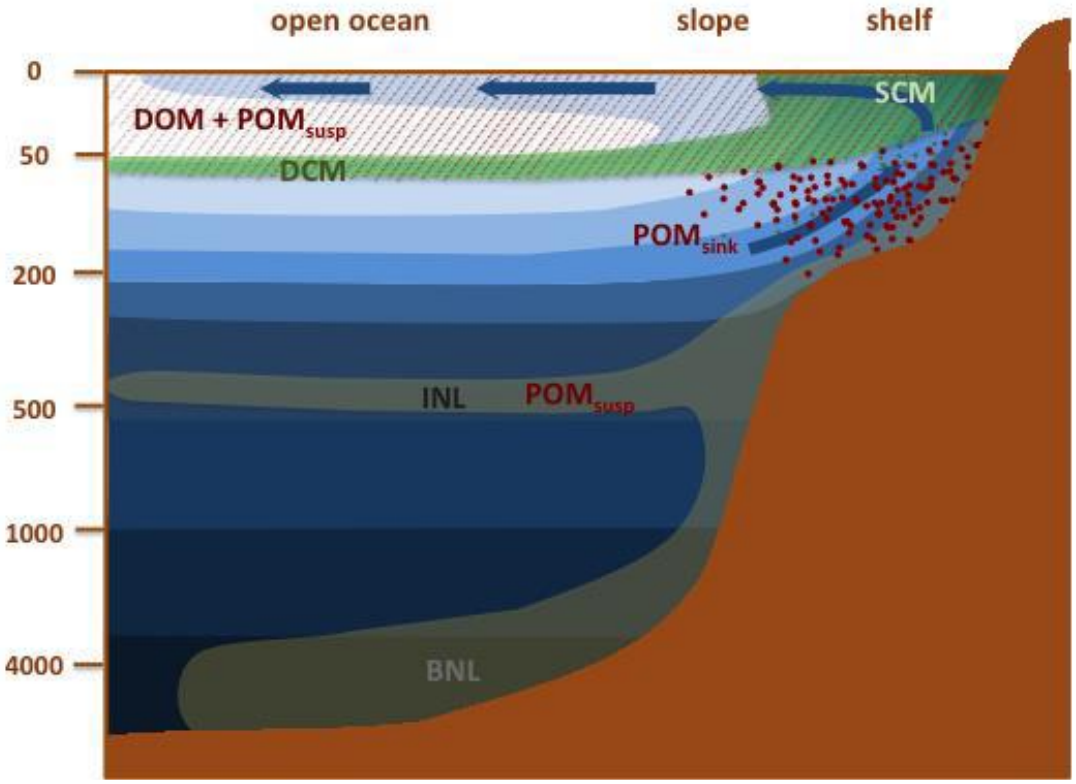

Figure 1.11: Scheme showing the export of dissolved (DOM), suspended particulate (POMsusp) and sinking (POMsink) organic matter in the EBUE of the CanCS through upwelling filaments and intermediate (INL) and bottom (BNL) nepheloid layers. Background color palette from dark blue to light blue indicates water temperature from cold to warm; blue arrows indicate the direction of the cold upwelled waters over the shelf and further direction offshore; green area shows the clorophyll distribution from a coastal surface chlorophyll maximum (SCM) to open ocean deep chlorophyll maximum (DCM); oblique dotted lines represent the area of DOM+POMsusp export; red dots indicate the POMsink and grey shades show the area of influence for the INL and BNL. Taken from Álvarez-Salgado and Arístegui (2015).

The distribution of POM in ocean margins is also controlled by the development of nepheloid layers (Fig 1.11**)** (McCave, 1986). Apart from the surface nepheloid layer that is associated with the primary produced biomass transported offshore by the upwelling filament, intermediate (INL) and bottom (BNL) nepheloid layers are commonly observed in the Mauritanian upwelling off Cape Blanc (Fischer et al., 2009, 2019; Karakaş et al., 2006), representing lateral inputs of organic material from the adjacent continental shelf and slope. Despite the experimental evidence of the presence of INL and BNL in the NW Africa upwelling system and its impact in the distribution of organic matter, the overall exchange rate between the coast and the open ocean is uncertain, due to estimations calculated by mass balance approaches (Ducklow & McCallister, 2004) rather than direct measurements. Alonso-González et al. (2009) carried out the first direct measurement of the lateral suspended POM export in the CanCS EBUE, reporting that it could account for 28 to 59% of the total mesopelagic respiration.

1.6 The FLUXES Project

FLUXES was a coordinated project funded by the Spanish Ministry of Science and Competitiveness entitled: 'Constraining organic carbon fluxes in an Eastern Boundary Upwelling system (Cape Blanc; NW Africa): the role of non-sinking carbon in the context of the biological pump'. It consisted of three sub-projects: biology (ref. PID2019-109084RB-C31), physical oceanography (ref. PID2019-109084RB-C32) and biogeochemistry (ref. PID2019-109084RB-C33). The latter is the subproject that mainly encompasses this thesis dissertation.

The main goal of the FLUXES project is to assess the relevance of DOM, suspended and sinking POM to the carbon fluxes and remineralization rates in the context of the biological pump in the Eastern Boundary Upwelling Ecosystem (EBUE) of NW Africa, specifically at the Cape Verde Frontal Zone (CVFZ), an area that connects the coastal and productive waters with the adjacent oligotrophic ocean. The main hypothesis to be tested is that offshore lateral advection of suspended POC and DOC, the secondary circulation at submesoscale and the vertical mixing contribute significantly to the export of organic carbon in EBUE's. The project consisted on a multidisciplinary observation program, based on two oceanographic cruises covering the large-scale variability in the first cruise (FLUXES I) and the meso- and submesoscale variability in the second cruise (FLUXES II; Fig. 1.12).

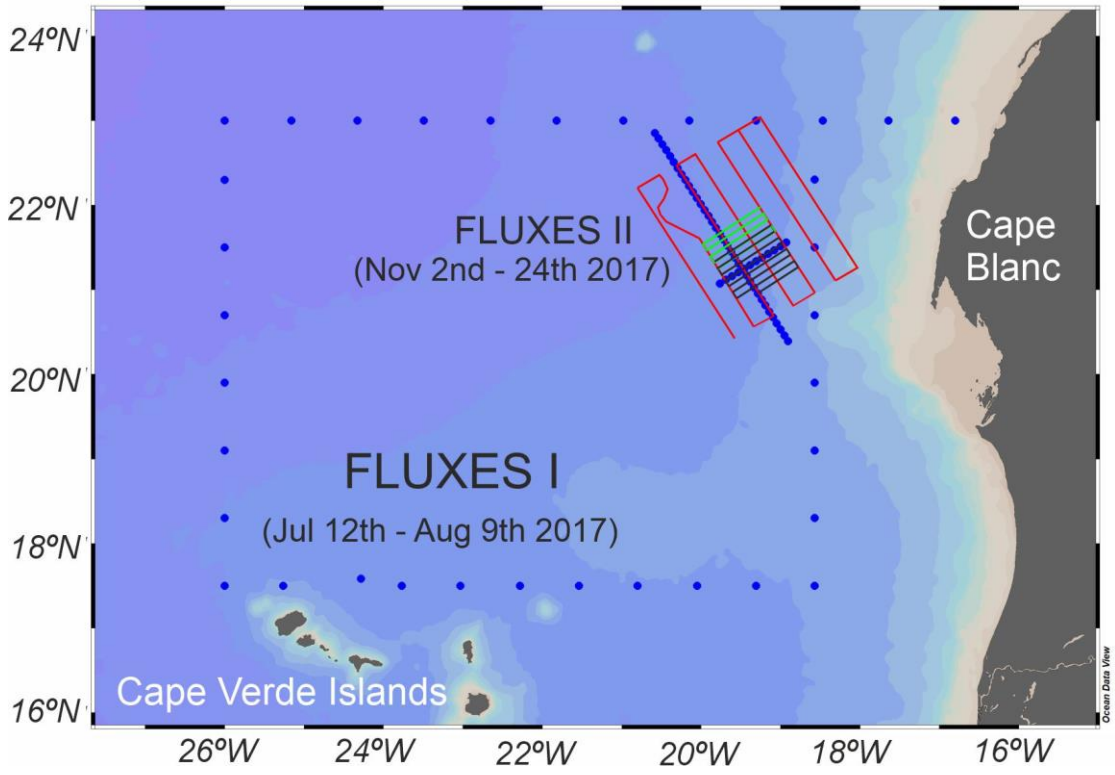

Figure 1.12: Map of the study area during cruises FLUXES I and FLUXES II at the Cape Verde Frontal Zone region. FLUXES I consisted on 35 hydrographic stations separated 30 NM arranged around a large-scale hydrographic box while FLUXES II consisted on three SeaSoar surveys and 48 hydrographic stations sampled at submesoscale resolution, every 5 NM.

1.7 Objectives and structure of this thesis dissertation

This PhD thesis aims to quantify the role of dissolved and suspended organic matter in the carbon biogeochemistry of the CVFZ. In order to fulfill this overall objective, we proposed the following specific objectives:

1. Assess the influence of the CVF and CBGF in the DOC and suspended POC distributions in the epipelagic layer of the CVFZ from a basin-scale approach on basis of the colored and fluorescent fractions of DOM and the physical and biogeochemical processes that dictate their variability.
2. Characterize the water masses present in the study area from their DOC, suspended POC, CDOM and FDOM properties. Evaluate the basin- and local-scale processes and structures that control the organic matter distribution and cycling in the mesopelagic and bathypelagic waters of the CVFZ.
3. Examine the coupling between the physical and biogeochemical properties and the impact that physical structures as mesoscale eddies, meanders and fronts produce in the biogeochemistry of DOC and suspended POC in the CVFZ at the meso- and

submeso-scale range. Assess the influence of the Sahara dust on the DOM variability through the optically active fraction of DOM.

4. Evaluate the role of the CVF and the CBGF on the carbon isotopic distribution of DOC (δ^{13}C-DOC) in the epipelagic waters of the CVFZ from the basin- to the meso- and submeso-scale. Characterize the water masses present in the study area from their carbon isotopic signature, analyze the biogeochemical transformations of DOC by its isotopic fractionation and establish the possible organic carbon sources.

On basis of these specific objectives, we have organized this thesis dissertation in the following chapters:

Chapter 1 presents a general introduction to the global carbon cycle, centered in the ocean and the main carbon pumps. A general overview of dissolved organic matter is presented, with focus on the optical and isotopic characterization approaches. Finally, a description of the study area and its oceanographic and biogeochemical relevance is presented.

Chapter 2 describes the biogeochemistry of DOC, POC and the optically active fraction of DOM in the CVFZ at the large scale during the FLUXES I cruise. The impact of the Cape Verde Front and the Cape Blanc Giant Filament on the distribution of the study variables and the biogeochemistry of epipelagic waters is studied. Local and basin-scale mineralization processes are investigated in the mesopelagic and bathypelagic waters, together with the production/consumption of organic matter in the dark ocean. The impact of nepheloid layers detached from the ocean margin is analyzed.

Chapter 3 describes the distribution of DOC, POC and the optically active fraction of DOM in the CVFZ at meso- and submesoscale resolution during the FLUXES II cruise. The tight coupling between physical and biogeochemical parameters, where physical submesoscale structures play an important role in the organic matter biogeochemistry is assessed. Moreover, the impact of atmospheric deposition of Sahara dust is postulated as a relevant source of fluorescent organic matter in the area. Local and basin-scale mineralization rates are analyzed in the mesopelagic waters.

Chapter 4 presents a detailed description of the methodology developed for the δ^{13}C-DOC measurements, consisting on an on-line coupling of a total organic carbon analyzer based on wet chemical oxidation with an isotope ratio mass spectrometer. Advantages and drawbacks of the methodology are discussed.

Chapter 5 assesses the δ^{13}C-DOC characterization of the tropical, subtropical and Cape Blanc Giant Filament domains in epipelagic waters and all the individual water masses present in the meso- and bathypelagic CVFZ during FLUXES I and FLUXES II, covering the large scale and the meso- and submesoscale range. The influence of the CVF and the CBGF as well as the water masses on the DOC isotopic distribution is analyzed, as well as the original carbon sources that may comprise the DOC pool in the area.

Chapter 6 presents a general discussion encompassing the results and specific discussion of each chapter, leading to the final conclusions of this thesis.

Chapter 7 includes the main conclusions obtained from this PhD thesis.

Chapter 2: New insights on dissolved organic matter cycling in the Cape Verde Frontal Zone from its optically active fraction

The research work presented in this chapter is prepared to be submitted to Progress in Oceanography.

Abstract

The DOC, POC and the optically active fraction of dissolved organic matter (DOM) has been investigated in the CVFZ. This is a highly dynamic system comprising 1) the thermohaline CVF, where North and South Atlantic central waters meet; 2) the Northwest Africa upwelling system, with the CBGF exporting organic matter produced over the shelf to the adjacent open ocean; and 3) the presence of intermediate and deep waters of contrasting origins (Mediterranean, Northern North Atlantic, Artic, Sub-Antarctic and Antarctic). A full-depth hydrographic box embracing the CVF and the CBGF was occupied in July-August 2017 to examine the impact of these hydrographic structures on the distribution of the DOC, suspended POC, CDOM and FDOM fractions of DOM. In the surface layer, absorption coefficients at selected wavelengths (254 and 320 nm) and fluorescence intensities of 5 identified components (3 humic- and 2 protein-like) were remarkably higher in the stratified, productive tropical surface waters South of the CVF and in the CBGF. On the contrary, subtropical surface waters North of the CVF were characterized by lower concentrations of optically active substances, probably due to both lower microbial production rates and more intense or sustained photochemical degradation than in the tropical and CBGF waters. This pattern results in a significantly lower average molecular weight of CDOM in subtropical waters, as suggested by the absorption spectral slopes. In the ocean interior, a low contribution of DOC (3.6 ± 2.1%) and suspended POC (4.5 ± 0.7%) to the organic matter mineralization was found, being the sinking POC the likely fraction supporting the local carbon demand. Although water mass mixing and large-scale mineralization along the water masses pathways from their respective formation areas were the main factors controlling the distributions of the optical properties of DOM, net generation of humic-like and net consumption of protein-like components were also observed locally in mesopelagic waters of the CVFZ. Remarkably, a well-developed bottom nepheloid layer (BNL) was noticed in bathypelagic waters close to the Mauritanian coast, characterized by prominent CDOM and humic-like FDOM signals that were not accompanied by an increase in AOU. The origin of these bottom CDOM and FDOM maxima is likely the release from 1) particles sinking from the epipelagic layer, ballasted with Sahara dust; and/or 2) from anoxic sediments. Absorption and fluorescence spectroscopy have allowed to gain understanding of the role of DOM in the carbon cycle of the CVFZ beyond the limited information provided by DOC profiles.

1. Introduction

Colored dissolved organic matter (CDOM) is the fraction of dissolved organic matter (DOM) capable of absorbing light at visible and UV wavelengths. CDOM is a ubiquitous component of the DOM pool in the ocean, although its contribution to dissolved organic carbon (DOC) varies depending on its proximity to the coast, being higher in coastal margins, where continental inputs transport larger amounts of these colored materials, and lower in open ocean waters (Coble, 2007; Nelson and Siegel, 2013). CDOM is a useful tracer for mixing processes and ocean mesoscale circulation structures such as meanders,

eddies and upwelling filaments (Coble, 2007; Stedmon and Nelson, 2015). CDOM also traces ocean biogeochemical processes; it is produced and consumed during organic matter processing in marine food webs and it is highly photoreactive and therefore degrades rapidly in the euphotic layer, producing smaller transparent organic carbon molecules, as well as carbon monoxide and dioxide (Del Vecchio and Blough, 2004; Swan et al., 2012; Twardowski and Donaghay, 2002). Absorption spectra of CDOM in natural marine waters are characterized by an exponential decay with increasing wavelength (λ), reaching undetectable values at $\lambda > 600$ nm. Variability in the spectra is caused by the natural occurrence of different chromophores. Drawing upon these properties, a series of indices that include absorption coefficients at specific wavelengths, coefficient ratios and spectral slopes are commonly used to trace the photochemical and biological processes in which CDOM is involved (Álvarez-Salgado et al., 2023; Nelson and Siegel, 2013). The reader is referred to Chapter 1 for more details about the CDOM properties.

Fluorescent DOM (FDOM) is the fraction of CDOM that emits part of the absorbed radiation in the form of blue fluorescence. The fluorescent properties of FDOM are limited to excitation wavelengths from 240 to 500 nm and emission wavelengths from 300 to 600 nm (Stedmon and Nelson, 2015). In natural waters, two main groups of fluorophores are the most abundant: protein-like, with emission wavelengths < 400 nm (UV range) and associated to the labile free or combined aromatic amino acids tyrosine, tryptophane and phenylalanine, and humic-like, with emission wavelengths > 400 nm (visible range), related to the recalcitrant humic and fulvic acids produced during organic matter degradation in soils or aquatic environments and that are highly sensitive to photodegradation (Coble, 2007; Stedmon and Nelson, 2015). The reader is referred to Chapter 1 for more details about the FDOM properties.

In this chapter, the dynamics of the colored and fluorescent fractions on DOM in the complex and highly-dynamic CVFZ is examined, located at the confluence of the North Atlantic Tropical and Subtropical zones, extending from Cape Verde Islands (17ºN) to Cape Blanc (21ºN). This region is characterized by the presence of a persistent thermohaline front, created by the confluence of the saltier, nutrient-poorer and oxygen-richer Eastern North Atlantic Central Water (ENACW) and the fresher, nutrient-richer and oxygen-poorer South Atlantic Central Water (SACW). This confluence feeds a rich meso- and submesoscale eddy field, which drives a vigorous exchange of salt, heat and nutrients (Campanero et al., 2022; Martínez-Marrero et al., 2008; Pelegrí and Peña-Izquierdo, 2015a;

Pérez-Rodríguez et al., 2001; Zenk et al., 1991). The area is also affected by the Canary Upwelling system, where large amounts of organic matter, including its colored and fluorescent fractions, are generated and exported offshore to the open ocean through upwelling filaments, as the Cape Blanc Giant Filament (CBGF) (Burgoa et al., 2021; Gabric et al., 1993; Helmke et al., 2005; Lovecchio et al., 2018; Pelegrí et al., 2006; Santana-Falcón et al., 2020). This region is therefore acting like a gateway through which organic matter from the upwelling region accesses the open ocean, with important implications for the biogeochemical functioning of the adjacent gyre. Below this highly dynamic epipelagic layer, meso- and bathypelagic waters are characterized by their richness in water masses of contrasting origin and biogeochemical history. Apart from the ENACW and SACW that encounter at the thermohaline Cape Verde Front and occupy the upper mesopelagic layer, three intermediate water masses are present in lower mesopelagic waters: Subpolar Mode Water (SPMW), with a Subpolar North Atlantic origin, Mediterranean Water (MW) and Antarctic Intermediate Water (AA) from the Subantarctic Front. In the bathypelagic layer, three water masses arrive to the area: Labrador Sea Water (LSW), and two flavors (upper and lower) of North East Atlantic Deep Water (NEADW), originally formed in the Northern North Atlantic but mixed with different proportions of Antarctic Bottom Water (AABW) (Fernández-Castro et al., 2019; Pastor et al., 2015; Valiente et al., 2022).

The hydrography and circulation (Burgoa et al., 2021) and the biogeochemistry of suspended and dissolved organic carbon and nitrogen (Valiente et al., 2022) have been recently studied in the CVFZ on the basis of the distributions obtained in a hydrographic box occupied during the FLUXES I cruise, in July-August 2017 (Fig. 2.1). Here, the optical properties of DOM (CDOM and FDOM) are examined, where the impact of 1) existing fronts and filaments in the upper ocean; and 2) mixing of water masses of contrasting origin in the ocean interior; together with 3) photochemical and microbial processes on the distributions of CDOM and FDOM are analyzed. This study will attempt to gain a better understanding of the origin, processing and fate of DOM in this buffering region, connecting the coastal and productive waters with the adjacent oligotrophic ocean and obtaining new insights about carbon sequestration through sinking particles and DOM cycling in the deep ocean.

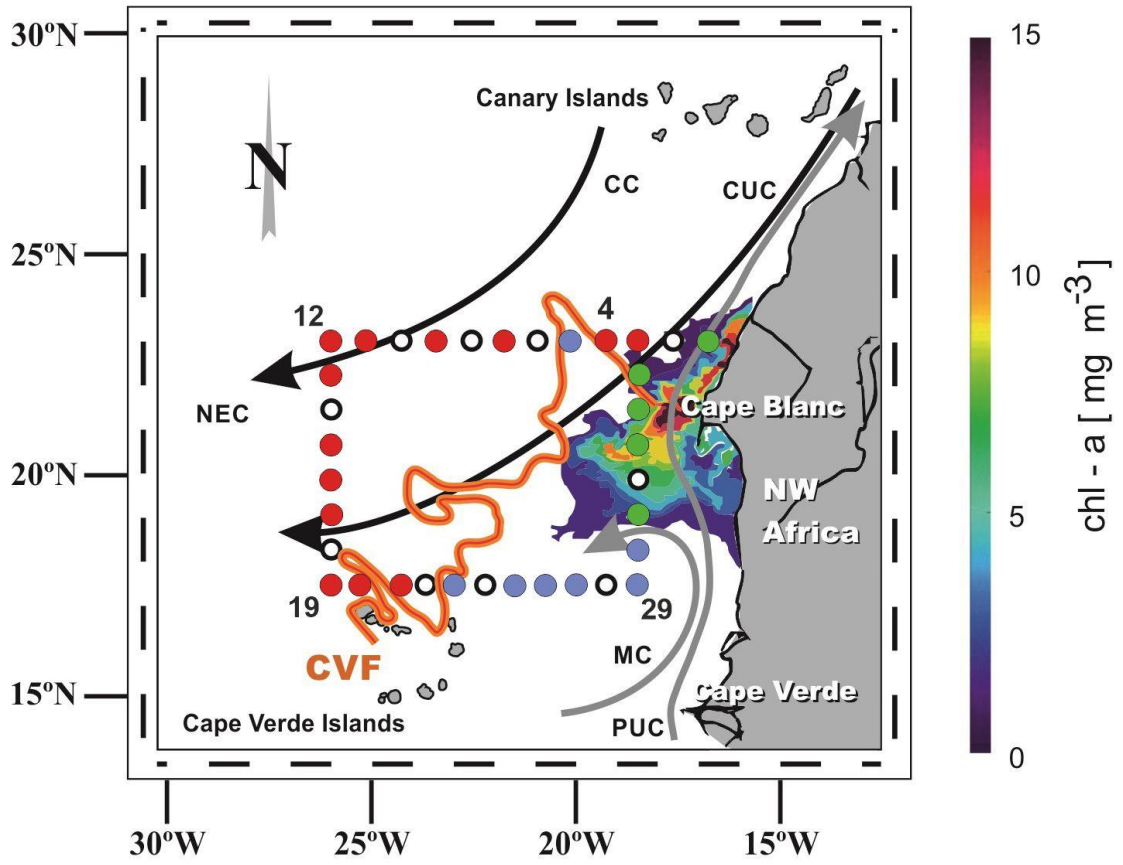

Figure 2.1. Map of the Fluxes I cruise. The colored dots represent the hydrographic stations with data of optical properties (CDOM and FDOM) (red: North of the CVF; blue: South of the CVF; green: waters of the CBGF) and the empty dots are the stations without data of the optical properties. Numbers indicate the station number from 1 to 35. Black arrows represent the Canary Current (CC), Canary Upwelling Current (CUC) and North Equatorial Current (NEC), grey arrows represent the Mauritania Current (MC) and the Poleward Undercurrent (PUC) (taken from Pelegrí and Peña-Izquierdo, 2015). The orange line represents the position of the CVF during the cruise (taken from Burgoa et al., 2021) and the colored contour represents the satellite Chlorophyll-a linked to the CBGF on July 24th 2017 (Copernicus Marine System). Modified from Valiente et al. (2022).

2. Materials and Methods

2.1 Sampling strategy and analytical procedures

The FLUXES I cruise took place from 12 July to 9 August 2017 on board R/V Sarmiento de Gamboa embarking and disembarking in Las Palmas (Canary Islands). Four transects defining a box were conducted off the coast of Mauritania in the CVFZ, with a total of 35 hydrographic stations 50 nautical miles apart (Fig. 2.1). Transects were named as North, West, South and East, depending on their relative position in the box. Water samples were collected using a rosette sampler equipped with 24 Niskin bottles of 12 liters. The rosette

was also equipped with conductivity-temperature-depth (SBE911 plus), oxygen (SBE43), fluorescence of chlorophyll (SeaPoint SCF) and turbidity (SeaPoint STM) sensors. Three types of stations were occupied: short (3h), medium (9h), and long (27h). Sampling depth range covered down to 4000 m in the medium and long stations, and down to 2000 m in the short stations.

2.2 Core variables

CTD conductivity, dissolved oxygen (O_2) and chlorophyll (Chl-*a*) fluorescence sensors were calibrated using water samples taken from the rosette. Salinity was calibrated using a Guildline 8410-A Portasal salinometer, and conductivity measurements were converted into practical salinity units using the (UNESCO, 1985) equation. Dissolved oxygen (O_2) was determined using the Winkler potentiometric method with the procedure described in Langdon (2010). Apparent oxygen utilization (AOU) was calculated following Benson and Krause (UNESCO, 1986), where AOU = O_2sat – O_2, (O_2sat being the oxygen saturation concentration at local potential temperature and salinity). Chl-*a* was determined following the method of Holm-Hansen et al. (1965). It consists of filtering 500 mL of water through a Whatman GF/F filter and, after that, pigments were extracted in acetone (90% v/v) stored at 4ºC in the dark for 24h and then analyzed with a Turner Designs bench fluorometer model 10 AU, previously calibrated with pure Chl-*a* (Sigma Co.)

The pycnocline, defined as the layer separating the surface mixed layer from the waters immediately below, was identified by the absolute maximum of the squared Brunt-Väisälä frequency, N^2_{max} (Doval et al., 2001). It was calculated as follows:

$$N^2_{max} = g \cdot \frac{\ln(\rho_z/\rho_{z-1})}{z-(z-1)} \tag{2.1}$$

where g is gravity acceleration (9.81 m s^{-2}), and ρ_z is water density at atmospheric pressure at depth z (in kg m^{-3}), calculated from salinity and temperature using the equation of (UNESCO, 1985).

2.3 DOC, POC, CDOM and FDOM determinations

Suspended organic carbon (POC) and nitrogen (PON) were determined by collecting 5 L of water from the Niskin bottles and filtering through 25 mm Whatman GF/F pre-combusted filters (450 ºC, 4h) using a vacuum system with a pressure difference <300 mm

Hg. Filters were then placed into 2 mL Eppendorf vials and dried for 12h in a vacuum desiccator with silica gel. After that, filters were stored in a freezer at -20ºC until analyzed in the base laboratory. Concentrations of POC and PON were determined by high temperature catalytic oxidation (900ºC) in a Perkin Elmer 2400 elemental analyzer. The filters were not exposed to HCl fumes after checking their negligible $CaCO_3$ content.

For dissolved organic carbon (DOC) determination, 25 mL of water were collected into pre-combusted borosilicate glass vials and frozen at -20ºC until their subsequent analysis in the laboratory, performed by high temperature catalytic oxidation (680ºC) in a Shimadzu TOC-V (Pt-catalyst). Seawater was not filtered due to the low concentration of particulate matter. Samples were melted, acidified (pH < 2) and degassed with high purity N_2 before measurements. Potassium hydrogen phthalate (KHP; Merck) was used as standard to calibrate the equipment and consensus reference materials provided by Hansell's CRM Program (University of Miami, USA) were used to check the instrument performance. Our concentrations for the deep-sea water reference (Batch 16 Lot # 05-16) were 44.9 ± 1.7 µmol L^{-1} (n = 10) while the certified values are 43-45 µmol L^{-1}.

Water samples for the analyses of the colored and fluorescent fractions of DOM were taken from the Niskin bottles in the medium and long stations, collected in 250 mL acid-cleaned glass bottles and filtered through pre-combusted (450ºC, 4h) 47 mm Whatman GF/F filters in an all-glass filtration system under a positive pressure of high purity N_2. Filtered seawater was stored in the dark allowing to warm up to room temperature until on board analyses in the respective measuring cuvettes of the spectrophotometer for CDOM and spectrofluorometer for FDOM. Absorption spectra of CDOM were recorded using a double-beam spectrophotometer Jasco V-750 from 700 to 250 nm at 0.5 nm intervals. The instrument was equipped with 100 mm path-length quartz cells and Milli-Q water was used as a reference blank. Absorption coefficient spectra $a_{CDOM}(\lambda)$ (m^{-1}) were corrected by subtracting the Milli-Q spectrum and then applying the equation:

$$a_{CDOM}(\lambda) = 23.03\ [Abs(\lambda) - Abs(600\text{-}700)] \quad (2.2)$$

where Abs(λ) is the absorbance at wavelength λ, Abs(600-700) is the average absorbance between 600 and 700 nm, which corrects for scattering primarily caused by fine particulate material and micro-air bubbles, and the factor 23.03 converts to natural logarithm and also considers the 0.1 m cell path length. The absorption coefficient indices used in this work

were $a_{CDOM}(254)$, $a_{CDOM}(325)$, the ratio $a_{CDOM}(254)/a_{CDOM}(365)$, the spectral slope of the wavelengths bands 275 nm-295 nm ($S_{275-295}$) and 350 nm-400 nm ($S_{350-400}$), and the ratio of both spectral slopes S_R (Catalá et al., 2018; Coble, 2007; Engelhaupt et al., 2003; Helms et al., 2008).

Fluorescence excitation-emission matrices (EEMs) of the samples were recorded with a Perkin Elmer LS-55 spectrofluorometer using 10 nm excitation and emission slit widths, an integration time of 0.25 s, an excitation range of 240-450 nm at 10 nm increments and an emission range of 300-560 nm at 0.5 nm increments. Blanks were measured using freshly produced ultrapure water following the same procedure. Processing of the EEMs started by subtracting the blank measurements from seawater EEMs and correcting the first and second order Rayleigh dispersion bands. Then, EEMs were normalized to the Raman area, which was estimated applying the trapezoidal rule of integration (Murphy et al., 2010) on the emission scan at excitation 350 nm of the Milli-Q water blanks. Afterwards, the absorbance spectra of each sample was used to correct the EEMs for inner filter effects (Kothawala et al., 2013). To test for instrument variability during the cruise, daily measurements were performed on a sealed Milli-Q cuvette (Perkin Elmer) to check for the Raman region, and p-terphenyl and tetraphenyl butadiene blocks (Starna) to check for protein- and humic-like substances regions, respectively (Catalá et al., 2015b).

A parallel factor analysis (PARAFAC) was applied to decompose the fluorescence signal of the EEMs into the underlying individual fluorescent components (Bro, 1997). The PARAFAC was based on 294 corrected EEMs and performed using the DOM Fluor 1.7 and drEEM Toolboxes for Matlab. Five components were obtained (Fig. 2.2) after validation through split-half analysis and random initialization steps (Murphy et al., 2013; Stedmon and Bro, 2008). Components 1-3 (C1, C2, C3) correspond to humic-like substances, whereas components 4-5 (C4, C5) correspond to protein-like substances. . The Excitation (Ex)/ Emission (Em) maxima (in nm) of each component obtained by the PARAFAC is: C1 (240 (360)/450); C2 (310/405); C3 (280 (390)/485); C4 (270/355); and C5 (240/340), where the value in brackets for C1 and C3 indicates secondary maxima.

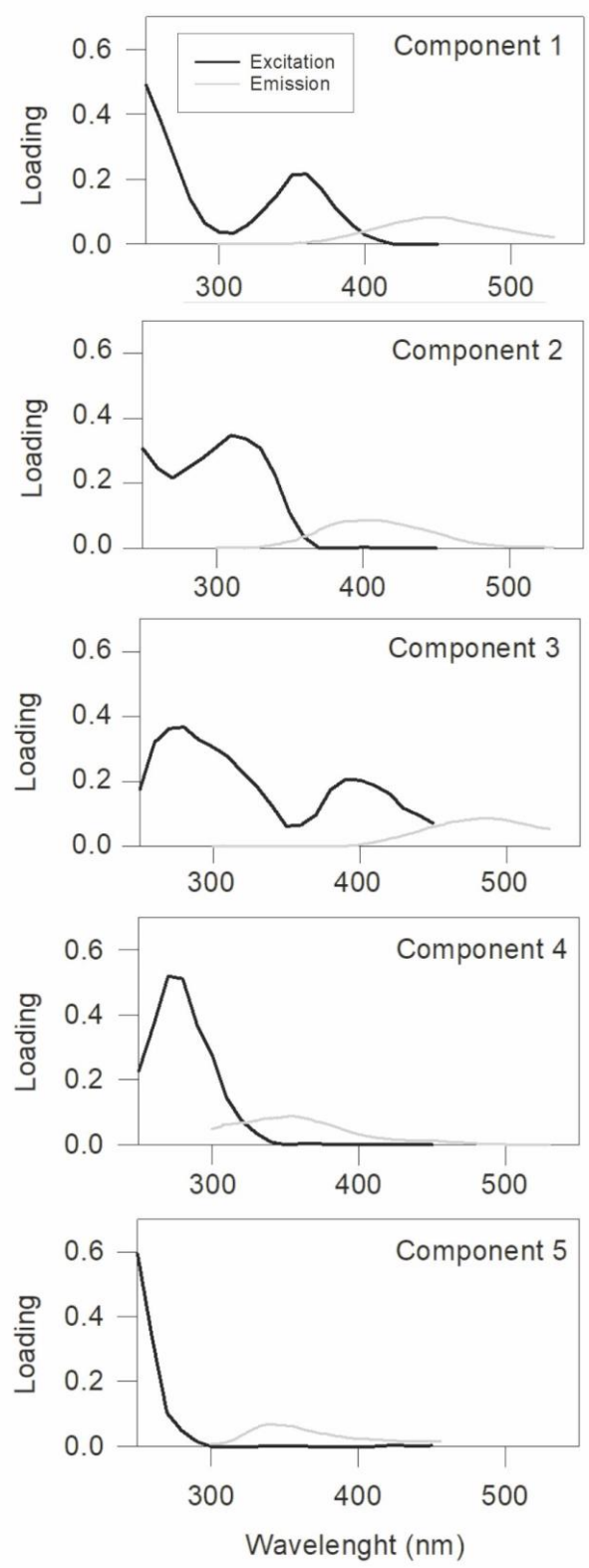

Figure 2.2. FDOM components derived from the PARAFAC analysis. Excitation (black) and emission (grey) spectra.

Moreover, C1 is a mixture of peaks A and C as defined by Coble (1996) and related to terrestrial humic-like substances. C2 is Coble's (1996) peak M, related to marine humic-like substances. C3 resembles peak D related to soil fulvic acids, i.e. of terrestrial origin (Stedmon et al., 2003). C4 and C5 are Coble's (1996) peaks T and B, identified as

tryptophan and tyrosine protein-like substances, respectively. For each component, we report the maximum fluorescence (Fmax) in Raman units (RU). The obtained C1 to C5 were compared to previous studies using the Openfluor database (openfluor.lablicate.com; Murphy et al. (2014)), matching them with high congruence $TCC_{Ex\text{-}Em} > 0.95$ (Tucker Congruence Coefficient of excitation and emission spectra). Components C1, C2, C4 and C5 were similar to those reported by Catalá et al. (2015b) and Jørgensen et al. (2011) for the global ocean, whereas C3 was similar to the C4 obtained by Martínez-Pérez et al. (2019) in the Mediterranean Sea.

Table 2.1. Thermohaline and chemical characteristics (average value ± uncertainty) of the water types (WT) included in the Optimum Multi-Parameter Analysis (OMP) of the water masses present in the Cape Verde Frontal Zone (CVFZ). Determination coefficients (R^2), standard errors of the estimates (SE) and number of samples (n) of the multiple-regression of the measured and back-calculated variables are also reported. Taken from the water mass analysis of Valiente et al. (2022).

WT	θ_i (ºC)	S_i	SiO_4H_{4i} (µmol kg^{-1})	NO_i (µmol kg^{-1})
SACW_18 [a]	18.03 ± 0.05	35.82 ± 0.03	5.1 ± 0.1	260 ± 8
MMW [b]	20.0 ± 0.5	37.00 ± 0.04	0.4 ± 0.3	225 ± 10
ENACW_15 [b]	15.3 ± 0.4	36.10 ± 0.02	2.2 ± 1.7	264 ± 8
SACW_12 [a]	12.0 ± 0.1	35.16 ± 0.01	10.8 ± 0.1	345 ± 7
ENACW_12 [c]	12.2 ± 0.4	35.66 ± 0.02	4.9 ± 0.2	322 ± 8
SPMW [c]	8.2 ± 0.4	35.23 ± 0.01	14.5 ± 0.4	386 ± 7
AA [a]	4.89 ± 0.03	34.51 ± 0.02	30.3 ± 0.8	464 ± 8
MW [c]	11.8 ± 0.1	36.50 ± 0.01	7.2 ± 0.7	304 ± 9
LSW [c]	3.4 ± 0.2	34.89 ± 0.12	19.5 ± 0.4	446 ± 9
UNEADW[d]	2.500 ± 0.003	34.940 ± 0.003	34.8 ± 0.3	447 ± 7
LNEADW[d]	1.980 ± 0.002	34.884 ± 0.003	44.4 ± 0.3	462 ± 7
R^2	0.999	0.999	0.988	0.977
SE	0.04	0.005	1.2	1.1
N	307	307	307	307

[a] This work, taken from the WOA13 in the Equatorial Atlantic
[b] Álvarez and Álvarez-Salgado (2009); Lonborg and Álvarez-Salgado (2014)
[c] Perez et al. (2001); Álvarez and Álvarez-Salgado (2009)
[d] Pérez-Rodríguez et al. (2001); Lonborg and Álvarez-Salgado (2014).

2.4 Optimum multiparameter (OMP) water mass analysis

A water type (WT) is a body of water formed in a particular region of the ocean and characterized by a unique combination of temperature, salinity and chemical properties (Tomczak, 1999). A specific water sample is a combination of different WTs in different proportions, which can be quantified through an optimum multiparameter (OMP) inverse

method (Karstensen and Tomczak, 1998). In this work, potential temperature (θ), salinity (S), silicate (SiO_4H_4) and NO were used as water mass tracers. The chemical parameter NO is defined as: $NO = O_2 + R_N \cdot NO_3^-$, with R_N = 9.3 mol O_2 / mol NO_3^- (Anderson, 1995) being the stoichiometric coefficient of oxygen consumption to nitrate production. A total of 11 WTs have been identified in the CVFZ: Madeira Mode Water (MMW); Eastern North Atlantic Central Water (ENACW) of 15ºC and 12ºC; South Atlantic Central Water (SACW) of 18ºC and 12ºC; Subpolar Mode Water (SPMW); Antarctic Intermediate Water (AA); Mediterranean Water (MW); Labrador Sea Water (LSW); and upper and lower North East Atlantic Deep Water (NEADW). Thermohaline and chemical properties of these WTs are summarized in Table 2.1.

To quantify the contribution of each WT to every sample, a set of 5 mass balance equations was solved using the values of θ, S, SiO_4H_4 and NO obtained for each sample collected during the cruise. The set of mass balance equations are:

$$\sum_i X_{ij} \cdot \theta_i = \theta_j + R\theta_j$$

$$\sum_i X_{ij} \cdot S_i = S_j + RS_j$$

$$\sum_i X_{ij} \cdot (SiO_4H_4)_i = (SiO_4H_4)_j + R(SiO_4H_4)_j \quad (2.3)$$

$$\sum_i X_{ij} \cdot NO_i = NO_j + RNO_j$$

$$\sum_i X_{ij} = 1 + R\sum$$

where X_{ij} is the proportion of water type i in a sample j; θ_i, S_i, $(SiO_4H_4)_i$ and NO_i are the values of θ, S, SiO_4H_4 and NO of WT i (Table 2.1); θ_j, S_j, $(SiO_4H_4)_j$ and NO_j are the values of each variable in sample j; and R are the residuals of the mass balance equations and the mass conservation for sample j. These mass balance equations were normalized and weighted considering the measurement error of each parameter. Since we have 11 WTs and only 5 linear mixing equations, five mixing groups (Fig. 2.3) were created based on expert knowledge of the hydrography of the study area (Valiente et al. 2022). The five groups of

WTs defined are: 1) MMW - SACW18 - ENACW15; 2) SACW18 - ENACW15 - SACW12 - ENACW12; 3) SACW12 - ENACW12 - SPMW - AA; 4) SPMW - AA - MW - LSW; and 5) MW - LSW - LNEADW - UNEADW. Samples in the epipelagic layer were excluded from the OMP analysis due to the non-conservative behavior of θ, S, SiO_4H_4 and NO because of exchange of mass, heat and gases with the atmosphere and intense biological activity. Thus, a total of 236 out of 320 samples were selected for the determination of the relative contribution of each WT to each water sample in the mesopelagic and bathypelagic layers. The remaining 84 samples correspond to the upper 200 m.

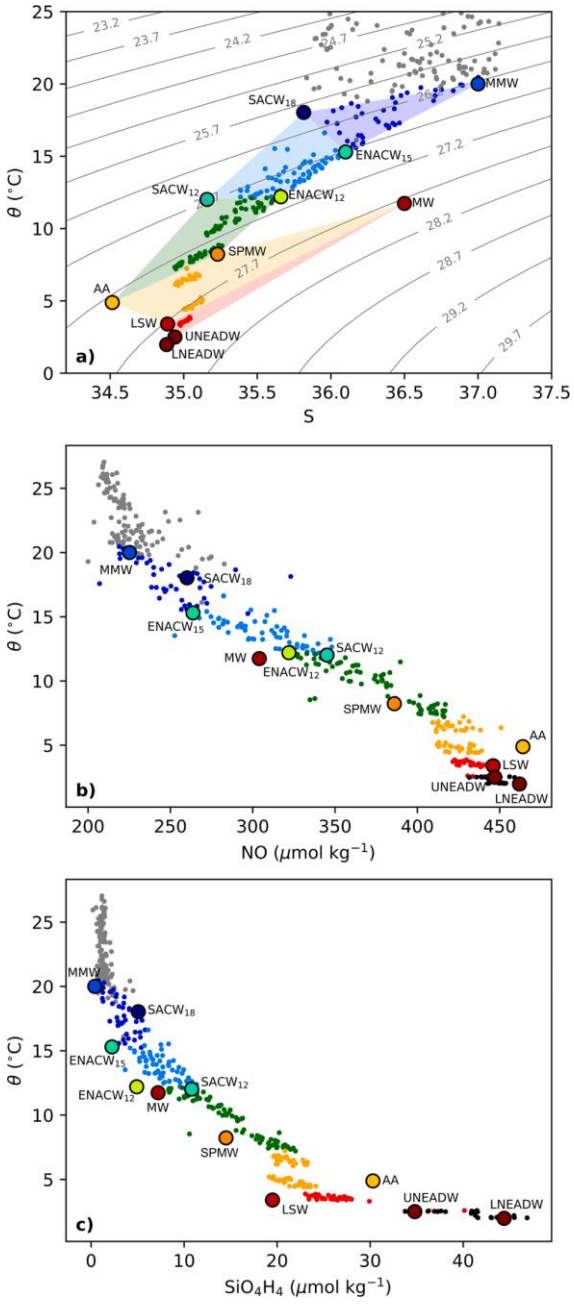

Figure 2.3. Potential temperature (θ) versus salinity (a), NO (b) and SiO_4H_4 (c) for FLUXES I. Dots represent the water samples collected and the shading colours in (a) identify the mixing group assigned to each sample. Potential density contours are also shown in (a).

Once the water type proportions (X_{ij}) are known and using the values of any measured variable (N), the water mass proportion-weighted average concentration of N in each water type, N_i or archetype value of N, is calculated as follows:

$$N_i = \frac{\sum_j X_{ij} \cdot N_j}{\sum_J X_{ij}} \tag{2.4}$$

where X_{ij} is the proportion of WT i in sample j and N_j is the concentration of N in sample j. The standard error of the archetype value was obtained as:

$$SE_{N_i} = \frac{\sqrt{\sum_j X_{ij}\left(N_j - N_i\right)^2}}{\sum_j X_{ij}} \tag{2.5}$$

Archetype values were determined for Z, S, θ, O_2, AOU, DOC, CDOM ($a_{CDOM}(254)$, $a_{CDOM}(325)$, $a_{CDOM}(254)/a_{CDOM}(365)$, $S_{275\text{-}295}$ and S_R) and FDOM (C1-C5). Finally, the proportion of the total volume of the samples occupied during the FLUXES I cruise (%VOL_i) by a given water type i was calculated as:

$$\%VOL_i = 100 \cdot \frac{\sum_j X_{ij}}{n} \tag{2.6}$$

where n = 236, is the number of samples collected below 200 m and included in the analysis.

2.5 Multiple regression models

The fraction of the total variability of any non-conservative chemical variable N (DOC, POC, CDOM, FDOM) that is explained by water mass mixing in the mesopelagic layer can be calculated by applying a multiple linear regression of N_j with the water mass proportions X_{ij} (Perez et al., 1993). A system of n linear equations (one per sample) with 11 coefficients (one per WT) has to be solved for each chemical variable as follows:

$$N_j = \sum_j X_{ij} \cdot n_i + R(N_j) \quad (2.7)$$

where n_i is the slope coefficient for WT i and $R(N_j)$ is the residual of the equation for sample j. The determination coefficient (R^2) indicates the percent of the total variability explained by mixing and the standard error (SE) of the estimate defines the accuracy of the fit. Note that the multiple linear regression cannot be applied to $a_{CDOM}(254)/a_{CDOM}(365)$, $S_{275\text{-}295}$ and S_R because they are not concentrations but slopes or ratios (i.e., qualitative variables).

Non-conservative variables depend not only on the mixing of water masses but also on the biogeochemical transformations that occur during that mixing. The variability associated to non-conservative processes is classified into (1) variability correlated with water mass proportions (basin-scale mineralization) and (2) variability independent of the water mass proportions (local-scale mineralization, in this case within the CVFZ). The first is modelled by the multiple linear regression of N_j with X_{ij}, (eq. 2.7). To account for the local-scale mineralization, the explanatory variable AOU is added to the linear regression model (eq. 2.8). A fitting parameter (coefficient β) is included to model the relationship between the chemical variables (N) with AOU (Álvarez-Salgado et al., 2013, 2014; Valiente et al., 2022):

$$N_j = \sum_j X_{ij} \cdot n_i + \beta \cdot AOU_j + R(N_j) \quad (2.8)$$

Remarkably, the coefficient β does not depend on WT mixing. In this sense, when calculating the multiple linear regression of DOC or POC with X_{ij} and AOU, the coefficient β indicates the contribution of DOC or POC to the local oxygen demand. Moreover, the contribution of DOC or POC to inorganic carbon production can be calculated by multiplying the coefficient β by the Redfield ratio of dissolved oxygen consumption to organic carbon mineralization of 1.4 mol O_2 mol C^{-1} (Anderson, 1995). Again, this multiple linear regression cannot be applied to $a_{CDOM}(254)/a_{CDOM}(365)$, $S_{275\text{-}295}$ and S_R.

3. Results

3.1 Hydrographic variability in the CVFZ

3.1.1 Epipelagic waters

The CVF is a thermohaline front that separates the warm and salty ENACW from the cooler and fresher SACW. It was first defined by Zenk et al. (1991) at the intersection of the 150

m isobath with the 36 isohaline. More recently, analyzing the FLUXES-I cruise data, Burgoa et al. (2021) extended this definition vertically and established an equation that defines the location of the front at any depth from 100 to 650 m, based on equal contributions (50%) of ENACW and SACW. We have used the latter definition of the CVF to classify the samples of the epipelagic layer (upper 200 m) into two hydrographic domains: 1) Subtropical, for the samples located to the North of the CVF, comprising most of the Northern and Western transects; and 2) Tropical, for samples located to the South of the CVF, that comprises mainly the Southern and part of the Eastern transect. Furthermore, a third domain consisting of upwelling filament waters, was identified. It was mainly located in the Eastern transect, comprising the stations affected by the CBGF, easily traceable by the satellite-derived surface chlorophyll distribution (Fig. 2.1).

A well-defined pycnocline was identified along the four transects of the FLUXES I hydrographic box (see solid line in Fig. 2.4). Deeper pycnocline depths were observed in the Subtropical domain with an average (SD) value of 51.2 (1.8) m. Shallowest depths were located in the Tropical domain with 33.6 (3.5) m. Finally, the pycnocline depth was 40.8 (1.9) m in the filament waters. Noticeably, the pycnocline at stn 5, in the Northern transect, was as shallow as 15 m because there was an intrusion of water from the Tropical domain at that position (Valiente et al., 2022).

The Subtropical domain was occupied by surface waters of North Atlantic origin, characterized by higher salinity (average of 36.6; $p < 0.0005$) compared to the surface South Atlantic waters (average of 36.1) which prevailed in the Tropical domain (Fig. 2.4a, Table 2.2). Temperature showed significantly higher values in the Tropical domain above the pycnocline (24.5 ºC, $p < 0.0005$) with respect to the Subtropical domain (23.3 ºC), but it reversed below the pycnocline, with a lower temperature in the Tropical (17.2ºC, $p < 0.0005$) compared to the Subtropical domain (19.3 ºC). Therefore, the temperature difference across the pycnoline was much higher (7.3 ºC) in the Tropical than in the Subtropical (4.0 ºC) domain. Consequently, the stability (N^2_{max}) at the pycnocline in the Tropical domain (1.6 (0.1) 10^{-3} s^{-2}) was more than 3-fold higher than in the Subtropical domain (4.8 (0.1) 10^{-4} s^{-2}), so hampering the exchange of solutes between the surface and subsurface layers. Upper mixed layer temperature in the filament waters was lower ($p < 0.0005$) than in the Subtropical and Tropical domains, as expected for recently upwelled waters, and the temperature difference across the pycnocline was 5.0 ºC (Table 2.2).

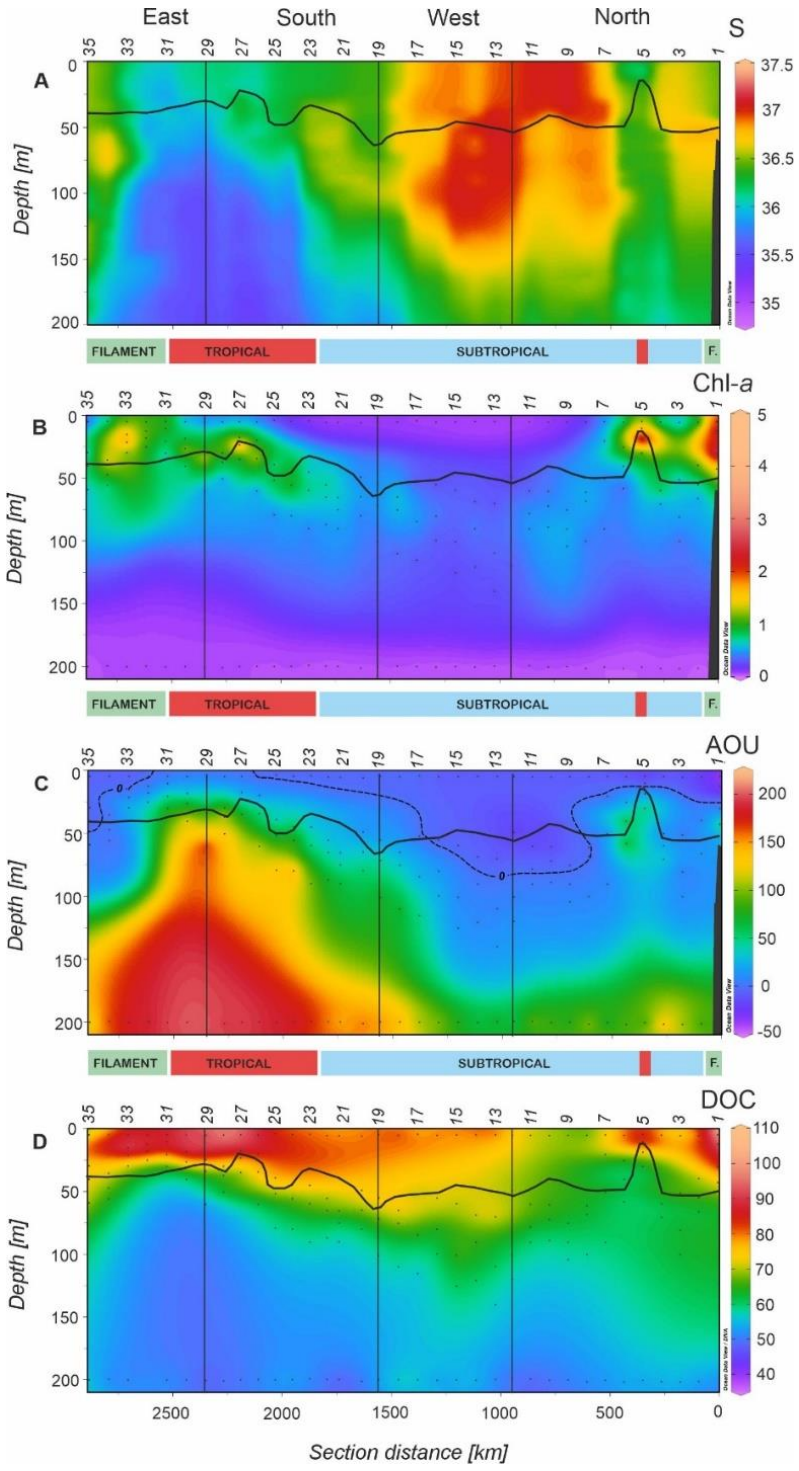

Figure 2.4. Distributions of A) salinity (S), B) chlorophyll-a (Chl-a) in µg L^{-1}, C) apparent oxygen utilization (AOU) in µmol Kg^{-1}, and D) dissolved organic carbon (DOC) in µmol Kg^{-1} in the epipelagic layer of the FLUXES I cruise. The vertical resolution of panel A (salinity) is 1 m, and dots represent samples in panels B, C and D. Horizontal black line show the position of the pycnocline and the vertical black lines represent the corners of the FLUXES hydrographic box. The black dotted line in panel C represents the isoline of 0 µmol Kg^{-1}. Odd station numbers are represented at the top of the first panel. Produced with Ocean Data View (Schlitzer, 2017).

The deep chlorophyll maximum (DCM) was located well below the pycnocline in the Subtropical domain, at an average depth of 75.8 (0.9) m, while in the Tropical domain the DCM was significantly ($p < 0.0005$) shallower, 37.9 (1.6) m, and much closer to the pycnocline. Conversely, in the filament domain, the DCM was shallower, 29.6 (2.0) m, and located above the pycnocline. Maximum Chl-*a* levels were observed in the Tropical and filament domains, corresponding with the shallowest DCM depths (Fig. 2.4b, Table 2.2). The Chl-*a* maximum at stn 5 corresponds to the intrusion of South Atlantic water in the Northern transect.

AOU above the pycnocline was positive (i.e., net community production is dominated by respiration processes resulting on oxygen consumption) in the three domains, being significantly higher ($p < 0.0005$) in the Tropical and filament domains than in the Subtropical domain (Fig. 2.4c). Differences were more pronounced below the pycnocline, where the less ventilated SACW in the Tropical and filament domains presented much higher AOU than the ENACW in the Subtropical domain.

Finally, DOC presented higher concentrations in the Tropical domain above the pycnocline with 87.0 (0.5) µmol L^{-1} ($p < 0.0005$). On the contrary, the highest DOC value at the DCM was found in the filament domain with an average of 77.9 (1.6) µmol L^{-1}. Below the pycnocline, values decreased and were constant at about 60 µmol L^{-1} in the three domains (Table 2.2, Fig. 2.4d). POC presented the highest concentrations in the filament domain above the pycnocline and at the DCM, with values of 14.0 (0.4) µmol L^{-1} and 13.1 (1.5) µmol L^{-1}, respectively, contrasting with a value of 3.7 (0.1) µmol L^{-1} in the Subtropical domain. Below the pycnocline, concentration decreased considerably in the filament domain to a value of 2.2 (0.2) µmol L^{-1}, being more similar to the others domains (Table 2.2). The C:N molar ratio of POM was higher in the subtropical domain above and below the pycnocline with average values of 9.1 (0.1) and 10.7 (0.1), respectively, increasing with depth. The highest C:N ratio increase with depth was found in the Tropical domain, which increased from 7.2 (0.1) to 9.4 (0.1).

Table 2.2. Thermohaline and chemical characteristics (average value ± SE) of the epipelagic waters above and below the pycnocline along the FLUXES I hydrographic box. Epipelagic domains are separated in three domains: Subtropical, Tropical and Filament. Components C1, C2, C4 and C5 corresponds with Coble's (1996) peaks A and C, peak M, peak T and peak B, respectively. Component C3 is similar to Stedmon's et al., (2003) peak D.

		Above pycnocline			**DCM**			**Below pycnocline**		
		Subtropical	Tropical	Filament	Subtropical	Tropical	Filament	Subtropical	Tropical	Filament
Z	(m)				75.8 ± 0.9	37.9 ± 1.6	29.6 ± 2.0			
θ	(ºC)	23.3 ± 0.1	24.5 ± 0.1	21.9 ± 0.1	20.6 ± 0.0	20.3 ± 0.2	21.2 ± 0.3	19.3 ± 0.0	17.2 ± 0.1	16.9 ± 0.4
S	(PSU)	36.6 ± 0.0	36.1 ± 0.0	36.2 ± 0.0	36.7 ± 0.0	36.1 ± 0.0	36.2 ± 0.1	36.6 ± 0.0	36.0 ± 0.0	36.1 ± 0.1
Chl-*a*	($\mu g\ L^{-1}$)	0.24 ± 0.01	0.62 ± 0.03	1.28 ± 0.05	0.55 ± 0.01	2.07 ± 0.17	1.62 ± 0.20	0.32 ± 0.00	0.74 ± 0.04	0.29 ± 0.05
AOU	($\mu mol\ kg^{-1}$)	3.2 ± 1.1	8.7 ± 2.4	8.7 ± 2.0	15.1 ± 1.4	77.7 ± 5.7	11.8 ± 5.5	41.6 ± 0.8	128.8 ± 2.5	108.0 ± 11.3
DOC	($\mu mol\ L^{-1}$)	72.0 ± 0.2	87.0 ± 0.5	81.1 ± 0.5	63.9 ± 0.2	71.9 ± 0.6	77.9 ± 1.6	59.9 ± 0.1	60.8 ± 0.3	59.0 ± 1.2
POC	($\mu mol\ L^{-1}$)	3.7 ± 0.1	7.8 ± 0.4	14.0 ± 0.4	2.6 ± 0.1	7.2 ± 0.5	13.1 ± 1.5	2.2 ± 0.0	3.7 ± 0.1	2.2 ± 0.2
PON	($\mu mol\ L^{-1}$)	0.41 ± 0.01	1.05 ± 0.06	1.68 ± 0.04	0.28 ± 0.00	1.03 ± 0.06	1.66 ± 0.19	0.21 ± 0.00	0.45 ± 0.02	0.27 ± 0.02
C:N		9.1 ± 0.1	7.2 ± 0.1	8.1 ± 0.1	9.1 ± 0.1	7.4 ± 0.2	7.9 ± 0.3	10.7 ± 0.0	9.4 ± 0.1	8.5 ± 0.3
$a_{CDOM}254$	(m^{-1})	1.31 ± 0.54	1.77 ± 0.01	1.61 ± 0.01	1.25 ± 0.01	1.59 ± 0.02	1.54 ± 0.04	1.15 ± 0.00	1.23 ± 0.01	1.15 ± 0.03
$a_{CDOM}325$	(m^{-1})	0.14 ± 0.002	0.31 ± 0.007	0.33 ± 0.005	0.19 ± 0.00	0.36 ± 0.01	0.33 ± 0.02	0.17 ± 0.00	0.25 ± 0.004	0.21 ± 0.005
*a*254/*a*365		26.56 ± 0.58	13.65 ± 0.40	9.64 ± 0.13	14.8 ± 0.2	9.1 ± 0.3	9.7 ± 0.5	14.61 ± 0.07	10.07 ± 0.11	10.70 ± 0.35
$S_{(275-295)}$	(10^{-2})	4.15 ± 0.03	3.33 ± 0.04	3.00 ± 0.12	3.58 ± 0.26	2.79 ± 0.46	2.96 ± 0.76	3.48 ± 0.01	2.79 ± 0.02	3.00 ± 0.06
$S_{(350-400)}$	(10^{-2})	1.86 ± 0.02	1.52 ± 0.01	1.30 ± 0.02	1.44 ± 0.15	1.30 ± 0.18	1.23 ± 0.35	1.37 ± 0.01	1.23 ± 0.01	1.26 ± 0.03
S_R		2.32 ± 0.02	2.20 ± 0.02	2.33 ± 0.02	2.55 ± 0.04	2.16 ± 0.03	2.44 ± 0.10	2.58 ± 0.01	2.27 ± 0.01	2.37 ± 0.01
C1	(10^{-3} RU)	11.2 ± 0.2	23.1 ± 0.6	27.6 ± 0.5	17.6 ± 0.3	31.8 ± 0.9	28.0 ± 2.1	17.4 ± 0.1	25.5 ± 0.3	21.0 ± 0.7
C2	(10^{-3} RU)	6.2 ± 0.2	12.8 ± 0.4	13.2 ± 0.3	10.1 ± 0.3	18.8 ± 0.6	14.7 ± 1.2	10.7 ± 0.1	15.9 ± 0.2	13.1 ± 0.4
C3	(10^{-3} RU)	2.9 ± 0.6	5.57 ± 0.1	7.27 ± 0.1	3.9 ± 0.1	7.2 ± 0.3	7.2 ± 0.5	4.2 ± 0.4	6.2 ± 0.1	5.4 ± 0.2
C4	(10^{-3} RU)	7.6 ± 0.1	14.3 ± 0.3	14.2 ± 0.3	6.7 ± 0.2	1.2 ± 0.6	1.2 ± 0.7	6.0 ± 0.1	6.8 ± 0.2	6.0 ± 0.5
C5	(10^{-3} RU)	15.0 ± 0.4	22.0 ± 1.5	10.1 ± 0.3	10.9 ± 0.5	7.2 ± 0.5	9.8 ± 1.1	8.7 ± 0.1	5.5 ± 0.2	3.6 ± 0.5

3.1.2 Ocean interior

It is well-known that the hydrography of the meso- and bathypelagic layers of the CVFZ is controlled by the mixing of water masses of contrasting origins (Pastor et al., 2015). Figure 2.5 presents the area where each water type sampled during the FLUXES-I cruise was dominant. The proportions of all water types in each transect are summarized in Table 3.A1 (Appendix). Whereas ENACW was present in similar proportions in the four transects, MMW concentrated in the Northern and Western transects, i.e. to the North of the CVF, while SACW was ubiquitous in the Southern and Eastern transects, i.e. to the South of the CVF. At intermediate levels, while SPMW was present in the four transects, AA concentrated mainly in the Southern and Eastern transects and MW was dominant in the Northern transect. Finally, both LSW and NEADW were present in the four transects, although shallower bottom depths in the Eastern transect led to a relatively smaller contribution of LNEADW. Weighted-average depths and percentages of sampled volume by every water type considering all transects together are summarized in Table 2.3. The most abundant water type in the central water domain (200 – 700 m) was ENACW of 12ºC, which represented 18.1% of the total sampled volume. For the intermediate waters domain (700 - 1500 m), the predominant water mass was AA, with 10.6% of the volume, and for the deep waters (1500 m - bottom) it was LSW with 15.6% of the volume.

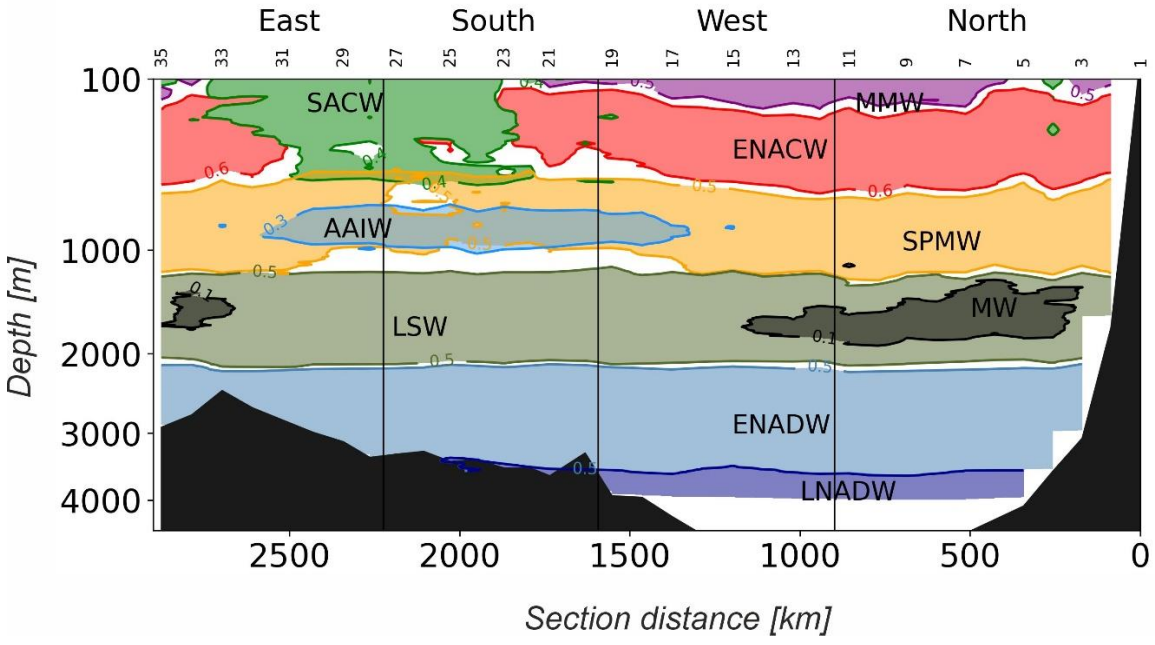

Figure 2.5. Distribution of water masses within the FLUXES I hydrographic box. The dominant water mass was represented at each depth and location.

Table 2.3. Thermohaline and chemical characteristics (archetype value ± SE) of mesopelagic waters. R2, proportion of the total variability explained by WT mixing; SE, standard error of the estimate. Components C1, C2, C4 and C5 corresponds with Coble's (1996) peaks A and C, peak M, peak T and peak B, respectively. Component C3 is similar to Stedmon's et al., (2003) peak D.

WT	VOL_i (%)	Z_i (m)	θ_i (ºC)	S_i (PSU)	AOU_i (µmol kg^{-1})	DOC_i (µmol L^{-1})	POC_i (µmol L^{-1})	C:N $(POM)_i$ mol C mol N^{-1}	$a_{CDOM}254_i$ (m^{-1})	$a_{CDOM}325_i$ (m^{-1})
SACW_18	4.8	102 ± 19	17.3 ± 0.5	36.1 ± 0.08	120.2 ± 15.4	58.9 ± 2.5	3.2 ± 1.2	9.9 ± 1.6	1.14 ±	0.22 ± 0.02
MMW	5.5	113 ± 13	18.9 ± 0.3	36.6 ± 0.07	50.9 ± 10.5	58.7 ± 1.6	2.7 ± 1.0	10.9 ± 1.3	1.10 ±	0.17 ± 0.02
ENACW_15	12.5	240 ± 14	15.2 ± 0.2	36.0 ± 0.04	117.8 ± 6.7	52.3 ± 1.7	1.5 ± 0.3	12.3 ± 0.9	0.96 ±	0.17 ± 0.01
SACW_12	7.3	336 ± 28	12.2 ± 0.3	35.5 ± 0.04	191.7 ± 5.4	49.9 ± 1.5	1.4 ± 0.2	12.4 ± 1.4	0.92 ±	0.19 ± 0.01
ENACW_12	18.1	442 ± 19	11.6 ± 0.2	35.5 ± 0.03	171.2 ± 4.8	48.5 ± 0.6	1.2 ± 0.1	12.5 ± 0.8	0.91 ±	0.17 ± 0.00
SPMW	7.2	809 ± 32	7.8 ± 0.2	35.1 ± 0.02	175.7 ± 4.2	44.8 ± 0.6	0.79 ± 0.06	14.5 ± 1.3	0.81 ±	0.15 ± 0.01
AA	10.6	873 ± 54	7.6 ± 0.3	35.1 ± 0.02	172.6 ± 5.7	45.1 ± 0.6	0.81 ± 0.06	14.2 ± 1.3	0.81 ±	0.15 ± 0.00
MW	3.1	1455 ± 118	5.2 ± 0.4	35.0 ± 0.02	119.4 ± 9.2	43.3 ± 0.9	0.70 ± 0.11	14.2 ± 2.2	0.79 ±	0.14 ± 0.01
LSW	15.6	1688 ± 46	4.5 ± 0.1	35.0 ± 0.01	104.0 ± 2.6	43.4 ± 0.5	0.67 ± 0.05	14.6 ± 1.1	0.76 ±	0.14 ± 0.00
UNEADW	11.7	2742 ± 93	3.1 ± 0.1	35.0 ± 0.01	88.0 ± 1.1	43.4 ± 0.6	0.68 ± 0.07	15.6 ± 1.3	0.83 ±	0.16 ± 0.01
LNEADW	3.7	3824 ± 101	2.4 ± 0.0	34.9 ± 0.00	85.1 ± 1.7	43.5 ± 1.0	0.71 ± 0.12	17.3 ± 2.0	0.82 ±	0.16 ± 0.01
R^2					0.94	0.63	0.26		0.85	0.59
SE					12.9	4.0	1.3		0.04	0.02

WT	$a_{CDOM}340_i$ (m^{-1})	$a_{CDOM}365_i$ (m^{-1})	$a254/a365$	$S_{(275\text{-}295)i}$ (10^{-2})	$S_{(350\text{-}400)i}$ (10^{-2})	S_{Ri}	C1 (10^{-3} RU)	C2 (10^{-3} RU)	C3 (10^{-3} RU)	C4 (10^{-3} RU)	C5 (10^{-3} RU)
SACW_18	0.17 ± 0.01	0.12 ± 0.01	10.5 ± 0.8	2.87 ± 0.12	1.19 ± 0.05	2.44 ± 0.11	23.3 ± 1.4	14.9 ± 1.1	5.8 ± 0.5	7.0 ± 1.7	7.5 ± 1.8
MMW	0.13 ± 0.01	0.08 ± 0.01	14.4 ± 1.2	3.45 ± 0.14	1.29 ± 0.06	2.69 ± 0.10	18.1 ± 1.8	10.8 ± 1.4	4.2 ± 0.5	7.3 ± 1.8	9.9 ± 1.7
ENACW_15	0.12 ± 0.01	0.08 ± 0.00	12.3 ± 0.5	3.01 ± 0.06	1.26 ± 0.05	2.43 ± 0.07	20.1 ± 0.5	13.0 ± 0.4	5.3 ± 0.2	5.2 ± 0.9	7.7 ± 1.4
SACW_12	0.13 ± 0.00	0.09 ± 0.00	10.1 ± 0.4	2.51 ± 0.04	1.14 ± 0.03	2.23 ± 0.06	23.7 ± 0.4	14.6 ± 0.3	6.6 ± 0.1	3.7 ± 0.5	5.4 ± 1.3
ENACW_12	0.12 ± 0.00	0.08 ± 0.00	11.5 ± 0.4	2.63 ± 0.04	1.29 ± 0.04	2.08 ± 0.04	22.6 ± 0.3	13.8 ± 0.2	6.4 ± 0.1	3.9 ± 0.4	6.1 ± 0.8
SPMW	0.10 ± 0.00	0.07 ± 0.00	12.1 ± 0.5	2.46 ± 0.02	1.43 ± 0.07	1.77 ± 0.06	22.7 ± 0.2	13.2 ± 0.2	6.8 ± 0.1	3.0 ± 0.4	5.7 ± 0.9
AA	0.10 ± 0.00	0.07 ± 0.00	12.2 ± 0.5	2.48 ± 0.03	1.46 ± 0.06	1.74 ± 0.05	23.2 ± 0.3	13.2 ± 0.2	6.9 ± 0.1	2.8 ± 0.4	4.9 ± 0.9
MW	0.10 ± 0.01	0.06 ± 0.00	13.3 ± 1.0	2.60 ± 0.05	1.66 ± 0.12	1.61 ± 0.08	23.1 ± 0.5	13.0 ± 0.3	7.0 ± 0.2	3.0 ± 1.0	5.6 ± 2.2
LSW	0.10 ± 0.00	0.06 ± 0.00	12.9 ± 0.4	2.65 ± 0.02	1.62 ± 0.04	1.66 ± 0.03	23.7 ± 0.3	13.2 ± 0.2	7.1 ± 0.1	3.1 ± 0.5	6.3 ± 1.1
UNEADW	0.11 ± 0.00	0.07 ± 0.00	12.3 ± 0.4	2.61 ± 0.03	1.59 ± 0.04	1.66 ± 0.04	25.6 ± 0.6	14.1 ± 0.3	7.8 ± 0.2	2.8 ± 0.3	8.6 ± 1.7
LNEADW	0.11 ± 0.01	0.07 ± 0.01	12.7 ± 0.7	2.61 ± 0.05	1.74 ± 0.16	1.58 ± 0.09	23.6 ± 0.7	13.8 ± 0.3	7.5 ± 0.2	3.2 ± 0.5	13.1 ± 4.0
R^2	0.62	0.57	0.38	0.83	0.97	0.70	0.63	0.58	0.76	0.19	0.11
SE	0.02	0.02	2.17	0.00	1.72	0.24	0.00	0.00	0.00	0.00	0.01

AOU, a canonical tracer for mineralization processes in the ocean interior, showed maximum values in the Southern and Eastern transects (Fig. 2.6a). The highest AOU corresponded to the SACW of 12ºC with an overall archetype value of 191.7 (5.4) µmol kg^{-1}, mainly located in the Southern and Eastern transects, and the lowest AOU corresponded to the MMW with an archetype value of 50.9 (10.5) µmol kg^{-1}, mainly located in the Northern and Western transects. In the intermediate and deep waters, AOU decreased with depth from 175.7 (4.2) µmol kg^{-1} in SPMW to 85.1 (1.7) µmol kg^{-1} in the LNEADW. Water types mixing (eq. 6) explained 94% of the variability of AOU in the meso- and bathypelagic waters of the CVFZ, but with a SE of 12.9 µmol kg^{-1}, i.e., an order of magnitude higher than the measurement error of about 1 µmol kg^{-1} (Table 2.3). This high ratio between the standard error and the measurement error indicates that water mass mixing alone is not able to explain the observed distribution of AOU in the ocean interior despite the high R^2 (Álvarez-Salgado et al., 2013).

DOC showed a distribution with vertically-coherent unexpected chimney-like structures of high DOC surrounded by areas of lower concentration (Fig. 2.6b), suggesting a connection between the organic matter produced in shallow levels with the deep waters. These columns of higher DOC are present in all transects. Nevertheless, archetype values showed the typical profile with higher values in shallower waters and a progressive decrease with increasing depth (Table 2.3). SACW of 18ºC, centered at 102 m, had and archetype concentration of 58.9 (1.9) µmol L^{-1} and the LNEADW, centered at 3823 m, a value of 42.9 (1.0) µmol L^{-1}. Water type mixing explained 63% of the DOC variability with an SE of 4.0 µmol L^{-1}. Compared to AOU, the R^2 is lower, but the SE is only 2-3-fold the measurement error of DOC. When AOU was added to the multiple linear regression of DOC with X_{ij} (eq. 2.8), the explained variability increased to 70%. Interestingly, a significant AOU-DOC β coefficient of -0.026 (0.015) mol C mol O_2^{-1} was obtained (Table 2.4), indicating that DOC mineralization contributed only to 3.6 (2.1) % of the inorganic carbon produced locally in the CVFZ (Valiente et al., 2022), assuming a $-O_2$:C Redfield ratio of 1.4 mol O_2 mol C^{-1} (Anderson, 1995).

POC decreased with depth from SACW_18 with a value of 3.2 (1.2) µmol L^{-1} to MW with a value of 0.70 (0.11) µmol L^{-1}, and then, values maintained constant to the deep waters (Table 2.3). Water type mixing explained 26% of the POC variability with an SE of 1.3 µmol L^{-1}, and when AOU was added to the model, the explained variability increased to 38% and the SE was reduced to 1.0 µmol L^{-1}. The AOU-POC β coefficient was -0.032

(0.005) mol C mol O_2^{-1} (Table 2.4), indicating that POC mineralization contributed to 4.5 (0.7) % of the inorganic carbon produced locally in the mesopelagic and bathypelagic waters. The C:N ratio of POM increased progressively with depth from 9.9 (1.6) in SACW_18 to 17.3 (2.0) in UNEADW (Valiente et al., 2022).

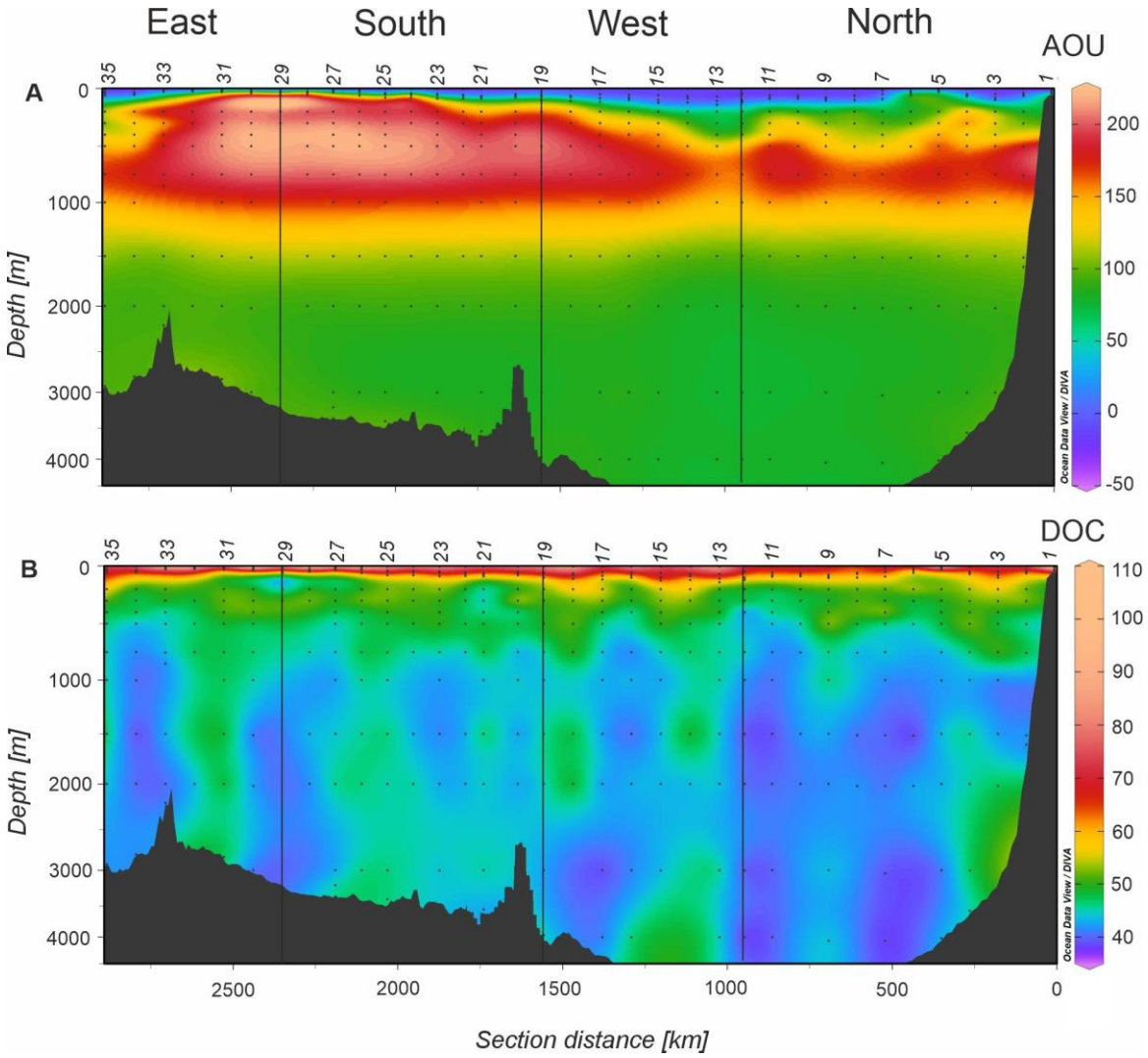

Figure 2.6. Full depth distributions of A) apparent oxygen utilization (AOU) in µmol Kg^{-1} and B) dissolved organic carbon (DOC) in µmol Kg^{-1}, of the FLUXES I cruise. Dots represent samples and vertical black lines represent the corners of the FLUXES I hydrographic box. Note that the y-axis (depth) is not linear. Odd station numbers are represented at the top of the first panel. Produced with Ocean Data View (Schlitzer, 2017).

3.2 Optical properties of colored and fluorescent DOM in the epipelagic layer

$a_{CDOM}(254)$ and $a_{CDOM}(325)$ are among the most commonly used absorption coefficients in marine organic matter biogeochemistry (Álvarez-Salgado et al., 2023). $a_{CDOM}(254)$ is a tracer for conjugated carbon double bonds in DOM and has been suggested as a proxy to the concentration of DOC (Catalá et al., 2018; Lønborg and Álvarez-Salgado, 2014).

Moreover, $a_{CDOM}(254)$ is not directly affected by solar radiation since very few solar photons of < 295 nm reach the Earth surface (Fichot and Benner, 2012). Conversely, $a_{CDOM}(325)$ is used as a proxy to the aromatic fraction of DOM and a tracer of microbial production and/or photochemical degradation processes due to its sensitivity to solar UV radiation (Iuculano et al., 2019; Nelson et al., 2004, 1998). The ratio $a_{CDOM}(254)/a_{CDOM}(325)$ is an indicator of the inverse of the CDOM molecular size (Dahlén et al., 1996; Engelhaupt et al., 2003), which is higher in freshly produced CDOM and decreases during microbial and photochemical degradation processes (Benner and Amon, 2015). Moreover, the spectral slope $S_{275\text{-}295}$ and S_R have been suggested as indices for photochemical transformations, average molecular weight and origin of DOM (Helms et al., 2008).

The optical properties of DOM varied considerably at the large scale in the epipelagic layer of the CVFZ, with clear differences between the Subtropical and Tropical-Filament domains (Fig. 5a-5d). Above the pycnocline, higher $a_{CDOM}(254)$ and $a_{CDOM}(325)$ values were found in the Tropical and filament waters domains, respectively (Table 2.2), and significant differences ($p < 0.0005$) were observed between the Tropical and Subtropical domains. Noticeably, $a_{CDOM}(325)$ presented values more than twice, 0.31 (0.1) m^{-1} and 0.33 (0.1) m^{-1}, in the Tropical and filament domains than in the Subtropical domain, 0.14 (0.02) m^{-1}. Below the pycnocline, $a_{CDOM}(254)$ and $a_{CDOM}(325)$ decreased, but maintained the highest values in the Tropical domain (Table 2.2; Figs. 2.7a and 2.7b). $a_{CDOM}(254)/a_{CDOM}(365)$ presented the highest values above the pycnocline and in the Northern and Western transects coinciding with the Subtropical domain (Table 2.2, Fig. 2.7c). This area matched with the lowest values of $a_{CDOM}(254)$ and $a_{CDOM}(325)$. The slope $S_{275\text{-}295}$ was also significantly higher above than below the pycnocline, with the highest values in the Subtropical domain (4.15 (0.03) 10^{-2} nm^{-1}; Table 2.2, Fig 2.7d). Similarly, S_R showed the highest values in the Subtropical domain and significantly higher ($p < 0.0005$) below than above the pycnocline.

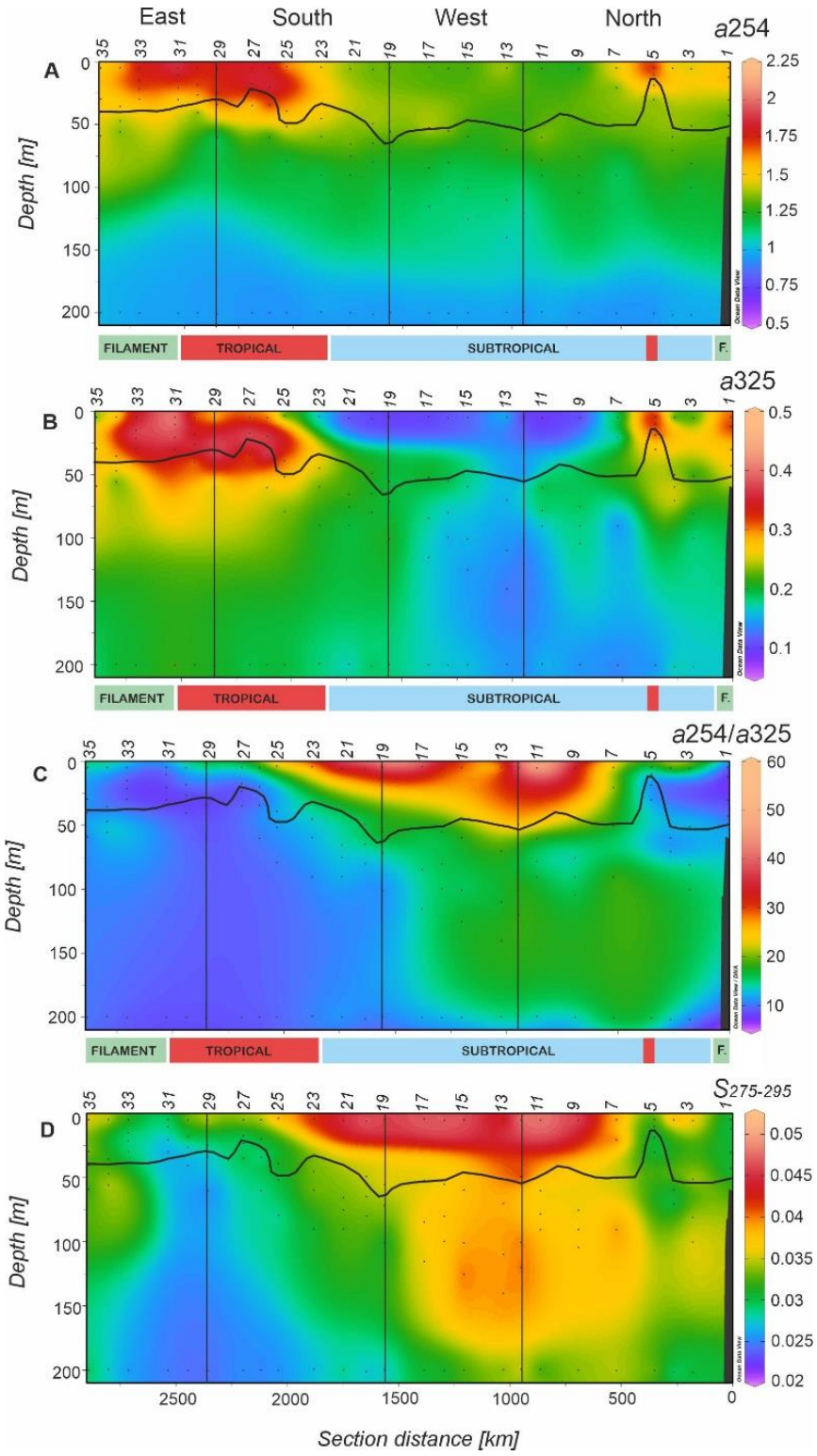

Figure 2.7. Distributions of A) absorption coefficient at 254 nm ($a_{CDOM}254$) in m^{-1}, B) absorption coefficient at 325 nm ($a_{CDOM}325$) in m^{-1}, C) ratio of absorption coefficients $a_{CDOM}254/a_{CDOM}365$ and D) spectral slope $S_{275-295}$ in the epipelagic layer of the FLUXES I cruise. Dots represent samples, horizontal black line show the position of the pycnocline and the vertical black lines represent the corners of the FLUXES hydrographic box. Odd station numbers are represented at the top of the first panel. Produced with Ocean Data View (Schlitzer, 2017).

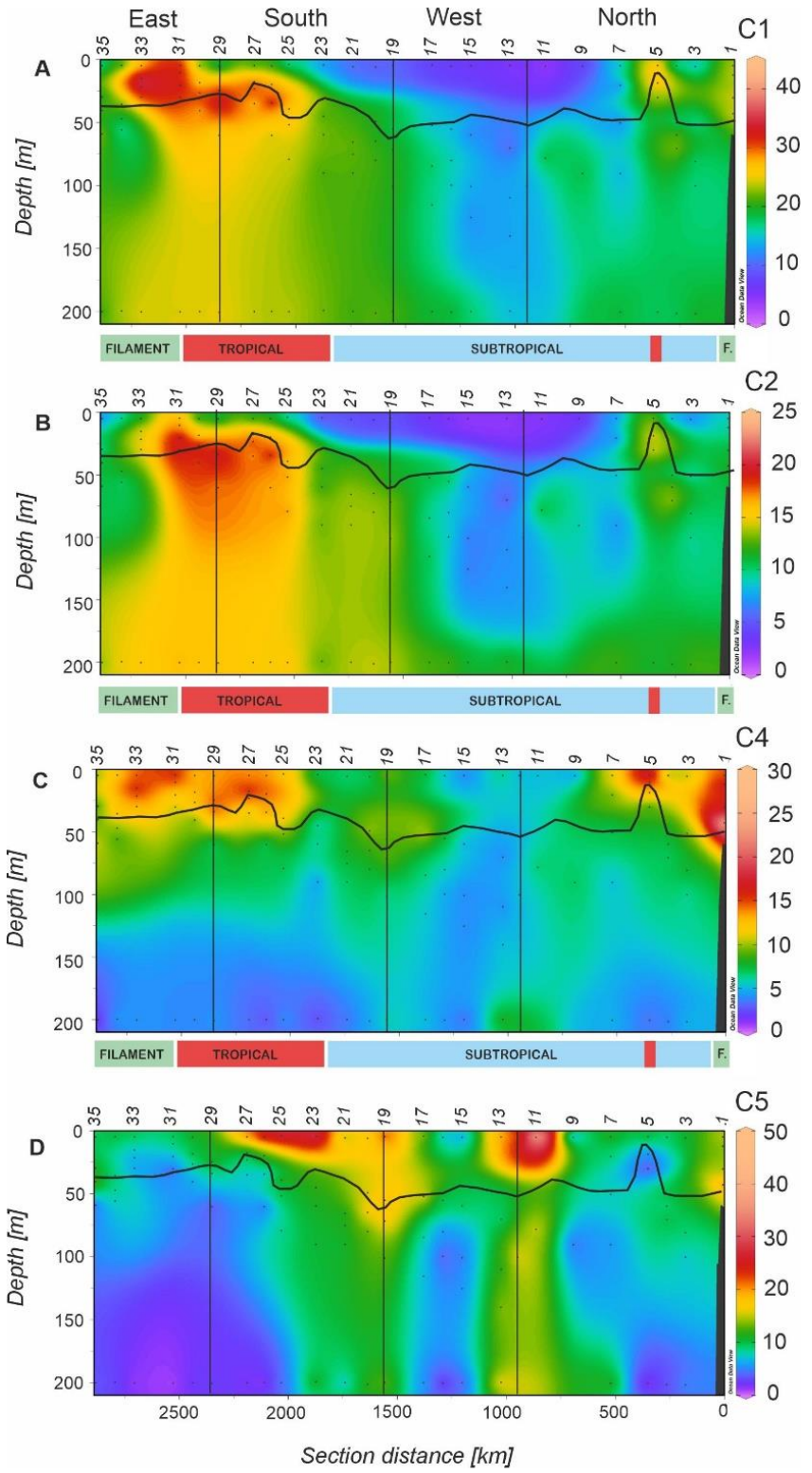

Figure 2.8. Distributions of A) fluorescence component C1 in 10^{-3} RU, B) fluorescence component C2 in 10^{-3} RU, C) fluorescence component C4 in 10^{-3} RU and D) fluorescence component C5 in 10^{-3} RU in the epipelagic layer of the FLUXES I cruise. Dots represent samples, horizontal black line show the position of the pycnocline and the vertical black lines represent the corners of the FLUXES hydrographic box. Odd station numbers are represented at the top of the first panel. Produced with Ocean Data View (Schlitzer, 2017).

Humic-like components C1 to C3 presented parallel distributions, with the highest values being recorded near the coast and centered at the DCM (Table 2.2, Fig. 2.8a and 2.8b). Above the pycnocline, values were higher in the filament domain, but below the pycnocline, higher values were observed in the Tropical domain. The correlation between the three humic-like components in the epipelagic layer was higher for C1-C3 ($R^2 = 0.92$) and lower for C1-C2 ($R^2 = 0.81$) and C2-C3 ($R^2 = 0.73$), implying that C2 was somewhat different from C1 and C3. In this regard, while C2 corresponds to humic-like substances of marine origin, C1 and C3 correspond to humic and fulvic acids of terrestrial origin, respectively (Coble, 1996; Stedmon et al., 2003). Despite the high correlation between C1 and C2, some differences were observed mainly above the pycnocline, where C1 was higher in the CBGF than in the Tropical domains. Regarding the protein-like components, C4 showed the highest values also in the surface mixed layer near the coast in the Tropical and filament domains. Then decreased with depth to more homogeneous values below the pycnocline, with significantly higher values ($p < 0.0005$) in the Tropical domain as compared with the Subtropical domain (Table 2.2, Fig. 2.8c). C5 (Fig. 2.8d) showed the highest values above the pycnocline and in the Tropical domain, but contrary to what have been observed for C4, below the pycnocline, higher values were found in the Subtropical domain (Table 2.2). Moreover, while maximum values of C4 are located at stn 1, 3, 25-33, for C5 are located at stn 11-12, 23-26, indicating therefore a different distribution of these components.

3.3 Optical properties of colored and fluorescent DOM in the meso- and bathypelagic layers

CDOM at the two chosen wavelengths, $a_{CDOM}(254)$ and $a_{CDOM}(325)$, decreased considerably with depth, from archetype values of 1.14 (0.05) and 0.22 (0.02) m^{-1} in SACW_18 to 0.76 (0.01) and 0.14 (0.01) m^{-1} in LSW, respectively. Noticeably, a significant increase in the bathypelagic water masses was observed, with archetype values of 0.82 (0.01) and 0.16 (0.01) m^{-1} in LNEADW, not accompanied by parallel increases in DOC nor AOU. This increment was most noticeable in the Eastern transect, followed by the Northern transect as can be observed in the CDOM sections of Fig. 2.9a & b and Table 3.A1, mainly associated to the Mauritanian continental slope. $a_{CDOM}(254)$ and $a_{CDOM}(325)$ showed high differences between transects, with the lowest values below 1000 m in the stations farthest from the coast, from stn 7 to stn 25. The $a_{CDOM}(254)/a_{CDOM}(365)$ ratio, a proxy for the average molecular weight of CDOM,

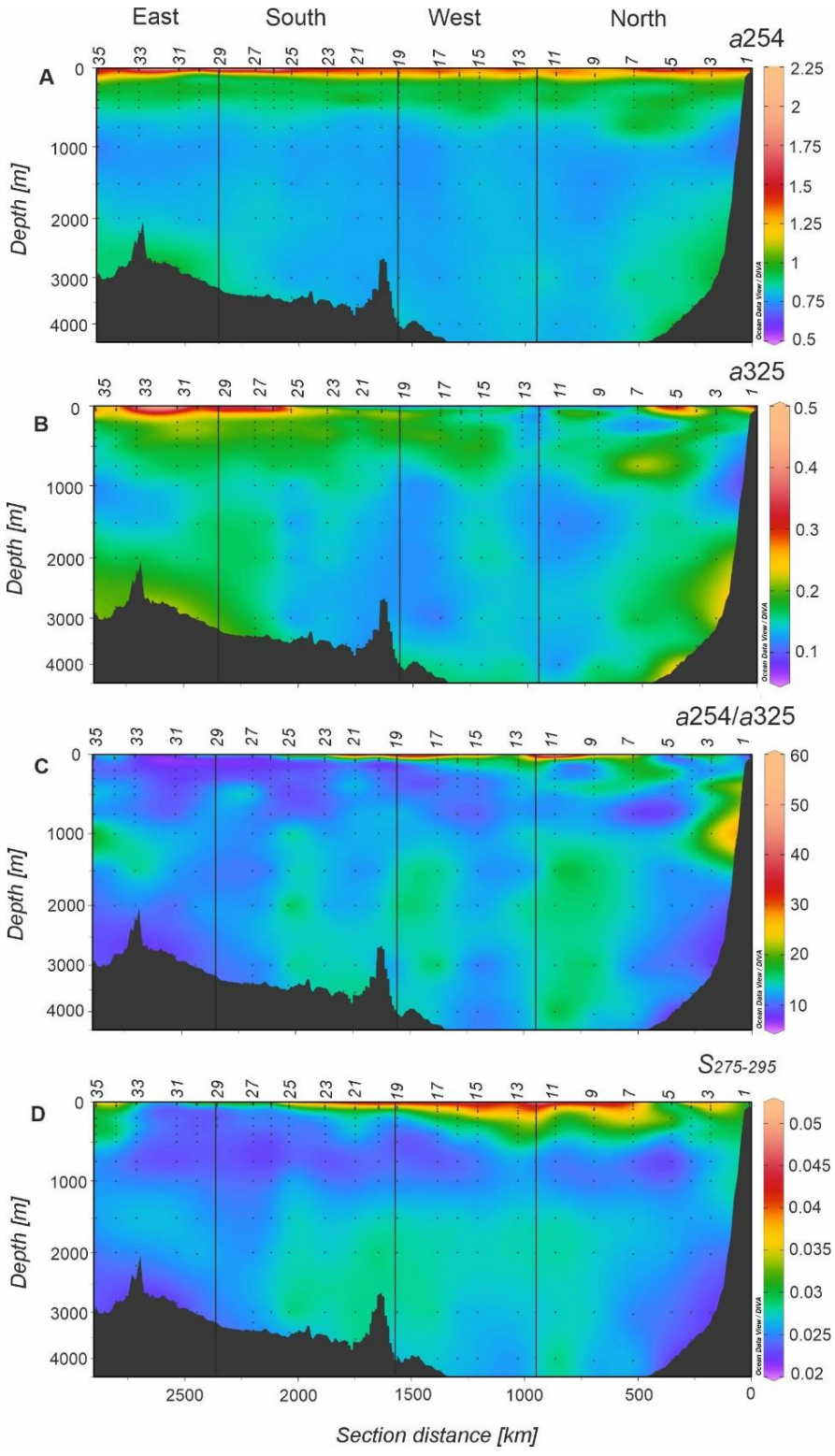

Figure 2.9. Full depth distributions of A) absorption coefficient at 254 nm (aCDOM254) in m-1, B) absorption coefficient at 325 nm (aCDOM325) in m-1, C) ratio of absorption coefficients aCDOM254/aCDOM365 and D) spectral slope S275-295 of the FLUXES I cruise. Dots represent samples and vertical black lines represent the corners of the FLUXES I hydrographic box. Note that the y-axis (depth) is not linear. Odd station numbers are represented at the top of the first panel. Produced with Ocean Data View (Schlitzer, 2017).

showed higher archetype values in the Northern and Western transects with a maximum of 15.8 (2.0) in the MMW (Table 3.A1), than in the Southern and Eastern transects. Particularly, the Eastern transect presented the lowest values, with a minimum of 8.7 (0.6) in the SACW_18. From stn 7 to stn 25, an area of relatively high $a_{CDOM}(254)/a_{CDOM}(365)$ (~20) was observed from 1000 m to bottom, compared to their surroundings (~10) forming chimney-like structures and matching with the DOC distribution (Fig. 2.9c). In this area, an increase of the spectral slope $S_{275\text{-}295}$ (Fig. 2.9d) and a decrease of S_R (not shown) were also observed.

Fluorophores C1 and C2 matched the distribution of CDOM, with the highest values in shallower waters at the Eastern and Southern transects (stn 25-35) and a remarkable increase in the near-bottom waters of the same transects (Fig. 2.10a and 2.10b). Maximum values of C1 were observed in the two NEADW water types at the Eastern transect with an average of 30.1 (1.8) and 32.1 (2.4) 10^{-3} RU, which were significantly higher ($p < 0.005$) than in the Western transect (Table 3.A1). C1 and C2 were also significantly higher ($p < 0.005$) in the Southern than in the Northern transects for the SACW of 12 and 18ºC but showed similar values in both transects for ENACW. For the intermediate waters, differences were found between SPMW and AA, being higher again in the Southern transect for C1, but similar for C2.

Regarding the protein-like C4 (Fig. 2.10c), it generally decreased with depth from central to intermediate waters. Then, it presented similar archetype values for intermediate and deep waters (Table 2.3). The highest archetype values were observed in the Northern transect, and the lowest in the Eastern one (Table 3.A1). Finally, C5 (Fig. 2.10d) showed similar archetype values in the central and intermediate waters, with a significant increase in deep waters. Nevertheless, this increase was not observable in the Eastern transect, which contained the lowest values of this component. On the contrary, the highest values were located in the Southern and Northern transects (Table 3.A1).

The distribution of particles (turbidity; Fig. 2.10e) is also presented to check for similarities with the distributions of CDOM and FDOM parameters. Turbidity shows columns of higher particle density that distributes from surface to bottom in the Eastern and Northern transects, being more intense in the former; significantly ($p < 0.005$) higher values were obtained for the Eastern transect although not for all the water masses (Table 3.A1).

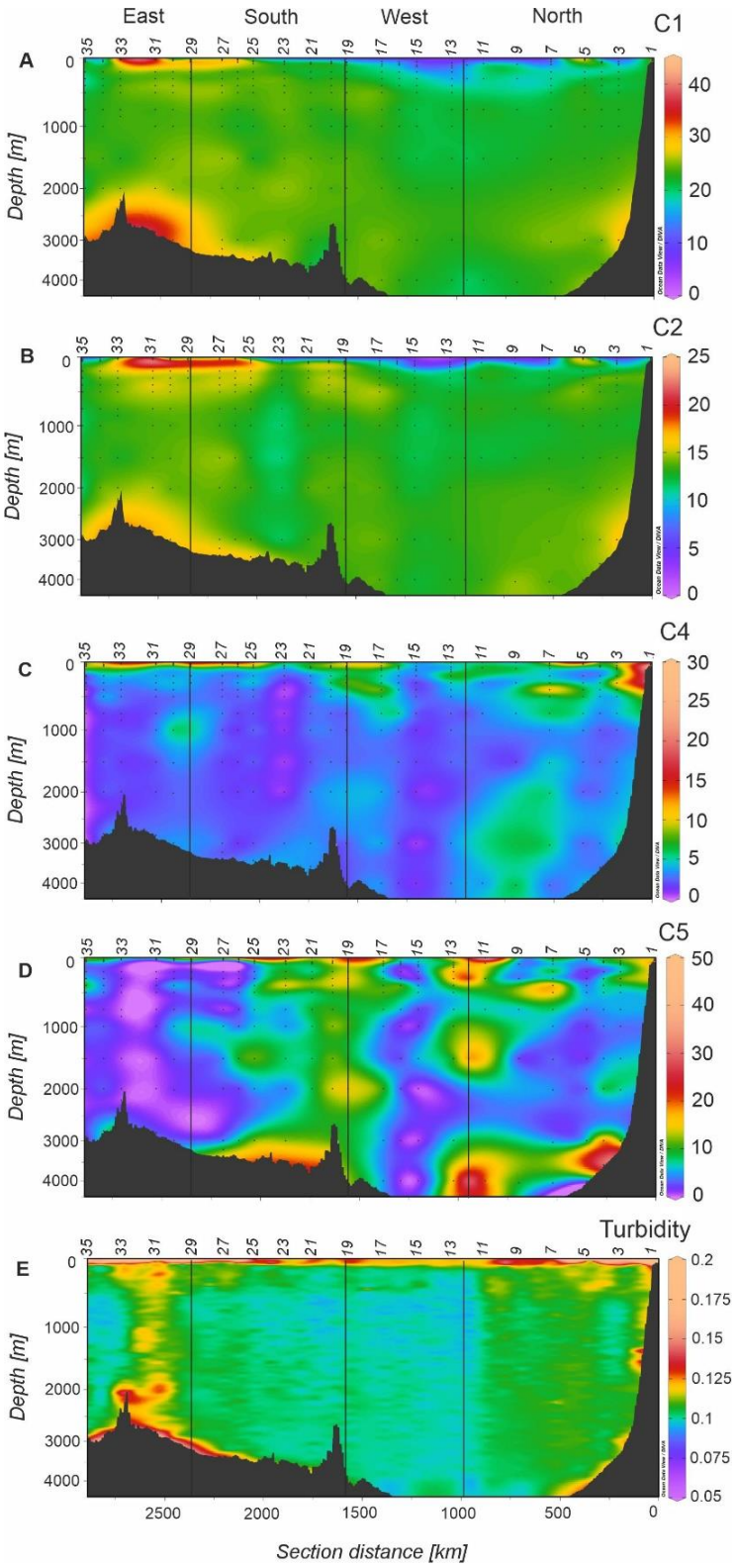

Figure 2.10. Full depth distributions of A) fluorescence component C1 in 10-3 RU, B) fluorescence component C2 in 10-3 RU, C) turbidity in NTU, D) fluorescence component C4 in 10-3 RU and E) fluorescence component C5 in 10-3 RU of the FLUXES I cruise. Dots represent samples and vertical black lines represent the corners of the FLUXES I hydrographic box. Note that the y-axis (depth) is not linear. Odd station numbers are represented at the top of the first panel. Produced with Ocean Data View (Schlitzer, 2017).

This high turbidity near the coast produces the characteristic nepheloid layers usually found in ocean margins (McCave, 1986). In Fig. 2.10e, the largest nepheloid layer occurs in surface waters close to the coast, from stn 1-7 and 26-35, coinciding with higher values of $a_{CDOM}(254)$, $a_{CDOM}(325)$, C1, C2 and C3 mainly at the second group of stations. It is related to the biomass accumulation due to the high primary production of the area (Gabric et al., 1993).

Nepheloid layers at intermediate (intermediate nepheloid layer, INL) and bottom depths (bottom nepheloid layer, BNL) are commonly observed in the study area too (Fischer et al., 2019, 2009; Karakaş et al., 2006; McCave, 1986). In the FLUXES I cruise no clear INL was found, instead a column of relatively homogeneous and elevated turbidity was observed through the mesopelagic layer, connecting epipelagic and bathypelagic waters. Finally, in the bathypelagic layer, a BNL was found with higher values at the Eastern transect between stn 29-35 and at the Northern transect between stn 1-7. This BNL is coincident with the high bottom values of $a_{CDOM}(254)$, $a_{CDOM}(325)$, C1, C2 and C3 at the same groups of stations.

Table 2.4. Parameters of the linear mixing (Eq. 2.7) and mixing-biogeochemical (Eq. 2.8) models. R2, determination coefficient; SE, standard error of the estimate; β, fitting parameter of the relationship between N1 and N2 independent of the mixing; SE (β), standard error of the estimation of β; p, significance level of the estimation of β; n, number of samples. Blanks correspond with non-significant observations.

N_1	N_2	R^2	SE	β	SE (β)	p	n
AOU		0.94	12.9				307
DOC		0.71	3.40				302
POC		0.26	1.30				302
DOC	AOU	0.70	3.4	-0.026	0.015	0.09	302
POC	AOU	0.38	1.0	-0.032	0.005	$2.2\ 10^{-10}$	302
$a_{CDOM}254$		0.85	0.04				236
$a_{CDOM}325$		0.59	0.02				236
$a_{CDOM}254$	AOU	0.85	0.04	-	-	-	236
$a_{CDOM}325$	AOU	0.60	0.02	-	-	-	236
C1		0.63	0.002				217
C2		0.58	0.001				217
C3		0.76	0.001				217
C4		0.19	0.003				217
C5		0.11	0.007				217
C1	AOU	0.64	0.002	$2.3\ 10^{-5}$	$9.1\ 10^{-6}$	0.01	217
C2	AOU	0.63	0.001	$2.5\ 10^{-5}$	$5.2\ 10^{-6}$	$2.3\ 10^{-6}$	217
C3	AOU	0.76	0.001	-	-	-	217
C4	AOU	0.29	0.002	$-2.2\ 10^{-5}$	$9.8\ 10^{-6}$	0.02	210
C5	AOU	0.12	0.007	-	-	-	217

Water type proportions (X_{ij}) (eq. 2.7) explained 85% and 59% of the $a_{CDOM}(254)$ and $a_{CDOM}(325)$ variability with an SE of 0.04 and 0.02 m^{-1}, respectively (Table 2.4). For comparison, the measurement error is 0.02 m^{-1}, i.e. of the same order than the SE. When AOU is added to the model, no increase was observed in the explained variability and the $a_{CDOM}(254)$-AOU and $a_{CDOM}(325)$-AOU β coefficients were not significant. Regarding the fluorescent fraction of DOM, water mass mixing explained 63%, 58%, 27% and 11% of the C1, C2, C4 and C5 components, with SE of 2, 1, 2 and 6 10^{-3} RU, respectively. The corresponding measurement errors of C1, C2, C4 and C5 are 0.5, 0.3, 0.2 and 0.4 10^{-3} RU, respectively, i.e., about an order of magnitude lower than the corresponding SE (Table 2.4). When AOU is added to the multiple regression model (eq. 2.8), the explained variability increased to 64%, 63%, 29% and 12%. The C1-AOU, C2-AOU and C4-AOU β coefficients were significant, with values of 2.3 (0.9) 10^{-5}, 2.5 (0.5) 10^{-5} and -2.2 (1.0) 10^{-5} RU kg^{-1} µmol (Table 2.4). On the contrary, the protein-like fluorophore C5 did not have a significant β coefficient with AOU.

4. Discussion

4.1 Factors controlling DOC, POC and C:N ratio of POM in epipelagic waters

Recently, Valiente et al. (2022) analyzed the DOC and POC in the CVFZ. In this chapter, a summary of the main results is presented, with some modifications concerning the epipelagic waters, where averages were calculated for the three domains instead of the four transects classification in the study of Valiente and colleagues.

DOC was higher in the filament and Tropical domains as was expected due to its proximity to the coast (Del Giorgio and Duarte, 2002; Gattuso et al., 1998). Moreover, the presence of the CBGF can export horizontally offshore the high DOC levels (Gabric et al., 1993; Lovecchio et al., 2018, 2017). POC was found to be higher also in the filament domain, closer to the coast. Van Camp et al. (1991) and Gabric (1993) estimated that around 50% of the POM produced in the coastal area could be exported offshore by the filament. The notably lower values found below the pycnocline could be explained by the estimated lateral export of POM and also by microbial degradation of labile compounds when POC is transported to subsurface waters (Ducklow et al., 2001). The lowest C:N ratio of POM was found in the surface mixed layer and in the Tropical domain (7.2 (0.2)), where fresh organic matter is produced coinciding with the highest values of Chl-*a* in the immediately below DCM (Table 2.1). On the contrary, the highest C:N values corresponded to the

Subtropical domain (10.7 (0.1)), further to the coast and with a lower rate of primary production. Values were always higher than the canonical Redfield ratio of 6.6 (Anderson, 1995; Redfield et al., 1963)**.** Martiny et al., 2013b, 2013a showed large spatial variation in the epipelagic ocean that differed substantially from the Redfield ratio, and proposed a C:N:P ratio of 137:18:1 in warm, nutrient-rich upwelling zones. This proposed C:N ratio of 7.6 is similar to that found in the epipelagic waters of the CVFZ.

4.2 Factors controlling CDOM and FDOM distributions in epipelagic waters

The distribution of the optically active fraction of DOM in the epipelagic layer during the FLUXES I cruise were influenced by the CVF and the CBGF. The presence of the CVF separates the saltier, oxygen-richer and nutrient-poorer waters of the Eastern North Atlantic, from the fresher, oxygen-poorer and nutrients-richer waters of the South Atlantic (Pelegrí and Peña-Izquierdo, 2015a; Zenk et al., 1991). This convergence creates a NE-SW front that crosses the FLUXES I hydrographic box from the Northeastern transect to the Southwestern transect (Fig. 2.1). The CBGF has been thoroughly studied over the last decades because of its importance for the offshore export of organic matter from the Mauritanian upwelling (Gabric et al., 1993; Lovecchio et al., 2018; Meunier et al., 2012; Sangrà, 2015), presenting higher Chl-*a* values, shallower DCM and lower water temperatures characteristic of upwelled waters.

The combination of the CVF and the CBGF led to the classification of the epipelagic layer into three domains (Subtropical, Tropical and filament). Absorption coefficients and fluorescence intensities were higher in the Tropical domain, which was fertilized by the nutrient-rich SACW and was characterized by a shallower, more stable pycnocline and higher Chl-*a* concentrations. These hydrographic conditions explain the observed net production and accumulation of CDOM and FDOM in the Tropical domain associated with a relatively higher primary production above the pycnocline and reduced exchange with the waters below the pycnocline due to a higher stratification. On the contrary, CDOM and FDOM concentrations were lower in the Subtropical domain, partly due to the lower nutrients concentrations of ENACW, deeper pycnocline and lower Chl-a levels, which lead to low production rates of these optically active substances, and partly due to intense photochemical degradation. As a result of the latter, minimum values of $a_{CDOM}(325)$ and maximum values of the $a_{CDOM}(254)/a_{CDOM}(325)$ ratio and the slope $S_{275\text{-}295}$ characteristic of photooxidation processes (Del Vecchio and Blough, 2004; Helms et al., 2008; Siegel et

al., 2005; Swan et al., 2012) were observed. Waters in this domain are transported southwestward by the Canary Current (see Fig. 2.1; Pelegrí and Peña-Izquierdo, 2015b), away from the influence of the upwelling system and therefore, are expected to contain lower inputs of fresh organic matter. The $a_{CDOM}(254)/a_{CDOM}(325)$ ratio is lower in the filament waters, indicating a larger molecular size in that area as expected due to the export of fresher organic matter from the Mauritanian upwelling. This is consistent with the size-reactivity continuum hypothesis, which states that fresher organic matter has a larger molecular size (Benner and Amon, 2015). Moreover, this recently upwelled water has not experienced a significant photochemical degradation. The spectral slope $S_{275\text{-}295}$ corroborated higher photochemical degradation in the Subtropical domain, mainly above the pycnocline of the Northern and Western transects, where inputs of fresher organic matter is less intense. Finally, the S_R parameter showed values > 2 indicative of the dominant marine origin of the DOM (Helms et al., 2008).

Humic-like substances followed the same distribution pattern than CDOM absorption coefficients. Higher values were found at the Eastern and the easternmost end of the Southern transects due to its proximity to the coast, where higher rates of primary production led to higher microbial respiration rates, leading to the production of the marine humic-like fluorophore C2 (Catalá et al., 2016; Nieto-Cid et al., 2006; Yamashita and Tanoue, 2008). C1 and C3, which are of terrestrial origin, are transported to the coast via continental runoff, e.g. from the Senegal River (Mbaye et al., 2016) or atmospheric deposition, e.g. Sahara dust (Arístegui et al., 2009; Campanero et al., 2022). This could explain the observed differences in the distribution of C1 and C2 above the pycnocline in the Filament domain, where higher fluorescence intensities of C1 was observed. Continental inputs originated from atmospheric dust deposition and/or river discharge are considered as relevant sources for ocean fertilization, contributing to enhance primary production and DOM generation (Baker and Croot, 2010; Buck et al., 2007; Schmidt et al., 2016). For instance, atmospheric inputs of Sahara dust have been related with an increment in primary production in the Subtropical Northeast Atlantic (Duarte et al., 2006) and also further south in the Atlantic Intertropical Convergence Zone (Ibánhez et al., 2022). However, dust deposition events can also contribute to enhance the heterotrophic bacterial production over the primary production as was observed in this study area (Pérez-Barrancos et al., 2022).

The protein-like fluorophores C4 and C5 showed a clear decrease below the pycnocline due to the labile nature of these materials, which are rapidly consumed by heterotrophic organisms (Jørgensen et al., 2011; Stedmon and Markager, 2005). C4 showed maximum values at the Eastern transect and the Northern and Southern transects near the coast, as expected since fresh and labile organic matter is produced in the coastal upwelling system and exported by the CBGF (Gabric et al., 1993). Moreover, when comparing C4 with DOC, we observed that a relatively higher concentration of C4 per DOC unit was present in the Filament domain, indicating that this domain contained a higher content of labile DOM.

4.3 Factors controlling organic matter distributions in the meso- and bathypelagic waters

The distribution of DOM and POM in the meso- and bathypelagic layers were influenced by the surface dynamics, where most of the organic matter is produced in situ by primary producers or exported from the shelf by the CBGF (Gabric et al., 1993; Meunier et al., 2012). A connection between the surface layer and the deep ocean was observed, mostly in the eastern transect due to its proximity to the coast and its larger concentration of sinking particulate organic matter. This connection can be observed in the columns of higher DOC reaching deep waters (Fig. 2.4b) and in the turbidity profiles (Fig. 2.8e). Previous studies in the region of Cape Blanc reported this surface-to-deep connection, related to the ballasting effect of lithogenic material produced in situ or from atmospheric inputs associated to processes of absorption-desorption of DOM onto particles (Bory and Newton, 2000; Campanero et al., 2022; Fischer et al., 2016; Fischer and Karakaş, 2009; Valiente et al., 2022; van der Jagt et al., 2018). Furthermore, the process of partial dissolution of sinking particles has been previously observed (Simon et al., 2002; Smith et al., 1992), and also the connection between the surface layer and the deep ocean in other regions (Gómez-Letona et al., 2022; Lopez et al., 2020; Ruiz-González et al., 2020).

The water mass analysis resulted in archetype DOC concentration of ENACW lower than those found by Álvarez-Salgado et al. (2013) and Lønborg and Álvarez-Salgado (2014) in the Eastern North Atlantic at 40ºN and 27-42ºN, respectively. A likely reason of this result is that ENACW at 40ºN is closer to its formation area and therefore, a younger and a DOC-richer water is expected at that latitude. However, archetype DOC values at intermediate and deep water masses are similar to that found in the previous studies. Moreover, water mass mixing explained 63% of the DOC variability, suggesting that basin-scale mixing and

mineralization processes are driving the DOC distribution. POC concentrations in the mesopelagic waters of the CVFZ (1.2-3.2 umol L) are lower to that found in Alonso-González et al. (2009) in the Canary current at 20-29ºN (3-8 umol L). This difference could be explained by the different location of the sampling sites, in the core of the Canary current in Alonso-González et al. (2009) and further south in this study, where the presence of the CBGF produce a high amount of sinking material (Fischer et al., 2009), enhanced by the ballasting effect of lithogenic particles originating by atmospheric deposition (Bory and Newton, 2000; Fischer and Karakaş, 2009). The increment in the C:N molar ratio with depth suggests preferential degradation of nitrogen-rich compounds (Álvarez-Salgado et al., 2013). Previous studies in the area also reported higher C:N ratios than the canonical Redfield ratio (Fischer et al., 2009; 2019; Nowald et al., 2015), but still lower than those found in this work. The likely reason could be a larger residence time of small particles that exacerbates the impact of preferential nitrogen mineralization.

We observed areas of higher CDOM and FDOM (C1 and C2) intensity in the BNL of the Eastern and Northern transects. These distributions could be caused by the release of CDOM and FDOM contained in particles sinking from the epipelagic layer, ballasted with Sahara dust, which connect the surface production with the BNL. Sahara dust contains humic-like FDOM that is release to the water column (Campanero et al., 2022). In this regard, fluorescence intensity of C1 is higher than C2 in the BNL, which is consistent with a terrestrial origin of this fluorescence signal. In addition, humic-like fluorescence can also be produced during the degradation of organic matter in sinking particles, being released when the particles reach the bottom, explaining the maximum of C2, with a marine origin. Independently of the origin of the humic-like fluorescence maxima, release form Sahara dust or degradation of sinking particles in mesopelagic waters, no increase of AOU in the BNL should be expected. Important fluxes of fast sinking organic particles and the presence of a well-developed BNL have been consistently reported in the CVFZ (Fischer et al., 2019, 2009; Karakaş et al., 2006; Ohde et al., 2015). Fischer et al. (2009) showed a BNL in the Cape Blanc region that slid along the bottom slope comprising particles with settling rates > 30 m d^{-1}. This BNL extended up to over 1000 m above the seafloor with some seasonal variability. Alternatively, the fluorescence humic-like maxima in the BNL could be related with the resuspension of reworked organic matter accumulated in anoxic sediments (Chen et al., 2016; Hedges and Keil, 1995; Kim and Kim, 2016) that will not produce any signal in the AOU too. The distribution of the protein-like components C4 and C5 did not match

the areas of higher particle density in the meso- and bathypelagic layers, probably due to a rapid degradation of these materials (Jørgensen et al., 2011; Stedmon and Markager, 2005).

4.4 Organic matter mineralization in the meso- and bathypelagic waters

The multiple linear regression of DOC and POC with water mass proportions (X_{ij}) in the FLUXES I hydrographic box, and the addition of AOU to each variable in the multiple regression model have been previously analyzed by Valiente et al. (2022). They observed that only a small fraction of DOC (3.6 ± 2.1%) and suspended POC (4.5 ± 0.7%) contributed to the production of inorganic carbon in the area covered by the hydrographic box. These DOC values are considerably lower to those obtained by Arístegui et al. (2002) for the world ocean (10-20%), by (Arístegui et al., 2003) in the south of the Canary Islands (26.5%), by (Carlson et al. (2010) in the deep North Atlantic (9-19%) or by Lønborg and Álvarez-Salgado, (2014) in the Eastern North Atlantic (26%). The fraction of POC is also lower to that found by Alonso-González et al. (2009), which estimated that 28-59% of POC could account for the total mesopelagic respiration in the Canary region. The low estimations found in this study could be explained by 1) the distance of the water masses in the study area from their formation sites are higher than in the study of Alonso-González et al. (2009) producing therefore a higher DOC degradation (Hansell et al., 2012; Hansell and Carlson, 2013) and 2) the ballasting effect of lithogenic material and the massive flux of biodegradable sinking POC transported laterally by the filament activity could be the main organic carbon contributor to the mesopelagic respiration in the CVFZ (Valiente et al. 2022).

Concerning the colored fraction of DOM, the multiple linear regression model showed that water mass mixing explained better $a_{CDOM}(254)$ (85%) than $a_{CDOM}(325)$ (59%). This pattern was also observed in previous studies in the eastern North Atlantic (Campanero et al., 2022; Lønborg and Álvarez-Salgado, 2014) and in the Mediterranean Sea (Catalá et al., 2018) and it is related to the exponential decay of the absorption coefficient with increasing wavelength, which produces higher relative measurement errors at longer wavelengths. In general, a larger measurement error tends to produce a lower R^2 (Álvarez-Salgado et al., 2013). When AOU was added to the model, no significant AOU β coefficients were obtained for $a_{CDOM}(254)$ and $a_{CDOM}(325)$, indicating that local mesopelagic mineralization processes did not affect significantly these DOM fractions in the CVFZ. Note that the residence time of mesopelagic waters in the hydrographic box has been calculated at around

60 days (Burgoa et al., 2021), which is too short to produce a significant and observable local signal of the degradation of dissolved organic matter. Furthermore, the fact that the SE of the linear regressions with X_{ij} are of the same order of the measurement error, may indicate that the analytical method is not accurate enough to catch these subtle local processes in such a short time scale.

Regarding the FDOM fraction, fluorophores C1 and C2 presented higher values of explained variability due to the water masses mixing (63% and 58%, respectively), contrary to the lower values observed for C4 and C5 (27% and 11%, respectively), related to protein-like materials and therefore more labile. Nevertheless, the SE of the FDOM components were an order of magnitude higher than the measurement error, indicating again that water mass mixing alone cannot explain the observed variability. Fluorophores C1 and C2 increased the explained variability when AOU was added to the model (64% and 63%, respectively), with significant positive β coefficients indicating the local production of refractory materials in the CVFZ. Therefore, contrary to CDOM, FDOM measurements are sensitive enough to detect the subtle local production that occurs in mesopelagic waters of the CVFZ. This generation of humic-like substances in the dark ocean are presumably related with the microbial carbon pump mechanism (Jiao et al., 2010). Moreover, the recent study of Xiao et al., (2023) proposed to use the relationship between FDOM and AOU as an indicator for evaluating the microbial carbon pump efficiency in the dark ocean.

The obtained β coefficients of 2.3 (0.9) and 2.5 (0.5) 10^{-5} RU kg^{-1} µmol for C1 and C2 are comparable to those obtained in previous observations made also in the CVFZ reported by Campanero et al. (2022; 1.8 (0.7) 10^{-5} RU kg^{-1}µmol), in the Mediterranean Sea reported by Martínez-Pérez et al. (2019; 2.1 (0.4) 10^{-5} RU kg^{-1}µmol) and in the global ocean reported by Catalá et al. (2015b) and Jørgensen et al. (2011) with β coefficients of 2.2 and 2.7 10^{-5} RU kg^{-1}µmol, respectively. Since DOC and suspended POC make a very small contribution to the local oxygen demand, it has been postulated that the main contributor to the local mineralization of organic matter is the sinking particles with high settling rates (Valiente et al., 2022). This idea would be consistent with the production of humic-like substances in the dark ocean of the CVFZ from these organic sinking particles. Finally, the variability of C4 explained by the water mass mixing model also increased (29%) when AOU was added to the model, but contrary to C1 and C2, the β coefficient was negative (-2.2 (1.0) 10^{-5} RU kg^{-1} µmol) indicating net consumption of protein-like materials in the dark ocean of the CVFZ and therefore, revealing their labile nature. This value is comparable to that obtained

in the Mediterranean Sea by Martínez-Pérez et al. (2019) for the peak T, with a peak T-AOU β coefficient of -3.7 (1.3) 10^{-5} RU kg^{-1} μmol.

5. Conclusions

The distribution of the DOC, POC and the optically active fraction of DOM in epipelagic waters of the CVFZ was controlled by the presence of the CVF and the CBGF. Tropical waters, South of the CVF, and CBGF waters contained higher concentration of the colored and fluorescent fractions of DOM, since these waters are nutrient-richer, present a shallower pycnocline and higher Chl-*a* levels. Photochemical degradation of DOM was particularly intense at the stations more distant from the coast, mainly occupied by Subtropical waters, North of the CVF, characterized by their oligotrophy.

In mesopelagic waters, concentrations of DOC and suspended POC were lower to values reported by previous studies further north in the Canary Current, probably explained by basin-scale mineralization and to the presence of the CBGF, which favored the sinking POC fraction. The low fraction that supports DOC and suspended POC to the organic matter mineralization suggests that sinking POC is the major organic matter fraction contributing to the meso- and bathypelagic respiration in the CVFZ.

The distributions of $a_{CDOM}(254)$ and $a_{CDOM}(325)$ in mesopelagic waters were explained mainly by the mixing of water masses and large-scale mineralization processes from their formation sites to the study area. Local generation of CDOM from mesopelagic organic matter decomposition was not observed, probably due to the very short residence time of mesopelagic waters in the study area and the relatively low sensitivity of the spectrophotometric measurements. On the contrary, the more sensitive fluorometric measurements showed a positive relationship of fluorescence components C1 and C2 with AOU, that points to the generation of humic-like compounds in the mesopelagic CVFZ by the microbial carbon pump mechanism, possibly originating from the decomposition of sinking organic carbon in the area. Conversely, the protein-like materials, represented by fluorescence component C4, were consumed as a result of their labile nature. A column of higher particle density was found at the Eastern and Northern transects, connecting surface and bottom waters, that lead to a well-developed bottom nepheloid layer (BNL) along the continental slope. An increase in the colored and fluorescent fractions of DOM, not accompanied by a parallel increase in AOU, was observed in this BNL. We hypothesized that DOM release from the sinking particles, either of allochthonous (ballasting Sahara

dust) or autochthonous (organic matter mineralization into particles) origin, and/or re-worked DOM released from the anoxic sediments below the BNL, could be the likely reasons for this signal.

Appendix: Chapter 2

Table 3.A1. Thermohaline and chemical characteristics (arquetype value ± SE) of meso- and bathypelagic waters during the FLUXES I cruise in the Northern, Western, Southern and Eastern transects.

			% VOL	
WT	North	West	South	East
SACW_18	4.5%	2.3%	6.7%	4.7%
MMW	8.5%	8.3%	3.5%	1.6%
ENACW_15	18.3%	14.7%	7.3%	10.4%
SACW_12	1.95%	3.7%	14.3%	8.8%
ENACW_12	16.9%	14.5%	16.6%	24.2%
SPMW	8.1%	8.3%	6.6%	6.8%
AA	7.2%	9.4%	12.8%	12.2%
MW	3.6%	3.1%	2.2%	3.5%
LSW	15.1%	15.9%	15.1%	15.8%
UNEADW	11.2%	13.0%	11.9%	11.4%
LNEADW	4.7%	6.8%	3.0%	0.5%
			AOU (μmol kg^{-1})	
WT	North	West	South	East
SACW_18	77 ± 24	77 ± 24	77 ± 24	77 ± 24
MMW	35 ± 12	35 ± 12	35 ± 12	35 ± 12
ENACW_15	99 ± 7	99 ± 7	99 ± 7	99 ± 7
SACW_12	149 ± 18	149 ± 18	149 ± 18	149 ± 18
ENACW_12	144 ± 7	144 ± 7	144 ± 7	144 ± 7
SPMW	164 ± 6	164 ± 6	164 ± 6	164 ± 6
AA	152 ± 11	152 ± 11	152 ± 11	152 ± 11
MW	113 ± 13	113 ± 13	113 ± 13	113 ± 13
LSW	99 ± 4	99 ± 4	99 ± 4	99 ± 4
UNEADW	85 ± 1	85 ± 1	85 ± 1	85 ± 1
LNEADW	83 ± 2	83 ± 2	83 ± 2	83 ± 2
			DOC (μmol L^{-1})	
WT	North	West	South	East
SACW_18	60.8 ± 4.5	60.8 ± 4.5	60.8 ± 4.5	60.8 ± 4.5
MMW	59.7 ± 2.7	59.7 ± 2.7	59.7 ± 2.7	59.7 ± 2.7
ENACW_15	51.4 ± 1.1	51.4 ± 1.1	51.4 ± 1.1	51.4 ± 1.1
SACW_12	47.9 ± 2.4	47.9 ± 2.4	47.9 ± 2.4	47.9 ± 2.4
ENACW_12	48.2 ± 1.1	48.2 ± 1.1	48.2 ± 1.1	48.2 ± 1.1
SPMW	44.4 ± 1.0	44.4 ± 1.0	44.4 ± 1.0	44.4 ± 1.0
AA	43.4 ± 1.1	43.4 ± 1.1	43.4 ± 1.1	43.4 ± 1.1
MW	41.8 ± 1.2	41.8 ± 1.2	41.8 ± 1.2	41.8 ± 1.2
LSW	41.8 ± 0.6	41.8 ± 0.6	41.8 ± 0.6	41.8 ± 0.6
UNEADW	41.9 ± 0.9	41.9 ± 0.9	41.9 ± 0.9	41.9 ± 0.9
LNEADW	41.1 ± 1.4	41.1 ± 1.4	41.1 ± 1.4	41.1 ± 1.4
			$a_{CDOM}254$ (m^{-1})	
WT	North	West	South	East
SACW_18	1.20 ± 0.11	1.20 ± 0.11	1.20 ± 0.11	1.20 ± 0.11
MMW	1.10 ± 0.07	1.10 ± 0.07	1.10 ± 0.07	1.10 ± 0.07
ENACW_15	0.95 ± 0.02	0.95 ± 0.02	0.95 ± 0.02	0.95 ± 0.02
SACW_12	0.94 ± 0.04	0.94 ± 0.04	0.94 ± 0.04	0.94 ± 0.04
ENACW_12	0.91 ± 0.02	0.91 ± 0.02	0.91 ± 0.02	0.91 ± 0.02
SPMW	0.84 ± 0.03	0.84 ± 0.03	0.84 ± 0.03	0.84 ± 0.03
AA	0.81 ± 0.02	0.81 ± 0.02	0.81 ± 0.02	0.81 ± 0.02
MW	0.79 ± 0.02	0.79 ± 0.02	0.79 ± 0.02	0.79 ± 0.02
LSW	0.80 ± 0.01	0.80 ± 0.01	0.80 ± 0.01	0.80 ± 0.01
UNEADW	0.85 ± 0.02	0.85 ± 0.02	0.85 ± 0.02	0.85 ± 0.02
LNEADW	0.84 ± 0.03	0.84 ± 0.03	0.84 ± 0.03	0.84 ± 0.03

		$a_{CDOM}325$ (m^{-1})		
WT	North	West	South	East
SACW_18	0.23 ± 0.04	0.23 ± 0.04	0.23 ± 0.04	0.23 ± 0.04
MMW	0.16 ± 0.03	0.16 ± 0.03	0.16 ± 0.03	0.16 ± 0.03
ENACW_15	0.15 ± 0.01	0.15 ± 0.01	0.15 ± 0.01	0.15 ± 0.01
SACW_12	0.17 ± 0.02	0.17 ± 0.02	0.17 ± 0.02	0.17 ± 0.02
ENACW_12	0.16 ± 0.01	0.16 ± 0.01	0.16 ± 0.01	0.16 ± 0.01
SPMW	0.16 ± 0.01	0.16 ± 0.01	0.16 ± 0.01	0.16 ± 0.01
AA	0.15 ± 0.01	0.15 ± 0.01	0.15 ± 0.01	0.15 ± 0.01
MW	0.14 ± 0.01	0.14 ± 0.01	0.14 ± 0.01	0.14 ± 0.01
LSW	0.14 ± 0.01	0.14 ± 0.01	0.14 ± 0.01	0.14 ± 0.01
UNEADW	0.16 ± 0.01	0.16 ± 0.01	0.16 ± 0.01	0.16 ± 0.01
LNEADW	0.17 ± 0.02	0.17 ± 0.02	0.17 ± 0.02	0.17 ± 0.02

		$a_{CDOM}254$/ $a_{CDOM}365$		
WT	North	West	South	East
SACW_18	10.8 ± 1.7	10.8 ± 1.7	10.8 ± 1.7	10.8 ± 1.7
MMW	15.8 ± 2.0	15.8 ± 2.0	15.8 ± 2.0	15.8 ± 2.0
ENACW_15	14.1 ± 0.8	14.1 ± 0.8	14.1 ± 0.8	14.1 ± 0.8
SACW_12	12.5 ± 2.3	12.5 ± 2.3	12.5 ± 2.3	12.5 ± 2.3
ENACW_12	13.6 ± 0.8	13.6 ± 0.8	13.6 ± 0.8	13.6 ± 0.8
SPMW	12.4 ± 1.2	12.4 ± 1.2	12.4 ± 1.2	12.4 ± 1.2
AA	13.9 ± 1.5	13.9 ± 1.5	13.9 ± 1.5	13.9 ± 1.5
MW	14.3 ± 1.9	14.3 ± 1.9	14.3 ± 1.9	14.3 ± 1.9
LSW	13.6 ± 0.7	13.6 ± 0.7	13.6 ± 0.7	13.6 ± 0.7
UNEADW	12.5 ± 0.8	12.5 ± 0.8	12.5 ± 0.8	12.5 ± 0.8
LNEADW	12.7 ± 1.5	12.7 ± 1.5	12.7 ± 1.5	12.7 ± 1.5

		$S_{275-295}$		
WT	North	West	South	East
SACW_18	2.98 ± 0.22	2.98 ± 0.22	2.98 ± 0.22	2.98 ± 0.22
MMW	3.60 ± 0.20	3.60 ± 0.20	3.60 ± 0.20	3.60 ± 0.20
ENACW_15	3.18 ± 0.08	3.18 ± 0.08	3.18 ± 0.08	3.18 ± 0.08
SACW_12	2.73 ± 0.20	2.73 ± 0.20	2.73 ± 0.20	2.73 ± 0.20
ENACW_12	2.77 ± 0.07	2.77 ± 0.07	2.77 ± 0.07	2.77 ± 0.07
SPMW	2.48 ± 0.05	2.48 ± 0.05	2.48 ± 0.05	2.48 ± 0.05
AA	2.54 ± 0.06	2.54 ± 0.06	2.54 ± 0.06	2.54 ± 0.06
MW	2.62 ± 0.07	2.62 ± 0.07	2.62 ± 0.07	2.62 ± 0.07
LSW	2.64 ± 0.03	2.64 ± 0.03	2.64 ± 0.03	2.64 ± 0.03
UNEADW	2.55 ± 0.06	2.55 ± 0.06	2.55 ± 0.06	2.55 ± 0.06
LNEADW	2.56 ± 0.11	2.56 ± 0.11	2.56 ± 0.11	2.56 ± 0.11

		S_R		
WT	North	West	South	East
SACW_18	2.56 ± 0.27	2.75 ± 0.24	2.42 ± 0.09	2.16 ± 0.13
MMW	2.76 ± 0.17	2.78 ± 0.08	2.48 ± 0.16	2.18 ± 0.31
ENACW_15	2.34 ± 0.12	2.69 ± 0.10	2.38 ± 0.10	2.34 ± 0.06
SACW_12	2.08 ± 0.25	2.30 ± 0.25	2.23 ± 0.08	2.24 ± 0.08
ENACW_12	1.90 ± 0.08	2.09 ± 0.10	2.16 ± 0.07	2.19 ± 0.06
SPMW	1.72 ± 0.14	1.77 ± 0.08	1.79 ± 0.09	1.81 ± 0.12
AA	1.55 ± 0.11	1.73 ± 0.09	1.83 ± 0.07	1.81 ± 0.10
MW	1.52 ± 0.14	1.59 ± 0.16	1.71 ± 0.15	1.69 ± 0.17
LSW	1.59 ± 0.06	1.59 ± 0.07	1.72 ± 0.06	1.76 ± 0.05
UNEADW	1.59 ± 0.05	1.64 ± 0.09	1.76 ± 0.07	1.67 ± 0.06
LNEADW	1.61 ± 0.10	1.51 ± 0.19	1.67 ± 0.10	1.49 ± 0.22

		Turbidity (10^{-2} NTU)		
WT	North	West	South	East
SACW_18	11.2 ± 2.5	11.2 ± 2.5	11.2 ± 2.5	11.2 ± 2.5
MMW	11.1 ± 0.03	11.1 ± 0.03	11.1 ± 0.03	11.1 ± 0.03
ENACW_15	11.0 ± 0.2	11.0 ± 0.2	11.0 ± 0.2	11.0 ± 0.2
SACW_12	10.9 ± 0.4	10.9 ± 0.4	10.9 ± 0.4	10.9 ± 0.4
ENACW_12	10.8 ± 0.5	10.8 ± 0.5	10.8 ± 0.5	10.8 ± 0.5
SPMW	10.5 ± 0.2	10.5 ± 0.2	10.5 ± 0.2	10.5 ± 0.2
AA	10.6 ± 0.4	10.6 ± 0.4	10.6 ± 0.4	10.6 ± 0.4
MW	10.6 ± 0.5	10.6 ± 0.5	10.6 ± 0.5	10.6 ± 0.5
LSW	10.6 ± 0.1	10.6 ± 0.1	10.6 ± 0.1	10.6 ± 0.1
UNEADW	10.5 ± 0.1	10.5 ± 0.1	10.5 ± 0.1	10.5 ± 0.1
LNEADW	10.5 ± 0.2	10.5 ± 0.2	10.5 ± 0.2	10.5 ± 0.2
		C1 (10^{-3} RU)		
WT	North	West	South	East
SACW_18	23.2 ± 2.1	23.2 ± 2.1	23.2 ± 2.1	23.2 ± 2.1
MMW	18.7 ± 2.5	18.7 ± 2.5	18.7 ± 2.5	18.7 ± 2.5
ENACW_15	19.1 ± 0.7	19.1 ± 0.7	19.1 ± 0.7	19.1 ± 0.7
SACW_12	21.6 ± 1.5	21.6 ± 1.5	21.6 ± 1.5	21.6 ± 1.5
ENACW_12	21.3 ± 0.6	21.3 ± 0.6	21.3 ± 0.6	21.3 ± 0.6
SPMW	22.1 ± 0.3	22.1 ± 0.3	22.1 ± 0.3	22.1 ± 0.3
AA	22.4 ± 0.4	22.4 ± 0.4	22.4 ± 0.4	22.4 ± 0.4
MW	22.6 ± 0.7	22.6 ± 0.7	22.6 ± 0.7	22.6 ± 0.7
LSW	22.9 ± 0.5	22.9 ± 0.5	22.9 ± 0.5	22.9 ± 0.5
UNEADW	24.7 ± 0.9	24.7 ± 0.9	24.7 ± 0.9	24.7 ± 0.9
LNEADW	22.8 ± 1.0	22.8 ± 1.0	22.8 ± 1.0	22.8 ± 1.0
		C2 (10^{-3} RU)		
WT	North	West	South	East
SACW_18	13.0 ± 1.5	13.0 ± 1.5	13.0 ± 1.5	13.0 ± 1.5
MMW	9.9 ± 1.5	9.9 ± 1.5	9.9 ± 1.5	9.9 ± 1.5
ENACW_15	12.3 ± 0.4	12.3 ± 0.4	12.3 ± 0.4	12.3 ± 0.4
SACW_12	13.7 ± 0.7	13.7 ± 0.7	13.7 ± 0.7	13.7 ± 0.7
ENACW_12	13.3 ± 0.3	13.3 ± 0.3	13.3 ± 0.3	13.3 ± 0.3
SPMW	13.0 ± 0.1	13.0 ± 0.1	13.0 ± 0.1	13.0 ± 0.1
AA	13.1 ± 0.2	13.1 ± 0.2	13.1 ± 0.2	13.1 ± 0.2
MW	13.0 ± 0.3	13.0 ± 0.3	13.0 ± 0.3	13.0 ± 0.3
LSW	13.1 ± 0.2	13.1 ± 0.2	13.1 ± 0.2	13.1 ± 0.2
UNEADW	14.3 ± 0.4	14.3 ± 0.4	14.3 ± 0.4	14.3 ± 0.4
LNEADW	14.0 ± 0.4	14.0 ± 0.4	14.0 ± 0.4	14.0 ± 0.4
		C3 (10^{-3} RU)		
WT	North	West	South	East
SACW_18	6.2 ± 0.8	6.2 ± 0.8	6.2 ± 0.8	6.2 ± 0.8
MMW	4.5 ± 0.9	4.5 ± 0.9	4.5 ± 0.9	4.5 ± 0.9
ENACW_15	5.1 ± 0.2	5.1 ± 0.2	5.1 ± 0.2	5.1 ± 0.2
SACW_12	6.0 ± 0.5	6.0 ± 0.5	6.0 ± 0.5	6.0 ± 0.5
ENACW_12	6.0 ± 0.2	6.0 ± 0.2	6.0 ± 0.2	6.0 ± 0.2
SPMW	6.5 ± 0.1	6.5 ± 0.1	6.5 ± 0.1	6.5 ± 0.1
AA	6.7 ± 0.1	6.7 ± 0.1	6.7 ± 0.1	6.7 ± 0.1
MW	6.8 ± 0.2	6.8 ± 0.2	6.8 ± 0.2	6.8 ± 0.2
LSW	7.0 ± 0.1	7.0 ± 0.1	7.0 ± 0.1	7.0 ± 0.1
UNEADW	7.9 ± 0.3	7.9 ± 0.3	7.9 ± 0.3	7.9 ± 0.3
LNEADW	7.4 ± 0.3	7.4 ± 0.3	7.4 ± 0.3	7.4 ± 0.3

	C4 (10^{-3} RU)			
WT	North	West	South	East
SACW_18	7.7 ± 3.2	7.7 ± 3.2	7.7 ± 3.2	7.7 ± 3.2
MMW	7.0 ± 2.3	7.0 ± 2.3	7.0 ± 2.3	7.0 ± 2.3
ENACW_15	5.0 ± 1.0	5.0 ± 1.0	5.0 ± 1.0	5.0 ± 1.0
SACW_12	5.5 ± 2.9	5.5 ± 2.9	5.5 ± 2.9	5.5 ± 2.9
ENACW_12	5.0 ± 0.8	5.0 ± 0.8	5.0 ± 0.8	5.0 ± 0.8
SPMW	3.8 ± 0.8	3.8 ± 0.8	3.8 ± 0.8	3.8 ± 0.8
AA	3.5 ± 0.7	3.5 ± 0.7	3.5 ± 0.7	3.5 ± 0.7
MW	3.0 ± 0.9	3.0 ± 0.9	3.0 ± 0.9	3.0 ± 0.9
LSW	3.2 ± 0.5	3.2 ± 0.5	3.2 ± 0.5	3.2 ± 0.5
UNEADW	3.9 ± 0.6	3.9 ± 0.6	3.9 ± 0.6	3.9 ± 0.6
LNEADW	4.1 ± 0.8	4.1 ± 0.8	4.1 ± 0.8	4.1 ± 0.8
	C5 (10^{-3} RU)			
WT	North	West	South	East
SACW_18	11.3 ± 3.6	11.3 ± 3.6	11.3 ± 3.6	11.3 ± 3.6
MMW	9.6 ± 3.5	9.6 ± 3.5	9.6 ± 3.5	9.6 ± 3.5
ENACW_15	8.3 ± 3.0	8.3 ± 3.0	8.3 ± 3.0	8.3 ± 3.0
SACW_12	6.5 ± 4.3	6.5 ± 4.3	6.5 ± 4.3	6.5 ± 4.3
ENACW_12	6.8 ± 1.6	6.8 ± 1.6	6.8 ± 1.6	6.8 ± 1.6
SPMW	5.4 ± 1.0	5.4 ± 1.0	5.4 ± 1.0	5.4 ± 1.0
AA	4.8 ± 2.0	4.8 ± 2.0	4.8 ± 2.0	4.8 ± 2.0
MW	5.5 ± 4.4	5.5 ± 4.4	5.5 ± 4.4	5.5 ± 4.4
LSW	6.1 ± 2.5	6.1 ± 2.5	6.1 ± 2.5	6.1 ± 2.5
UNEADW	10.5 ± 4.5	10.5 ± 4.5	10.5 ± 4.5	10.5 ± 4.5
LNEADW	13.8 ± 6.7	13.8 ± 6.7	13.8 ± 6.7	13.8 ± 6.7

Chapter 3: High-resolution variability of dissolved and suspended organic matter in the Cape Verde Frontal Zone

The research work presented in the chapter is also a contribution to the paper:

Campanero, R., Burgoa, N., Fernández-Castro, B., Valiente, S., Nieto-Cid, M., Martínez-Pérez, A.M., Gelado-Caballero, M.D., Hernández-Hernández, N., Marrero-Díaz, Á., Machín, F., Rodríguez-Santana, Á., Hernández-García, I., Delgado-Huertas, A., Martínez-Marrero, A., Arístegui, J., Álvarez-Salgado, X.A., 2022. High-resolution variability of dissolved and suspended organic matter in the Cape Verde Frontal Zone. Front Mar Sci 9. https://doi.org/10.3389/FMARS.2022.1006432

Abstract

Distributions of DOM and suspended POM, and their chromophoric (CDOM) and fluorescent (FDOM) fractions, are investigated at high resolution (< 10 km) in the CVFZ during fall 2017. In the epipelagic layer (< 200 m), meso- and submesoscale structures (meanders, eddies) captured by the high resolution sampling dictate the tight coupling between physical and biogeochemical parameters at the front. Remarkably, fluorescent humic-like substances show relatively high fluorescence intensities between 50 and 150 m, apparently not related to local mineralization processes. We hypothesize that it is due to the input of Sahara dust, which transports highly re-worked DOM with distinctive optical properties. In the mesopelagic layer (200-1500 m), our results suggest that DOM and POM mineralization occurs mainly during the transit of the water masses from the formation sites to the CVFZ. Therefore, most of the local mineralization seems to be due to fast-sinking POM produced in situ or imported from the Mauritanian upwelling. These local mineralization processes lead to the production of refractory CDOM, an empirical evidence of the microbial carbon pump mechanism. DOM released from these fast-sinking POM is the likely reason behind the observed columns of relatively high DOC surrounded by areas of lower concentration. DOM and POM dynamics in the CVFZ has turned out to be very complex, in parallel to the complexity of meso- and submesoscale structures present in the area. On top of this high resolution variability, the input of Sahara dust or the release of DOM from sinking particles have been hypothesized to explain the observed distributions.

1. Introduction

The Cape Verde Frontal Zone is located in the Eastern margin of the North Atlantic Ocean, off the Mauritanian coast (Fig. 3.1). In this area, NACW, transported southwards by the Canary Current, meets SACW, transported northwards by the Mauritanian Current, creating a well-defined northeast-southwest thermohaline front (Burgoa et al., 2021; Martínez-Marrero et al., 2008; Pelegrí and Peña-izquierdo, 2015; Pérez-Rodríguez et al., 2001; Zenk et al., 1991). This area is also under the influence of the NW Africa Eastern Boundary Upwelling Ecosystem (Messié and Chavez, 2015). The interaction of the upwelling system with the frontal zone leads to the formation of the Giant Filament of Cape Blanc, which exports large amounts of organic matter offshore (Gabric et al., 1993; Ohde et al., 2015). Mixing processes between NACW and SACW and the interaction of the filament with the front nourishes an intense meso- and submesoscale activity in the form of meanders and eddies that create a highly dynamic system (Arístegui et al., 2009; Lovecchio et al., 2022, 2018). In particular, submesoscale processes (spatial scale 1 - 10 km and temporal scale of 1 - 10 days) have been demonstrated to be relevant in vertical transport of limiting nutrients to the euphotic layer and thus, controlling primary

production, carbon fixation and the biological carbon pump efficiency (Capet et al., 2008; Hernández-Hernández et al., 2020; Hosegood et al., 2017; Lévy et al., 2012).

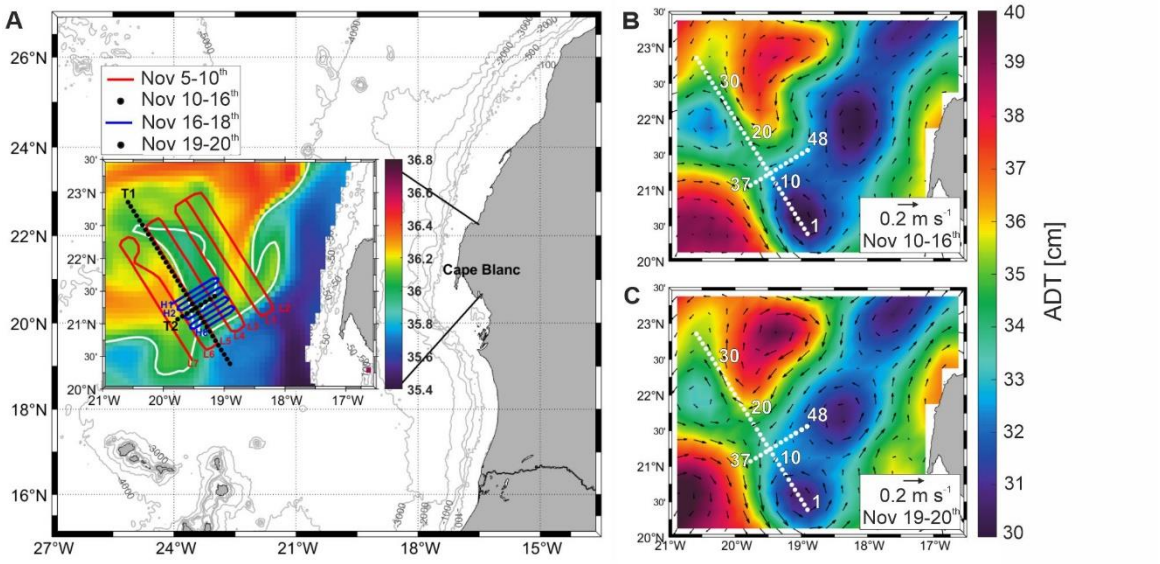

Figure 3.1. A) Map of FLUXES II cruise presenting the low-resolution (red line) and high-resolution (blue line) SeaSoar grids and the two biogeochemical transects, T1 and T2 (black dots) over a salinity plot representing an average of all cruise days (Nov 5th – 20th) at 155.85 m depth. Made with GLORYS reanalysis. The white line represents the Cape Verde Front at a salinity of 36.045. Average Absolute Dynamic Topography with derived geostrophic field superimposed at the time of B) T1 and C) T2.

Organic matter (OM) either produced in situ or transported from elsewhere contributes differently to the BCP depending on whether it is dissolved (DOM), suspended (POM) or sinking (Boyd et al., 2019; Sanders et al., 2014). DOM is the largest pool of OM in the oceans; it is made up of myriads of compounds of marine and terrestrial origin, participating in a wide variety of production, transformation and removal processes (Hansell, 2013; Repeta, 2015). Although most of the DOM pool is refractory, either of autochthonous or allochthonous origin, a small fraction is photo-reactive and/or bioavailable (Hansell, 2013) and contributes to the BCP through the recycling and export of marine primary production. The optical properties of DOM allow to go a step further in the chemical and structural characterization of the colored and fluorescent fractions of DOM and its role in the BCP (Nelson and Gauglitz, 2016; Stedmon and Nelson, 2015). Colored dissolved organic matter (CDOM) is the fraction of DOM that absorbs light in the UV and visible spectrum (del Vecchio and Blough, 2002). The most commonly used absorption coefficients for tracing the different CDOM fractions are positioned at 254 nm ($a_{CDOM}(254)$) and 325 nm ($a_{CDOM}(325)$), which are proxies to the concentration of conjugated carbon double bonds (Weishaar et al., 2003) and aromatic rings (Nelson et al., 2004), respectively. The

absorption spectral slopes between 275 and 295 nm ($S_{275-295}$) and between 350 and 400 nm ($S_{350-400}$) and its ratio S_R are commonly used to trace the origin, photochemical transformations, and average molecular weight of DOM (Helms et al., 2008). See Chapters 1 and 2 for further details of the colored properties of DOM. A small fraction of CDOM can re-emit light at a longer wavelength and it is called fluorescent DOM (FDOM). FDOM is divided into two main groups of fluorophores with contrasting excitation/emission wavelengths as were described in Chapters 1 and 2 of this dissertation.

Similarly to DOM, the vertical profiles of suspended POC and the C:N molar ratio of POM are used to trace the role of POM in the BCP (Nowicki et al., 2022). POC accumulates in the surface mixed layer, where it is produced, and then is transported downwards by advection and turbulent diffusion processes (Lévy et al., 2012; Nagai et al., 2015). Its concentration decreases dramatically through the epi- and mesopelagic layers, where it is consumed. Preferential consumption of N over C compounds leads to an increase of the C:N molar ratio with depth (Álvarez-Salgado et al., 2014). Conversely, the fate of sinking POM is mainly dictated by the settling velocity of the aggregates of marine snow, which can sink at tenths to hundreds of meters per day (Nowald et al., 2009; Riley et al., 2012).

The aim of this chapter is to disentangle the variability of DOM and POM in the CVFZ at the meso- and submesoscale range in relation to the physical and biogeochemical processes operating in the area during fall, the time of the year of most intense upwelling activity. First, we focus on the epipelagic layer (< 200 m depth), where the dominant physical processes are associated to the high-resolution variability created by meso- and submesoscale (meanders, eddies) structures at the front. Second, we study the mesopelagic layer (200 - 1500 m), where the dominant physical process is the mixing of water masses of contrasting origin. For the epipelagic layer we aim to test the impact of meso- and submesoscale structures on the biogeochemistry of the front, with particular emphasis on POM, DOM and its colored and fluorescent fractions, which present an anomalous band of elevated humic-like fluorescence below the pycnocline. For the mesopelagic layer we aim to assess whether the high mesoscale activity in the epipelagic layer has an imprint in the mesopelagic layer, the relevance of local vs. basin scale mineralization processes on the OM distributions, and the contribution of DOM and POM to the local apparent oxygen utilization at the front.

2. Materials and Methods

2.1 Sampling strategy and analytical procedures

Data used in this study were collected during the FLUXES II cruise (2-24 November 2017, on board R/V Sarmiento de Gamboa), in the CVFZ. The cruise consisted on two main activities: 1) three SeaSoar grids for high-resolution characterization of the CVFZ; and 2) two biogeochemical transects at high spatial resolution (5 nautical miles, NM; 9.3 km). The SeaSoar (MKII, Chelsea Instruments) was equipped with conductivity-temperature-depth (CTD, SBE 911 plus), oxygen (SBE 43), fluorescence (SeaPoint SCF) and turbidity (SeaPoint STM) sensors. All the measures were carried out with a constant cruising speed of 8 knots, covering the depth range of 0-450 m. The first SeaSoar grid consisted of 7 transects covering a box of 120 x 90 NM (222.2 x 166.7 km) for a general characterization of the study area and the second grid consisted of 8 transects that covered a box of 45 x 35 NM (83.3 x 64.8 km) (Fig. 3.1a). The third and last grid will not be considered in this manuscript. Current velocities were measured with a 75 kHz RDI ship Acoustic Doppler Current Profiler (sADCP) configured in narrow band (long range). The sADCP provided along track raw data every 5 minutes from 36 to 800 m depth. The three SeaSoar grids is a focus of a dedicated chapter by Burgoa (2022). Here, they will be used just to contextualize the two high-resolution (5 NM) biogeochemical transects performed after the first and second SeaSoar grids.

Sampling during the high resolution transects was carried out using a rosette sampler equipped with conductivity-temperature-depth (SBE911 plus), oxygen (SBE43), fluorescence of chlorophyll (SeaPoint SCF), turbidity (SeaPoint STM), transmittance (WetLabs C-Star) and nitrate (SUNA V2, SeaBird) sensors. The rosette included 24 Niskin bottles of 12 liters for water collection. A total of 48 hydrographic stations were sampled with 10 levels each from surface to 1500 m. The first transect consisted of a 175 NM (324 km) long section with 36 sampling stations and a horizontal resolution of 5 NM (9.3 km). The second transect, perpendicular to the first one, was 55 NM (102 km) long with 12 stations and the same horizontal resolution as in the first transect (Fig. 3.1a).

2.2 Core variables

Conductivity, dissolved oxygen (O_2), fluorescence of chlorophyll (Chl-*a*) and nitrate sensors were calibrated with discrete water samples collected from the rosette. A procedure

adapted from Langdon (2010) was used to determine the dissolved oxygen (O_2) on board by the Winkler potentiometric method. The apparent oxygen utilization (AOU) was calculated following Benson and Krause (UNESCO, 1986), where AOU = O_2sat – O_2, with O_2sat being the oxygen saturation. Determination of Chl-*a* was made according to the method of Holm-Hansen et al. (1965). Samples for inorganic nutrient determination were taken in 25 mL polyethylene vials directly from the Niskin bottle and kept frozen at -20ºC until analyzed in the base laboratory. Nutrient concentrations were determined by segmented flow analysis in an Alliance Futura autoanalyser. Nitrate, nitrite, phosphate, and silicate were determined colorimetrically as described in Hansen and Koroleff (1999). Ammonium concentration was determined using the fluorometric method of Kérouel and Aminot (1997). The pycnocline, which separates the surface mixed layer from the waters immediately below, was calculated following the Eq. 2.1 in Chapter 2.

2.3 Organic matter variables

Suspended POC, nitrogen (PON) and DOC determinations followed the sampling procedures and analysis described in Chapter 2. The analytical procedures for measuring the CDOM and FDOM fractions are also described in Chapter 2. In this Chapter, the CDOM parameters $a_{CDOM}(254)$, $a_{CDOM}(325)$, the spectral slope of the wavelengths bands 275-295 ($S_{275-295}$) and, 350-400 ($S_{350-400}$), and the ratio S_R are used. Regarding FDOM, the time constrains of the high-resolution sampling strategy followed during the occupation of the biogeochemical transects hindered the recording of excitation-emission matrices (EEMs) that were carried out in the FLUXES I cruise. Instead, four excitation-emission (Ex/Em) wavelength pairs were selected following Coble (1996). These Ex/Em pairs were 250/435 nm (peak A, general humic-like substances), 340/440 nm (peak C, terrestrial humic-like substances), 320/410 nm (peak M, marine humic-like substances) and 280/350 nm (peak T, tryptophan-like substances).

2.4 Optimum multiparameter (OMP) mesopelagic water mass analysis

An optimum multiparameter (OMP) inverse method (Karstensen and Tomczak, 1998; Poole and Tomczak, 1999) was employed to determine the relative contribution of each water type (WT) to every sample collected through the mesopelagic layer. The reader is referred to Chapter 2 of this dissertation where a detailed description of the methodology is presented. Briefly, the proportion of each WT in a given water sample can be achieved by solving a set of linear mixing equations for volume, θ, S, SiO_4H_4 and NO in a non-

negative less-squares sense (Eq 2.3). The thermohaline and chemical characteristics of each WT were taken from the literature (Table 2.1 in Chapter 2). For the FLUXES II cruise, a total of 9 WTs have been identified down to 1500 m: MMW; ENACW of 15ºC and 12ºC; SACW of 18ºC and 12ºC; SPMW; AA; MW and LSW. Four mixing groups were created based on expert knowledge of the hydrography of the study area (Valiente et al. 2022). The four groups of WTs defined are: 1) MMW - SACW18 - ENACW15; 2) SACW18 - ENACW15 - SACW12 - ENACW12; 3) SACW12 - ENACW12 - SPMW - AA; and 4) SPMW - AA - MW – LSW (Fig. 3.2). The water mass analysis includes samples below 200 m, where the parameters used behaves conservatively. In this case, a total of 290 out of 480 samples were included in the OMP analysis.

Once the water type proportions (X_{ij}) are calculated and using the values of any measured variable (N), the water mass proportion-weighted average concentration of N in each water type, N_j or archetype value of N, is calculated (Eq. 2.4). The standard error (SE) is also calculated following Eq. 2.5. For the FLUXES II cruise, archetype values were determined for Z, S, θ, NO_3^-, AOU, DOC, POC, PON, CDOM indices and FDOM indices. To determine the fraction of the total variability of N due to water mass mixing, a multiple linear regression of N_j with the water types proportions (X_{ij}) is performed (Eq. 2.7). The determination coefficient (R^2) indicates the percent of explained variability and the standard error (SE) defines the goodness of the fit. To consider the combined effect of mixing and biogeochemical processes on the variable N, the explanatory variable AOU is added to the linear regression model (Eq. 2.8), incorporating a coefficient (β) that relates the chemical variable N with AOU (Álvarez-Salgado et al., 2014, 2013; Valiente et al., 2022). Interestingly, the coefficient β does not depend on the WT mixing and represents the rate of change of variable N with AOU.

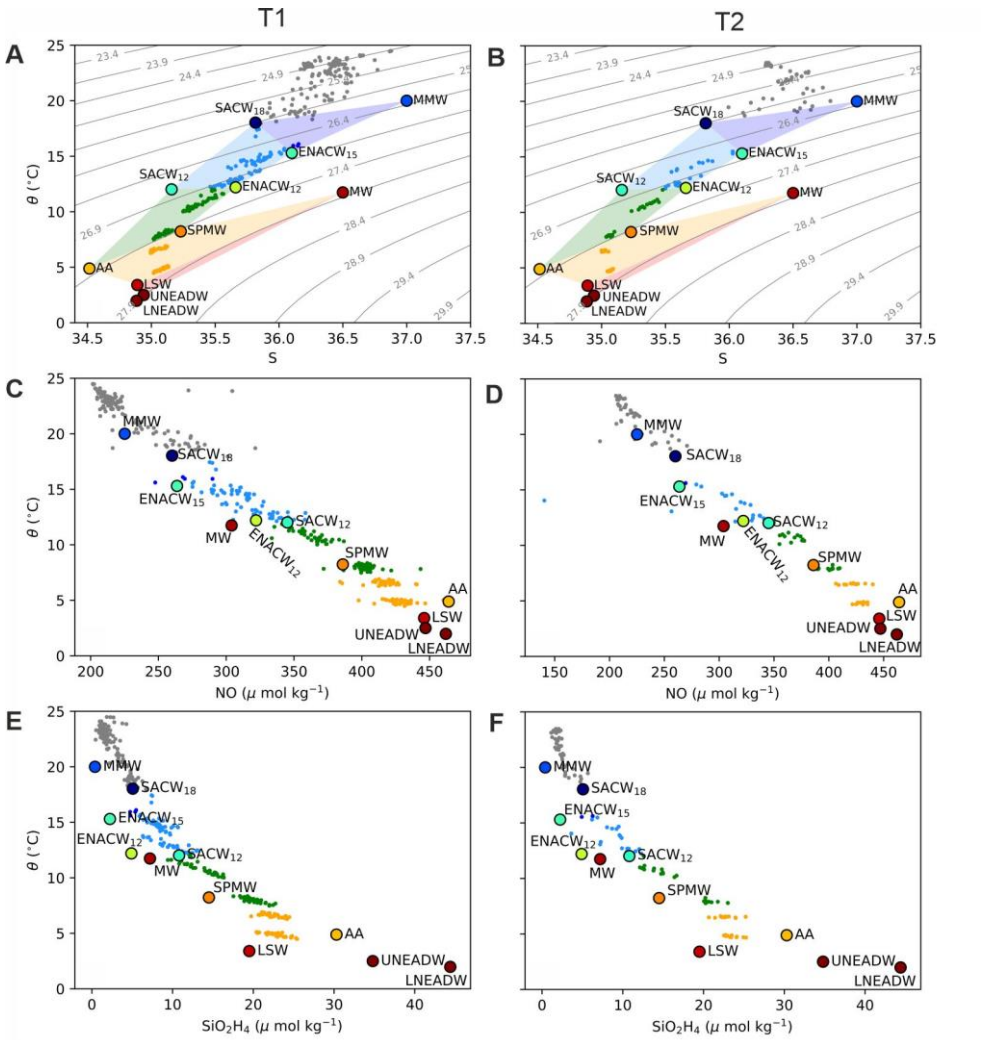

Figure 3.2. A, B) Potential temperature versus salinity, C, D) NO and E), F) SiO2H4 for the T1 (left) and T2 (right) during the FLUXES II cruise. Dots represent the water samples collected and the colored shadow areas in A) and B) identify the mixing group assigned to each sample. The four established mixing groups are: 1) MMW-SACW18-ENACW15; 2) SACW18-ENACW15-SACW12-ENACW12; 3) SACW12-ENACW12-AA-SPMW; and 4) AA-SPMW-MW-LSW. Potential density contours are also shown in A) and B).

3. Results

3.1 High-resolution mapping of the CVFZ in November 2017

When biogeochemical transect T1 was occupied (November 10th to 16th) satellite altimetry images revealed that most of the transect (stn 13 to 36) was edging the southwestern front of an anticyclonic eddy situated immediately to the northeast (Fig. 3.1b). In contrast, the southern end of T1 (stn 1 to 13) was affected by a cyclonic eddy, whose core was at stn 4-5 (Fig. 3.1b). During the occupation of the biogeochemical transect T2 (November 19th to 20th) the anticyclonic eddy displaced slightly to the northwest, changed its shape and intensified while the cyclonic eddy moved slightly to the south and weakened its intensity (Fig. 3.1c).

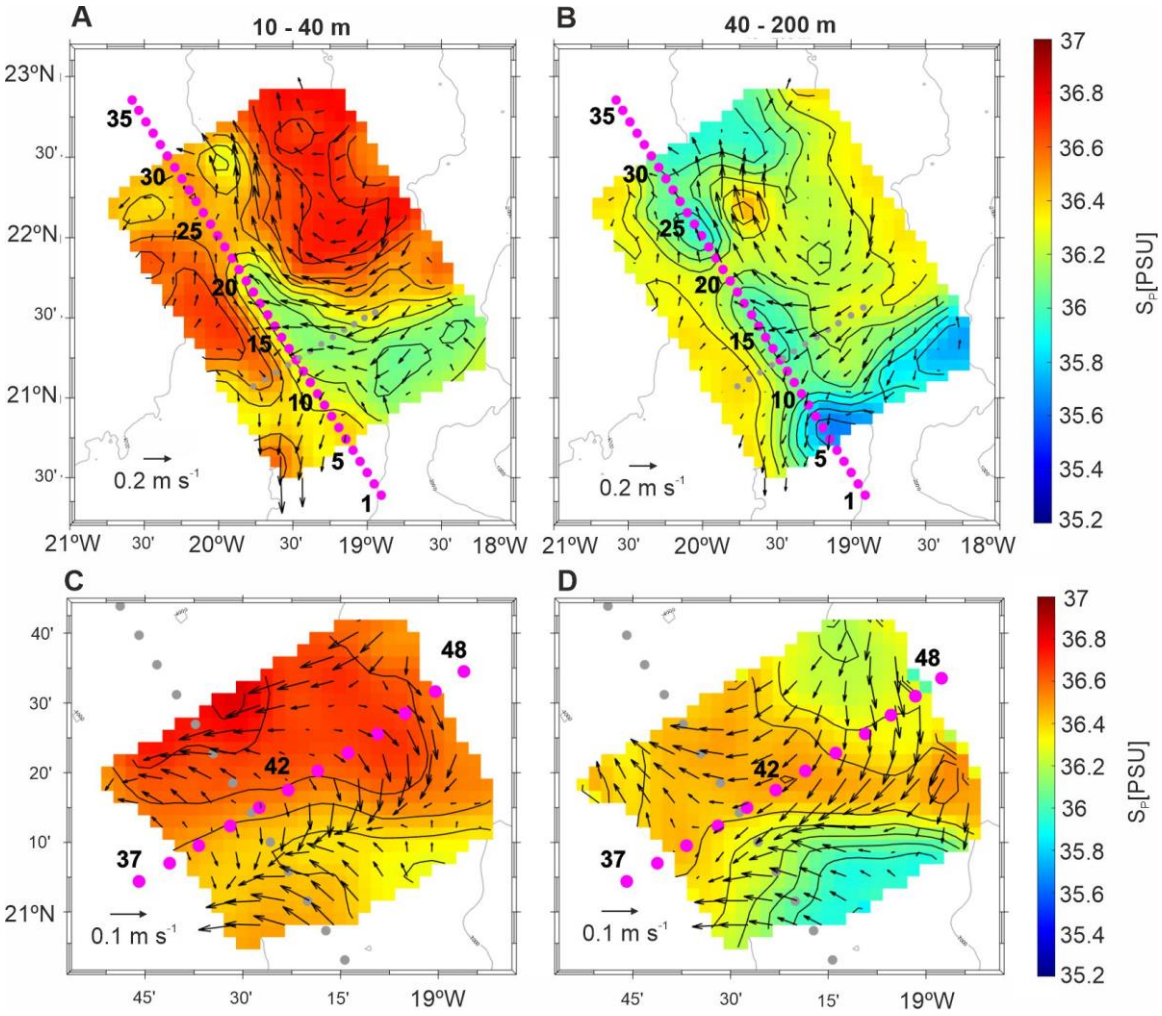

Figure 3.3. Average interpolated grids of salinity and horizontal velocity field superimposed between 10-40 m and 40-200 m at the time of A) and B) T1 and C) and D) T2. Current velocities were measured with the ship ADCP.

A shallow intrusion of low salinity (S < 36.2) is clearly identified in the upper 40 m during the first SeaSoar grid (Fig. 3.3a), which extended along the southern part of T1 and intruded through a body of higher salinity (S > 36.2). Between 40 - 200 m, the low salinity water body extended from the southeast to the northwest, occupying the southern half of T1. In addition, another water body with similar characteristics was located in the northern sector of the transect, leaving a narrow area of high salinity in between (Fig. 3.3b). Biogeochemical transect T2 was occupied 3-4 days later than T1. Intense changes occurred in the salinity and current velocity plots, revealing that T2 was not synoptic with T1 at least in the upper 40 m, where the tongue of low salinity water (Fig. 3.3a, b) disappeared, being occupied by a high salinity surface water body (Fig. 3.3c). Below 40 m, the less saline water (S < 36.2) was displaced to the south being replaced by a higher salinity water body

(S > 36.2) (Fig. 3.3d). A detailed analysis of the high-resolution mesoscale activity during the cruise can be found in Burgoa (2022).

Figure 3.4 shows the correspondence between transect L5 of the first SeaSoar grid and biogeochemical transect T1. L5 was occupied on November 8th in 15.6 hours from northwest to southeast, while T1 transect took from November 10th to 16th from southeast to northwest. This means that the northwestern end of T1 was sampled 8 days after the SeaSoar grid while the southeastern end was sampled only 2 days after the SeaSoar grid. It is noticeable that the same mesoscale structures were observed during the occupations of L5 and T1, but larger differences were observed in the northern half of the transect consisting of a spatial displacement of the structures approximately 50 km to the north at the time of T1 occupation. On the contrary, the southern sector matched quite well due to a closer proximity in time.

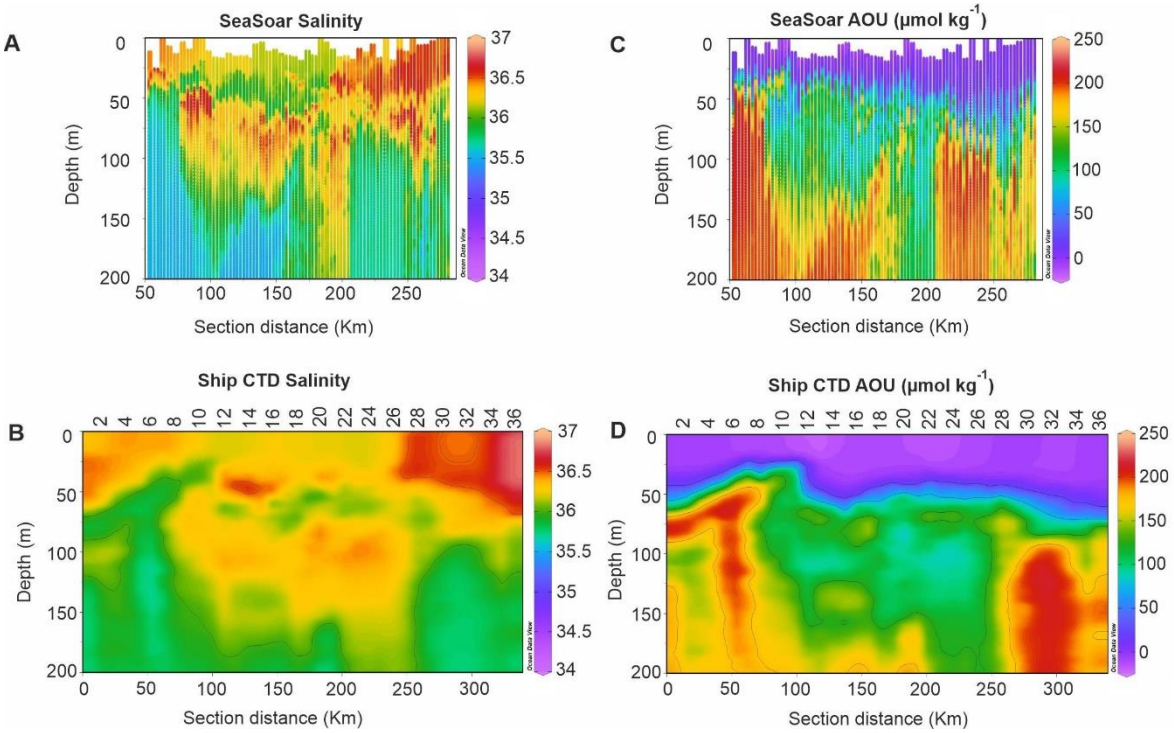

Figure 3.4. Vertical sections of A, B) salinity and C, D) AOU comparing the SeaSoar L5 leg (upper pannels) with the T1 (lower panels). Note that both transects coincide in location but not in time. SeaSoar L5 was occupied in Nov 8th and T1 was occupied from Nov 11th to 16th. Track distance is counting from southeast to northwest. Produced with Ocean Data View (Schlitzer, 2017).

3.2 Hydrographic variability of epipelagic waters along the biogeochemical transects

The CVF separates the warm and salty NACW from the cooler and fresher SACW. Zenk et al. (1991) defined the CVF as the intersection of the 150 m isobath with the 36 isohaline.

Recently, Burgoa et al. (2021) extended its definition vertically and established an equation which define the front location at any depth from 100 to 650 m, based on an equal contribution (50%) of NACW and SACW. In the 100-200 m depth range the definition of Zenk et al. (1991) is very consistent with the Burgoa et al. (2021) and so we will use it to establish the hydrographic domains described below.

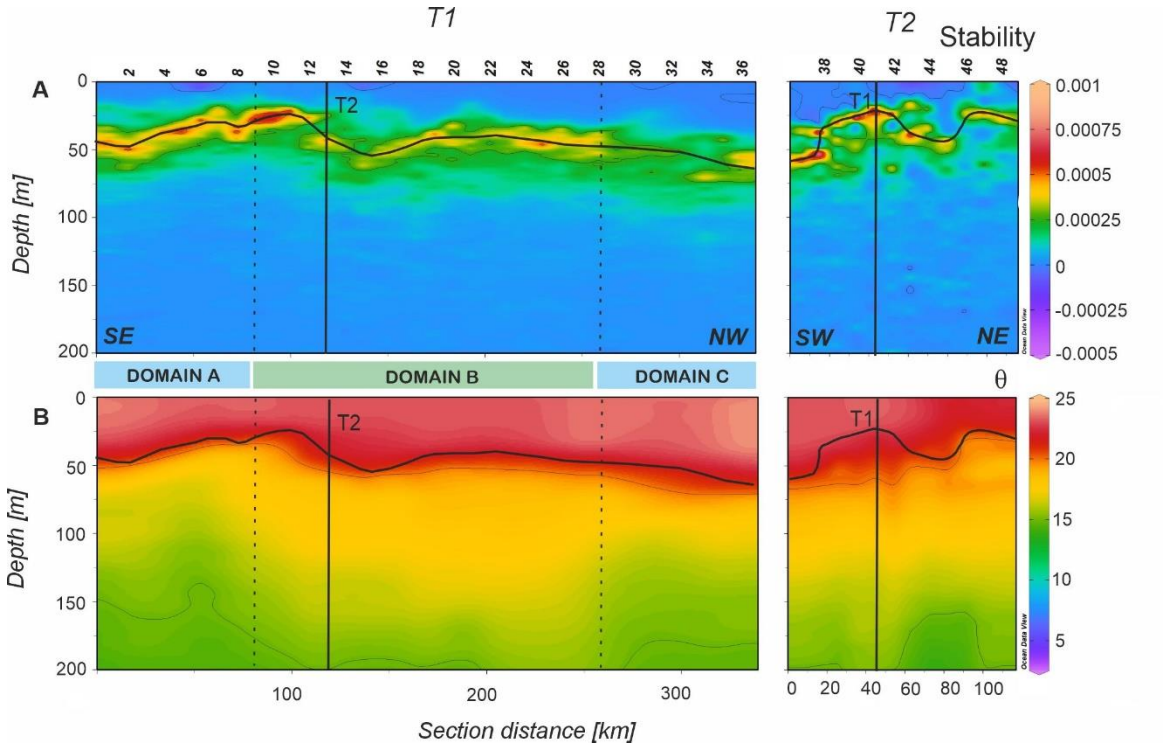

Figure 3.5. Distributions of A) stability of the water column in (s^{-2}) and B) potential temperature (θ) in the epipelagic layer of the FLUXES II cruise for the T1 (left) and T2 (right). The orientation is indicated at the bottom of the first panel (A) for T1 (SE, Southeast and NW, Northwest) and T2 (SW, Southwest and NE, Northeast). T1 is divided into three domains (A, B and C) separated by vertical dotted lines at stn 9 and 28. Dots represent samples and vertical black lines show the position of the orthogonal transect T2 and T1, respectively. Horizontal black line shows the position of the pycnocline, and was drawn from the stability profile. Section distance is counting from southeast to northwest in T1 and from southwest to northeast in T2. Produced with Ocean Data View (Schlitzer, 2017).

A well-marked pycnocline along T1 and T2 was identified (thick black line in Fig. 3.5a) ranging from 24 to 64 m (average, 42 m), which separates the warmer surface mixed layer from the colder sub-surface waters below. Three hydrographic domains were identified below the pycnocline along T1 according to the position of the CVF at 150 m. The depth of the 36 isohaline showed a marked variability, from 40 m at stn 6-8 to more than 200 m at stn 23-27. The CVF was crossed at stn 9 and 28 (dotted vertical lines in Figs. 3.5, 3.6, 3.7 & 3.8). In domains A (stn 1-9) and C (stn 28-36) the low salinity SACW was the prevailing water mass, whereas domain B was mainly occupied by the high salinity NACW.

Remarkably, a filament-shaped low-salinity intrusion was identified along domains A and B, consisting of a 25 m thick layer of water with S < 36 from 50 to 80 m. In domain A, the intrusion appeared connected with a SACW uplift, while in domain B, this lens of low salinity intruded into a body of higher salinity just below the pycnocline (Fig. 3.6a, horizontal dotted line). In domain B and above this intrusion, a thin layer of higher salinity was observed coinciding with the position of the pycnocline, with maximum values at stns 13-15. Below the intrusion, there was a thicker high salinity water body down to 150 m with NACW characteristics coinciding with higher values of temperature (Fig. 3.5b) and lower values of AOU (Fig. 3.6b) and NO_3^- (Fig. 3.6c).

In domain C, an intrusion of high salinity water (S > 36.5) in the surface mixed layer (Fig. 3.6a) coincided with the highest values ($p < 0.0005$) of θ, 23.30 ± 0.04 ºC (Fig. 3.5b; Table 3.1) and the lowest values ($p < 0.0005$) of Chl-a, 0.37 ± 0.01 µg L^{-1} (Fig. 3.6d; Table 3.1). Below the pycnocline down to 200 m, temperatures were significantly different between the three domains, with the highest values found in domain B ($p < 0.0005$; Table 3.2), occupied by NACW.

AOU was higher at the surface mixed layer in domain A (1.73 ± 1.44 µmol kg^{-1}) and domain C (-1.46 ± 0.64 µmol kg^{-1}) (Table 3.1), which contrasts with the significantly lower ($p < 0.0005$) values found in domain B (-4.57 ± 0.62 µmol kg^{-1}), suggesting higher net primary production in this sector. Below the pycnocline, average values of AOU were quite similar in domains A and C and again significantly lower ($p < 0.0005$) in domain B (Table 3.1), coinciding with the warmer and saltier water body of NACW (Fig. 3.6b). The shallow and low salinity intrusion in this domain was also traceable in the AOU profile with slightly higher levels at 50-80 m.

NO_3^- distributions measured by a SUNA probe were well correlated with salinity (R^2 = 0.72, n = 9417) and especially with AOU (R^2 = 0.96, n = 9417). In domain A, the 20 µmol kg^{-1} nitrate isoline uplifted from 90 m at stn 1 to 50 m at stn 8 (Fig. 3.6c). Then, the isoline deepened abruptly to 165 m, coinciding with the CVF. In domain B, the 20 µmol kg^{-1} nitrate isoline remained below 165 m attributable to the body of nutrient-poor NACW located above this depth. Finally, at stn 28, the isoline raised abruptly up to 100 m coinciding again with the CVF and the dominance of the nutrient-richer SACW in domain C.

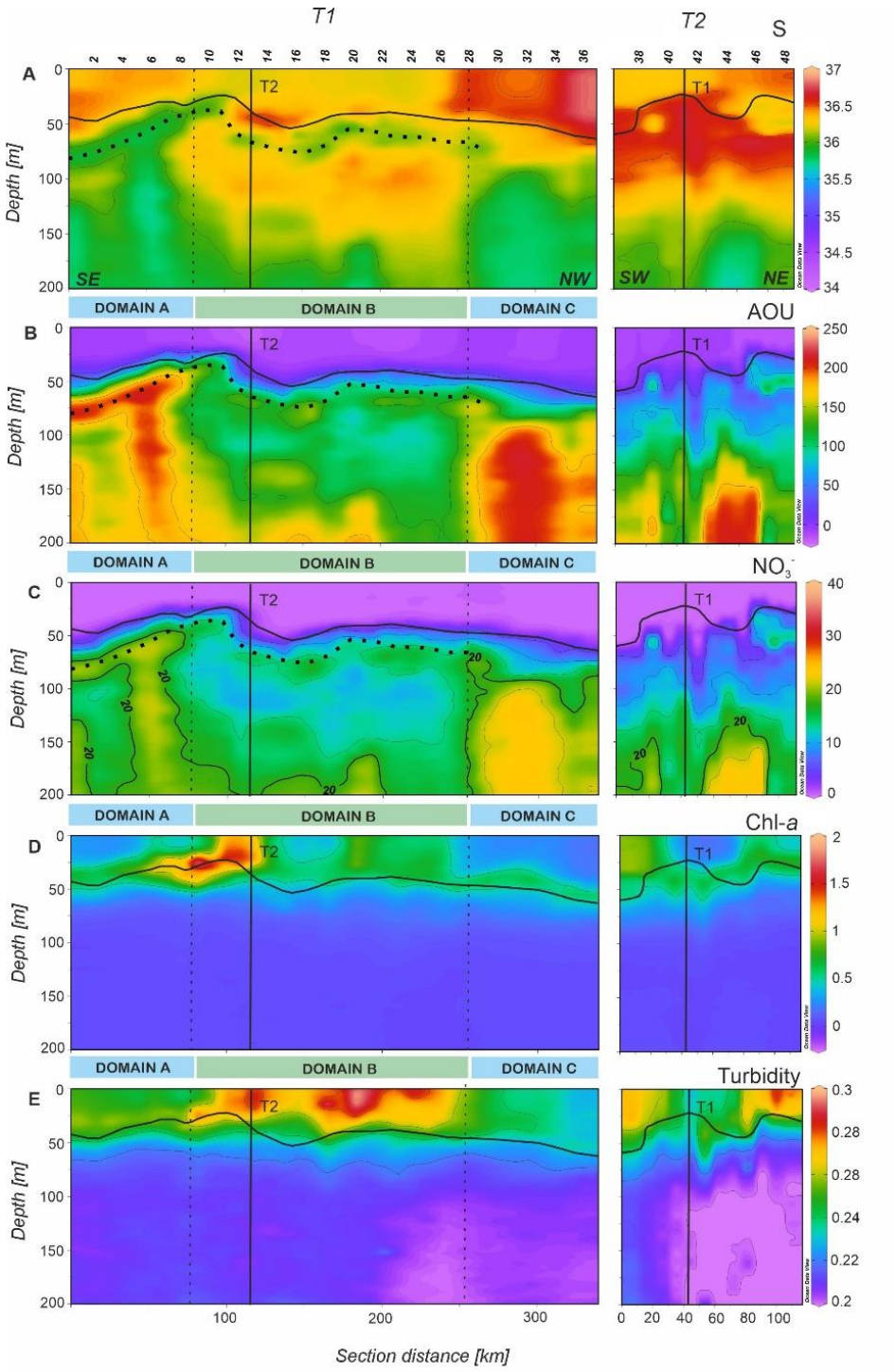

Figure 3.6. Distributions of A) salinity (S), B) apparent oxygen utilization (AOU) in µmol Kg^{-1}, C) nitrate (NO_3^-) in µmol Kg^{-1}, D) chlorophyll-a (Chl-a) in µg L^{-1} and E) turbidity in NTU in the epipelagic layer of the FLUXES II cruise for the T1 (left) and T2 (right). All measurements were obtained at 1 dbar vertical resolution. T1 is divided into three domains (A, B and C) separated by vertical dotted lines at stn 9 and 28. Vertical black lines show the position of the orthogonal transects T2 and T1, respectively. Horizontal black line show the position of the pycnocline and horizontal black dotted line in a, b and c profiles show the position of the less saline intrusion (see text). Section distance is counting from southeast (S) to northwest (N) in T1 and from southwest (W) to northeast (E) in T2 (labelled at the bottom of the first panel). Produced with Ocean Data View (Schlitzer, 2017).

The shallow and low salinity intrusion present in domain B was also perceptible in the high NO_3^- concentrations observed just below the pycnocline. Below the pycnocline, average values of NO_3^- were significantly different between the three domains, with the lowest values found in domain B ($p < 0.0005$).

The DCM roughly coincided with the position of the pycnocline (Fig. 3.6d), being at 33.8 m in domain A and at 45.5 m in domain C, while in domain B high chlorophyll reached the surface layer. Maximum values of Chl-*a* >1.5 µg L^{-1} were found at stn 8-13, at the boundary between domains A and B. It is also noticeable that at stn 8-15, 18-26, 37-39 and 45-47, Chl-*a* was distributed homogeneously through the surface mixed layer instead of concentrating at the DCM. Turbidity (Fig. 3.6e) shows the highest particle concentrations in the surface mixed layer and, particularly in domain B. In this domain, turbidity decreased northwestward, coinciding with lower values of Chl-*a* and higher values of temperature and salinity. Below the pycnocline, particle concentration decreased markedly, with significant differences between the three domains ($p < 0.0005$) and decreasing northwestward.

As explained in section 3.1, T2 was not synoptic with T1 and therefore failed to provide the desired 3D view of the CVFZ. Higher salinity water coming from the north displaced the low salinity water from the central sector of T1 at the time when T2 was occupied (Fig. 3.3a & c). Salinity was also higher below the pycnocline, indicative again of this substitution of less salinity by higher salinity waters (Fig. 3.6a). The SACW was located deeper at approximately 140 m, and the CVF was not observed along this transect. Chl-*a* distribution showed higher values at both ends of T2 and lower in the middle (Fig. 3.6d). The distribution of turbidity was parallel to Chl-a with higher particle concentration at both ends of the transect (Fig. 3.6e). Below the pycnocline, less turbidity was detected in the northeastern side of this section.

3.3 DOM, POM, CDOM and FDOM distributions in epipelagic waters along the biogeochemical transects

DOC presented an average concentration of 76.0 ± 0.8 µmol L^{-1} along T1 in the surface mixed layer, with a maximum value of 97 µmol L^{-1} located at stn 21 (Fig. 3.7a), coinciding with the highest values of Chl-*a* and turbidity (Fig. 3.6d & e). DOC decreased significantly with depth, but the distribution was not homogenous: columns of relatively high DOC values extending down to 200 m were surrounded by areas of lower concentration. DOC

showed a significant correlation with AOU in epipelagic waters below the pycnocline (orthogonal distance regression (ODR); DOC = -0.15 (± 0.01)·AOU + 75.5 (± 1.3); R^2 = 0.49; n = 116). Surface mixed layer waters were excluded from this correlation because of the impact of gas exchange with the atmosphere. According to the slope of this regression, DOC supports 21% of the oxygen demand in the epipelagic waters, assuming a Redfieldian -O_2/C stoichiometric ratio of 1.4 mol O_2 mol C^{-1} (Anderson, 1995). Considering the three domains separately, domain B presented a significantly more negative slope (-0.18 ± 0.02) than domains A and C (-0.13 ± 0.04 and -0.15 ± 0.03, respectively). Therefore, while DOC supports 25.3% of the oxygen demand in domain B, this value decreases to only 18.5% and 21.0% in domains A and C, respectively.

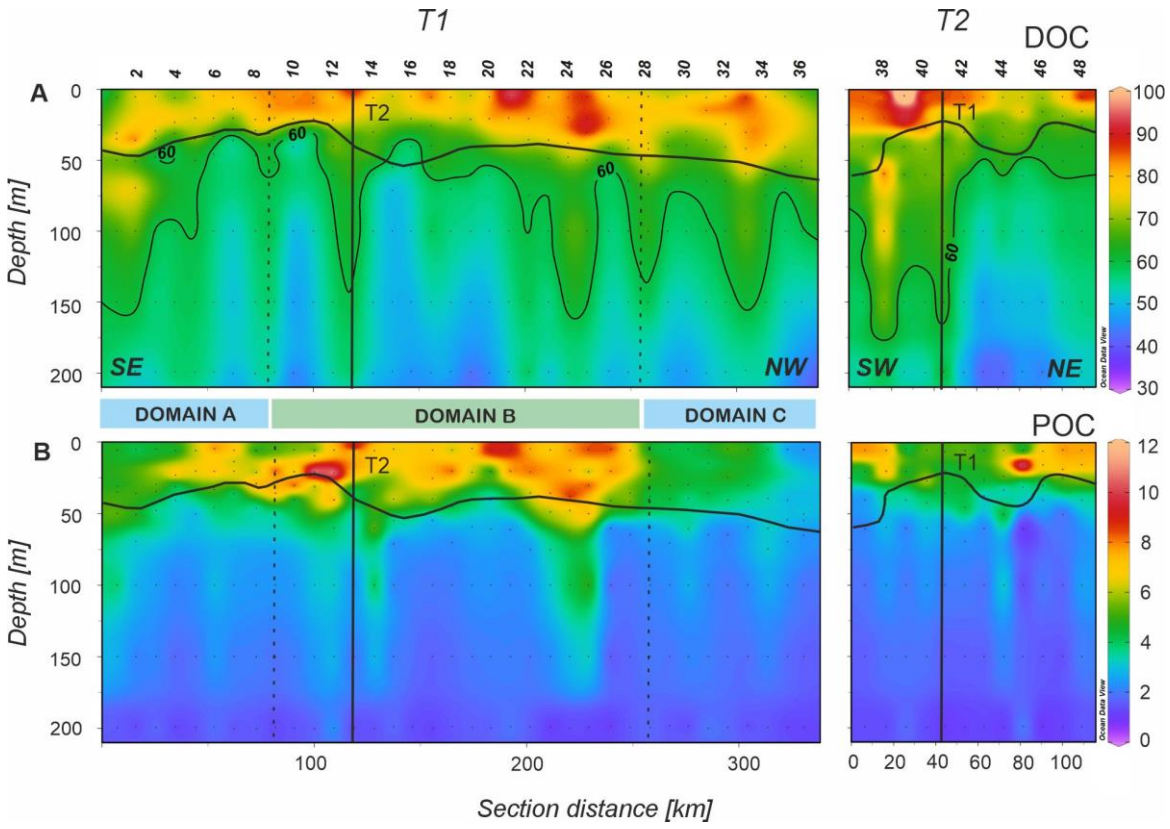

Figure 3.7. Distributions (A) dissolved organic carbon (DOC) in µmol Kg^{-1} and (B) suspended particulate organic carbon (POC) in µmol Kg^{-1} in the epipelagic layer of the FLUXES II cruise for the T1 (left) and T2 (right). T1 is divided into three domains (Domain A, Domain B and Domain C) separated by vertical dotted lines at stn 9 and 28. Dots represent samples and vertical black lines show the position of the orthogonal transect T2 and T1, respectively. Horizontal black line shows the position of the pycnocline. Section distance is counting from southeast (SE) to northwest (NW) in T1 and from southwest (SW) to northeast (NE) in T2 (labelled at the bottom of the first panel). Produced with Ocean Data View (Schlitzer, 2017).

The highest POC concentrations were observed at the surface mixed layer in domain B with an average value of 7.02 ± 0.35 µmol L^{-1} (Fig. 3.7b; Table 3.1). On the contrary, the lowest surface POC concentrations were found in domain C (3.88 ± 0.17 µmol L^{-1}). An

average value of 2.78 ± 0.21 µmol L^{-1} was obtained below the pycnocline all along T1, decreasing significantly ($p < 0.05$) from domain A to domain C (Table 3.1). POC correlated significantly with Chl-*a* (ODR; POC = 4.0 (± 0.2)·Chl-*a* + 1.7 (± 0.2); $R^2 = 0.54$; n = 235) and with DOC (ODR; POC = 0.21 (± 0.02)·DOC – 9.8 (± 0.7); $R^2 = 0.44$; n = 235) through the epipelagic layer. PON resembled the distribution of POC (ODR; POC = 7.4 (± 0.1)·PON + 0.6 (± 0.1); $R^2 = 0.92$; n = 235; data not shown). The C:N molar ratio of POM increased significantly with depth ($p < 0005$), from values > 8 in the surface mixed layer to values > 11 below the pycnocline for the three domains (Table 3.1). We also examined the correlation of the sum of DOC and POC with AOU (ODR; (DOC + POC) = -0.17 (± 0.02)·AOU + 80.32 (± 1.40); $R^2 = 0.50$; n = 116).

The slope of the linear regression indicates that the dissolved and suspended particulate OM fractions support together 23.6% of the oxygen demand in the epipelagic waters below the pycnocline, the remaining being therefore supported by the sinking OM fraction. Again, domain B presented a significantly more negative slope (-0.21 ± 0.03) for the DOC+POC vs AOU correlation than domains A (-0.15 ± 0.04) and C (-0.16 ± 0.03). Therefore, DOC+POC supports 29.5% of the oxygen demand of epipelagic waters below the pycnocline of domain B, while only 20.4% and 22.6% in domains A and C, respectively.

The distribution of $a_{CDOM}(254)$ (Fig. 3.8a), a proxy to the abundance of conjugated carbon double bonds in DOM (Catalá et al., 2018; Lønborg and Álvarez-Salgado, 2014) was characterized by higher levels in the surface mixed layer that decreased gradually with depth (Table 3.1). The correlation of $a_{CDOM}(254)$ with DOC was significant (ODR; DOC = 38.0 (± 1.7)·$a_{CDOM}(254)$ + 11.4 (± 2.1); $R^2 = 0.67$; n = 240). Regarding $a_{CDOM}(325)$ (Fig. 3.8b), a proxy to the aromatic fraction of DOC (Nelson et al., 2004), the highest values were found again in the surface mixed layer with 0.30 ± 0.01 m^{-1}. Below the pycnocline the average value was significantly lower ($p < 0.005$) at 0.26 ± 0.01 m^{-1}. $S_{275\text{-}295}$, a proxy for the average molecular weight, origin and photochemical transformations of DOM, showed higher values in the surface mixed layer, with an average of 3.26 ± 0.04 10^{-2} nm^{-1} for T1 (Table 3.1). The average value decreased below

Table 3.1. Thermohaline and chemical characteristics (average value ± SE) of the epipelagic waters above and below the pycnocline and at the deep chlorophyll maximum (DCM) along the biogeochemical transect T1. Domains A, B and C correspond to stns 1-8, 9-28 and 29-36, respectively.

		Above pycnocline			**DCM**			**Below pycnocline**		
		Dom A	Dom B	Dom C	Dom A	Dom B	Dom C	Dom A	Dom B	Dom C
Z pycnocline	(m)				34.0 ± 2.7	39.6 ± 1.6	45.7 ± 2.9			
θ	(ºC)	23.00 ± 0.05	22.99 ± 0.02	23.30 ± 0.04	21.37 ± 0.57	21.84 ± 0.27	22.75 ± 0.18	16.08 ± 0.04	17.30 ± 0.03	16.65 ± 0.06
S	(PSU)	36.38 ± 0.01	36.31 ± 0.01	36.58 ± 0.01	36.28 ± 0.06	36.34 ± 0.05	36.56 ± 0.04	35.95 ± 0.01	36.19 ± 0.00	35.96 ± 0.01
Chl-*a*	(µg L^{-1})	0.63 ± 0.03	0.66 ± 0.01	0.37 ± 0.01	1.57 ± 0.30	1.17 ± 0.25	0.83 ± 0.09	0.15 ± 0.01	0.12 ± 0.00	0.11 ± 0.00
AOU	(µmol kg^{-1})	1.73 ± 1.44	-4.57 ± 0.62	-1.46 ± 0.64	53.64 ± 15.91	35.65 ± 8.84	15.27 ± 2.90	165.41 ± 1.09	120.00 ± 0.62	170.39 ± 1.54
NO_3^-	(µmol kg^{-1})	1.43 ± 0.63	0.83 ± 0.31	0.65 ± 0.21	6.82 ± 1.92	4.21 ± 1.09	1.80 ± 1.53	19.28 ± 1.76	16.47 ± 0.95	17.72 ± 2.00
DOC	(µmol L^{-1})	75.3 ± 1.3	77.2 ± 1.2	74.8 ± 1.3	69.4 ± 2.0	69.0 ± 1.9	70.8 ± 2.2	60.1 ± 1.6	57.5 ± 1.2	58.4 ± 2.1
POC	(µmol L^{-1})	5.9 ± 0.4	7.0 ± 0.4	3.9 ± 0.2	6.0 ± 0.7	6.3 ± 0.7	3.6 ± 0.2	3.0 ± 0.4	3.0 ± 0.3	2.1 ± 0.2
PON	(µmol L^{-1})	0.69 ± 0.05	0.86 ± 0.05	0.48 ± 0.03	0.71 ± 0.08	0.68 ± 0.07	0.42 ± 0.04	0.28 ± 0.04	0.30 ± 0.04	0.20 ± 0.02
C:N		8.74 ± 0.26	8.24 ± 0.14	8.30 ± 0.22	8.56 ± 0.32	9.39 ± 0.54	8.93 ± 0.50	11.20 ± 0.54	11.24 ± 0.41	11.25 ± 0.71
$a_{CDOM}254$	(m^{-1})	1.65 ± 0.04	1.74 ± 0.02	1.58 ± 0.06	1.61 ± 0.05	1.55 ± 0.03	1.47 ± 0.01	1.33 ± 0.06	1.25 ± 0.03	1.24 ± 0.05
$a_{CDOM}325$	(m^{-1})	0.29 ± 0.01	0.31 ± 0.01	0.28 ± 0.04	0.33 ± 0.02	0.29 ± 0.01	0.26 ± 0.01	0.30 ± 0.03	0.25 ± 0.01	0.26 ± 0.01
$S_{(275-295)}$	(10^{-2})	3.23 ± 0.06	3.23 ± 0.04	3.40 ± 0.12	2.89 ± 0.10	3.10 ± 0.07	3.31 ± 0.09	2.61 ± 0.08	2.84 ± 0.03	2.76 ± 0.05
$S_{(350-400)}$	(10^{-2})	1.59 ± 0.05	1.55 ± 0.04	1.76 ± 0.06	1.47 ± 0.08	1.54 ± 0.06	1.65 ± 0.12	1.41 ± 0.07	1.37 ± 0.03	1.33 ± 0.05
S_R		2.06 ± 0.05	2.11 ± 0.03	1.96 ± 0.09	2.01 ± 0.11	2.04 ± 0.06	2.05 ± 0.10	1.93 ± 0.10	2.10 ± 0.04	2.11 ± 0.05
Peak A	(10^{-3} RU)	27.0 ± 0.8	29.1 ± 0.6	23.0 ± 1.0	31.3 ± 1.9	29.9 ± 1.3	24.9 ± 1.9	31.6 ± 0.9	31.2 ± 0.6	30.7 ± 0.8
Peak C	(10^{-3} RU)	10.7 ± 0.5	11.3 ± 0.3	8.6 ± 0.5	13.4 ± 0.1	12.6 ± 0.7	9.9 ± 0.6	14.5 ± 0.4	14.3 ± 0.3	14.2 ± 0.5
F(320/410)	(10^{-3} RU)	11.7 ± 0.5	12.2 ± 0.3	10.2 ± 0.8	15.1 ± 1.3	14.1 ± 0.8	11.4 ± 0.8	16.6 ± 0.6	16.3 ± 0.4	16.4 ± 0.6
Peak T	(10^{-3} RU)	14.8 ± 0.8	17.2 ± 0.7	15.2 ± 1.4	14.6 ± 1.3	14.3 ± 0.6	12.5 ± 0.7	11.7 ± 0.9	11.6 ± 0.5	10.9 ± 0.8
Peak A/F(320/410)		2.38 ± 0.04	2.41 ± 0.02	2.45 ± 0.06	2.12 ± 0.06	2.15 ± 0.05	2.23 ± 0.07	1.92 ± 0.03	1.91 ± 0.01	1.89 ± 0.02

the pycnocline ($2.76 \pm 0.03\ 10^{-2}\ nm^{-1}$), with the maximum value found in domain B (Table 3.1). Regarding the ratio S_R, average values were characteristic of ocean waters, similar above and below the pycnocline (2.08 ± 0.03 and 2.07 ± 0.04, respectively for T1) and no significant differences were found among the three domains.

Fluorescence intensities of Coble's (1996) humic-like peaks M and C showed a strong positive linear correlation ($R^2 = 0.93$). Therefore, both fluorophores display the same distribution in the study area. Overlapping of their respective fluorescence intensities is the anticipated reason behind this particular behavior. Consequently, we decided to use the fluorescence intensity of peak M as a measure of the concentration of humic-like substances in general, either marine or terrestrial. To avoid any confusion, we will use the term F(320/410) hereinafter. In general, the intensities of F(320/410) (Fig. 3.8c) are lower in the surface mixed layer (Table 3.1). Remarkably, immediately below the pycnocline (between 50 and 150 m), F(320/410) presented a band of relatively high fluorescence with a maximum value of 24×10^{-3} RU. Below this band, values decreased to about 15×10^{-3} RU at 200 m. Analyzing the relationship between F(320/410) and AOU, three groups of samples can be identified (Fig. 3.9). Group 1 (green) represents the surface mixed layer (above the pycnocline) with low AOU; Group 2 (light blue) show the usual trend of humic-like substances accumulation with increasing AOU below the pycnocline; and Group 3 (navy blue) the anomalously high fluorescence of humic-like substances below the pycnocline. Coble's (1996) peak A also shows a good correlation with F(320/410) ($R^2 = 0.77$) but the differences in the distribution of both fluorophores occur specifically in the surface mixed layer, where the ratio peak A/F(320/410) reaches particularly high values (Fig. 3.8e). Significant differences between the three domains were not found, but there the ratio peak A/F(320/410) was significantly higher ($p < 0.001$) above than below the pycnocline (Table 3.1). The protein-like fluorophore (peak T; Fig. 3.8d) showed higher intensities in the upper 30 m and decreased abruptly with depth. For the surface mixed layer, peak T in domain A was significantly lower ($p < 0.025$) than in domain B, and at the DCM, domain C was characterized by significantly lower peak T intensities than domain B ($p < 0.05$). Below the pycnocline, the distribution was not homogeneous and, analogously to DOC, columns of higher peak T intensities were found reaching down to 200 m.

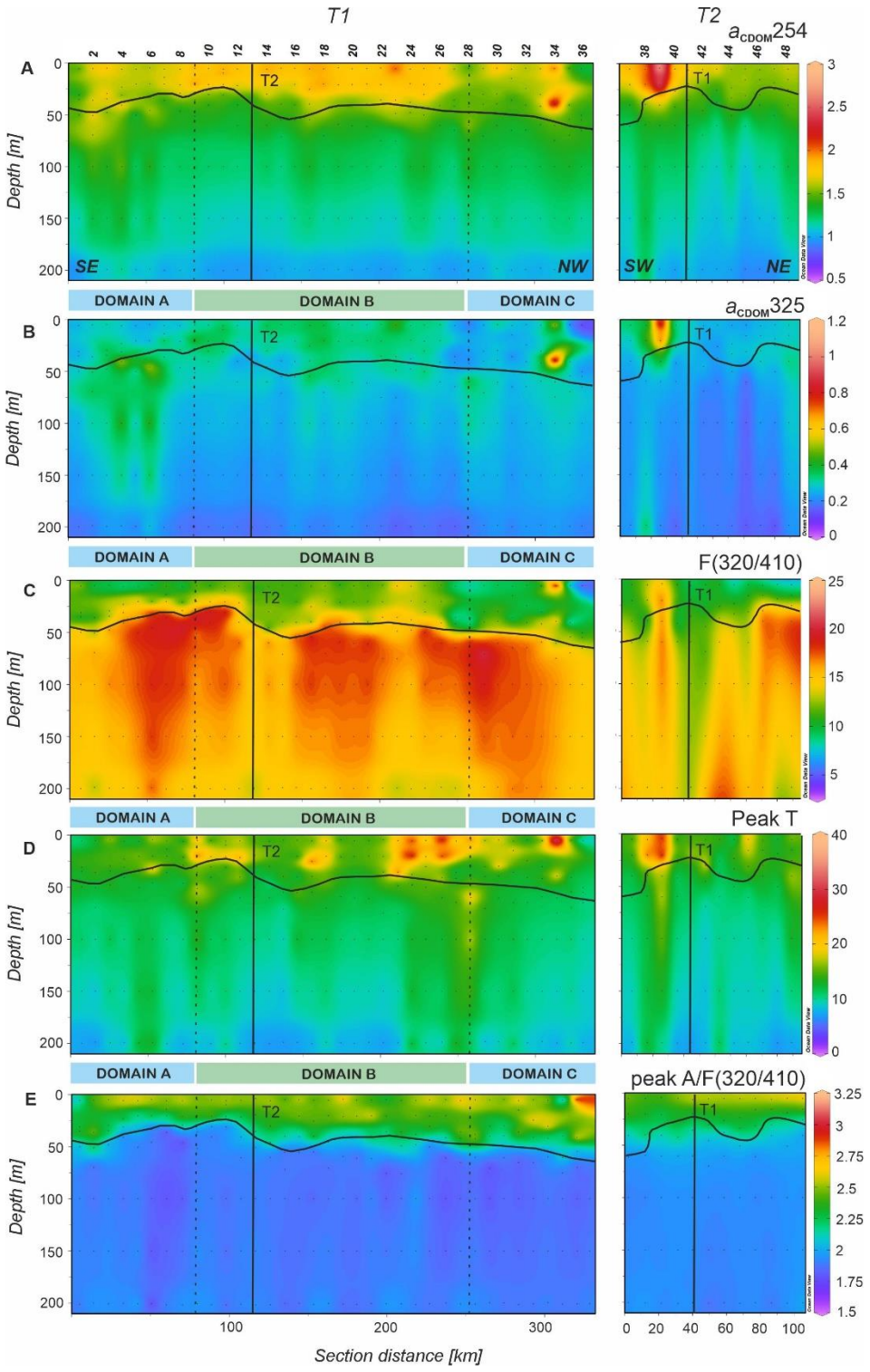

Figure 3.8. Distributions of (A) absorption coefficient at 254 nm ($a_{CDOM}254$) in m^{-1}, (B) absorption coefficient at 325 nm ($a_{CDOM}325$) in m^{-1}, (C) fluorescence at Ex/Em pair 320/410 nm (F(320/410)) in 10^{-3} RU, (D) fluorescence at Ex/Em pair 280/350 nm (peak T) in 10^{-3} RU, and (E) peak A to F(320/410) ratio (peak A/F(320/410)) in the epipelagic layer of the FLUXES II cruise for the T1 (left) and T2 (right). T1 is divided into three domains (A-C) separated by vertical dotted lines at stn 9 and 28. Dots represent samples and vertical black lines show the position of the orthogonal transect T2 and T1, respectively. Horizontal black line shows the position of the pycnocline. Section distance is counting from southeast (SE) to northwest (NW) in T1 and from southwest (SW) to northeast (NE) in T2 (labelled at the bottom of the first panel). Produced with Ocean Data View (Schlitzer, 2017).

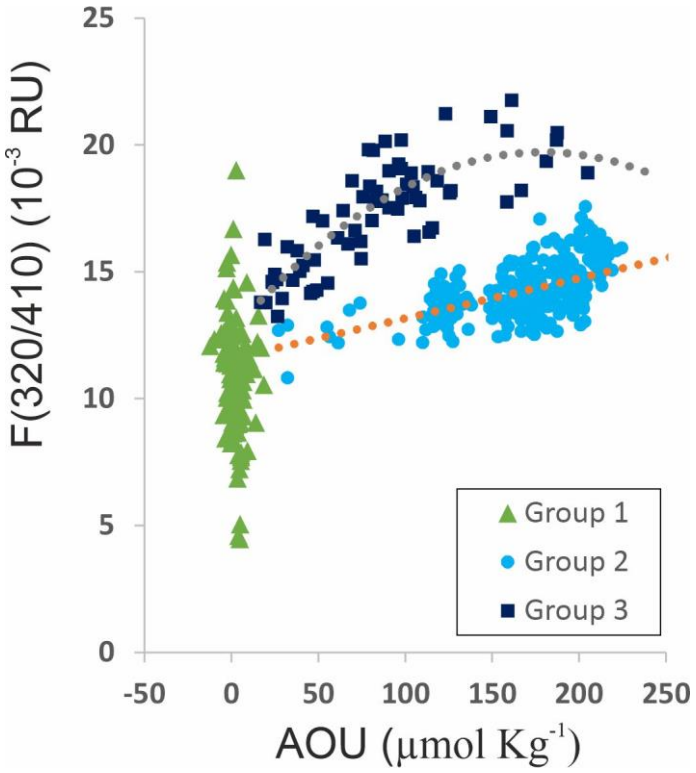

Figure 3.9. Fluorescence intensity F(320/410) versus apparent oxygen utilization (AOU) for the whole dataset. Group 1 (green triangles) represent the surface layer samples (above the pycnocline), Group 2 (blue dots) represent the usual trend below the pycnocline in ocean waters and Group 3 (dark blue squares) represent the high fluorescent band.

When T2 was occupied, DOC showed the highest value at the surface of stn 39 with 116.7 µmol L^{-1} and lower values were found in the eastern end of the transect. Below the pycnocline, higher DOC values were measured in the western end with a similar distribution in columns as in T1. POC resembled the distribution of turbidity with higher values at both ends of T2 and slightly lower at the middle of the section. CDOM and FDOM measurements were also similar to those in T1 except for a remarkably higher value above the pycnocline at stn 39 in all the profiles (Fig. 3.8). F(320/410) showed similarly high intensity as in T1 below the pycnocline in the easternmost part of the transect, whereas at stns 40-42 the intensity was lower.

3.4 Hydrography of mesopelagic waters

The shallowest central water mass, SACW_18, was centered at 165 ± 25 m and represented 3.2% of the total sampled water volume (Table 3.2; Fig. 3.10). MMW was centered at 201 ± 1 m but represented only 0.1% of the total volume, so it was almost negligible. ENACW_15 was below MMW, at an average depth of 232 ± 11 m and represented 12.3% of the total sampled volume. The last two central water masses were SACW_12 and

ENACW_12, centered at 339 ± 24 and 453 ± 17 m (Table 3.2), and with a total sampled volume of 8.6 and 26.1%, respectively. Therefore, ENACW_12 was the most representative central water mass of the study area.

The intermediate and upper deep waters were occupied by four water masses. SPMW and AA were placed at 813 ± 20 and 904 ± 36 m (Fig. 3.10), and represented 10.4 and 20.2% of the total sampled water volume, respectively (Table 3.2). These water masses were followed by MW and LSW, centered at 1225 ± 62 and 1443 ± 26 m, and representing 5.6 and 13.4% of the total sampled water volume, respectively.

AOU in the central waters showed lower values in the central part of T1 between stn 8 and 28 that corresponded with a higher contribution of ENACW (Fig. 3.11a). Maximum AOU levels were observed in SACW_12, with an archetype concentration of 191.0 ± 4.2 µmol kg^{-1}, followed by ENACW_12 and SPMW with 186 and 187 µmol kg^{-1}, respectively (Table 3.2). The lowest value in the central waters was 112 µmol kg^{-1} for MMW, and in the deep waters, the archetype AOU concentration was 128 µmol kg^{-1} for LSW.

3.5 DOM, POM, CDOM and FDOM distributions in the mesopelagic waters

DOC showed a gradual decrease with depth starting with an archetype value of 52.8 ± 1.9 µmol L^{-1} in SACW_18 and ending with 41.8 ± 0.7 µmol L^{-1} in LSW (Fig. 3.11b). Water mass mixing (eq. 2.7) explained 40% of the DOC variability in the CVFZ with an SE of 4.5 µmol L^{-1} (Table 3.3). When adding AOU to the multiple linear regression model (eq. 2.8), the DOC - AOU coefficient was not significant. The distribution of POC (Fig. 3.11c) was similar to DOC, with a general decrease of concentration with depth.

The mixing model (eq. 7) explained 38% of POC variability with a SE of 0.4 µmol L^{-1} and as for the case of DOC, when including AOU in the regression model (eq. 8), the POC - AOU coefficient was not significant. Regarding of PON, the distribution was similar to POC with a high correlation between both variables (ODR; POC = 11.6 (± 0.4)·PON + 0.29 (± 0.03); R^2 = 0.76; n = 288). The multiple linear regression model explained 54% of the variability of PON in the CVFZ with a SE of 0.03 µmol L^{-1} and again no significant PON - AOU coefficient was found when adding AOU to the multiple regression model.

Table 3.2. Thermohaline and chemical characteristics (arquetype value ± SE) of mesopelagic waters. R^2, proportion of the total variability explained by WT mixing; SE, standard error of the estimate.

WT	VOL_i (%)	Z_i (m)	θ_i (ºC)	S_i (PSU)	AOU_i (µmol kg^{-1})	$NO_3^-{}_i$ (µmol kg^{-1})	DOC_i (µmol L^{-1})	POC_i (µmol L^{-1})	PON_i (µmol L^{-1})	C:N $(POM)_i$ mol C mol N^{-1}
SACW_18	3.20	165 ± 25	15.4 ± 0.4	35.8 ± 0.04	173.2 ± 8.1	24.6 ± 1.2	52.8 ± 1.9	1.9 ± 0.2	0.16 ± 0.02	12.2 ± 0.9
MMW	0.10	201 ± 1	15.9 ± 0.4	36.1 ± 0.04	112.0 ± 13.6	15.4 ± 2.7	53.1 ± 7.3	1.3 ± 0.4	0.09 ± 0.02	14.7 ± 2.2
ENACW_15	12.30	232 ± 11	14.6 ± 0.2	35.9 ± 0.03	155.3 ± 4.8	21.8 ± 0.8	51.2 ± 0.9	1.5 ± 0.1	0.11 ± 0.01	13.9 ± 0.6
SACW_12	8.60	339 ± 24	12.6 ± 0.3	35.6 ± 0.04	191.0 ± 4.2	28.2 ± 0.9	47.8 ± 1.0	1.6 ± 0.1	0.12 ± 0.01	14.4 ± 0.7
ENACW_12	26.10	453 ± 17	11.4 ± 0.2	35.5 ± 0.02	186.2 ± 2.6	29.3 ± 0.5	46.6 ± 0.6	1.4 ± 0.1	0.10 ± 0.01	15.4 ± 0.4
SPMW	10.40	813 ± 20	7.6 ± 0.1	35.1 ± 0.01	187.1 ± 2.3	32.4 ± 0.3	43.5 ± 1.0	1.1 ± 0.1	0.06 ± 0.00	18.3 ± 0.7
AA	20.20	904 ± 36	7.4 ± 0.2	35.1 ± 0.02	176.9 ± 3.2	31.5 ± 0.3	43.1 ± 0.6	1.1 ± 0.1	0.06 ± 0.00	17.7 ± 0.6
MW	5.60	1224 ± 62	5.8 ± 0.2	35.1 ± 0.01	148.6 ± 6.2	29.1 ± 0.8	41.2 ± 1.0	0.9 ± 0.1	0.05 ± 0.01	19.1 ± 1.1
LSW	13.40	1443 ± 26	5.0 ± 0.1	35.1 ± 0.01	127.8 ± 2.6	26.6 ± 0.32	41.8 ± 0.7	0.9 ± 0.1	0.05 ± 0.00	19.5 ± 0.7
R^2					0.96	0.97	0.38	0.38	0.54	0.32
SE					6.61	1.72	4.54	0.44	0.03	3.71

WT	$a_{CDOM}254_i$ (m^{-1})	$a_{CDOM}325_i$ (m^{-1})	$S_{(275\text{-}295)i}$ (10^{-2})	$S_{(350\text{-}400)i}$ (10^{-2})	S_{Ri}	Peak A_i (10^{-3} RU)	Peak C_i (10^{-3} RU)	F(320/410) (10^{-3} RU)	Peak T_i (10^{-3} RU)	Peak $A/F(320/410)_i$ (10^{-3} RU)
SACW_18	1.09 ± 0.05	0.22 ± 0.02	2.71 ± 0.07	1.32 ± 0.08	2.11 ± 0.11	30.4 ± 1.1	14.3 ± 0.6	16.3 ± 0.8	9.4 ± 0.7	1.87 ± 0.16
MMW	0.99 ± 0.10	0.16 ± 0.04	3.14 ± 0.33	1.27 ± 0.15	2.47 ± 0.11	25.6 ± 1.4	11.5 ± 0.6	13.3 ± 0.1	11.2 ± 6.2	1.93 ± 0.12
ENACW_15	1.01 ± 0.01	0.19 ± 0.01	2.83 ± 0.05	1.31 ± 0.04	2.19 ± 0.05	27.9 ± 0.4	12.9 ± 0.2	14.4 ± 0.2	8.6 ± 0.4	1.94 ± 0.05
SACW_12	0.98 ± 0.02	0.20 ± 0.01	2.57 ± 0.05	1.32 ± 0.07	2.03 ± 0.07	29.8 ± 0.4	13.8 ± 0.2	15.2 ± 0.2	8.1 ± 0.4	1.96 ± 0.05
ENACW_12	0.94 ± 0.01	0.19 ± 0.01	2.59 ± 0.03	1.41 ± 0.05	1.93 ± 0.04	29.3 ± 0.2	13.5 ± 0.1	14.8 ± 0.1	7.8 ± 0.3	1.99 ± 0.03
SPMW	0.84 ± 0.01	0.17 ± 0.01	2.46 ± 0.04	1.65 ± 0.13	1.64 ± 0.07	28.8 ± 0.3	13.1 ± 0.1	13.9 ± 0.2	6.7 ± 0.3	2.07 ± 0.05
AA	0.85 ± 0.01	0.17 ± 0.01	2.48 ± 0.04	1.63 ± 0.08	1.65 ± 0.05	29.0 ± 0.3	13.2 ± 0.1	14.0 ± 0.1	6.9 ± 0.3	2.08 ± 0.04
MW	0.83 ± 0.03	0.16 ± 0.02	2.53 ± 0.10	1.72 ± 0.15	1.58 ± 0.09	29.1 ± 0.4	12.9 ± 0.2	13.7 ± 0.2	6.9 ± 0.6	2.12 ± 0.06
LSW	0.85 ± 0.03	0.17 ± 0.02	2.51 ± 0.08	1.73 ± 0.09	1.57 ± 0.06	29.6 ± 0.2	13.0 ± 0.1	13.8 ± 0.1	7.2 ± 0.4	2.14 ± 0.03
R^2	0.42	0.11				0.42	0.572	0.603	0.15	
SE	0.1	0.06				0.002	0.001	0.001	0.002	

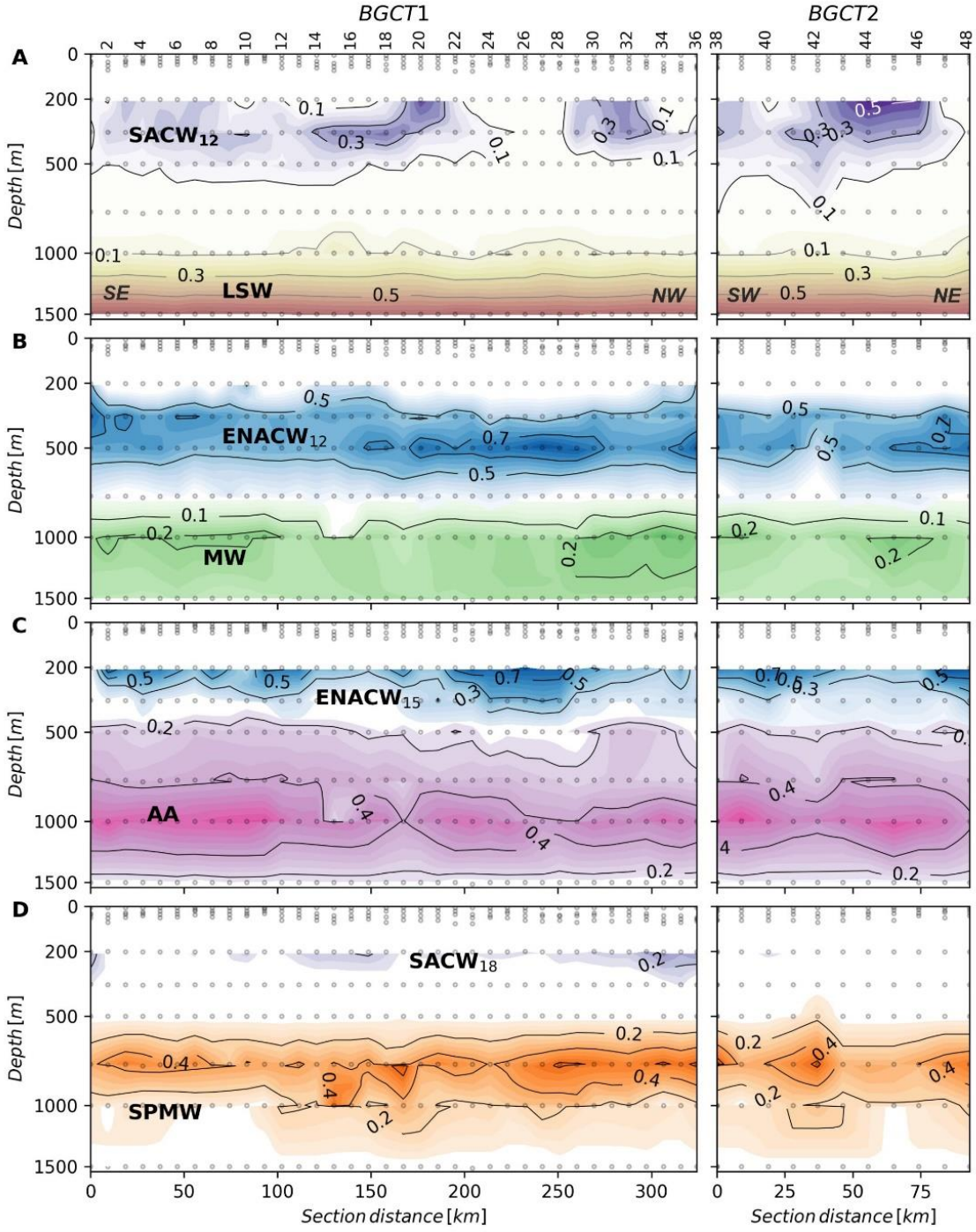

Figure 3.10. Distributions of the water masses present in the CVFZ during the FLUXES II cruise. Water mass proportions in this figure were derived from an OMP analysis applied to CTD data at 1 dbar vertical resolution. θ and S were measured directly with the CTD, while SiO_4H_4 and NO values were reconstructed by fitting the measured water sample concentrations to a non-linear combination of variables directly measured with the CTD (θ, S, O_2). The distribution of the water-masses among the panels was designed to avoid contour overlapping and does not follow an oceanographic criteria. (A) SACW_12 and LSW; (B) ENACW_12 and MW; (C) ENACW_15 and AA; and (D) SACW_18 and SPMW. Section distance is counting from southeast (SE) to northwest (NW) in T1 and from southwest (SW) to northeast (NE) in T2 (labelled at the bottom of the first panel).

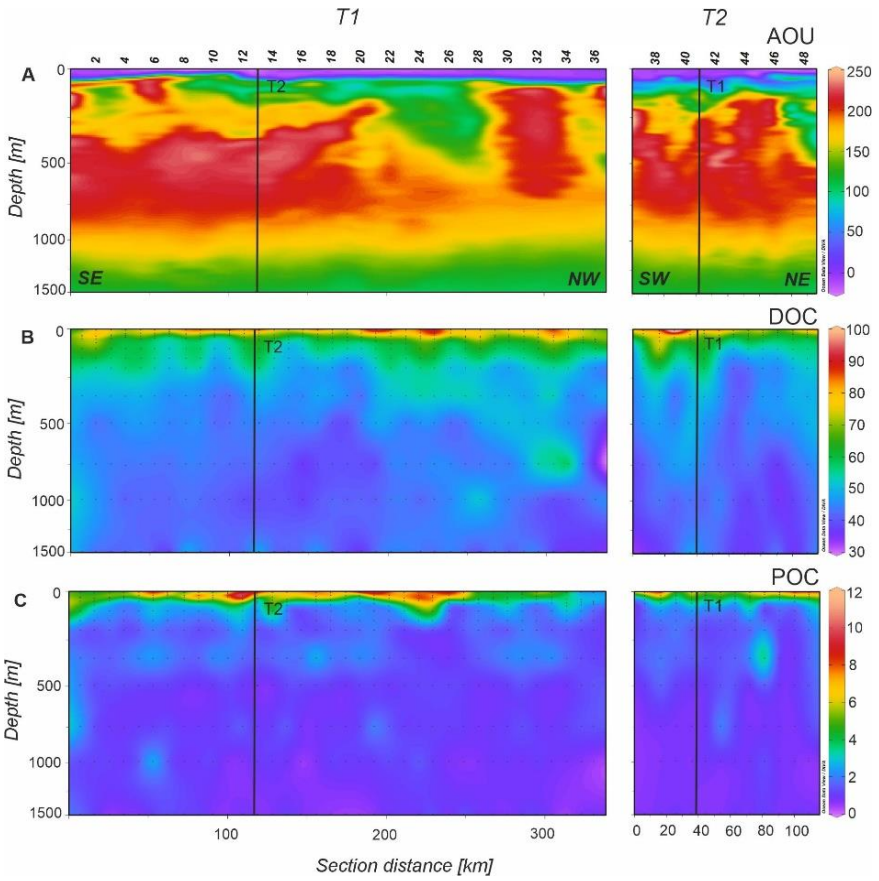

Figure 3.11. Distributions of (A) apparent oxygen utilization (AOU) in µmol Kg^{-1}, (B) dissolved organic carbon (DOC) in µmol Kg^{-1}, and (C) suspended particulate organic carbon (POC) in µmol Kg^{-1} in the 0-1500 m depth range of the FLUXES II cruise for the T1 (left) and T2 (right). Dots represent samples (AOU measurements were obtained at 1 dbar vertical resolution) and vertical black lines show the position of the orthogonal transect T2 and T1, respectively. Note that the y-axis (depth) is not linear. Section distance is counting from southeast (SE) to northwest (NW) in T1 and from southwest (SW) to northeast (NE) in T2 (labelled at the bottom of the first panel). Produced with Ocean Data View (Schlitzer, 2017).

The C:N ratio of POM increased significantly with depth, from an archetype value of 12.23 ± 0.90 in SACW_18 to a value of 19.48 ± 0.68 in LSW (Table 3.2). It is noticeable that the ratio was the highest in the northern part of T1 from stn 24 to 36 and in the depth range of 750-1500 m with a maximum local value of 27.49 in stn 32 at 1500 m.

Regarding the distribution of CDOM, archetype values of $a_{CDOM}(254)$ were the highest in SACW_18 and then decreased with depth to the lowest value found in MW (Table 3.2; Fig. 3.12a). The mixing model explained 42% of the $a_{CDOM}(254)$ variability in the dark ocean and increased to 44% when AOU is added to the linear regression. In this case, the $a_{CDOM}(254)$ - AOU coefficient was significant (0.0023 ± 0.0009 m^{-1} kg µmol^{-1}; Table 3.3). Archetype $a_{CDOM}(325)$ values of the different water masses ranged between 0.16 m^{-1} in MMW and MW, and 0.22 m^{-1} in SACW_18 (Fig. 3.12b). The WTs mixing model explained only 11% of the $a_{CDOM}(325)$ variability, increasing to 13% when adding the AOU variable

to the model and the $a_{CDOM}(325)$ - AOU coefficient was also significant (0.0014 ± 0.0005 m^{-1} kg µmol^{-1}; Table 3.3). In the central waters, the highest value of the spectral slope $S_{275-295}$ was found in MMW and then decreased with depth and remained stable in the intermediate and deep waters. Concerning the ratio S_R, in the central water masses the highest value corresponded to the MMW and then decreased in LSW (Table 3.2).

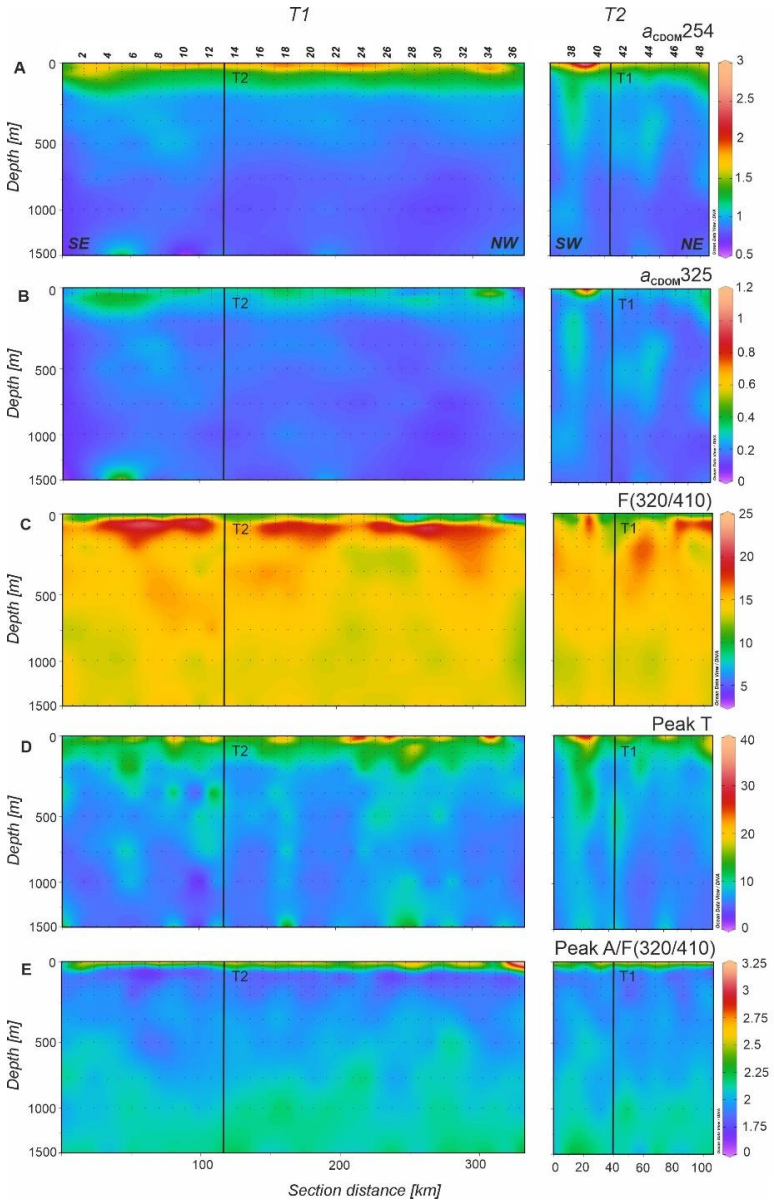

Figure 3.12. Distributions of (A) absorption coefficient at 254 nm ($a_{CDOM}254$) in m^{-1}, (B) absorption coefficient at 325 nm ($a_{CDOM}325$) in m^{-1}, (C) fluorescence at Ex/Em pair 320/410 nm (F(320/410)) in 10^{-3} RU, (D) fluorescence at Ex/Em pair 280/350 nm (peak T) in 10^{-3} RU, and (E) peak A to F(320/410) ratio (peak A/F(320/410)) in the 0-1500 m depth range of the FLUXES II cruise for the T1 (left) and T2 (right). Dots represent samples and vertical black lines show the position of the orthogonal transect T2 and T1, respectively. Note that the y-axis (depth) is not linear. Section distance is counting from southeast (SE) to northwest (NW) in T1 and from southwest (SW) to northeast (NE) in T2 (labelled at the bottom of the first panel). Produced with Ocean Data View (Schlitzer, 2017).

With regard to FDOM, the maximum intensity of F(320/410) in the central waters was recorded in SACW_18 associated with the subsurface maxima situated just below the high fluorescence intensity band all along T1 (Fig. 3.12c). F(320/410) intensity decreased from SACW_12 to LSW, although it remained quite constant in intermediate waters. The distribution of peak A to F(320/410) (Fig. 3.12e) indicates that differences occur mainly in the surface mixed layer. Protein-like fluorescence intensities gradually decreased with depth reaching the lowest levels at 800 m in SPMW and then increased again but very slightly. In Fig. 3.12d it is noticeable the columns of high peak T intensity reaching 1500 m depth in T1 and T2 profiles. The mixing model explained 60% of the total variability of F(320/410) in mesopelagic waters with a SE of 8 10^{-4} RU. On the contrary, only 15% of peak T variability was explained by the mixing model with a SE of 2.2 10^{-3} RU. When AOU is added to the multiple linear regression, the explained variability of F(320/410) increased to 61% with a significant F(320/410) - AOU coefficient ($1.8 \pm 0.7\ 10^{-5}$ RU kg μmol^{-1}) whereas inclusion of AOU in the multiple regression of peak T does not produce a significant peak T – AOU coefficient (Table 3.3).

4. Discussion

4.1 Physical-biogeochemical coupling in the CVFZ

The main hydrographic structures found in the area are the thermohaline front (CVF) and the intrusion of low salinity (S < 36) located below the pycnocline along T1. This nutrient-rich lens about 20-30 m thick extended along the first 135 NM (250 km) of T1 and provided nutrients to the immediately above surface waters, contributing to the high values of Chl-*a* along these domains (Figs. 3.6c & d). Hosegood et al. (2017) also brought up the importance of mesoscale processes in injecting nutrients to the euphotic zone and stimulating higher levels of primary production. Moreover, the southern sector of T1 was affected by a cyclonic eddy (Figs. 3.1b & c) transporting SACW that is responsible for the uplift of the pycnocline from stns 1 to 10, explaining also the connection with the low salinity intrusion observed in the southern section of T1. On the contrary, the middle and mostly the northern sector of T1 were affected by an anticyclonic eddy that deepened the pycnocline. Additionally, current velocities indicate that waters affected by the anticyclonic eddy were moving northward, distributing the Chl-*a* and turbidity in that direction, while currents in the southern part of the transect were less intense and directed southward (Figs. 3.3a & b).

Table 3.3. Parameters of the linear mixing (Eq. 7) and mixing-biogeochemical (Eq. 8) models. R2, determination coefficient; SE, standard error of the estimate; β, fitting parameter of the relationship between N1 and N2 independent of the mixing; SE (β), standard error of the estimation of β; p, significance level of the estimation of β; n, number of samples. Blanks correspond with non-significant observations.

N_1	N_2	R^2	SE	β	SE (β)	p	n
AOU		0.96	6.61				290
DOC		0.40	4.54				289
POC		0.38	0.44				289
PON		0.54	0.03				289
DOC	AOU	0.40	4.55	-	-	-	288
POC	AOU	0.38	0.44	-	-	-	288
PON	AOU	0.54	0.03	-	-	-	288
$a_{CDOM}254$		0.42	0.10				289
$a_{CDOM}325$		0.11	0.06				289
$a_{CDOM}254$	AOU	0.44	0.09	0.0023	0.0009	0.008	289
$a_{CDOM}325$	AOU	0.13	0.06	0.0014	0.0005	0.010	289
F(320/410)		0.60	0.0008				288
Peak T		0.15	0.0022				286
F(320/410)	AOU	0.61	0.0008	0.000018	0.000007	0.015	288
Peak T	AOU	0.15	0.0022	-	-	-	286

The average values of DOC in the epipelagic layer are very similar to that found in Valiente et al. (2022) in the same area during summer 2017. They reported similar DOC distribution patterns with columns of relatively high values interspersed with areas of low concentration. This phenomenon could be related with the intense meso- and submesoscale activity in this frontal zone, where mixing can favor the downward transport of DOC and POC (Lévy et al., 2012; Nagai et al., 2015) combined with the dissolution of fast sinking particles as previously suggested by Lopez et al. (2020). Moreover, fast sinking particles in this area are linked to Sahara dust inputs, which plays an important ballasting role and therefore transporting DOC adsorbed onto these particles down to the dark ocean. Numerous studies related the presence of lithogenic material originating from NW Africa with a higher efficiency of the biological carbon pump, increasing the particle density and settling rates (Fischer et al., 2016; Iversen et al., 2010; van der Jagt et al., 2018). Similar striped-like patterns were also observed for POC, especially at stn 24-25.

The linear correlation between DOC and AOU indicates that DOC supported about 21% of the oxygen demand of epipelagic waters. When considering both the dissolved and suspended organic carbon fraction, the value increased slightly to 23.6%, revealing that the sinking organic carbon fraction should be the main contributor to oxygen consumption and OM mineralization in the epipelagic layer. DOC contribution to the oxygen demand in epipelagic waters is similar to previously reported in other areas: e.g. 21% in the Red Sea (Calleja et al., 2019), 15-41% in the Sargasso Sea (Hansell and Carlson, 2001), 21-47% in the South Pacific and 18-43% in the Indian Ocean (Doval and Hansell, 2000), and 30% in the Eastern Subtropical North Pacific, north of the gyre (Abell et al., 2000). It is noticeable the significant differences in the DOC-AOU slope in mesopelagic waters between domains A, B and C. The higher contribution of DOC and suspended POC to the oxygen demand in domain B is likely due to larger production of fresh OM in this domain, therefore susceptible to faster degradation.

A significant linear relationship between DOC and $a_{CDOM}(254)$ was found, which suggests that the latter could be used as an optical proxy of the former as was stated in previous works (Catalá et al., 2018; Lønborg and Álvarez-Salgado, 2014). The linear ODR of DOC and $a_{CDOM}(254)$ for the whole sample set of epipelagic and mesopelagic waters ($R^2 = 0.80$, n = 478) yielded an origin intercept of 9.7 (± 1.0) µmol L^{-1}, similar to the values found by (Lønborg and Álvarez-Salgado, 2014) in the Eastern North Atlantic (10 µmol L^{-1}) and by Catalá et al. (2018) in the Mediterranean Sea (9 µmol L^{-1}). The slope of the regression, 39.1 (± 0.9) m^2 $mmol^{-1}$, was also close to those found in the two previous studies in the NE Atlantic, 40 (±1) m^2 $mmol^{-1}$, and the Mediterranean Sea, 46 (±1) m^2 $mmol^{-1}$. Exploring the relationship between $a_{CDOM}(254)$ and DOC in different ocean areas is a subject of interest in order to decipher whether there is a universal relationship between both parameters or if it varies depending on the region.

Since $a_{CDOM}(325)$ is a proxy for the concentration of aromatic dissolved organic compounds, it is expected to be sensitive to solar irradiation that produce photodegradation (Catalá et al., 2015a; Nelson et al., 2004). Nevertheless, in the CVFZ we found significantly higher $a_{CDOM}(325)$ values above than below the pycnocline. Since the elevated values of $S_{275-295}$ and peak A/F(320/410) indicate active DOM photodegradation in the surface mixed layer, the high $a_{CDOM}(325)$ levels there should be due to an in situ production and/or external supply exceeding photodegradation. In this regard, the existence of an external CDOM and FDOM source is hypothesized in the next section. Note that the high levels of

the peak A/F(320/410) ratio in the surface mixed layer are due to the much higher sensitivity of F(320/410) than peak A to phtochemical degradation when irradiated with natural UV light (Martínez-Pérez et al., 2019).

4.2 Humic-like fluorescence maximum in epipelagic waters

The CVFZ is, to the best of our knowledge, the first marine system where a layer of relatively high humic-like fluorescence intensity is found below the pycnocline, preferentially down to 150 m (Fig. 3.8c), although this signal is also detectable in mesopelagic waters (Fig. 3.12c). Its relationship with AOU (dark blue squares in Fig. 3.9) does not follow the expected linear trend, with a slope of 2.8 10^{-5} RU·kg^{-1}·µmol, due to microbial respiration (light blue circles in Fig. 3.9). This slope is in accordance with the values reported in other studies covering the world ocean: 2.5 10^{-5} RU·kg^{-1}·µmol in Catalá et al. (2015a) and 2.7 10^{-5} RU·kg^{-1}·µmol in Jørgensen et al. (2011). We hypothesize that the input of Sahara dust could be the reason behind this band of relatively high humic-like fluorescence intensity compared to their surroundings. To test this hypothesis, we ran an experiment consisting on adding Sahara dust (collected in a quartz fiber filter) to seawater to obtain the seawater-soluble fraction (SSF) and analyzed the changes of the DOM characteristics. A quartz fibre filter (QFF) was placed in a high volume (60 m^3 h^{-1}) aerosol collector (MCV, model CAV-A/M) at Pico de la Gorra (27º 56´ N, 15º 33´ W, 1930 m above sea level) during the Sahara dust episode of 14-15/07/2022. A total of 407.98 mg of dust were collected on a surface of 18 cm x 22.8 cm during 12 hours (6 p.m. - 6 a.m.). One sixteenth, 1/16 of this filter was placed in a glass beaker with 100 mL of seawater inside an ultrasounds bath during 40 minutes. Same procedure was followed with a 1/16 blank QFF filter. DOC and DOM optical properties were measured on the original seawater and on both seawater soluble fractions, SSF (blank filter and the filter with Sahara dust), after filtration (Whatman 0.4 µm PP).

The results of this comparison is shown in Table 3.4: while the DOC supplemented by 25.50 mg of Sahara dust in 100 mL of seawater (67.6 ± 1.3 µmol L^{-1}) is comparable to the concentration found in the epipelagic waters below the pycnocline (57 - 77 µmol L^{-1}; Table 3.1), F(320/410) values are 6 - 10 times higher in the Sahara dust, which suggest that Sahara dust contains highly reworked DOM with a large proportion of humic-like compounds. $a_{CDOM}(325)$ is >4 times higher than in situ and significant changes are also observed in $S_{(275-295)}$ and S_R (Table 3.1 & Table 3.4). In particular, S_R values for the CDOM transported

by Sahara dust was 0.9, i.e. lower than 1, which is distinctive of DOM with continental origin (Helms et al., 2008).

Table 3.4. DOC and DOM characteristics of the seawater soluble fractions (SSF) of the blank filter, the filter with Sahara dust and the difference between them.

		blank filter SSF	**Sahara dust SSF**	**Sahara dust - blank**
DOC	μmol L^{-1}	76.7 ± 0.7	144.3 ± 1.1	67.6 ± 1.3
F(320/410)	10^{-3} RU	72.0 ± 1.2	177.5 ± 1.9	105.5 ± 2.2
F(340/440)	10^{-3} RU	41.9 ± 1.3	114.3 ± 2.3	72.4 ± 2.0
F(280/350)	10^{-3} RU	15.5 ± 0.1	35.1 ± 1.0	19.6 ± 1.0
$a_{CDOM}254$	m^{-1}	1.75 ± 0.05	5.11 ± 0.05	3.36 ± 0.07
$a_{CDOM}325$	m^{-1}	0.36 ± 0.05	1.75 ± 0.05	1.40 ± 0.07
S(275-295)	10^{-2}	3.1 ± 0.2	1.70 ± 0.04	1.19 ± 0.06
S(350-400)	10^{-2}	2.2 ± 0.1	1.43 ± 0.01	1.32 ± 0.02
S_R		1.43 ± 0.16	1.19 ± 0.04	0.90 ± 0.05

4.3 Local mineralization in the water masses of the mesopelagic layer of the CVFZ

The distribution of DOC, POC and PON in mesopelagic waters showed the expected decrease with depth due to production in the surface layer and subsequent mineralization at depth. POC concentration was very low compared to other studies in the Canary Current System (Alonso-González et al., 2009; Arístegui et al., 2020). As shown in Valiente et al. (2022), these differences could be due to the influence of the giant filament of Cape Blanc, which exports the suspended POC fraction further offshore whereas the sinking POC fraction is mineralized in the epipelagic and upper mesopelagic waters. The C:N molar ratios of POM reported in this work for both the epi- and mesopelagic layers are higher than the canonical Redfield ratio of 6.6 (Anderson, 1995; Redfield et al., 1963) and also higher than values reported in other works (see compilation by Schneider et al., 2003). The ratio increases from 8 at the surface, 11 at the base of epipelagic layer (200 m), to 19.5 at the base of the mesopelagic layer (1500 m). Similar values were found in Valiente et al. (2022) for a wider sampling area in the CVFZ and in a different season. This increase of the C:N molar ratio of suspended OM with depth indicates a preferential degradation of N

compounds at shallower depths, and therefore, increased the relative abundance of C over N with depth (e.g., Alvarez-Salgado et al., 2014).

The water mass mixing model (eq. 7) explained 40%, 38% and 54% of the variability of DOC, POC and PON, respectively, and no significant increase of the variability explained by the model occurs when adding AOU as explanatory variable. These results indicate that the imprint of mineralization observed in mesopelagic waters of the CVFZ does not occur locally but during the pathway of the water masses from their respective formation sites to the CVFZ. The low contribution of DOC and POC to local mineralization also suggests sinking POC should be the primary support for the local oxygen demand. Nevertheless, other works further north in the Canary Current system (Arístegui et al., 2020, 2003), where the concentration of suspended POC is much higher, found that this fraction was the main support for mesopelagic respiration there. These authors argued that advection of this suspended particulate material from the adjacent coastal productive waters is the reason behind this behavior.

Mixing and mineralization are the main processes controlling DOM and POM variability in mesopelagic waters, but other processes like absorption-desorption of DOM onto particles exist and can be relevant as abiotic removal of DOM from the upper layers (Druffel and Williams, 1990). This mechanism is related with the well-known ballasting effect of the lithogenic material (both biominerals and atmospheric inputs) (Bory and Newton, 2000; Fischer et al., 2016; Fischer and Karakaş, 2009; van der Jagt et al., 2018) and could explain the columns of high DOC concentration through the epipelagic layer observed in the CVFZ, where the flux of sinking particles is substantial.

Contrary to what has been observed for DOC, POC and PON, the mixing models for $a_{CDOM}(254)$ and $a_{CDOM}(325)$ improved significantly when AOU was included (Table 3.3) indicating that local mineralization processes at the CVFZ contributed to explain the variability of the colored but not the bulk fraction of DOM. Moreover, the regression coefficients of $a_{CDOM}(254)$ and $a_{CDOM}(325)$ with AOU were positive, indicating the generation of colored organic compounds with increasing AOU. Given that we have not observed significant local DOC mineralization, the accumulation of $a_{CDOM}(254)$ and $a_{CDOM}(325)$ should be related to the predominant mineralization of the sinking fraction of POC as already suggested in a previous work (Valiente et al., 2022). Therefore, part of $a_{CDOM}(254)$ and $a_{CDOM}(325)$ would represent refractory by-products of the mineralization

of bioavailable sinking organic carbon, in agreement with the microbial carbon pump concept (Catalá et al., 2015a; Jiao et al., 2010; Legendre et al., 2015), which states that a fraction of the labile OM respired by marine organisms is converted to recalcitrant DOM. In other systems, as the Mediterranean Sea, where the contribution of sinking POC is less important, the coefficients of $a_{CDOM}(254)$ and $a_{CDOM}(325)$ with AOU are negative (Catalá et al., 2018), indicating a net consumption of this colored fraction rather than its production.

Regarding the fluorescent fraction of DOM, the mixing model explained 60% of the total variability of F(320/410), indicating that basin scale processes occurring from the WTs formation sites to the CVFZ were the main drivers of the variability. On the contrary, the explained variability of peak T was only 15%, revealing the lability of these protein-like compounds that are produced mainly in the upper layers of the ocean (Jørgensen et al., 2011). Inclusion of AOU improved significantly the mixing model for F(320/410), indicating that local mineralization processes contributed to the production of F(320/410) in the mesopelagic layer of the CVFZ, with an AOU coefficient of 1.8 (±0.7) 10^{-5} RU µmol kg^{-1} (Table 3.3). This value is very similar to that reported in Martínez-Pérez et al. (2019) for the Mediterranean Sea (2.1 ± 0.4 10^{-5} RU µmol kg^{-1}), who applied the same mixing-AOU model. These coefficients, independent of water mass mixing, are somewhat lower than the slope of the direct linear F(320/410)-AOU correlation: 2.8 RU µmol kg^{-1} (this work; Fig S4), 2.7 10^{-5} RU µmol kg^{-1} (Jørgensen et al., 2011) or 2.5 RU µmol kg^{-1} (Catalá et al., 2015a). This indicates that direct correlations overestimate the conversion factors of labile into refractory DOM.

5. Conclusions

The distribution of DOM, POM and its colored and fluorescent fractions is dictated by meso- and submesoscale structures (eddies, meanders) that were captured at a high-resolution sampling (< 10 km) and showed a tight coupling between physical and biogeochemical parameters. A relatively high band of fluorescent humic-like DOM below the pycnocline is hypothesized to be released from sinking Sahara dust particles based on an anomalous relationship with apparent oxygen utilization. In the mesopelagic layer, the mineralization of DOM and POM occurs mainly during the transit of the water masses from their respective formation sites to the CVFZ since a low contribution is observed to the local oxygen demand. The local mineralization is dictated by fast-sinking POM (autochthonous or allochthonous) favored by the well-known ballasting effect of lithogenic

material that have been studied previously in the NW African upwelling system. This local mineralization leads to an increment in the C:N ratio due to preferential nitrogen compounds consumption and also to the production of colored refractory DOM through the microbial carbon pump mechanism, as indicated by the positive relationship between $a_{CDOM}(254)$, $a_{CDOM}(325)$ and F(320/410) with AOU.

Chapter 4: Methodology for $\delta^{13}C$-DOC analysis by WCO-IRMS

The results presented in this chapter are also a manuscript in preparation.

Abstract

Historically, isotopic analysis of δ^{13}C of marine DOC have meant a challenge for the scientific community due to its low concentration and the high content of salts in seawater samples. Several methodologies and technical advances have been developed since the first analysis in the late 1960's but still nowadays, the methodology is far to be completely routinely and automated. In this chapter, the online coupling between a persulfate-based total organic carbon analyzer and an isotope ratio mass spectrometer is described with the objective to obtain the δ^{13}C-DOC of marine samples. The methodology follows the setup first described by Osburn and St. Jean (2007) with some modifications related with the use of a cryogenic trap and a lower persulfate to sample ratio. Analytical precision and accuracy usually lower than 0.5‰ are within values reported previously by other authors. Consensus reference material of deep seawater (700 m, Florida Strait) resulted in a value of -25.2 ± 0.4‰.

1. Introduction

The World ocean contains one of the largest active reservoir of reduced carbon on Earth, being the dissolved organic carbon pool (662 Pg C; Hansell et al., 2009) similar in size to atmospheric CO_2 (860 Pg C; Friedlingstein et al. 2020). This reservoir is composed by thousands of different compounds with contrasting lifetimes (Dittmar, 2015; Hansell, 2013) with the more recalcitrant molecules reaching lifetimes of a several thousand years (Williams and Druffel, 1987; Zigah et al., 2017). DOC is of key component of ocean biogeochemical cycles that is involved in a variety of physical, biogeochemical and biological processes such as molecular aggregation or disaggregation, photo-oxidation, bacterial degradation, or formation of recalcitrant DOC and storage in the deep ocean (Carlson and Hansell, 2015). In this regard, δ^{13}C measurements provide relevant information about cycling, primary sources, fluxes and fate of DOC in the ocean (Barber et al., 2017; Broek et al., 2020; Esposito et al., 2019). The reader is referred to Chapter 1 for more details.

δ^{13}C-DOC studies in marine environments have been carried out since the 1960's and several techniques and methodologies have been developed since then. All these methods are based on the oxidation of DOC to CO_2 and the subsequent determination of ^{12}C and ^{13}C in CO_2. Traditionally there are three ways for oxidizing DOC: wet chemical oxidation, UV oxidation and high temperature oxidation (Beaupré, 2015). Any of them present advantages

and drawbacks, and the difficulties are associated with the salt matrix in seawater and the low DOC concentrations, usually ranging between 35 and 100 µM (Hansell et al., 2009). With the aim to obtain a reasonable sample throughput, the methodology requires the on-line coupling between a Total Organic Carbon Analyzer with an Isotope Ratio Mass Spectrometer (TOC-IRMS). Wet Chemical Oxidation - IRMS (WCO-IRMS) technique has been successfully used in the literature and consists on using an oxidizing reagent (usually sodium or potassium persulfate) to oxidize the DOC. It has the disadvantage of a low oxidation efficiency for complex organic molecules because the large amount of chlorine in seawater competes with DOC to be oxidized by persulfate. Nevertheless, those problems were overcome by taking proper precautions when analyzing seawater (Bouillon et al., 2006; Lang et al., 2013; Osburn and St-Jean, 2007; Yu et al., 2015). Simultaneously, UV oxidation - IRMS (UVO-IRMS) has also been improved considerably over the last two decades (Beaupré et al., 2007; Walker et al., 2019, 2017) and it is characterized by its low blanks and reliable δ^{13}C-DOC measurements, but it has a low sample throughput and high water volumes requirements as a drawback. Finally, it is the High Temperature Oxidation - IRMS (HTO-IRMS) technique, with the advantages of a low sample volume and very efficient DOC oxidation, especially for complex and recalcitrant molecules such as humic acids (Barber et al., 2017; Federherr et al., 2014; Kim et al., 2015; Lalonde et al., 2014). Alternatively to bulk δ^{13}C-DOC analysis, other methods have been employed with the aim of measure the carbon isotopic composition of DOC fractions and/or DOC constituents, including ultra-filtration (UF) or solid phase extraction (SPE) that leads to isotope analysis HMW vs. LMW (e.g. Zigah et al., 2017), DOC constituents such as humic compounds, lipids, proteins and carbohydrates (e.g. Loh et al., 2004) or even black carbon (Ziolkowski & Druffel, 2010).

In this thesis, we have chosen the wet chemical oxidation technique, following the methodology developed by (Osburn and St-Jean, 2007). Briefly, the setup consists on a Total Organic Carbon Analyzer (Model 1010 OI Analytical) coupled to an isotope ratio mass spectrometer (DeltaPlus XL, Thermo Scientific). Sample and reagent are introduced and mixed into a digestion vessel at 98º C up to 10 minutes, and then, a carrier gas flows into the vessel purging the CO_2 that was released during the chemical oxidation. The gaseous sample is driven through a purification system interface for removing water and halides and introduced into a chromatographic column before analysis in the IRMS instrument. Some modifications in the line setup and in the reagent volume have been done

with respect to the method of (Osburn and St-Jean, 2007), reducing the persulfate to chloride molar ratio and still observing a good DOC recovery in seawater. These modifications have led to reduce the system and reagent blank, enhancing the reproducibility and accuracy of the measurements. In summary, in this chapter, we will show a detailed description of the WCO-IRMS method with some modifications and improvements with respect to the previous studies, adapted for analyze $^{13}C/^{12}C$ ratios of DOC in seawater.

2. Experimental

2.1 Reagents, standards and samples

2.1.1 Sodium persulfate

Sodium persulfate ($Na_2S_2O_8$, Merk >99.0%) was used as the oxidizing reagent for the wet chemical oxidation of DOC to CO_2. It was prepared at a concentration of 1.69 M in 18 MΩ Milli-Q water. Purification of the reagent is essential prior to its use to eliminate organic traces, consisting on placing the solution in a microwave for about 5 minutes until it boils and then let it cool down in a cold-water recipient (McKenna and Doering, 1995; Osburn and St-Jean, 2007). After that, the solution is placed in an ultrasonic bath for another 5 minutes to remove all the dissolved gases, especially the residual CO_2. This last step is a novelty that has not been previously reported and resulted in a good cleaning procedure. Persulfate solutions were prepared in 0.5 L borosilicate glassware and were replaced after a maximum of two weeks of use.

2.1.2 Sample acidification

Oceanic water has an average concentration of dissolved inorganic carbon (DIC) of around 2000 µM near the surface and 2160 µM at 1 km depth (Sharp, 2017 and references therein). It is essential to remove completely this inorganic carbon prior to the organic carbon oxidation step. The TOC analyzer includes an automated system to acidify the sample and remove the inorganic carbon in the form of CO_2, which can be quantified in the infrared detector. However, we decided not to use the automated acidification system as the acid itself were found to be a major source of contamination when added with the dispensing pump despite its cleanliness and purification. We chose to acidify the samples manually immediately after being collected with high purity HCl (Sigma-Aldrich, 36.5-38.0%, BioReagent) to reach a pH <2. At the time of analysing the sample, a purge process is

carried out in the carbon analyzer that removes the inorganic CO_2 before adding the persulfate.

2.1.3 δ^{13}C measurements and reference standards

The $\delta^{13}C$ isotopic value of any sample is expressed in delta notation, as per thousand deviations of the $^{13}C/^{12}C$ ratio of the sample relative to the ratio of the Vienna Peedee Belemnite international standard (VPDB). The equation is as follows: $\delta^{13}C_S = (R_S / R_{St} - 1)$ x 1000, where R_S is the $^{13}C/^{12}C$ ratio of the sample and R_{St} the ratio of the VPDB standard.

Solutions of potassium phthalate (KHP, $C_8H_5K0_4$), sucrose ($C_{12}H_{22}O_{11}$) and potassium oxalate monohydrate ($C_2H_2K_2O_5$, hereafeter K-oxalate) were used, which are reference materials with high solubility and easily oxidizable by sodium persulfate. Their $\delta^{13}C$ were obtained by analyzing the standards in solid form in an elemental analyzer (EA-IRMS) system, that was calibrated with IAEA and USGS carbon isotope standards resulting in $\delta^{13}C$ of -25.73 ± 0.14‰, -11.65 ± 0.22‰ and -35.55 ± 0.15‰ respectively for KHP, sucrose and K-oxalate. Solution standards were prepared at different concentrations in 18 MΩ Milli-Q water for routine analysis. Nitrogen 5.0 was used as carrier gas for the carbon analyzer that was replaced by helium 5.0 before entering the IRMS.

2.1.4 Natural samples

Oceanic water from the North Atlantic was used to conduct oxidation efficiency experiments and seawater $\delta^{13}C$-DOC calibration. It was collected during two oceanographic cruises (FLUXES I, July - August 2017; FLUXES II, November 2017) on board R/V Sarmiento de Gamboa, that took place in the Cape Verde Frontal Zone in the eastern North Atlantic margin (the reader is referred to Figure 1.12 of Chapter 1). The carbon isotopic analysis of the samples collected during these two cruises is the main goal of the methodology developed in this chapter, and the results are presented in Chapter 5 of this dissertation.

2.2 Instrumental

The on-line coupling of the persulfate oxidation total organic carbon analyzer with the continuous flow isotopic ratio mass spectrometer (WCO-IRMS) are represented in Figure 4.1. Specifically, the set-up is designed for the isotopic analysis of DOC in marine environments. The characteristics of all the components are described below.

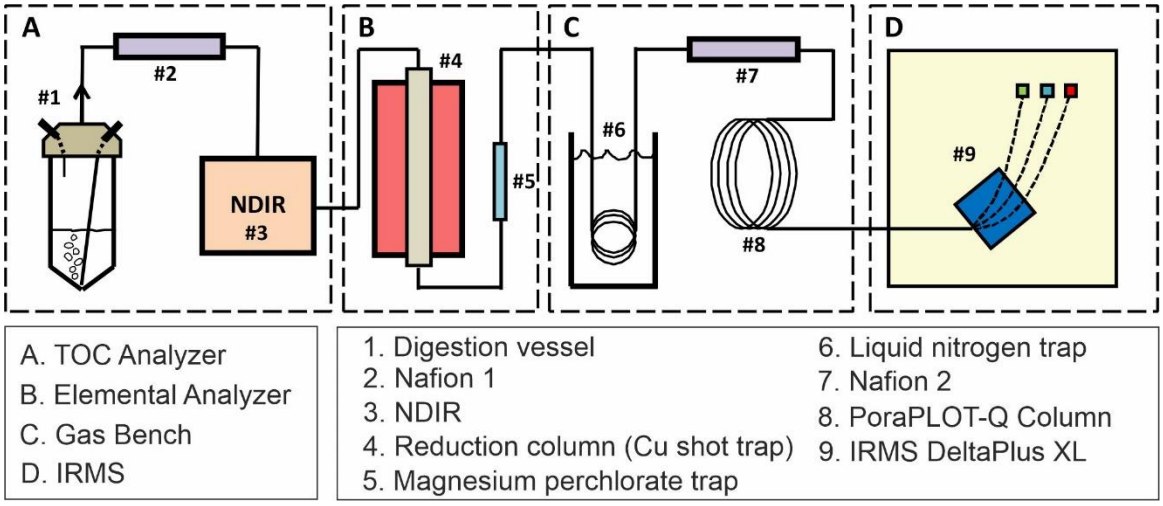

Figure 4.1. Schematic diagram of the on-line coupling between a Total Organic Carbon Analyzer and an Isotope Ratio Mass Spectrometer.

2.2.1 Total organic carbon analyzer

TOC Model 1010 of OI Analytical includes two phases of analysis called reaction and detection, that apply to both the detection of DIC first and DOC later. As we explain above, we chose to acidify manually the samples so the automated acidification system was removed off the analyzer. Therefore, the reaction + detection of DIC step is employed just for purging the inorganic carbon. DIC purging time (TIC Detect) was set at 1:30 min. In the reaction phase, a volume of reagent is added along with the sample in the digestion vessel and produce CO_2. During the detection phase, a flow of nitrogen circulates from the bottom of the digestion vessel and purge the CO_2, driving it to the non-dispersive infrared detector (NDIR) (Fig. 4.2). Before CO_2 detection in the NDIR, the sample is driven through a Nafion water trap. DOC reaction time (TOC React) was set at 10 min that is the maximum time allowed by the software, and DOC purging time (TOC Detect) was set at 5 min, enough time to transfer the sample from the digestion vessel to a liquid nitrogen trap, used for concentrating the analyte.

The modifications that we made in the TOC analyzer includes: a) addition of a CO_2 trap (Carbosorb) in the carrier gas line prior to enter in the TOC analyzer; b) removal of the drierite water trap due to contamination problems; c) removal of the continuous purging of the reagents and change the original containers for borosilicate bottles and d) general flow adjustment for pressure equilibrium between the on-line devices. With these modifications, we obtained better results minimizing the signal blank.

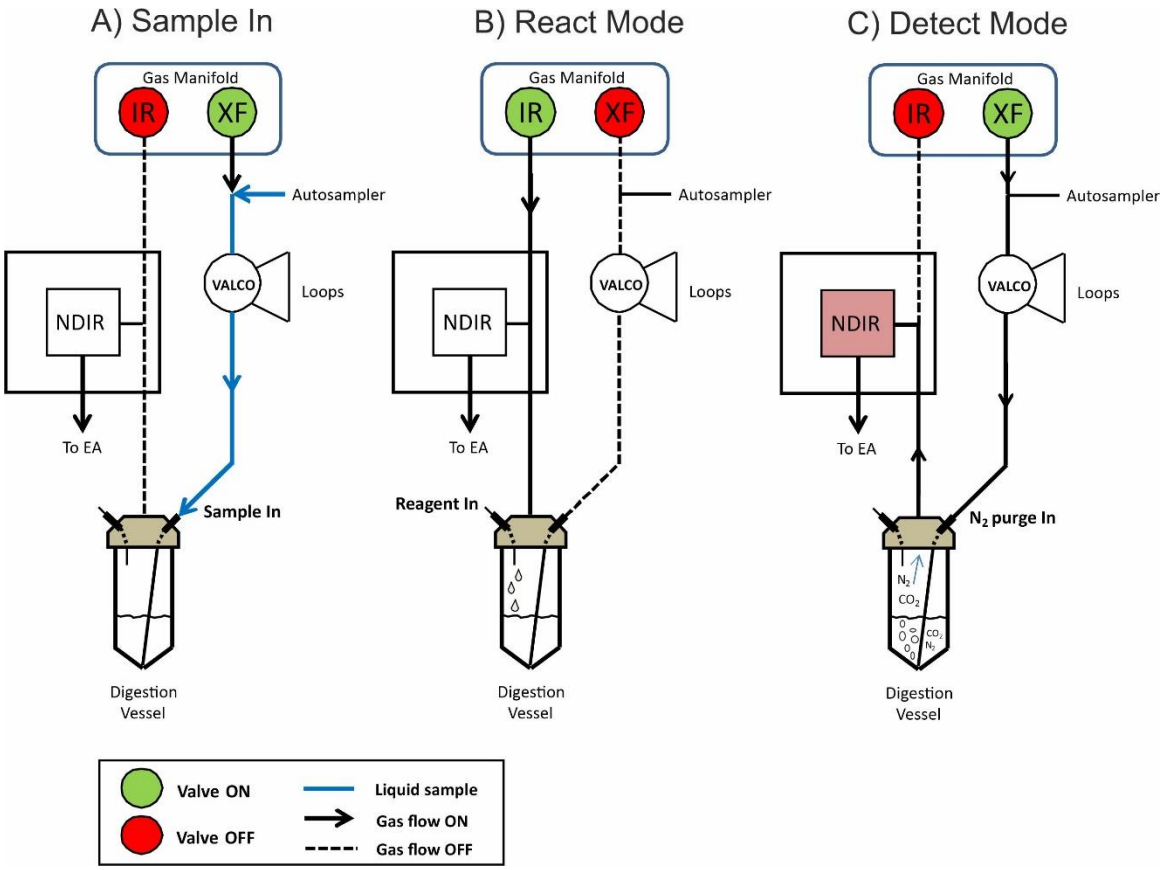

Figure 4.2. Functioning of the TOC Analyzer. Blue line represents the liquid sample path to the digestion vessel. Black arrows represent the direction of the gas. Stripped lines indicate a closed path.

2.2.2 Elemental analyzer

The output of the NDIR is connected by 1/8'' stainless steel tubing directly to a reduction column that is situated in the oven of an elemental analyzer (Fisons). The column is at a temperature between 400 and 500 ºC enabling the retention of the halides presented in seawater (Lalonde et al., 2014; Osburn and St-Jean, 2007). It consists of a quartz tube 45 cm long and 2 cm in diameter and filled in its central part with copper chips, leaving the endings (10 cm each side) filled with quartz chips. As soon as the gas flow exits the reduction column, it is passed through a water trap filled with magnesium perchlorate.

2.2.3 Cryogenic trap and Gas Bench

This device works as a gas distributor, and it was developed in the Stable Isotope Biogeochemistry Laboratory (IACT, CSIC-UGR). Its main components are the cryogenic trap, the chromatographic column and the open split system. The gas distributor is controlled by a central valve (Valco) of eight ports and establishes the connections between the different components in two possible positions called load and injection. In load mode, all the gas flow from the carbon analyzer circulates through a stainless steel loop situated

above a liquid nitrogen Dewar and, returning to the Valco, continues to an exit vent. In this mode, the sample is freeze and concentrated in the cryogenic trap when the loop is programmed to get into the liquid nitrogen (Fig. 4.3a). In the second position called injection, while the sample is still trapped in the liquid nitrogen container, a flow of helium from other Valco port circulates in the opposite direction to that of the sample + carrier nitrogen, changing the carrier gas to helium. Once the sample is released from the cryogenic trap, the analyte is sent towards a chromatographic column (CP-PoraPLOT-Q) of 27.5 m long x 0.32 mm (ID) (Fig. 4.3b). The column selects all the entering molecules by size along its path and exits the CO_2 at a certain time separated from other molecules. Finally, the analyte reaches the open split system consisting of two vessels 50 mm long and 0.5 mm in diameter, one for the reference CO_2 and the other for the sample (Fig. 4.4). Both vessels contain silica capillary that connects directly to the IRMS inlet system.

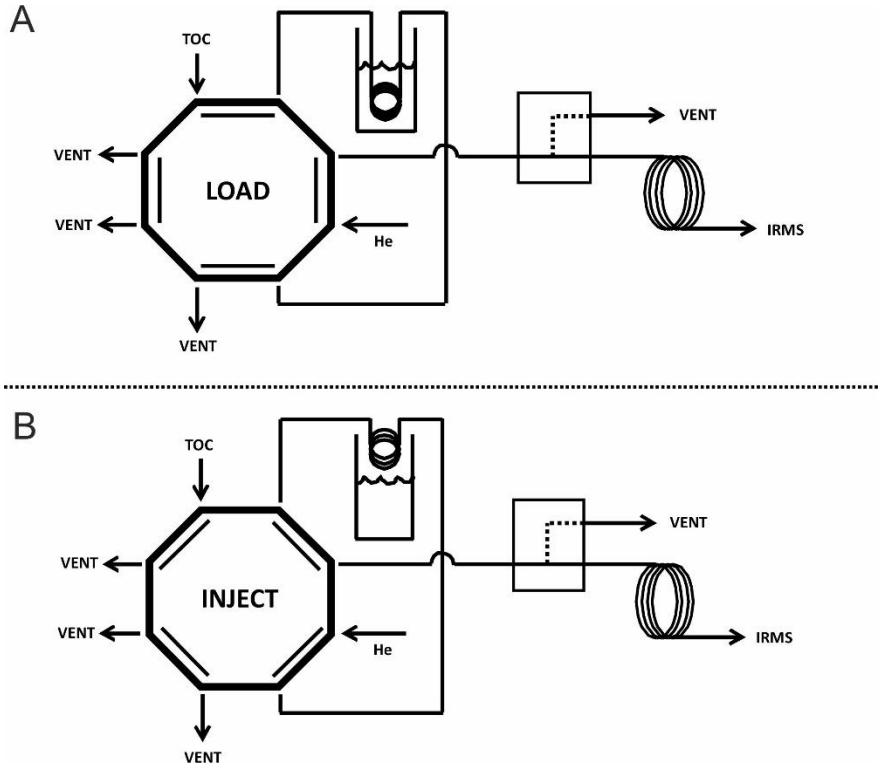

Figure 4.3. Schematic functioning of the Gas Bench system. A) indicates the Load position of the Valco valve where the sample coming from the TOC Analyzer is trapped in the liquid nitrogen. B) indicates the Inject position of the Valco valve, where the sample is released from the liquid nitrogen and sent to the IRMS.

Two flow rates are combined in order to displace the sample along the system. First, a fast flow (50 mL/min) of nitrogen 5.0 purges the sample and drive it from the carbon analyzer to the loop situated in the cryogenic trap. Second, a slow flow (1 mL/min) of helium 5.0 displaces the previous nitrogen carrier gas while the sample is freeze and then moves the analyte to the chromatographic column and the open split system. Compared to the method

of Osburn and St. Jean (2007), we included the cryogenic trap that allows CO_2 to concentrate enough to obtain a good signal with no need to increase the IRMS gain resistors.

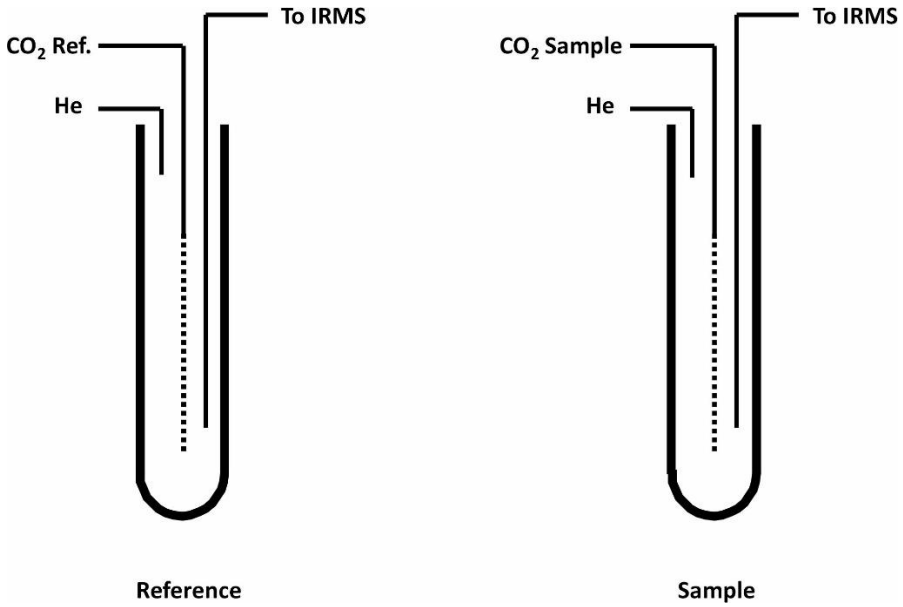

Figure 4.4. Open Split system for the CO_2 reference gas and sample gas that introduce the sample and the carrier gas into the IRMS. Dotted line indicates the range movement of the CO_2 capillary. In the high position, outgoing gas does not enter the IRMS, and in the low position, outgoing gas enters the IRMS. The left helium (He) capillary prevents the entrance of atmospheric air into the IRMS.

2.3 Calibration

Calibration curves were made from two CO_2 bottles (Bottle-L, 254 ppm of CO_2, $\delta^{13}C$ = -3.08‰; Bottle-P, 512 ppm of CO_2, $\delta^{13}C$ = -36.34‰). This calibration consists on a direct injection of a known amount of CO_2 in the main flow of carrier gas, so it does not depend on the oxidation reaction with persulfate and therefore, there are no CO_2 losses due to a possible oxidation inefficiency neither a reagent blank influence (see section 2.5). The CO_2 injection procedure was carried out in two different ways: 1) bypassing CO_2 using a 3-ways connector located at the entry of the Nafion water trap, so 100% of the CO_2 is injected directly in the path to the cryogenic trap, and 2) injecting CO_2 directly in the digestion vessel through a septum port. This second way can help to verify the quantity of CO_2 that is purged in the digestion chamber at the established detection time. Longer detection times imply higher CO_2 recovery, but also more background contamination in the cryogenic trap from the carrier gas flow. We found an optimum detection time of 5 min for the established flow rate for having a good recovery of CO_2 and low background signal. This calibration improves the accuracy of DOC standards recovery since it allows comparing directly with

the CO_2-bottle curves assuming that they represent 100% recovery for a specific amount of carbon injected.

2.4 DOC oxidation in seawater

Aiken (1992) showed that the presence of chloride in a concentration above 0.02 M produce a lower DOC recovery than expected for short reaction times. This is because DOC, chloride and any other oxidizable species in seawater compete for the persulfate radical anion $S_2O_8^{2-}$. In addition, the Cl^- and Br^- reaction rates are much faster than for organic compounds (Peyton, 1993) and also halides in seawater are extremely much more abundant than organics, reducing greatly the chances of reaction between sulfate radical anions and organic carbon molecules (Osburn and St-Jean, 2007). For seawater, McKenna and Doering (1995) established a persulfate to sample molar ratio of 8.75 from an oxidation experiment in which the volume of added persulfate was progressively increased. After that, Osburn and St-Jean (2007) chose to double the persulfate concentration used in previous works from 0.84 to 1.69 M although they maintained the persulfate to sample molar ratio of 8.75. Since then, no more studies have been published to our knowledge regarding DOC oxidation with persulfate. In our study, two experiments were performed to determine experimentally the amount of DOC in seawater that sodium persulfate can oxidize. In the first experiment, increasing volumes of two standards dissolved in both Milli-Q water and seawater were analyzed with a fixed volume of persulfate. In the second experiment, a fixed volume of seawater was oxidized with increasing amounts of persulfate, as was previously performed by McKenna and Doering (1995). Both experiments are explained in detail in the Results section.

To confirm the results of the oxidation experiment, DOC recovery was tested analyzing several samples from the FLUXES cruises (Eastern North Atlantic margin, Cape Verde Frontal Zone) with the WCO system described here and in parallel at the Organic Geochemistry Laboratory (IIM, CSIC) using a high temperature oxidation carbon analyzer (HTO) model Shimadzu TOC-V, obtaining comparable results. The reference seawater (CRM-DSW; Florida strait, Batch 08-18) provided by D. Hansell laboratory (University of Florida, USA) was also analyzed with a DOC recovery within the certified range for this water.

2.5 Blank quantification, linearity and δ^{13}C corrections

When analyzing samples with very low DOC concentration as marine samples, it is essential to characterize and quantify the blank in order to correct it properly. All techniques that analyze δ^{13}C-DOC using TOC-IRMS systems have to make this blank correction. The ultraviolet DOC oxidation (UV-IRMS) technique has the advantage of presenting very low system blanks (Beaupré et al., 2007). On the contrary, HTO and WCO techniques have significantly higher blanks that can reach up to 30% of the total signal in the case of WCO and, therefore, require a special handling to obtain high quality results (Lalonde et al., 2014; Osburn and St-Jean, 2007; Panetta et al., 2008).

There are three types of blanks: system blank, reagent blank and Milli-Q blank (Bouillon et al., 2006; de Troyer et al., 2010; Panetta et al., 2008). The system blank is a sum of contamination from various sources along the system, like impurities of the carrier gas, valves and connector leaks, Teflon tubing permeability or possible waste products from the different components due to their degradation. Separately, they are almost negligible but as a whole they are significant as they accumulate with the sample in the cryogenic trap. This blank can be quantified by running an analysis without sample and reagents. The reagent blank refers to the carbon contained in the persulfate. Despite the effort of purifying it, this blank is quite significant and the larger is the volume of reagent added to the vessel, the larger is the signal blank. The system and reagent blanks can be considered as one blank since both are present when analyzing any sample. Finally, the Milli-Q blank is only present in the standard solutions prepared in Milli-Q water. It can be quantified performing a Milli-Q water analysis and subtracting the system and reagent blanks.

Linearity test must be done prior to analyze samples in order to calibrate the isotopic ratio, which is dependent of the signal intensity. It is performed by progressively increasing the pressure of the

erence CO_2 gas with the aim of obtaining a representative range of intensities in the IRMS instrument. Linearity correction is applied using the formula described in Brand (2004):

$$\delta_{corr} = \delta_{obt} - m_{lin}(I_S - I_{ref}) \quad (4.1)$$

where δ_{corr} is the δ^{13}C linearity-corrected value, δ_{obt} is the raw δ^{13}C obtained in the IRMS, m_{lin} is the slope of the linearity test and, I_s and I_{ref} are the intensities of the sample and the reference, respectively.

Once the linearity deviation is corrected, a mass balance equation for subtracting the blank is applied as follows (e.g. Lang et al., 2012):

$$\delta^{13}C_S = \frac{(\delta^{13}C_T * A_T) - (\delta^{13}C_B * A_B)}{(A_T - A_B)} \quad (4.2)$$

where δ^{13}C is the isotopic value, A is the obtained area, S is the sample, B is the blank and T (total) is the sum of sample plus blank. For a proper mass balance correction, an accurate quantification of $\delta^{13}C_B$ and A_B is essential (see section 3.2).

3. Results and discussion

3.1 DOC oxidation experiments

In order to optimize the sample and reagent volume, we determined experimentally the oxidation capacity of sodium persulfate in seawater by performing two experiments. In the first experiment, increasing amounts of two standards (KHP and sucrose) prepared at 1.5 mg L^{-1} were mixed with 3 mL of sodium persulfate. The standards were dissolved in Milli-Q water and seawater (surface seawater of the North Atlantic with a salinity of 35 and a DOC concentration of 61.3 ± 0.9 µM). Milli-Q and surface seawater were analyzed previously to determine their carbon content and δ^{13}C. Figure 4.5a shows the good DOC recovery of the two standards dissolved in Milli-Q water for all the volumes added and an accurate δ^{13}C (Fig. 4.5b) when compared with the values obtained when analyzing the solids by EA-IRMS. Figure 4.5c shows that DOC oxidation in the surface seawater is effective up to 2 mL of sample and then, DOC recovery slightly decrease. Its δ^{13}C shows depleted values at 3 and 4 mL when the oxidation is incomplete (Fig. 4.5d). Finally, standards dissolved in seawater shows good DOC recovery up to 2 mL of sample while for 3 and 4 mL its recovery is lower (Fig. 4.5e). Its δ^{13}C signature were slightly displaced to depleted values from 2 mL of sample compared to the EA-IRMS value (Fig. 4.5f). This deviation is similar to that obtained in the seawater alone and can be further corrected for any sample with the two-standard correlation explained in the next section.

The second experiment consisted on performing successive analyses with a fixed sample volume (2 mL) of seawater and an increasing reagent volume (0, 0.2, 0.5, 1, 2, 3, 4 and 5 mL) as in (McKenna and Doering, 1995). These authors used a different TOC analyzer (OI Analytical Model 700), a smaller sample volume (0.34 mL) and a persulfate concentration of 0.84 M. In our experiment, the concentration was doubled to 1.69 M. Sample volume was established optimizing peak intensity at IRMS and DOC recovery,

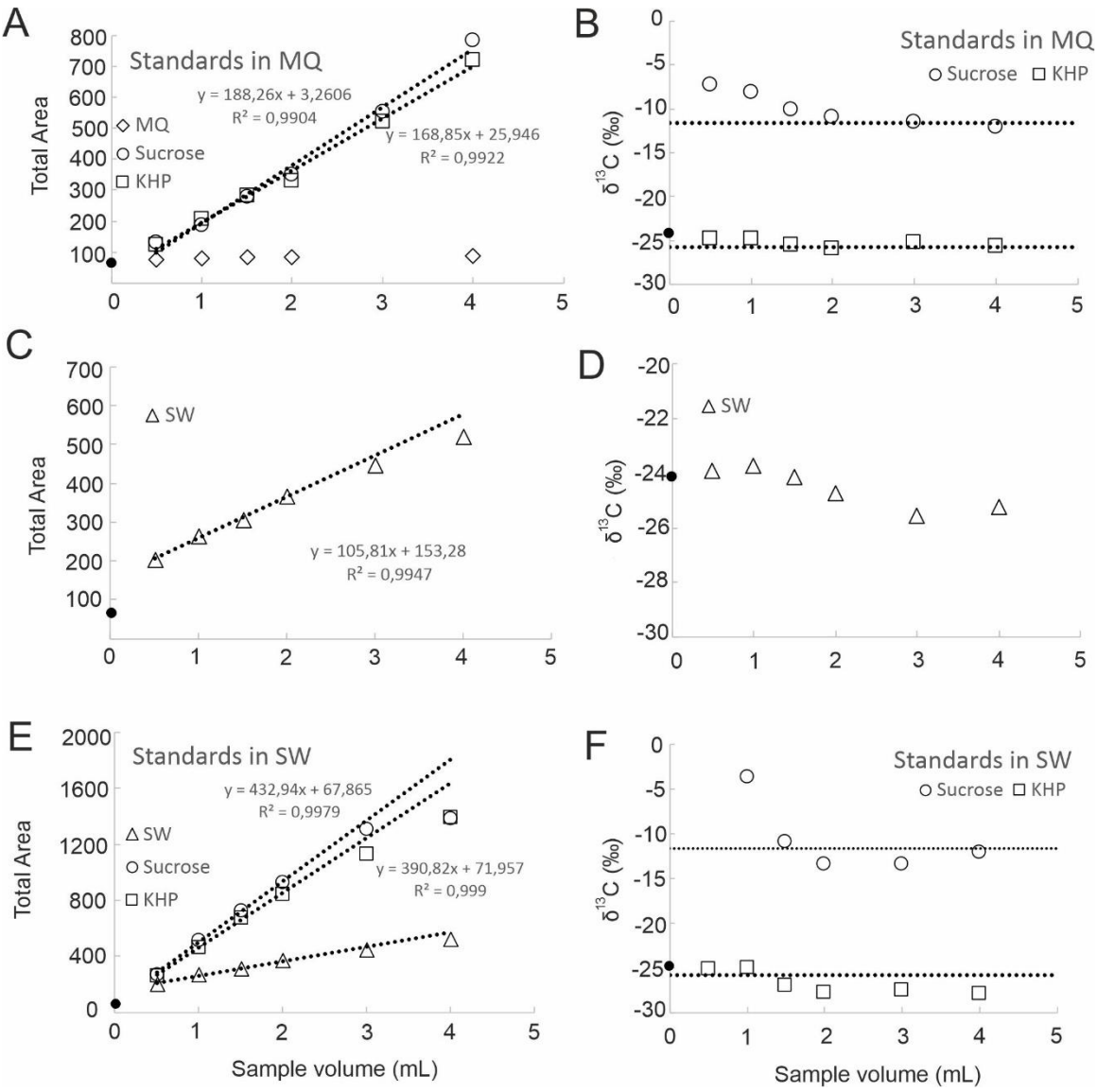

Figure 4.5. DOC and δ^{13}C-DOC recovery of KHP and sucrose both dissolved in Milli-Q water (A, B) and seawater (E, F). Seawater used as solvent is analyzed separately (C, D). Standards were prepared at 1.5 mg L^{-1}. Sample volume is set from 0.5 to 4 mL. Reagent volume is always 3 mL. Black dot represents the reagent blank area (A, C, E) and reagent blank δ^{13}C (B, D, F). Horizontal dotted lines in B and F represent the δ^{13}C of KHP (-25,73‰) and sucrose (-11,75‰) obtained in solid form by EA-IRMS.

trying to minimize the amount of halides and halogens that are released in gaseous form during the digestion process. These released gases compete for persulfate with DOC, consume quickly the chemical traps and produce corrosion in the line. Finally, it was set empirically at 2 mL as the optimum volume taking into account the previous statements. The seawater analyzed is the same than in the first experiment. The results (Fig. 4.6a) show an asymptotic relationship between the reagent volume and DOC recovery, reaching constant DOC concentrations from 3 mL of reagent. Values become slightly enriched in ^{13}C when increasing the volume of reagent (Fig. 4.6b) and no asymptotic values were obtained. Inefficient DOC oxidation results in depleted ^{13}C values due to preferential

oxidation of light (i.e., ^{12}C enriched) molecules (Follett et al., 2014; Oba and Naraoka, 2008; Yu et al., 2015). Conversely, δ^{13}C analysis of specific compounds showed that recalcitrant DOC as lipids or low molecular weight (LMW) DOC (Broek et al., 2020; Loh et al., 2004; Williams and Gordon, 1970; Zigah et al., 2017) presented lower δ^{13}C signatures compared to total DOC. Therefore, if DOC oxidation is inefficient, an enrichment in ^{13}C would be expected since the depleted recalcitrant components would resist persulfate oxidation. A likely reason for the observed results is that the δ^{13}C of the reagent blank enriched in ^{13}C with increasing volume (Fig. 4.6b), and the more volume of reagent added, the larger the effect of the blank on the bulk δ^{13}C-DOC, despite the blank correction applied.

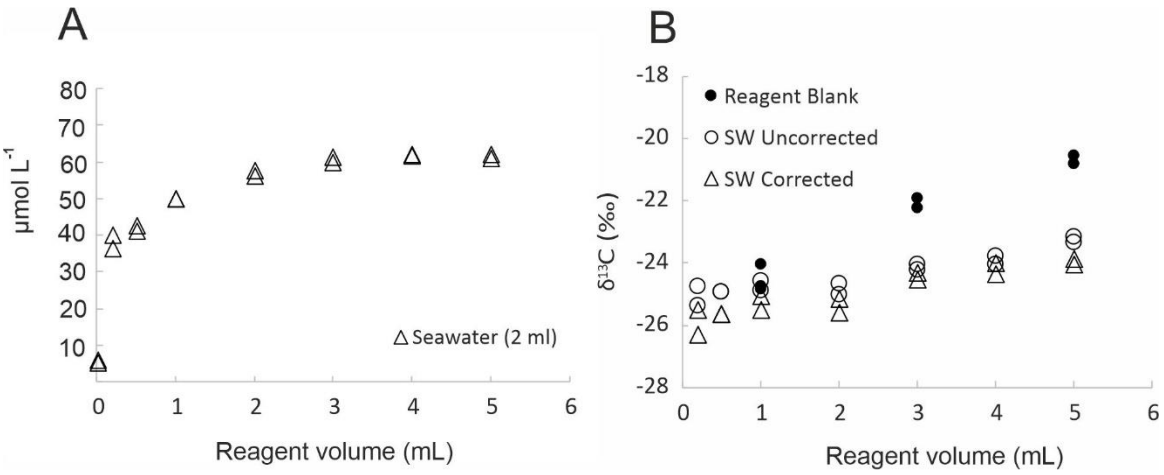

Figure 4.6. A) DOC recovery (µmol L^{-1}) with increasing volume of persulfate reagent. Sample volume of seawater (SW) is always 2 mL. B) δ^{13}C of reagent blank (filled circles), seawater uncorrected (empty circles) and seawater corrected to reagent blank (empty triangles) with the mass balance equation (eq. 4.2).

To verify the DOC recovery based on the previous experiment, several seawater samples from the FLUXES cruises and consensus reference material (CRM) were analyzed by adding 2 mL of sample and 3 mL of persulfate. These samples were also analyzed by the HTO-DOC method (Shimadzu TOC-V) to make a DOC recovery comparison between both methods (Table 4.1). Similar DOC recovery was observed, usually with differences lower than 10 µM. The CRM analysis resulted in an isotopic value of -25.2 (0.4) ‰, a depleted value than previously reported by other authors, ranging from -23.2 to -19.9‰ (Kim et al., 2015; Kirkels et al., 2014; Lalonde et al., 2014; Lee and Kim, 2018). Nevertheless, its DOC concentration was 43.0 (1.6) µM, within the certified value of 41-44 µM reported for this batch. Since there is not an international standard for δ^{13}C-DOC, the isotopic value of this seawater does not determine the method validation. The results show that 2 mL of seawater with typical DOC concentrations (40-90 µM) can be efficiently oxidized with 3 mL of

purified sodium persulfate at 1.69 M (400 g/L). This means a persulfate to sample molar ratio of 4.64, practically half than that previously reported by McKenna and Doering (1995) of 8.75 and one third of that used by Peltzer et al., (1996) of 13.1 with no significant loss of performance.

3.2 Blank correction and δ^{13}C isotopic signature

A number of factors must be taken into account when the intensity and isotopic value of the blank ($\delta^{13}C_B$) is obtained. When the TOC analyzer has been down for a while, even overnight, the peak intensity of the reagent blank is unusually high due to accumulated contamination in the reagent dispensing pump, the tubing or the digestion vessel. It is therefore essential to perform numerous reagent blank analyses (usually reagent is added, but without sample) as a clean-up procedure before starting a regular sequence. The intensity of the blank gradually decreases until stable values around 10 µM are reached. This reagent blank still accounts for about 25% of the total signal for the analysis of a seawater with a DOC concentration of 40 µM.

$\delta^{13}C_B$ usually starts with more depleted values and stabilizes with successive analyses. Over many months of analyzing and testing, the usual $\delta^{13}C_B$ obtained by direct measurement are between -20 and -25‰. As discussed in section 2.5, it is important to establish the $\delta^{13}C_B$ as precisely as possible to apply accurately the mass balance correction. Reagent blank analyses typically have an intensity of less than 1000 mV and therefore their δ^{13}C may be not reliable as it is below the precision range of the IRMS instrument (Bouillon et al., 2006; Lang et al., 2012). In this situation, it has to be obtained indirectly. One possibility to obtain the $\delta^{13}C_B$ is by analyzing a reference material at different concentration (Lalonde et al., 2014; Osburn and St-Jean, 2007; Panetta et al., 2008) and plotting the $\delta^{13}C_T$ versus the inverse of the peak area. From the slope and the blank area, the $\delta^{13}C_B$ can be calculated approximately. Another possibility is using the mass balance equation (eq. 2) from the standards analysed and calculate the $\delta^{13}C_B$ using the theoretical δ^{13}C of the standard reference material. Here, both methods were tested and non-significant differences were observed when analysing directly the reagent blank compared with the indirect estimations. Therefore, we decided to use the raw δ^{13}C of the reagent blank as $\delta^{13}C_B$.

To correct the δ^{13}C isotopic signature of the reference standards, the Milli-Q blank correction must be applied, which is the sum of the reagent blank (including the system blank) and the Milli-Q water used to prepare the standard solution. Analysis of Milli-Q

water samples were performed, showing a DOC concentration of 12.6 ± 2.4 µM and a δ^{13}C of -24.5 ± 0.4‰ (n = 6). When subtracting the reagent blank contribution, the Milli-Q blank results in 2.1 ± 1.0 µM. For δ^{13}C correction of natural samples, only the reagent blank has to be discounted, as mentioned above.

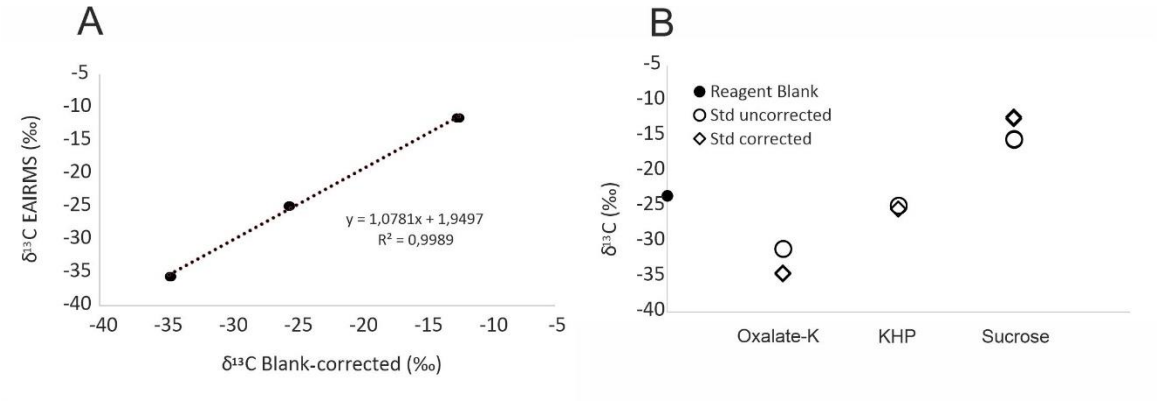

Figure 4.7. A) δ^{13}C obtained by EA-IRMS against blank-corrected δ^{13}C of standards K-oxalate, KHP and sucrose. B) Uncorrected and corrected δ^{13}C of standards K-oxalate, KHP and sucrose.

As a last step for data correction, the linear correlation between KHP, sucrose and K-oxalate standards (-25.77, -11.65 and -35.55‰, respectively) is performed, relating the δ^{13}C signature obtained by EA-IRMS (Y-axis) against the blank-corrected δ^{13}C signature (X-axis) (Fig. 4.7a). The resulting equation is applied to any sample for a more precise correction. Figure 4.7b presents the analysis of KHP, sucrose and K-oxalate standards showing the raw and blank-corrected values. Larger differences between the raw and corrected values are observed for K-oxalate and sucrose standards because their δ^{13}C value are more distant from the δ^{13}C values of the blank. On the other hand, the KHP standard has a very similar δ^{13}C to that of the blank, so the differences are very small.

3.3 Precision of the measurements and sample carry-over

Minimizing the influence of contaminants along the line is decisive to obtain measurements of acceptable precision and accuracy. Extra care must be taken in this regard, from reagent purification, effective sealing of connections and valves, use of high purity carrier gases or the proper maintenance of chemical traps. In addition, the $\delta^{13}C_B$ value has to be obtained precisely by performing numerous reagent blank analyses prior to any sample or standard sequence, in order to correct it later. The lower the influence of the blank, the better the accuracy of the measurement of DOC concentration and δ^{13}C. Ideally, the system should be in continuous operation to ensure adequate stability and to avoid further variability in the accuracy of the results. With these precautions, the measurement of δ^{13}C-DOC in

marine environments can be achieved, where the concentration reaches values as low as 40 µM.

To evaluate the precision of δ^{13}C-DOC by the WCO-IRMS method, several replicates of the standards KHP, sucrose, and K-oxalate were run at concentrations of 0.5, 1 and 1.5 mg L^{-1} dissolved in Milli-Q water (Table 4.1). For each sample vial, two replicates were performed. The precision obtained for each standard was 0.33 (n=6), 0.39 (n=6) and 0.32‰ (n=4) for KHP, sucrose, and K-oxalate, respectively. For a KHP dilution at 1 mg L^{-1} (n=3) it is 0.1‰. For reagent blanks, the precision is <0.7‰ (n=8). For a North Atlantic seawater, the precision is typically 0.1‰ (n=4) and for the CRM water is 0.5‰ (n=6; see Table 1). These values are similar to those obtained by other authors in seawater; for example 0.3‰ in the WCO-IRMS method (Osburn and St-Jean, 2007) or 0.5‰ and 0.2‰ in the HTO-IRMS method (Federherr et al., 2014; Lalonde et al., 2014), respectively.

Table 4.1. Reference standards KHP, sucrose and K-oxalate analyzed at 83.3, 166.7 and 250.0 µM. δ^{13}C-DOC values ± standard error (SE) obtained by WCO-IRMS and by EA-IRMS in solid form. Average values of all replicates and differences (‰) between the two methods are shown. CRM, consensus reference material (Florida Strait, 700 m depth, Batch 18) provided by D. Hansell Lab (U. Miami).

	WCO-IRMS				EA-IRMS		
Sample	Concentration (µM)	δ^{13}C-DOC (‰)	SE	n	δ^{13}C-DOC (‰)	SE n=3	Difference (‰)
KHP	83.3	-25.3	0.18	2			
KHP	166.7	-26.3	0.05	2			
KHP	250.0	-27.1	0.06	2			
Sucrose	83.3	-11.4	0.35	2			
Sucrose	166.7	-12.9	0.22	2			
Sucrose	250.0	-13.4	0.09	2			
K-oxalate	83.3	-36.2	0.17	2			
K-oxalate	166.7	-35.2	0.22	2			
CRM		-25.2	0.42	6			
KHP	Average	-26.2	0.33	6	-25.73	0.05	0.47
Sucrose	Average	-12.6	0.39	6	-11.65	0.03	0.91
K-oxalate	Average	-35.7	0.32	4	-35.55	-	0.15

The accuracy of the measurements was established by comparing the δ^{13}C of the standards obtain by this method with the δ^{13}C obtained by solid in EA-IRMS. After corrections, for KHP the difference is 0.45‰, for sucrose 0.91‰ and for K-oxalate 0.15‰, being adequate differences between the different techniques.

The sample carry-over effect was also tested and no influence of previous samples was observed during the analysis of samples or standards with different δ^{13}C. The design of the line prevents for this effect, as there is always a DIC purge step prior to the DOC purge, so that if any DOC rest remains in the line from the previous sample, it is removed during the DIC purge step of the next sample. The DIC gases produced in this phase are not collected in the cryogenic trap and the gas flow can pass freely to the exiting vent removing any rest or contamination accumulated from the previous sample.

4. Comments and conclusions

The present study shows the coupling between a wet chemical oxidation total organic carbon analyzer and an isotope ratio mass spectrometer (WCO-IRMS) for obtaining δ^{13}C-DOC signatures in natural waters, specifically for oceanic waters. We followed the methodology developed firstly by St-Jean (2003) and continued by Osburn and St-Jean (2007) with some modifications, including the use of a cryogenic trap of liquid nitrogen for CO_2 concentration, which avoids the need to amplify the IRMS resistors, and the use of a lower persulfate to sample ratio than was previously established (4.64 now vs. previous 8.75). This reduction in the persulfate was tested by performing two oxidation experiments and observing that DOC recovery was effective with a lower ratio than previously reported. Thus, the sample and reagent volumes were set as 2 and 3 mL, respectively. The reduction of the reagent volume decreases the signal of the blank, which is an advantage for correct the δ^{13}C values and improving the accuracy of the results.

However, this methodology is still far from being simple or routine considering the maintenance required and the costs of the materials employed. Regarding maintenance, the main reagent needed to be replaced is the reduction column, which in the presence of halogens from seawater consumes the copper chips very quickly. Approximately 30-40 analyses can be performed before flow clogging, which in continuous operation means replacement approximately every one or two days. The process of changing the reduction column involves stopping the analysis for a few hours until the blank signal is reduced and stabilized again. Also, the thermocouple that controls the temperature of the digestion vessel is corroded after two or three months of use due to the oxidizing environment and

chlorinated gases released from the reaction. Additionally, a continuous supply of liquid nitrogen is also required to keep the cryogenic trap operative as well as a high volume of high purity carrier gases (in this case nitrogen and helium).

The time consumed by each analysis was optimized so that while one sample is circulating through the chromatographic column, the next is already reacting in the digestion vessel. With this optimization, each analysis lasts 30 minutes, which is a quite acceptable sample throughput. Considering that the software can be programmed with sequences of up to 88 samples, it is possible to perform continuous analysis during day and night. In fact, it is highly recommended to keep the system continuously working to ensure a blank signal stability, which can change every time the line is stopped, even for a few hours. In conclusion, the method developed in this study permits to obtain δ^{13}C-DOC isotopic signatures and DOC concentration in seawater with similar precision to previous works and other techniques, which is a tool of growing scientific interest that will shed light on studies related to carbon balances and biogeochemical cycles in the current scenarios of global change.

Chapter 5: Carbon isotopic signature of dissolved organic carbon ($\delta^{13}C$-DOC) in the Cape Verde Frontal Zone (CVFZ)

The results presented in this chapter are also a manuscript in preparation.

Abstract

Stable carbon isotopic composition of DOC (δ^{13}C-DOC) has been reported for the first time in the CVFZ, covering from surface to bottom waters at large-scale resolution (cruise FLUXES I) and from surface to 1500 m depth at submeso-scale resolution (cruise FLUXES II). DOC isotopic values ranged from -29.4 to -21.3 ‰, which are in accordance with the isotopic fractionation of C3 plants. Moreover, other carbon sources apart from primary production are expected to be present in the bulk DOC such as terrestrial inputs from atmospheric deposition or river discharge, or hydrothermal fluids from other oceanic areas. Epipelagic waters showed significant differences between tropical, subtropical and CBGF waters. The heaviest isotopic signatures were found in the upwelled waters near the coast, where fresh organic matter is produced and exported offshore by the CBGF. Conversely, lower values corresponded to the subtropical waters transported southwards by the Canary Current with a lower content of labile organic matter. In the meso- and bathypelagic waters, an optimum multiparameter inverse method was applied to calculate average δ^{13}C-DOC values for each water mass present in the area. A slight depletion in δ^{13}C were observed with depth from the central to intermediate waters, while maintained invariant through intermediate and deep waters, indicating low DOC biochemical transformations or that it did not leave a significant imprint on the isotopic composition. Weak correlation with AOU supports this statement. Relationships between DOC isotopic deviation with FDOM independent of the water mass mixing indicate higher δ^{13}C for protein-like substances and lower δ^{13}C for humic-like substances. Comparison with previous studies showed that our δ^{13}C-DOC values extended over a wider range than previously reported, probably explained by the contribution of several carbon sources and effects of labile DOC in near surface waters due to the high primary production. Nevertheless, further research is necessary to characterize the different DOC fractions and their individual isotopic signatures to decipher in detail the primary carbon sources of this highly dynamic area.

1. Introduction

Marine DOC is one of the major reduced carbon pools on Earth, representing almost the same amount of carbon than the carbon dioxide (CO_2) accumulated in the atmosphere (Fasham et al., 2001; Friedlingstein et al., 2020). Phytoplankton primary production occurring in the surface layer of the world ocean is the ultimate origin of most of the DOC in the marine environment (Carlson and Hansell, 2015). Only a small fraction, about 2 Pg

C y^{-1}, of the 50 Pg C produced annually in the surface ocean (Chavez et al., 2010; Field et al., 1998) survives to photochemical and microbial-loop processing, and it is exported to the ocean interior where it is used by prokaryotes and partly transformed into biologically recalcitrant molecules that accumulated in the ocean interior creating the vast inventory of DOC (Hansell, 2013; Jiao et al., 2011).

During photosynthesis, algal cells discriminate against ^{13}C when dissolved inorganic carbon is reduced from oxidation state +4 to 0 to be incorporated into organic material (Park and Epstein, 1960). This fractionation process is called carboxylation, and is conducted by an enzymatic reaction mainly driven by the enzyme ribulose-1,5-bisphosphate-carboxilase/oxygenase (RubisCO) resulting in a depleted carbon isotopic ratio relative to the DIC source (Farquhar et al., 1982; O'Leary, 1981). In the ocean, aqueous CO_2 and bicarbonate ion (HCO_3^-) are available as primary carbon sources, and seems that both species are assimilated by phytoplankton (Burkhardt et al., 1999; Degens et al., 1968a; Keller and Morel, 1999; Laws et al., 1997; Popp et al., 1998). Therefore, the carbon isotopic composition of phytoplankton is determined by the carbon fractionation during the diffusive or actively transport of DIC, by isotopic discrimination during enzymatic carboxylation and finally by the isotopic composition of the inorganic carbon source (Hayes, 1993). Moreover, additional environmental and biological factors affect the extent of the isotopic fractionation during photosynthesis, for example, temperature, CO_2 partial pressure, light availability, variations in the community composition, algal growth rate and cell geometry (Burkhardt et al., 1999; Degens et al., 1968a; Laws et al., 1997; Popp et al., 1998; Rau et al., 1992). The reader is referred to Chapter 1 for additional details.

Microbial degradation is the other major biogeochemical process affecting DOC, however, very little is known about the carbon fractionation during its mineralization. In addition, Ostrom and Fry (1993) suggested that carbon isotopic composition of DOC tend to be less affected by degradation than organic biomarkers. Labile compounds are primarily degraded, leaving a DOC fraction enriched in recalcitrant molecules that are exported to the dark ocean (Hansell et al., 2012). Previous analyses of δ^{13}C-DOC in different DOC size fractions showed that the HMW fraction with a higher content of labile material presented enriched δ^{13}C values than the LMW that contains molecules with a more recalcitrant nature. Moreover, the relative proportion of LMW increases with depth, resulting in a slight depletion of the bulk δ^{13}C-DOC (Broek et al., 2020; Zigah et al., 2017). This carbon fractionation to depleted values with DOC degradation is linked with the individual DOC

constituents and its initial δ^{13}C value, where a higher proportion of isotopically depleted compounds is present in the RDOC pool.

Carbon isotopes are a powerful tool for tracing the DOC history, since its isotopic ratio reflects the carbon primary sources (Beaupré, 2015; Hoefs, 1975). The DOC pool is composed of myriads of different compounds, and then, it is expected that more than one carbon source is present on its composition even more when some of the DOC components have been dated in more than 10,000 years surviving over several oceanic cycles (Williams and Druffel, 1987; Zigah et al., 2017; Ziolkowski and Druffel, 2010). The carbon isotopic signature of the bulk DOC represents the sum of all isotopic ratios of its individual constituent molecules and studying the different fractions of DOC and specific compounds helps to differentiate between potential primary sources (Beaupré, 2015). Apart from primary production in the upper layers of the ocean, other organic carbon sources are present in the DOC pool, originating in the ocean itself or from terrestrial inputs (Follett et al., 2014), including black carbon (Kuhlbusch, 1998; Masiello and Druffel, 1998), inputs of C3 and C4 terrestrial plants (McNichol and Aluwihare, 2007; Raymond and Bauer, 2001) or organic carbon from hydrothermal vents (Lang et al., 2006; McCarthy et al., 2010). Moreover, some authors indicated a possible small source of marine C4 photosynthetic pathway (Roberts et al., 2007; Xu et al., 2012).

δ^{13}C-DOC depth profiles were reported for the first time in the Northeast Pacific Ocean in the pioneering study of Williams and Gordon (1970). They found that δ^{13}C-DOC profiles were nearly constant with depth and had no remarkable correlation with temperature, salinity, oxygen, nutrients or season, concluding that DOC was stable to biochemical transformations when exported to the deep ocean. Further studies published data in other areas covering different oceans and latitudes, obtaining similar results and corroborating the lack of prominent features in the δ^{13}C-DOC (Bauer et al., 1998a, 1998b; Ding et al., 2020; Druffel et al., 1992; Eadie et al., 1978; Griffith et al., 2012; Tanaka et al., 2010; Walker et al., 2017). More recently, Druffel et al. (2019) found a correlation between surface δ^{13}C-DOC and sea surface temperature, probably attributed to the δ^{13}C imprint of primary producers.

This chapter presents for the first time the δ^{13}C distribution of DOC in the CVFZ from surface to deep waters at two spatial resolutions (large- and. submeso-scale) with the aim of deciphering 1) if the surface mesoscale structures as fronts, meanders and filaments, and

the transition from coastal to open ocean waters have an impact on the isotopic composition of DOC; 2) isotopically characterize the different water masses present in the study area and 3) gain new insights on DOC cycling at the surface and ocean interior of the CVFZ.

2. Materials and Methods

2.1 Sampling strategy and analytical procedures

Data used in this study was collected during two oceanographic cruises in 2017 on board the R/V Sarmiento de Gamboa (Fig. 5.1). The first cruise, FLUXES I, was conducted from 12th July to 9th August and consisted on 35 hydrographic stations 50 nautical miles apart defining a box that covered most of the CVFZ. This box consisted of four transects (North, West, South and East) based on their relative position and samples were taken from surface to bottom. Three types of stations were occupied: day stations (9h, 14 depths from surface to bottom), night stations (3h, 10 depths from surface to 2000 m) and long stations (27h, from surface to bottom). The second cruise, FLUXES II, was conducted from 2 to 24th November and consisted on a submeso-scale sampling, with 48 hydrographic stations 5 nautical miles apart and performed along two perpendicular transects with a Northwest-Southeast (T1, 36 stations) and Northeast-Southwest (T2, 12 stations) orientation in front of Cape Blanc. Samples were taken at 10 depths from surface to 1500 m. Water samples were collected using a rosette sampler equipped with 24 Niskin bottles of 12 liters. The rosette was also equipped with conductivity-temperature-depth (SBE911 plus), oxygen (SBE43), fluorescence of chlorophyll (SeaPoint SCF) and turbidity (SeaPoint STM) sensors.

Dissolved oxygen was measured by the Winkler potentiometric method following a variant of the method of Langdon (2010). Apparent oxygen utilization (AOU) was calculated following Benson and Krause (UNESCO, 1986) where $AOU = O_2sat - O_2$, with O_2sat being the oxygen saturation. Determination of Chl-*a* was made according to the method of Holm-Hansen et al. (1965). Absorption coefficient spectra of colored dissolved organic matter (CDOM) were obtained on board in a spectrophotometer Jasco-

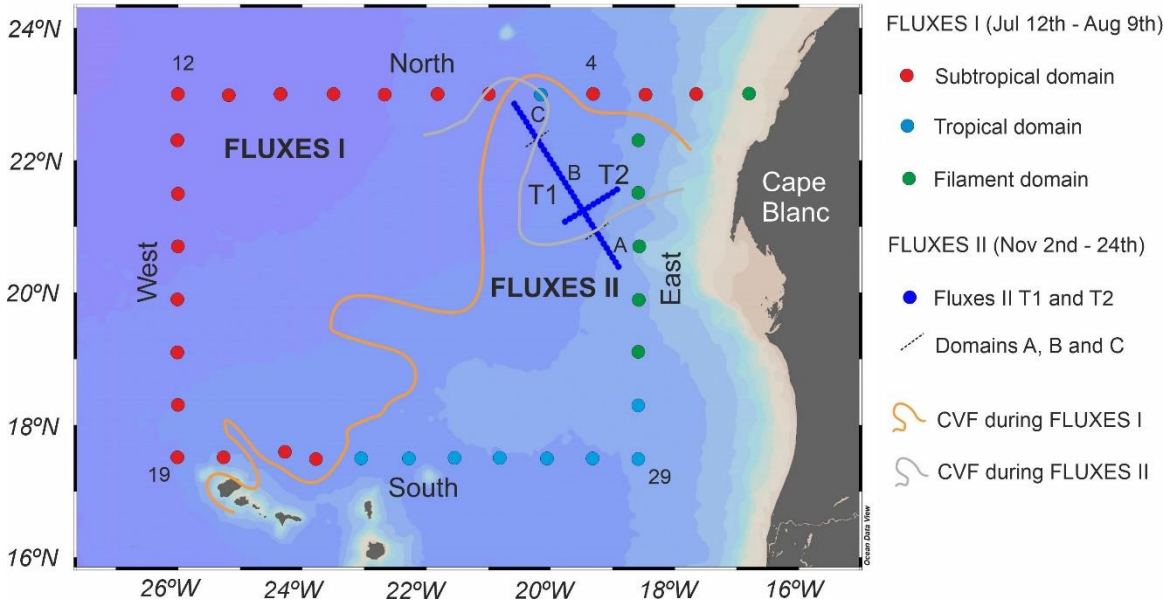

Figure 5.1. Map of the FLUXES I and FLUXES II surveys. The colored dots represent the epipelagic classification of the hydrographic stations for FLUXES I (red: North of the CVF; light blue: South of the CVF; green: waters of the CBGF) and FLUXES II (intense blue: hydrographic transects T1 and T2). Numbers indicate the station number from 1 to 35 for FLUXES I. T1 of FLUXES II is divided into domains A, B and C depending on the position of the CVF. The orange and the grey lines represent the position of the CVF during FLUXES I (taken from Burgoa et al., 2021) and FLUXES II (position determination based on Chapter 3 of this dissertation), respectively.

V 750 equipped with 100 mm path length quartz cells. In this chapter we use the absorption coefficient at 254 nm, $a_{CDOM}(254)$. Fluorescence of dissolved organic matter (FDOM) measurements were carried out on board in a Perkin Elmer LS-55 spectrofluorometer. Specific Excitation/Emission (Ex/Em) pairs were selected as described by Coble (1996). These Ex/Em pairs were 250/435 nm (peak A, general humic-like substances), 340/440 nm (peak C, terrestrial humic-like substances), 320/410 nm (peak M, marine humic-like substances) and 280/350 nm (peak T, tryptophan-like substances). Moreover, during the FLUXES I cruise, EEMs were conducted and individual fluorescent components were obtained by decomposing the fluorescence signal of the EEMs applying a parallel factor analysis (PARAFAC). From the five components obtained, only C1, C2 and C4 are used in this chapter, representing C1 and C2 the humic-like substances and C4 the protein-like substances. C1 is the sum of peaks A and C, C2 is similar to peak M and C4 is similar to peak T. For more details of the measurements see Chapters 2 and 3 of this dissertation.

For DOC determination, 25 mL of water were collected into pre-combusted borosilicate glass vials and frozen at -20ºC until their subsequent analysis in the laboratory, using a high temperature catalytic oxidation (680ºC) total organic carbon analyzer model Shimadzu

TOC-V (Pt catalyst). Seawater was not filtered due to the low concentration of suspended particulate organic matter. Samples were melted, acidified to pH < 2 and degassed with high purity N_2 before measurement. The performance of the instrument was tested with consensus reference materials provided by D. Hansell's CRM Program (University of Miami, USA). Our concentration for the deep-sea water reference (Batch 16 Lot # 05-16) was 44.9 ± 1.7 µmol L^{-1} (n = 10) while the certified value was 43-45 µmol L^{-1}. The pycnocline, which separates the surface mixed layer from the waters immediately below, was calculated following the Eq. 2.1 of Chapter 2.

2.2 δ^{13}C-DOC determination

Water samples for the carbon isotopic characterization of DOC were taken at all stations and all depths in the two oceanographic cruises, with a total of 409 samples in FLUXES I and 477 samples in FLUXES II. Water was collected directly from the Niskin bottles in 40 mL borosilicate vials previously combusted at 450ºC. Immediately after collection, samples were acidified with 0.2 mL of high purity HCl (Sigma-Aldrich, 36.5-38.0%, BioReagent) to a pH < 2 and stored in the dark at 4ºC. Once in the base laboratory, samples were analyzed using a Total Organic Carbon analyzer (Model 1010 OI Analytical) coupled with an isotope ratio mass spectrometer Delta Plus XL (Thermo). This TOC analyzer was a wet chemical-based device using sodium persulfate (Merck, 1.68 M) as oxidizing reagent. A detailed description of the isotopic methodology is reported in Chapter 4 of this dissertation. The δ^{13}C isotopic value is expressed in delta notation, as parts per thousand deviations of the $^{13}C/^{12}C$ ratio of the sample relative to the ratio of the Vienna Peedee Belemnite international standard (VPDB). The equation is as follows:

$\delta^{13}C_S = (R_S / R_{St} - 1) \times 1000$, where R_S is the $^{13}C/^{12}C$ ratio of the sample and R_{St} the ratio of the VPDB standard (0.01123720).

$$\delta^{13}C_S = \left(\frac{R_S}{R_{St}} - 1\right) * 1000 \qquad (5.1)$$

Since an international standard for δ^{13}C-DOC does not exist, method validation was tested by analyzing water-soluble isotope standards (potassium phthalate (KHP, $C_8H_5K0_4$), sucrose ($C_{12}H_{22}O_{11}$) and potassium oxalate monohydrate ($C_2H_2K_2O_5$)) as well as previously measured natural samples. Analysis of the consensus reference material (CRM) for δ^{13}C-DOC provided by D. Hansell Lab resulted in a value of -25.2 (0.4) ‰, a depleted signature

compared to previous analyses made by other stable isotope laboratories. Previous analyses range between -23.2 and -19.9‰ for the same location and depth (Florida Strait, 700 m depth) although different batches (Kim et al., 2015; Kirkels et al., 2014; Lalonde et al., 2014; Lee and Kim, 2018). However, analyses of KHP, sucrose and potassium oxalate matched with their δ^{13}C analyzed separately in solid form by EA-IRMS with a precision < 0.5‰.

2.3 Water mass analysis

The optimum multiparameter (OMP) inverse method (Karstensen and Tomczak, 1998; Poole and Tomczak, 1999) was employed as described in detail in Chapter 2. In this Chapter, archetype values of δ^{13}C-DOC were calculated for all the water masses (Eq. 2.4) along with the fraction of the total variability of δ^{13}C-DOC due to water mass mixing (Eq. 2.7). Since the delta notation is a ratio, we first converted it into a concentration value (^{13}C-DOC concentration), by obtaining the $^{13}C/^{12}C$ ratio of each sample (Rs) following the equation:

$$R_S = \left(\frac{\delta^{13}C_S}{1000} + 1\right) * R_{St} \tag{5.2}$$

and multiplying then by its DOC concentration. Finally, to consider the combined effect of mixing and biogeochemical processes on the Rs, the explanatory variable AOU is added to the linear regression model (Eq. 2.8), incorporating a coefficient (β) that relates the chemical variable N with AOU. In addition, the optical variables $a_{CDOM}254$, peak C, peak M and peak T was used to calculate the multiple regression model with ^{13}C-DOC. Similarly, multiple linear regressions between ^{13}C-DOC and optical variables were calculated for epipelagic waters using salinity instead of water mass proportion. Only the waters located below the pycnocline were used to correct water mass mixing.

3. Results

3.1 Hydrographic variability in the CVFZ

Epipelagic water during FLUXES I were classified on basis of their relative position regarding the CVF and the CBGF (see Chapter 2). Three domains were identified 1) Subtropical, situated North of the CVF and covering the Northern and Western transects; 2) Tropical, situated South of the CVF and covering the Southern transect; and 3) Filament,

situated at the Eastern transect in the waters affected by the CBGF (Fig. 5.1). The pycnocline, that separates the surface mixed layer from the waters below, was found at an average depth of 45 m. The deepest pycnocline was located in the Subtropical domain at an average depth of 51 m, followed by the Filament domain, established at 41 m and finally by the Tropical domain that presented the shallowest pycnocline at 34 m. Similarly, in epipelagic waters of FLUXES II, three domains (A, B and C) were identified along the biogeochemical transect 1 (T1) (see Chapter 3) based on the position of the CVF, this time sampled at high-resolution (Fig. 5.1). Domains A and C corresponded to Tropical waters originated South of the Front, whereas domain B consisted on Subtropical waters originated North of the CVF, showing contrasting features in salinity, AOU, NO_3^- or Chl-*a*, among others. The pycnocline was established at an average depth of 42 m, becoming deeper from South to North with average values of 36, 41 and 54 m for domains A, B and C, respectively.

Regarding meso- and bathypelagic waters, water types of contrasting origin were identified based on previous knowledge of the area and using an OMP analysis. Central waters were occupied by SACW of 18 and 12ºC, ENACW of 15 and 12ºC and MMW. Intermediate waters were occupied by SPMW, AA and MW. Finally, the deep waters were a mixing of LSW and two NEADW types, Upper and Lower. During the FLUXES II cruise, the two NEADW types were not sampled because the sampling depth was established down to 1500 m.

3.2 Distribution of δ^{13}C-DOC during FLUXES I

DOC distribution in the epipelagic layer presented the highest values in the surface mixed layer of the Tropical domain with 87.0 (0.5) µmol L^{-1}. At the DCM, DOC values slightly decreased being maximum in the Filament domain with 77.9 (1.6) µmol L^{-1}. Below the pycnocline, similar values were found in the three domains.

Regarding the carbon isotopic composition of DOC, significant differences ($p < 0.0005$) in δ^{13}C-DOC were found between the three domains above the pycnocline, with the lowest values in Subtropical waters, followed by Tropical and Filament waters, respectively. At the DCM, similar values were obtained in Subtropical and Tropical waters, while significantly higher values were measured in the Filament domain ($p < 0.05$). Below the pycnocline, again significant differences ($p < 0.0005$) were found between the three domains but contrary to that was observed in the surface mixed layer, the lowest values

were found in the filament waters followed by the Tropical and Subtropical waters, respectively. When comparing average values above and below the pycnocline, we found always significantly depleted signatures ($p < 0.0005$) below the pycnocline in the three domains (Table 5.1). Depth profile presented in Fig. 5.2a corroborates a ^{13}C enrichment near the coast with the highest δ^{13}C signatures at stn 1-4 and 29-35 coinciding with the highest values of DOC. At stn 1-4, a δ^{13}C-DOC around -22, -23‰ reached down to 200 m. On the contrary, lower δ^{13}C values were recorded at stns 6-20, coinciding with the Subtropical domain and the open ocean waters transported southwestwards by the CC.

Multiple linear regression between ^{13}C-DOC, practical salinity and $a_{CDOM}254$, peak C, peak M, peak T and PARAFAC components C1, C2 and C4 was tested for the samples located below the pycnocline. Positive correlation with significant β coefficients was found for all the parameters.

Archetype DOC values ranged from 58.9 (2.5) µmol L^{-1} in SACW_18 to 43.4 (0.6) µmol L^{-1} in LNEADW. The main feature of the DOC distribution was the vertical chimney-like structures that connects the surface waters with the deep ocean. Those structures contained a DOC concentration of around 50 µmol L^{-1}, contrasting with their surroundings that present concentrations of 40-45 µmol L^{-1}.

Archetype δ^{13}C-DOC signatures were calculated for all the WTs present in the meso- and bathypelagic waters of the CVFZ, reporting for the first time to our knowledge a type δ^{13}C-DOC value for a specific water mass. Those values are summarized in Table 5.2. Archetype δ^{13}C-DOC ranged between -24.7 (0.3) ‰ in SACW_18 and -26.3 (0.2) ‰ in UNEADW, presenting significantly ($p < 0.05$) enriched values in the shallower central water masses and similar values between the central and deep waters. When analyzing differences between transects, only the Northern transect presented significant differences at some water masses compared with the Western (SACW_18, ENACW_15 and LSW), Southern (SACW_18, MMW and LSW) and Eastern (SPMW and LSW) transects, being always enriched in ^{13}C in the Northern transect (Table 5.2).

Table 5.1. Thermohaline and chemical characteristics (average value ± SE) of the epipelagic waters above and below the pycnocline and in the deep chlorophyll maximum along the FLUXES I hydrographic box. Epipelagic waters are separated into three domains: Subtropical, Tropical and Filament (see main text).

		Z (db)	θ (ºC)	S (PSU)	DOC (µmol L^{-1})	δ^{13}C-DOC (‰)
	Subtropical		23.3 ± 0.1	36.6 ± 0.0	72.0 ± 0.2	-24.8 ± 0.04
Above pycnocline	Tropical		24.5 ± 0.1	36.1 ± 0.0	87.0 ± 0.5	-23.8 ± 0.06
	Filament		21.9 ± 0.1	36.2 ± 0.0	81.1 ± 0.5	-23.4 ± 0.05
	Subtropical	75.8 ± 0.9	20.6 ± 0.0	36.7 ± 0.0	63.9 ± 0.2	-24.9 ± 0.3
DCM	Tropical	37.9 ± 1.6	20.3 ± 0.2	36.1 ± 0.0	71.9 ± 0.6	-24.5 ± 0.3
	Filament	29.6 ± 2.0	21.2 ± 0.3	36.2 ± 0.1	77.9 ± 1.6	-23.4 ± 0.5
	Subtropical		19.3 ± 0.0	36.6 ± 0.0	59.9 ± 0.1	-25.2 ± 0.02
Below pycnocline	Tropical		17.2 ± 0.1	36.0 ± 0.0	60.8 ± 0.3	-24.9 ± 0.03
	Filament		16.9 ± 0.4	36.1 ± 0.1	59.0 ± 1.2	-25.6 ± 0.12

In Fig. 5.2b some differences can be appreciated in the δ^{13}C-DOC distribution. At stns 1-3, higher δ^{13}C values were present, reaching down to 3000 m along the continental margin. A similar column of enriched δ^{13}C values can be found at stns 23-25, coinciding with the area close to the Cape Verde islands and at stns 31-33. On the contrary, areas of depleted values were distributed at stns 12, 19-21 and below 750 m at stns 25-30.

The fraction of the total variability of δ^{13}C-DOC due to water mass mixing was calculated by the multiple linear regression model (Eq. 2.7). Water mass mixing explained 70% of the total ^{13}C-DOC concentration in the FLUXES I hydrographic box, with an SE of 0.04 µmol L^{-1}. When adding AOU to the model to observe the variability independent of the water mass mixing (Eq. 2.8), no increase in the explained variability was observed and the β coefficient was not significant.

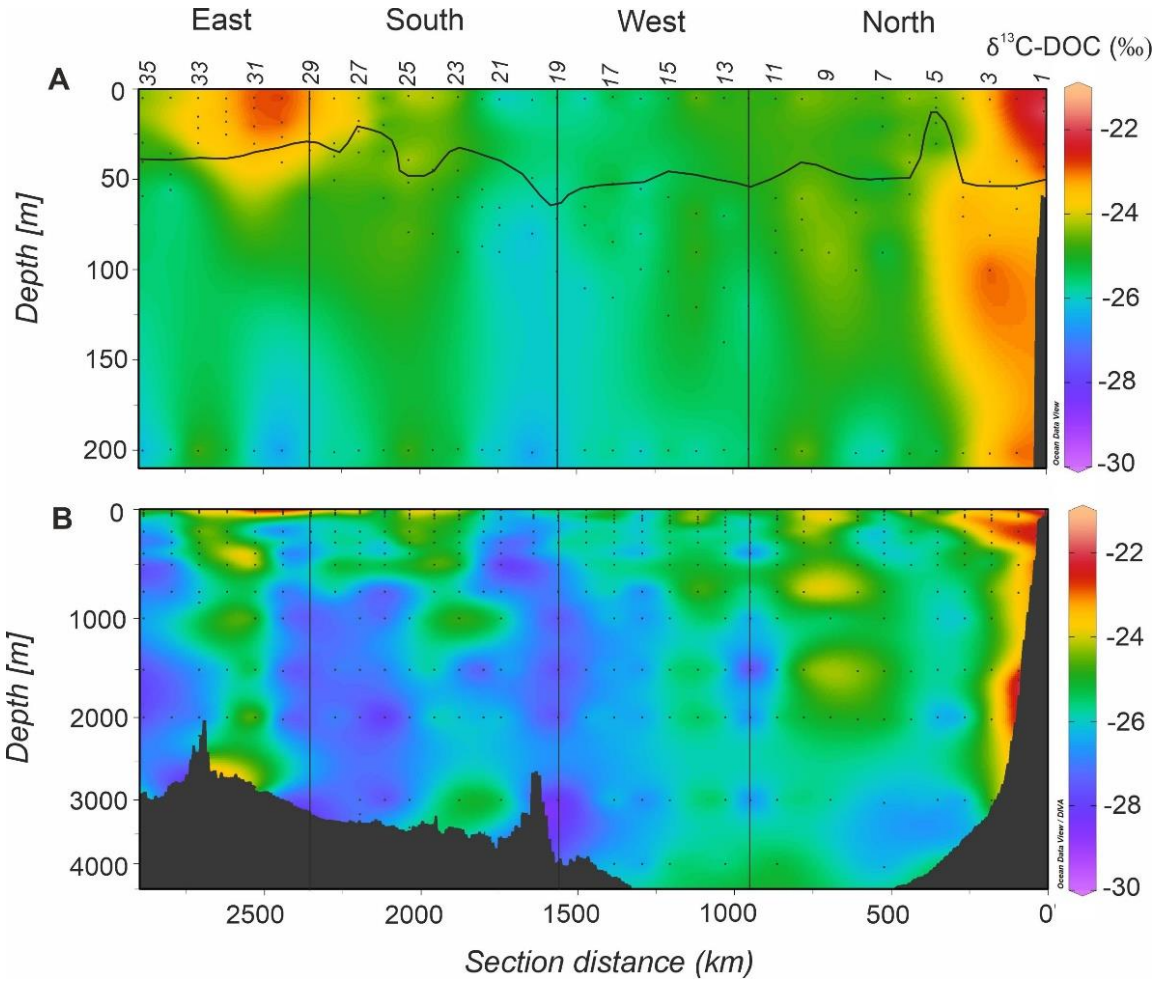

Figure 5.2. Distributions of δ^{13}C-DOC (‰) in the A) 0 - 200 m and B) 0 - 4500 m during the FLUXES I cruise. Dots represent samples, horizontal black line in panel A shows the position of the pycnocline and the vertical black lines represent the corners of the FLUXES I hydrographic box. Odd station numbers are represented at the top of the first panel. Produced with Ocean Data View (Schlitzer, 2017).

The multiple regression model between ^{13}C-DOC, water mass proportion (X_{ij}) and optical properties showed positive correlation and significant β coefficients with $a_{CDOM}254$ and peak T. Conversely, no significant correlation was found for peaks C and M, instead PARAFAC component C2 (similar to peak M) showed negative significant correlation. Determination coefficients R^2 were high for all the parameters with values of 0.69, 0.70, 0.67 and 0.68 for $a_{CDOM}254$, peak T, C2 and C4, respectively (Table 5.5).

Table 5.2. Thermohaline and chemical characteristics (archetype value ± SE) of meso- and bathypelagic waters along the FLUXES I hydrographic box. R^2, proportion of the total variability explained by WT mixing; SE, standard error of the estimate. δ^{13}C-DOC values for the full data and by transects North, West, South and East.

WT	VOL_i (%)	Z_i (db)	θ_i (ºC)	S_i (PSU)	AOU_i (µmol kg^{-1})	DOC_i (µmol L^{-1})	δ^{13}C-DOC_i (‰)
SACW_18	4.8	102 ± 19	17.3 ± 0.5	36.1 ± 0.08	120.2 ± 15.4	58.9 ± 2.5	-24.7 ± 0.3
MMW	5.5	113 ± 13	18.9 ± 0.3	36.6 ± 0.07	50.9 ± 10.5	58.7 ± 1.6	-25.0 ± 0.3
ENACW_15	12.5	240 ± 14	15.2 ± 0.2	36.0 ± 0.04	117.8 ± 6.7	52.3 ± 1.7	-25.3 ± 0.2
SACW_12	7.3	336 ± 28	12.2 ± 0.3	35.5 ± 0.04	191.7 ± 5.4	49.9 ± 1.5	-25.7 ± 0.2
ENACW_12	18.1	442 ± 19	11.6 ± 0.2	35.5 ± 0.03	171.2 ± 4.8	48.5 ± 0.6	-25.6 ± 0.2
SPMW	7.2	809 ± 32	7.8 ± 0.2	35.1 ± 0.02	175.7 ± 4.2	44.8 ± 0.6	-25.9 ± 0.3
AA	10.6	873 ± 54	7.6 ± 0.3	35.1 ± 0.02	172.6 ± 5.7	45.1 ± 0.6	-25.9 ± 0.2
MW	3.1	1455 ± 118	5.2 ± 0.4	35.0 ± 0.02	119.4 ± 9.2	43.3 ± 0.9	-25.9 ± 0.5
LSW	15.6	1688 ± 46	4.5 ± 0.1	35.0 ± 0.01	104.0 ± 2.6	43.4 ± 0.5	-26.1 ± 0.2
UNEADW	11.7	2742 ± 93	3.1 ± 0.1	35.0 ± 0.01	88.0 ± 1.1	43.4 ± 0.6	-26.3 ± 0.2
LNEADW	3.7	3824 ± 101	2.4 ± 0.0	34.9 ± 0.00	85.1 ± 1.7	43.5 ± 1.0	-26.1 ± 0.3
R^2					0.94	0.63	
SE					12.9	4.0	

	δ^{13}C-DOC (‰)			
	North	West	South	East
SACW_18	-23.8 ± 0.5	-25.9 ± 0.3	-25.2 ± 0.3	-24.6 ± 0.9
MMW	-24.4 ± 0.5	-25.5 ± 0.3	-25.9 ± 0.5	-24.9 ± 2.8
ENACW_15	-24.9 ± 0.3	-25.6 ± 0.1	-25.7 ± 0.4	-25.4 ± 0.6
SACW_12	-25.1 ± 0.6	-25.9 ± 0.4	-25.8 ± 0.3	-25.5 ± 0.7
ENACW_12	-25.2 ± 0.3	-25.6 ± 0.2	-25.8 ± 0.3	-25.8 ± 0.4
SPMW	-25.2 ± 0.3	-26.1 ± 0.5	-26.4 ± 0.7	-26.4 ± 0.5
AA	-25.2 ± 0.5	-26.0 ± 0.4	-26.1 ± 0.3	-26.1 ± 0.6
MW	-25.3 ± 0.8	-26.1 ± 0.7	-26.4 ± 1.8	-26.4 ± 1.1
LSW	-25.2 ± 0.4	-26.3 ± 0.3	-26.6 ± 0.3	-26.5 ± 0.5
UNEADW	-25.9 ± 0.3	-26.4 ± 0.5	-26.5 ± 0.4	-25.4 ± 0.6
LNEADW	-25.9 ± 0.3	-26.3 ± 0.4	-26.4 ± 1.5	-27.2 ± 2.3

3.3 Distribution of δ^{13}C-DOC during FLUXES II

DOC presented the highest values in the surface mixed layer with an average of 76.0 (0.8) µmol L^{-1} along the T1. Maximum values were found at stn 21 that coincided with Chl-*a* and turbidity maxima. At the DCM, similar values between the three domains were obtained with DOC concentration of around 70 µmol L^{-1}. Finally, below the pycnocline, values decreased to around 59 µmol L^{-1} and presented vertical chimney-like structures.

Distribution of δ^{13}C-DOC in epipelagic waters of the FLUXES II cruise showed similar values between the three domains (A, B and C) above the pycnocline with no significant differences between them (Table 5.3). A similar distribution was found at the DCM. Below the pycnocline, a significantly ($p < 0.05$) depleted average value was found in domain C compared to domains A and B. When comparing average values above and below the pycnocline, always significantly depleted values were found below the pycnocline in the three domains (Table 5.3). The highest signatures were observed at stns 15-17, with values around -23, -24‰ forming a column reaching down to 200 m (Fig. 5.3a).

Analysis of multiple correlation between ^{13}C-DOC, salinity and optical properties showed positive correlation for $a_{CDOM}254$ and peaks C, M and T, with significant β coefficients for all the variables.

Table 5.3. Thermohaline and chemical characteristics (average value ± SE) of the epipelagic waters above and below the pycnocline and in the deep chlorophyll maximum along the FLUXES II biogeochemical transect 1. Domains A, B and C correspond to stn 1-8, 9-28 and 29-36, respectively.

		Z (db)	θ (ºC)	S (PSU)	DOC (µmol L^{-1})	δ^{13}C-DOC (‰)
Above pycnocline	Dom A		23.00 ± 0.05	36.38 ± 0.01	75.3 ± 1.3	-24.5 ± 0.2
	Dom B		22.99 ± 0.02	36.31 ± 0.01	77.2 ± 1.2	-24.5 ± 0.1
	Dom C		23.30 ± 0.04	36.58 ± 0.01	74.8 ± 1.3	-24.5 ± 0.2
DCM	Dom A	34.0 ± 2.7	21.37 ± 0.6	36.28 ± 0.06	69.4 ± 2.0	-24.5 ± 0.3
	Dom B	39.6 ± 1.6	21.84 ± 0.3	36.34 ± 0.05	69.0 ± 1.9	-24.7 ± 0.2
	Dom C	45.7 ± 2.9	22.75 ± 0.2	36.56 ± 0.04	70.8 ± 2.2	-24.8 ± 0.2
Below pycnocline	Dom A		16.08 ± 0.04	35.95 ± 0.01	60.1 ± 1.6	-25.0 ± 0.2
	Dom B		17.30 ± 0.03	36.19 ± 0.00	57.5 ± 1.2	-25.0 ± 0.2
	Dom C		16.65 ± 0.06	35.96 ± 0.01	58.4 ± 2.1	-25.5 ± 0.2

Table 5.4. Thermohaline and chemical characteristics (archetype value ± SE) of mesopelagic waters along the FLUXES II biogeochemical transects. R^2, proportion of the total variability explained by WT mixing; SE, standard error of the estimate.

WT	$\%VOL_i$	Z_i (db)	θ_i (ºC)	S_i (PSU)	AOU_i (µmol kg^{-1})	DOC_i (µmol L^{-1})	$\delta^{13}C\text{-}DOC_i$ (‰)
SACW_18	3.2%	165 ± 25	15.4 ± 0.4	35.8 ± 0.04	173.2 ± 8.1	52.8 ± 1.9	-25.3 ± 0.4
MMW	0.1%	201 ± 1	15.9 ± 0.4	36.1 ± 0.04	112.0 ± 13.6	53.1 ± 7.3	-26.8 ± 0.8
ENACW_15	12.3%	232 ± 11	14.6 ± 0.2	35.9 ± 0.03	155.3 ± 4.8	51.2 ± 0.9	-25.7 ± 0.2
SACW_12	8.6%	339 ± 24	12.6 ± 0.3	35.6 ± 0.04	191.0 ± 4.2	47.8 ± 1.0	-25.8 ± 0.2
ENACW_12	26.1%	453 ± 17	11.4 ± 0.2	35.5 ± 0.02	186.2 ± 2.6	46.6 ± 0.6	-26.0 ± 0.1
SPMW	10.4%	813 ± 20	7.6 ± 0.1	35.1 ± 0.01	187.1 ± 2.3	43.5 ± 1.0	-26.5 ± 0.2
AA	20.2%	904 ± 36	7.4 ± 0.2	35.1 ± 0.02	176.9 ± 3.2	43.1 ± 0.6	-26.3 ± 0.2
MW	5.6%	1224 ± 62	5.8 ± 0.2	35.1 ± 0.01	148.6 ± 6.2	41.2 ± 1.0	-26.3 ± 0.3
LSW	13.4%	1443 ± 26	5.0 ± 0.1	35.1 ± 0.01	127.8 ± 2.6	41.8 ± 0.7	-26.4 ± 0.2
R^2					0.96	0.40	
SE					6.61	4.54	

Archetype DOC values decreased gradually with depth ranging from 52.8 (1.9) µmol L^{-1} in SACW to 41.8 (0.7) µmol L^{-1} in LSW. Contrary to that was observed in FLUXES I, DOC chimney-like structures were not so evident at this sampling scale at mesopelagic waters, being observable only within the first 500 m. As for the case of FLUXES I, the water mass analysis was applied to obtain the archetype values of δ^{13}C-DOC for the water masses present during the FLUXES II cruise (Table 5.4). Archetype values ranged between -25.3‰ (0.4) in SACW_18 and -26.8‰ (0.8) in MMW. Overall, values were significantly depleted at intermediate and deep waters (about 1‰) compared to the central waters, indicating a ^{13}C depletion with increasing depth. Below 200 m, the δ^{13}C-DOC was distributed in areas with values around -25‰ at stn 1-3, 14-22 and 27-31, surrounded by areas with values around -26.5‰ at stn 4-13, 23-26 and 32-36 (Fig. 5.3b). The multiple linear regression of ^{13}C-DOC concentration and the water mass proportions (X_{ij}) was used to calculate the fraction of the total variability due to water mass mixing. The model resulted in a 37% of explained variability, with an SE of 0.04 µmol L^{-1}. When adding AOU to the model, no increase in the explained variability was observed and the β coefficient was not significant. The multiple regression model between ^{13}C-DOC, X_{ij} and optical properties showed not significant correlations with any of the parameters (Table 5.5).

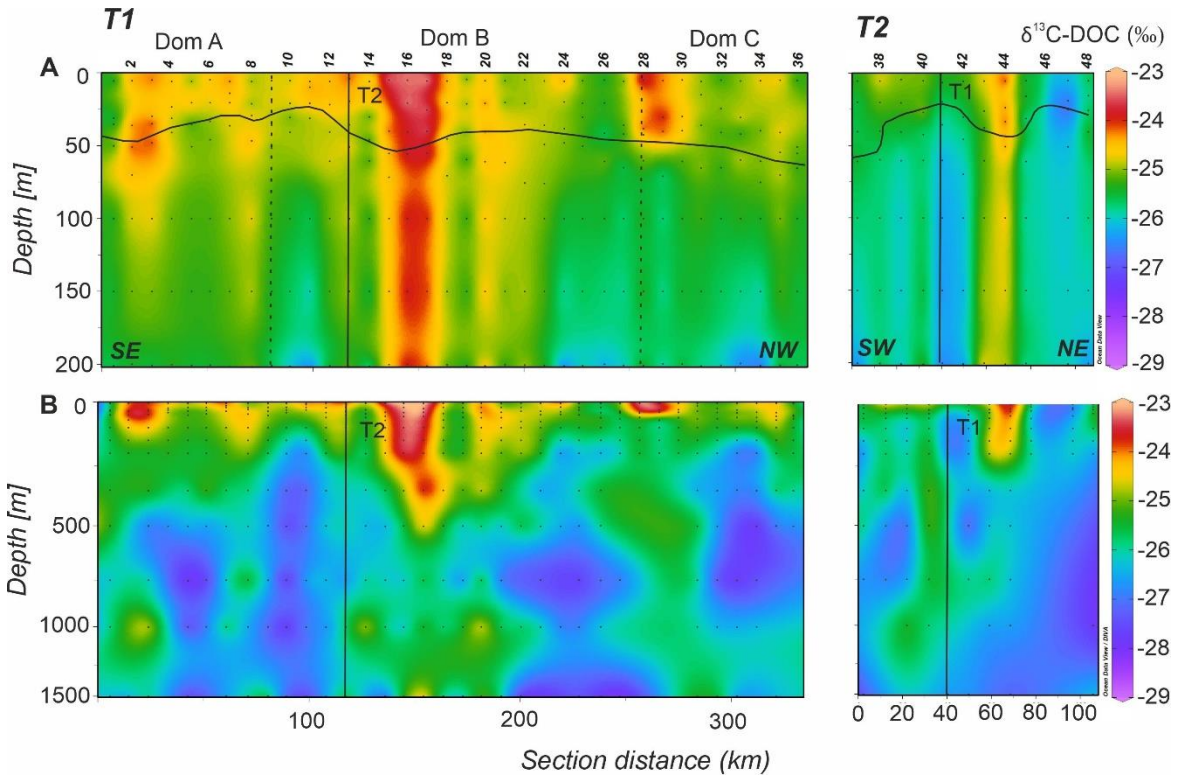

Figure 5.3. Distributions of δ^{13}C-DOC (‰) in the A) 0-200m and B) 0-1500 m during the FLUXES II cruise for the T1 (left) and T2 (right). T1 is divided into three domains (Domain A, Domain B and Domain C) separated by vertical dotted lines at stn 9 and 28. Dots represent samples and vertical black lines show the position of the orthogonal transect T2 and T1, respectively. Horizontal black line in panel A shows the position of the pycnocline. Section distance is counting from southeast (SE) to northwest (NW) in T1 and from southwest (SW) to northeast (NE) in T2 (labelled at the bottom of panel A). Produced with Ocean Data View (Schlitzer, 2017).

4. Discussion

4.1 δ^{13}C-DOC variability in epipelagic waters of the CVFZ

4.1.1 Large scale variablity during FLUXES I

The CVF and the CBGF play and important role in the δ^{13}C-DOC distribution in epipelagic waters, since significant differences were found for the different domains. Higher values were found in the waters affected by the CBGF, where large amounts of fresh organic matter are produced and exported offshore (Gabric et al., 1993; Lovecchio et al., 2018; Meunier et al., 2012). Previous studies reporting δ^{13}C of the different DOC fractions, found that labile molecules as carbohydrates and proteins contained enriched ^{13}C values compared to the bulk DOC analysis (Loh et al., 2004; Williams and Gordon, 1970; Zigah et al., 2017). These findings are consistent with the observed values in the filament waters, where the newly produced and exported organic matter contained higher amounts of labile materials (Hansell, 2013), and therefore could result into enriched bulk δ^{13}C-DOC. On the contrary,

lower values were obtained in the Subtropical domain, situated North of the CVF and consisting on waters transported southwestwards by the Canary Current (Pelegrí and Peña-Izquierdo, 2015a). These waters, originating at northern areas could experience a depletion in ^{13}C along its way to the CVFZ, by selective consumption of the labile components of DOC. Finally, the Tropical domain situated South of the CVF contained δ^{13}C-DOC signatures situated midway between the two other domains. A likely reason could be the fact that waters coming from the South Atlantic contained higher concentrations of inorganic nutrients (Pastor et al., 2008; Pelegrí and Peña-Izquierdo, 2015b) leading to higher primary production rates and, consequently, ^{13}C enriched compounds.

A depletion in δ^{13}C-DOC with depth was observed when comparing the surface mixed layer and the waters below the pycnocline. The reason for this distribution could be similar to that of the horizontal gradient from coastal to offshore waters: new DOC production by phytoplankton in the upper layers are enriched in ^{13}C due to its relatively higher content of labile compounds like carbohydrates and proteins. Heterotrophic bacteria rapidly consume these molecules of labile nature once DOC is exported to subsurface waters, leaving an imprint in the δ^{13}C-DOC since the more recalcitrant molecules as lipids tend to contain lower δ^{13}C signatures (Loh et al., 2004; Williams and Gordon, 1970). Another possible explanation for this trend, complementary to the previous one, is related to carbon fractionation from photochemical degradation of organic matter. Oba and Naraoka (2008) found in an experiment of organic matter oxidation with UV radiation that DOC experienced an enrichment in δ^{13}C with longer exposure times, due to a kinetic effect favoring the reaction of the ^{12}C-^{12}C molecules over the ^{12}C-^{13}C molecules. This is consistent with the higher δ^{13}C-DOC found in the upper layers of the study area where photochemical decomposition occurs (see Chapters 2 and 3; Campanero et al., (2022). Nevertheless, waters of the Subtropical domain are subjected to longer residence time than Tropical waters and therefore a higher photochemical degradation should be expected. This process was clearly observed in the properties of colored DOM (see Chapter 2) but not in δ^{13}C, indicating that this process does not leave an imprint in the isotopic composition. Finally, the positive multiple correlation of ^{13}C-DOC with salinity and $a_{CDOM}254$ and FDOM peaks (Table 5.5) indicates that higher concentrations of those parameters showed higher values of ^{13}C-DOC, similar to heavier δ^{13}C-DOC signatures.

4.1.2 Submesoscale variability during FLUXES II

The high-resolution approach carried out during the FLUXES II cruise showed that δ^{13}C-DOC was not affected significantly by the intense meso- and submesoscale processes that were found regarding the physical and other biogeochemical properties in the area (Burgoa, 2022; Campanero et al., 2022; see Chapter 3 for more details). Transect 1 crossed the CVF at stn 9 and 28, but the carbon isotopic signatures showed no significant differences at that position, indicating that the different carbon sources and carbon fractionation are not distinguishable at such a high-resolution. The surface mixed layer presented similar δ^{13}C-DOC values between the three domains, whereas below the pycnocline, only domain C presented lower values than the other domains. A probable explanation is that domain C was characterize by having a deeper pycnocline and the lowest concentration of Chl-*a* (Campanero et al., 2022; Chapter 3 of this dissertation), leading to a lower export of ^{13}C enriched organic matter to subsurface waters. The higher δ^{13}C-DOC signatures observed in the surface mixed layer were probably due to the higher relative abundance of enriched labile compounds originated in situ by primary producers. The isotopic signature decreased with depth probably resembling heterotrophic consumption of the labile materials. Similar to FLUXES I, positive correlation between ^{13}C-DOC with salinity and $a_{CDOM}254$ and FDOM peaks are indicative of heavier δ^{13}C-DOC with higher concentrations of those parameters. The same positive correlation was found for the protein-like and humic-like substances, unlike the opposite trend found in the meso- and bathypelagic ocean (Table 5.5). A likely reason is that in epipelagic waters, higher concentrations of both protein-like and humic-like substances are present (see distributions in Chapter 2), resulting in a positive relationship with ^{13}C-DOC, that is significantly higher than in mesopelagic waters.

4.1.3 Comparison of FLUXES I and FLUXES II δ^{13}C-DOC in epipelagic waters

The large-scale sampling carried out in the FLUXES I cruise covered a wider and more representative area of the CVFZ, where significant differences in the carbon isotopic signatures were found between the three domains of the epipelagic layer. On the contrary, the high-resolution approach during the FLUXES II cruise showed less horizontal variability in δ^{13}C-DOC, despite the intense meso- and submesoscale activity found in other variables such as salinity, oxygen or nutrients and physical processes like fronts, meanders and eddies (Fig. 5.4a & b) (Burgoa et al., 2021; Campanero et al., 2022; Martínez-Marrero et al., 2008; Zenk et al., 1991). Moreover, the vertical gradient in δ^{13}C-

DOC showed some differences between the two cruises, being smaller in the FLUXES II cruise, with a decrease of about 0.5-1‰ from the average value of the surface mixed layer to the average value below the pycnocline (Table 5.3), and greater in the FLUXES I cruise, with a decrease higher than 1‰ at the Tropical and Filament waters (Table 5.1). However, similar decrease in δ^{13}C-DOC was found in the Subtropical domain of FLUXES I compared with the three domains of FLUXES II. The greater differences in epipelagic waters of FLUXES I compared to FLUXES II are expected since a wider area with contrasting waters were sampled during the FLUXES I cruise.

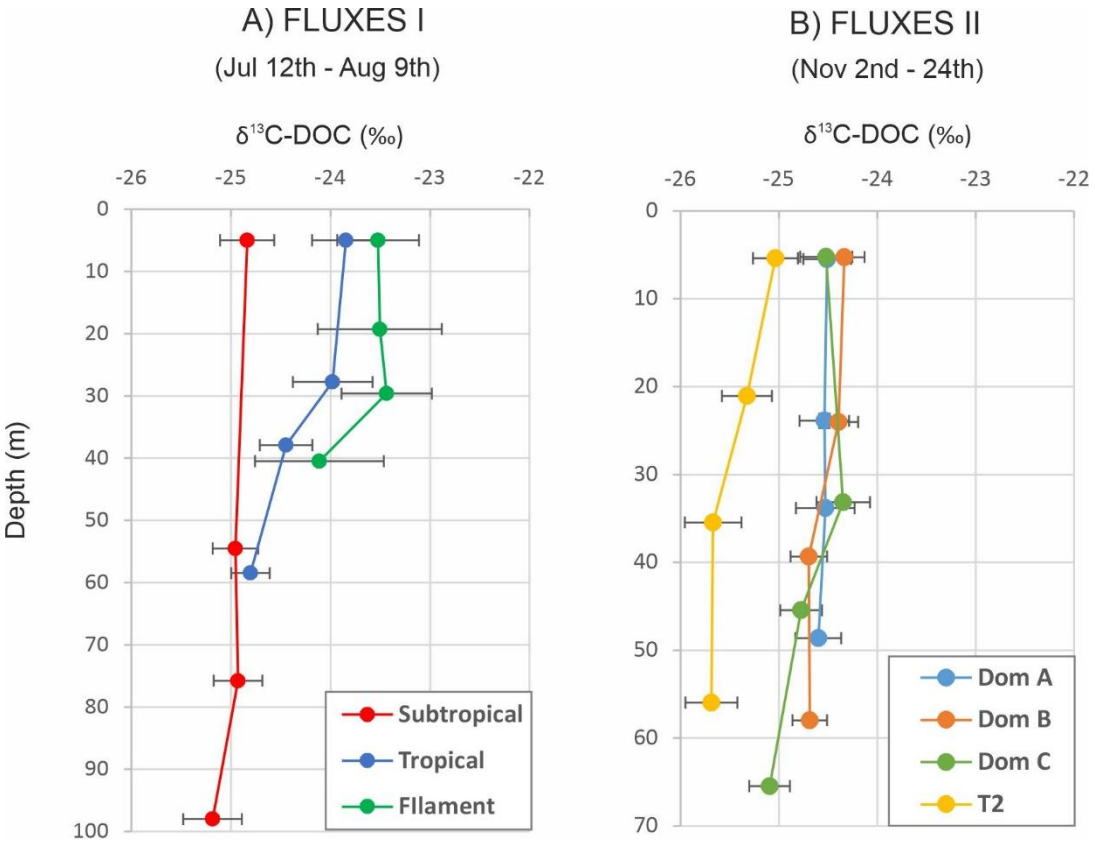

Figure 5.4. δ^{13}C-DOC (‰) averages of the epipelagic domains of A) FLUXES I and B) FLUXES II.

4.2 δ^{13}C-DOC variability in meso- and bathypelagic waters of the CVFZ during FLUXES I and FLUXES II

The meso- and bathypelagic waters of the CVFZ are characterized by a slight δ^{13}C-DOC depletion of about 1‰ from the central to the deep water masses, and maintained invariant between the intermediate and deep waters. Few significant differences were

Table 5.5. Parameters of the linear mixing (Eq. 2.7) and mixing-biogeochemical (Eq. 2.8) models for the epipelagic and mesopelagic + bathypelagic waters of the FLUXES I and FLUXES II cruises. In the epipelagic waters, the parameter salinity was used to correct for water mass mixing. R2, determination coefficient; SE, standard error of the estimate; β, fitting parameter of the relationship between N1 and N2 independent of the mixing; SE (β), standard error of the estimation of β; p, significance level of the estimation of β; n, number of samples. Blanks correspond with non-significant observations.

N_1	N_2	R^2	SE	β	SE (β)	p	n	N_1	N_2	R^2	SE	β	SE (β)	p	n
	Epipelagic								Mesopelagic + Bathypelagic						
FUXES I															
								^{13}C-DOC		0.70	0.04				284
								^{13}C-DOC	AOU	0.71	0.04	-	-	-	284
^{13}C-DOC	$a_{CDOM}254$	0.80	0.04	0.34	0.02	$2.6\ 10^{-21}$	68	^{13}C-DOC	$a_{CDOM}254$	0.69	0.04	0.29	0.06	$1.7\ 10^{-6}$	216
^{13}C-DOC	Peak C	0.41	0.07	19.0	4.1	$1.5\ 10^{-5}$	65	^{13}C-DOC	Peak C	0.66	0.04	-	-	-	212
^{13}C-DOC	Peak M	0.44	0.07	18.3	3.6	$3.8\ 10^{-6}$	65	^{13}C-DOC	Peak M	0.65	0.04	-	-	-	212
^{13}C-DOC	Peak T	0.65	0.05	18.7	2.3	$2.5\ 10^{-11}$	61	^{13}C-DOC	Peak T	0.70	0.04	6.0	1.1	$2.6\ 10^{-7}$	202
^{13}C-DOC	C1	0.51	0.06	10.5	1.8	$4.5\ 10^{-7}$	60	^{13}C-DOC	C1	0.67	0.04	-	-	-	200
^{13}C-DOC	C2	0.38	0.07	13.6	3.6	$4.2\ 10^{-4}$	60	^{13}C-DOC	C2	0.67	0.04	-0.10	0.05	0.04	200
^{13}C-DOC	C4	0.40	0.07	11.2	2.8	$1.5\ 10^{-4}$	60	^{13}C-DOC	C4	0.68	0.04	3.1	1.5	0.05	180
FUXES II															
								^{13}C-DOC		0.37	0.05				212
								^{13}C-DOC	AOU	0.37	0.05	-	-	-	212
^{13}C-DOC	$a_{CDOM}254$	0.59	0.06	0.21	0.03	$1.8\ 10^{-10}$	104	^{13}C-DOC	$a_{CDOM}254$	0.37	0.05	-	-	-	210
^{13}C-DOC	Peak C	0.48	0.07	14.0	3.3	$5.5\ 10^{-5}$	104	^{13}C-DOC	Peak C	0.37	0.05	-	-	-	210
^{13}C-DOC	Peak M	0.46	0.07	10.2	2.7	$2.6\ 10^{-4}$	104	^{13}C-DOC	Peak M	0.37	0.05	-	-	-	210
^{13}C-DOC	Peak T	0.50	0.07	9.7	2.0	$5.6\ 10^{-6}$	104	^{13}C-DOC	Peak T	0.37	0.05	-	-	-	210

observed between the four transects of the FLUXES I hydrographic box, except for some water masses that were ^{13}C enriched in the Northern transect. The similar δ^{13}C-DOC signatures at the intermediate and deep waters are indicative of a lack of relevant biochemical fractionation of DOC once is exported to the deep ocean, revealing that most of the DOC pool is refractory (Hansell, 2013; Williams and Gordon, 1970). However, previous studies of DOC cycling in the area and other regions showed that the microbial carbon pump is an effective mechanism of deep DOC removal and also of generation of recalcitrant molecules such as humic-like components (Campanero et al., 2022; Catalá et al., 2015; Jiao et al., 2010; Martínez-Pérez et al., 2019; Xiao et al., 2023), but seems to have a minor impact on the bulk δ^{13}C-DOC. The multiple linear regression model of ^{13}C-DOC concentration and water mass proportions (X_{ij}) explained 70% of the total variability, indicating that water mass mixing at basin scale was the main process controlling the isotopic variability in the meso- and bathypelagic waters of the CVFZ. Moreover, when adding AOU to the model with the aim to observe the local processes independent of the water mass mixing, no increase in the explained variability nor a significant β coefficient were observed, showing that local processes did not play a relevant role affecting the isotopic carbon signature of DOC. A likely reason for this observation is that the residence time of the water in the FLUXES I box was calculated in 60 days (Burgoa et al., 2021), precluding the observation of significant local processes. The multiple correlation of ^{13}C-DOC with X_{ij} and optical properties showed positive correlation with protein-like substances (peak T) and negative correlation with humic-like substances (C2), showing again that labile compounds contained heavier δ^{13}C values than refractory DOC. The lack of isotopically heavier labile compounds in the dark ocean due to its rapid degradation, leaves an isotopically depleted bulk δ^{13}C-DOC, where the primary carbon source of the individual DOC constituents reflects the isotopic bulk signature.

Similar to FLUXES I, the mesopelagic layer of FLUXES II was characterized by a slight depletion in δ^{13}C-DOC of about 1‰ from the central to the intermediate and deep water masses (Table 5.4). δ^{13}C-DOC water masses archetype values of FLUXES II resulted depleted of about 0.5‰ when comparing with the same water masses archetype values of FLUXES I (Fig 5.5). Some arguments that could explain the observed differences are related with seasonality, sampling resolution or even a methodological shift. Regarding seasonality, the two cruises were conducted during different seasons of the year (summer and fall) and changes in some biogeochemical processes like intensity of the upwelling or

atmospheric inputs of Sahara dust could affect the isotopic deviation. Upwelling is present all year round as well as Saharan dust events, though higher upwelling intensity could be occurring during fall (Arístegui et al., 2009) and events of Sahara dust deposition are intensified during summer (Kumar et al., 2018). On the other hand, sampling location and resolution of the two cruises was different, involving changes in DOC properties and biogeochemical processes that could affect the isotopic composition. Finally, a least likely but not excluding possibility could be related with an artificial deviation during the isotopic analysis considering the huge amount of samples and the several months that it took to be analyzed. The methodology is far to be routinely, with many aspects that affect the results including changes of reagents, chemical traps, carrier gases, undetected leaks and changes in the blanks, among others.

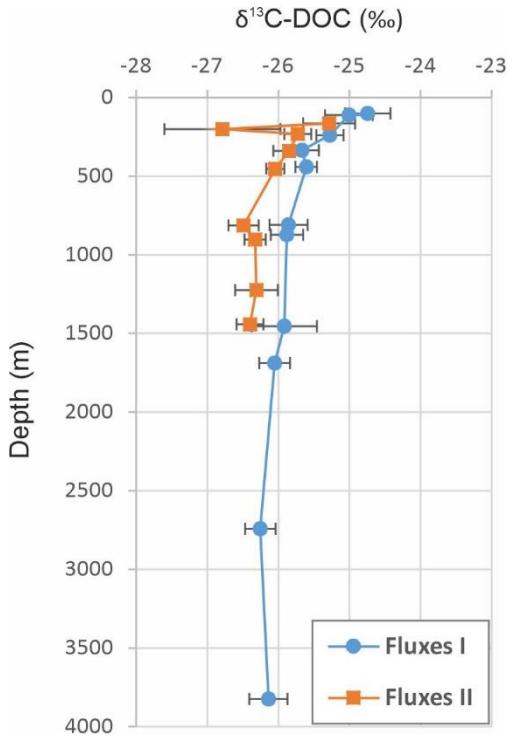

Figure 5.5. Archetype values of δ^{13}C-DOC (‰) for all the water masses sampled during FLUXES I (blue circles) and FLUXES II (orange squares). Note that during the FLUXES II cruise, the maximum sampling depth was set at 1500 m.

During the FLUXES II cruise, water mass mixing explained 37% of the total variability, contrasting with 70% that was found in FLUXES I. When adding AOU to the model, no increase in the explained variability was found and the β coefficient was not significant. A likely reason for this low percentage compared to the FLUXES I cruise is probably due to the sampling resolution, in such a way that the covered area during the FLUXES II cruise was not large enough to capture a significant imprint in the basin scale properties. The

multiple correlation of ^{13}C-DOC with X_{ij} and optical properties showed not significant relationships probably due to the the lower spatial coverage of this cruise.

4.3 Comparison of the results with previous studies

When comparing our results with other studies of δ^{13}C-DOC, we found some differences in the bulk carbon isotopic signatures and a wider δ^{13}C range in our study sampling site. Previous studies reported a small δ^{13}C range of marine total DOC, ranging from -20 to -24‰ and covering contrasting oceanic areas. The Pacific Ocean have been thoroughly studied at some representative sampling points as the Central North Pacific (Broek et al., 2020; Druffel et al., 2019, 1992; Follett et al., 2014; Zigah et al., 2017), Western North Pacific (Ding et al., 2020; Lee et al., 2020; Tanaka et al., 2010) and Eastern North Pacific (Bauer et al., 1998b; Beaupré et al., 2007; Lang et al., 2007; Williams and Gordon, 1970). Other places were also studied such as the Arctic Ocean (Griffith et al., 2012), the North Atlantic Ocean (Broek et al., 2020; Druffel et al., 1992; Esposito et al., 2019; Loh et al., 2004) and the Gulf of Mexico (Walker et al., 2017). Table 5.6 shows a compilation of the main studies reporting δ^{13}C-DOC up to date in marine waters, classified by oceanic region. Nevertheless, our δ^{13}C-DOC observations are consistent with a photosynthetic origin of C3 plants, which usually ranges from -22 to -31‰ (Farquhar et al., 1982; Tcherkez et al., 2006; Young et al., 2013) and are also consistent with the fact that most of phytoplankton uses this metabolic pathway (Descolas-Gros and Fontugne, 1985; O'Leary, 1981). Moreover, both aqueous CO_2 and HCO_3^- carbon species presenting a δ^{13}C difference of about 9‰ (Mook et al., 1974) are assimilated by photosynthetic organisms (Burkhardt et al., 1999; Degens et al., 1968a; Keller and Morel, 1999; Laws et al., 1997; Popp et al., 1998), leading to a wide DOC isotopic range. The high variety in environmental features in the CVFZ could be the likely reasons explaining those differences with previous studies and the wider isotopic range. The CVFZ is one of the most productive waters in the Earth with hugh amounts of labile DOC, contrasintg with the more aged intermediate and deep waters, containing less DOC and with more recalcitrant nature. Moreover, atmospheric inputs of Sahara dust may have a relevant role in the isotopic values. Another reason that could explain partly the differences is related with methodology practices. Our δ^{13}C values correspond to total organic carbon, i. e. DOC + POC, since water was not filtered to separate the particulate fraction and therefore, a proportion of POC is present in the analyses that could shift the DOC isotopic signatures to depleted values (Eadie et al., 1978).

Table 5.6. Carbon isotopic signatures of total DOC in marine environment. UVO: ultraviolet oxidation; HTCO: high temperature catalytic oxidation; WCO: wet chemical oxidation; IRMS: isotope ratio mass spectrometer.

Region	Method	Depth (m)	δ^{13}C (‰)	Reference
Eastern North Pacific	UVO-IRMS	1900	-22.5	Williams et al. (1969)
Eastern North Pacific	UVO-IRMS	0 to 2940	-24.4 to -21.2	Williams and Gordon (1970)
Eastern North Pacific	UVO-IRMS	25 to 4100	-22.4 to -20.3	Bauer et al. (1998a)
Eastern North Pacific	UVO-IRMS	22 to 4097	-22.4 to -21.1	Bauer et al. (1998b)
Eastern North Pacific	HTCO-IRMS	25 to 700	-20.3 to -19.5	Lang et al. (2007)
Eastern North Pacific	UVO-IRMS	20	-23.0 to -20.9	Beaupré et al. (2007)
Central North Pacific	UVO-IRMS	3 to 5720	-22.3 to -20.4	Druffel et al. (1992)
Central North Pacific	HTCO-IRMS	20 to 1800	-21.2 to -20.8	Loh et al. (2004)
Central North Pacific	UVO-IRMS	21 to 915	-23.2 to -20.4	Walker et al. (2011)
Central North Pacific	UVO-IRMS	50 to 2000	-23.4 to -21.6	Follet et al. (2014)
Central North Pacific	UVO-IRMS	0 to 4500	-24.9 to -20.8	Zigah et al. (2017)
Central North Pacific	UVO-IRMS	7.5 to 2500	-22.7 to -20.8	Broek et al. (2017)
Central Pacific (15ºS to 55ºN)	UVO-IRMS	0 to 4900	-22.7 to -20.3	Druffel et al. (2019)
Western North Pacific	HTCO-IRMS	0 to 3500	-21.7 to -20.4	Kim et al. (2015)
Western North Pacific	UVO-IRMS	0 to 4000	-23.5 to -20.5	Ding et al. (2020)
Western North Pacific	UVO-IRMS	10 to 4900	-23.6 to -21.8	Tanaka et al. (2010)
Western North Pacific	HTCO-IRMS	0 to 900	-26.9 to -18.3	Zhang et al. (2019)
Western North Pacific	HTCO-IRMS	Surface	-23.3 to -20.6	Lee et al. (2020)
Sargasso Sea	HTCO-IRMS	3 to 1500	-21.3 to -20.8	Loh et al. (2004)
Sargasso Sea	HTCO-IRMS	2600	-23.5 to -20.3	Lang et al. (2007)
Sargasso Sea	HTCO-IRMS	2600	-21.4 (± 0.3)	Panetta et al. (2008)
Sargasso Sea	WCO-IRMS	2600	-19.5 (± 0.4)	Bouillon et al. (2006)
Sargasso Sea	UVO-IRMS	3 to 4454	-21.8 to -20.2	Druffel et al. (1992)
Florida Strait	HTCO-IRMS	700	-23.2 (± 0.1)	Kirkels et al.(2014)
Florida Strait	HTCO-IRMS	700	-21.5 (± 0.1)	Lee and Kim (2018)
Mid Atlantic Bight	WCO-IRMS	2 to 90	-23.4 to -22.8	Osburn and St. Jean (2007)
Eastern North Atlantic	HTCO-IRMS	< 15	-23.6 to -21.9	Esposito et al. (2019)
Eastern North Atlantic	WCO-IRMS	5 to 4065	-29.4 to -21.3	Campanero et al. (2023)
Central North Atlantic	UVO-IRMS	7.5 to 2500	-22.7 to -21.9	Broek et al. (2020)
Caribbean	HTCO-IRMS	30 to 1430	-22.2 to -22.1	Jeffrey (1969)
North Atlantic	HTCO-IRMS	40 to 1866	-23.1 to -22.2	Jeffrey (1969)
St. Lawrence Estuary	HTCO-IRMS	Surface	-23.5 to -20.9	Lalonde et al. (2014)
St. Lawrence Estuary	HTCO-IRMS	0 to 300	-23.5 to -20.0	Barber et al. (2017)
Canada basin, Arctic	UVO-IRMS	5 to 3807	-24.4 to -21.4	Griffith et al. (2012)
Gulf of Mexico	UVO-IRMS	0 to 2000	-22.1 to -20.7	Walker et al. (2017)
Gulf of Mexico	WCO-IRMS	0 to 3600	-24.2 to -19.6	Jeffrey (1969)
South Pacific	WCO-IRMS	0 to 2700	-25.5 to -19.9	Eadie et al (1978)
Southern Ocean	WCO-IRMS	o to 550	-24.2 to -20.8	Eadie et al (1978)
Southern Ocean	UVO-IRMS	3 to 5440	-22.7 to -21.3	Druffel and Bauer (2000)

This proportion is as much as 14.7% in the filament domain above the pycnocline and a minimum of 3.5% in the Subtropical domain below the pycnocline in the FLUXES I cruise, revealing that POC influence could be affecting in some degree to the DOC isotopic deviation.

In addition, total δ^{13}C-DOC is composed by more than one source apart from primary production (Follett et al., 2014 and references therein). Terrestrial inputs and/or hydrothermal fluids with depleted δ^{13}C values are presumably additional sources in the DOC pool, for example black carbon and other terrestrial refractory plant-derived compounds as lignins, tannins, cutins, etc. (Zhang et al., 2019; Zigah et al., 2017). In the NW Africa, the influence of the Sahara desert plays an important role in the adjacent ocean, where atmospheric dust plumes has a major impact on the ocean biogeochemistry affecting oceanic carbon uptake, phytoplankton growth and primary production (Eglinton et al., 2002; Gelado-Caballero, 2015; Kumar et al., 2018). Complementary results reported in chapters 2 and 3 of this thesis dissertation corroborates the presence of terrestrial-derived materials in the water column of the CVFZ from the fluorescent dissolved organic matter (FDOM) observations, presenting the hypothesis that atmospheric deposition could be responsible of a higher band of FDOM established at the pycnocline (Campanero et al., 2022). All these particular features that are present in the CVFZ could be the likely reasons behind the broader δ^{13}C-DOC range observed when comparing with previous studies in other areas. Nevertheless, additional data such as δ^{13}C compound-specific analysis of DOC or different DOC fractions should be necessary to decipher more precisely the different carbon sources that comprises the DOC pool in the CVFZ.

5. Conclusions

δ^{13}C-DOC in epipelagic waters was controlled by DOC composition and primary production. Recently produced DOC showed heavier isotopic signatures due to the higher concentration of labile compounds like carbohydrates and proteins. Filament waters presented the highest δ^{13}C, where fresh organic matter is produced by the upwelling of cold nutrient-rich waters that are exported offshore by the CBGF. The CVF, that separates waters from the North and South Atlantic, also influenced the δ^{13}C-DOC composition. Subtropical waters North of the CVF contained the lowest δ^{13}C values, indicating a lower presence of labile compounds and on the contrary, tropical waters South of the CVF showed higher δ^{13}C values due to a higher presence of inorganic nutrients that led to higher primary

production. DOC isotopic signatures decreased with depth, linked to a selectively consumption of the isotopically heavier labile components in the upper layers of the ocean. In the meso- and bathypelagic layers, a slight decrease in the isotopic deviation occurred from the central to the deep waters showing the recalcitrant nature of DOC in the dark ocean. Moreover, the low correlation with AOU indicated that local processes of mineralization did not affect significantly to the isotopic composition of DOC. The negative correlation between ^{13}C-DOC and humic-like substances corroborates that this kind of recalcitrant molecules contain depleted δ^{13}C values. The δ^{13}C-DOC range of about 8‰ between surface and deep waters resembles the high biogeochemical variability in the CVFZ and the contrasting carbon sources with different isotopic fractionation that comprises the DOC pool. A hypothesis is that apart from primary production, a significant fraction of DOC in the CVFZ may be originating from other sources with depleted δ^{13}C values that decreased the isotopic signature of total DOC composition, probably related with terrestrial inputs from atmospheric deposition of Sahara dust or river discharge. Further research is necessary to corroborate this hypothesis by analyzing different DOC fractions separately since the total DOC analysis produce overlaps in δ^{13}C between the different carbon sources.

Chapter 6: General discussion

This chapter deals with the discussion of several items that have not been covered in detail in the individual chapters. Moreover, they are transversal and may include more than one chapter of this dissertation. First of all, section 1 is a summary that encompasses the main results obtained from this thesis and the links between the different chapters. Section 2 presents the differences between the large-scale, meso- and submeso-scale sampling strategies, and the different oceanographic structures and processes covered during FLUXES I and II. Section 3 refers to the main advantages and drawbacks of using either selected fluorescence peaks or PARAFAC components. Sections 4 and 5 include the analytical challenges of the methodology for obtaining the isotopic analysis of DOC in seawater samples, the comparison with other methodologies, the information extracted and limitations that presents. Section 6 deals with the relationship between δ^{13}C-DOC and the optical properties of DOM to evaluate whether they are complementary in the interpretation of results. Finally, in section 7, future research directions in the field are suggested.

1. General overview

The CVFZ is a singular place where a variety of processes and structures act at different spatial and temporal scales **(**Fig 6.1**)**. The area is acting as a buffering zone, connecting the productive coastal waters with the adjacent oligotrophic ocean and exporting organic material from the coast to offshore. The epipelagic waters are influenced by the presence of the CVF on the one hand and by the CBGF on the other hand. Mesoscale structures like eddies, fronts and meanders define the variability of DOM, POM, CDOM and FDOM. Moreover, atmospheric inputs of Sahara dust affect to the distribution, by entering terrestrial-derived organic matter that was observed in a band of high FDOM established below the pycnocline. In the meso- and bathypelagic waters, the distribution of DOM, POM, CDOM and FDOM is explained mainly by large-scale water mass mixing and mineralization processes, however, local processes also affected the distribution to a lesser extent. DOC and suspended POC contributed in 3.6 ± 2.1% and 4.5 ± 0.7% to the local oxygen demand, respectively. $a_{CDOM}254$, $a_{CDOM}325$ and the humic-like substances (FDOM components C1 and C2 and FDOM peak M) was generated in the dark ocean of the CVFZ by the microbial carbon pump mechanism. On the contrary, protein-like substances (FDOM component C4) were degraded locally in the meso- and bathypelagic waters due to its labile nature. DOC distribution showed the presence of vertical chimney-like structures, established from surface to deep waters and related probably with processes of adsorption/desorption onto particles both allochthonous (e.g. lithogenic particles from

Sahara dust) or autochthonous (e.g. biogenic particles). These columns are hypothesized to be transporting and therefore sequestering organic carbon from surface to deep waters, enhancing the biological carbon pump process.

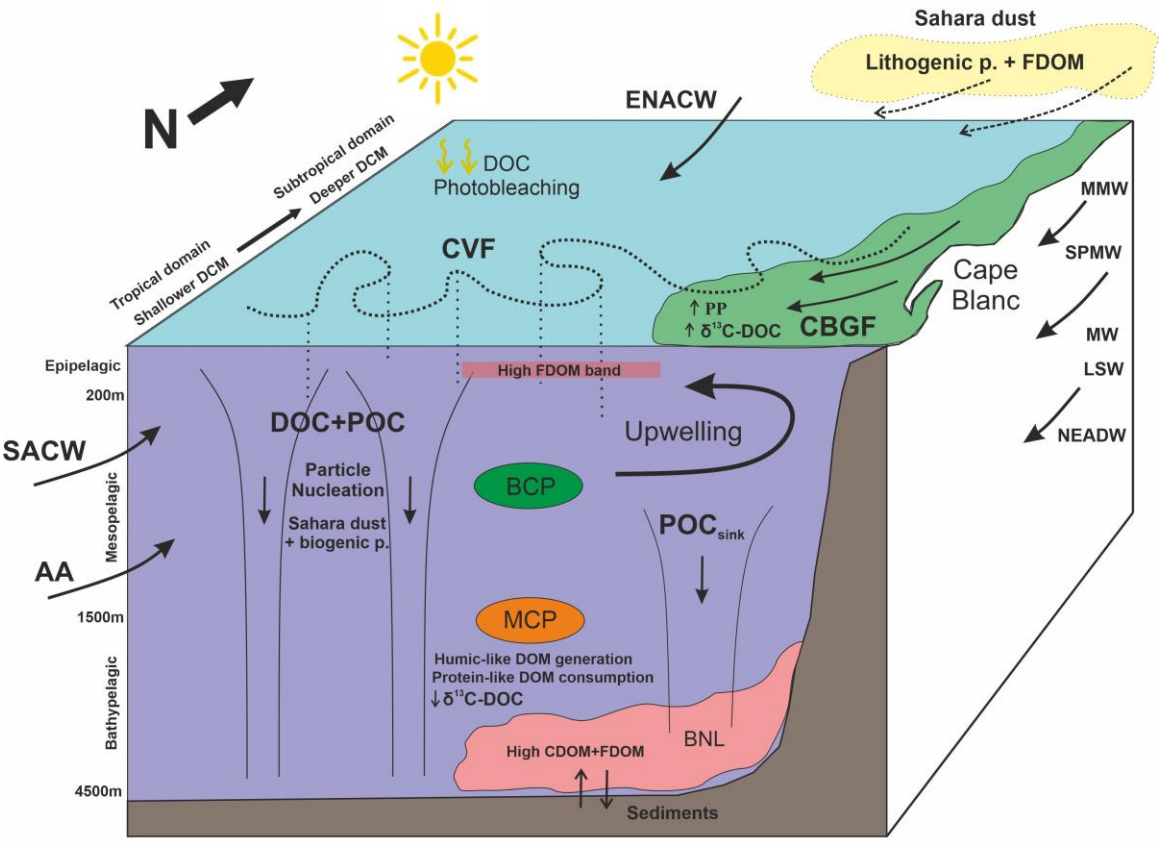

Figure 6.1. Conceptual model showing the main biogeochemical features analyzed in this thesis dissertation. ENACW, Eastern North Atlantic Central Water; SACW, South Atlantic Central Water; MMW, Madeira Mode Water; SPMW, Subpolar Mode Water; AA, Antarctic Intermediate Water; MW, Mediterranean Water; LSW, Labrador Sea Water; NEADW, North East Atlantic Deep Water; CVF, Cape Verde Front; CBGF, Cape Blanc Giant Filament; PP, primary production; DCM, deep chlorophyll maximum; BCP, biological carbon pump; MCP, microbial carbon pump; BNL, bottom nepheloid layer; p., particles; vertical dotted lines represent the depth extension of the CVF down to 600 m. The depth indication is not linear.

Additionally, a column of higher particle density present in the coastal waters also connecting the surface with the deep led to a well-developed BNL extending along the continental slope. CDOM and FDOM showed an increase associated to this BNL and not accompanied by an increase in AOU, suggesting either dissolution of DOM from the sinking particles or resuspension processes of DOM released from the anoxic sediments. Finally, the isotopic analysis of DOC showed a high $\delta^{13}C$ range (from -29.4 to -21.3‰) resembled the high variability in the CVFZ, one of the most productive regions on Earth. Results corroborated that the fresher organic matter with enriched $\delta^{13}C$ values was

originated in the surface coastal and filament affected-waters, and immediately below the surface mixed layer, the more labile fraction of DOC was degraded. In mesopelagic waters, a very slight depletion in δ^{13}C-DOC with depth suggested selectively consumption of the more ^{13}C enriched components whereas no differences were observed in the bathypelagic waters, revealing the refractory nature of the dark ocean DOC pool.

2. Large-scale vs. meso- and submeso-scale sampling strategies

Ocean processes occur at different spatial and temporal scales, from millimeters to kilometers and from seconds to millennia. There is not an exact distinction between different scales since natural processes cover a continuum of both time and space (Fig. 6.2), but the scientific community established a classification of processes following the next spatio-temporal parameters:

- Large-scale: > 100 km, months to years.
- Meso-scale: 10-100 km, days to months.
- Submeso-scale: 0.1-10 km, few days.

Depending on the processes focus of study, a sampling strategy must be chosen to properly cover the spatial and temporal resolution of interest. In the FLUXES Project, the possibility of perform two oceanographic cruises gave us the opportunity to complement a wide spectrum of sampling resolution from the large-scale in the FLUXES I cruise to the submeso-scale in the FLUXES II cruise.

The large-scale sampling in the FLUXES I cruise (Chapter 2) with hydrographic stations separated 50 nautical miles captured differences between waters North and South the CVF and waters affected by the CBGF. The transition from the coastal productive waters to the open ocean oligotrophic waters was also observed. Sampling in the mesopelagic and bathypelagic waters at a large scale allowed observations of basin-scale circulation and water mass mixing processes. Moreover, local processes of organic matter mineralization were better traced through dissolved and suspended organic carbon consumption and humic-like substances production during large-scale sampling due to the wider area covered. A wider area implies a longer residence time of each water mass and, therefore, the possibility of observing a higher signal of biogeochemical processes.

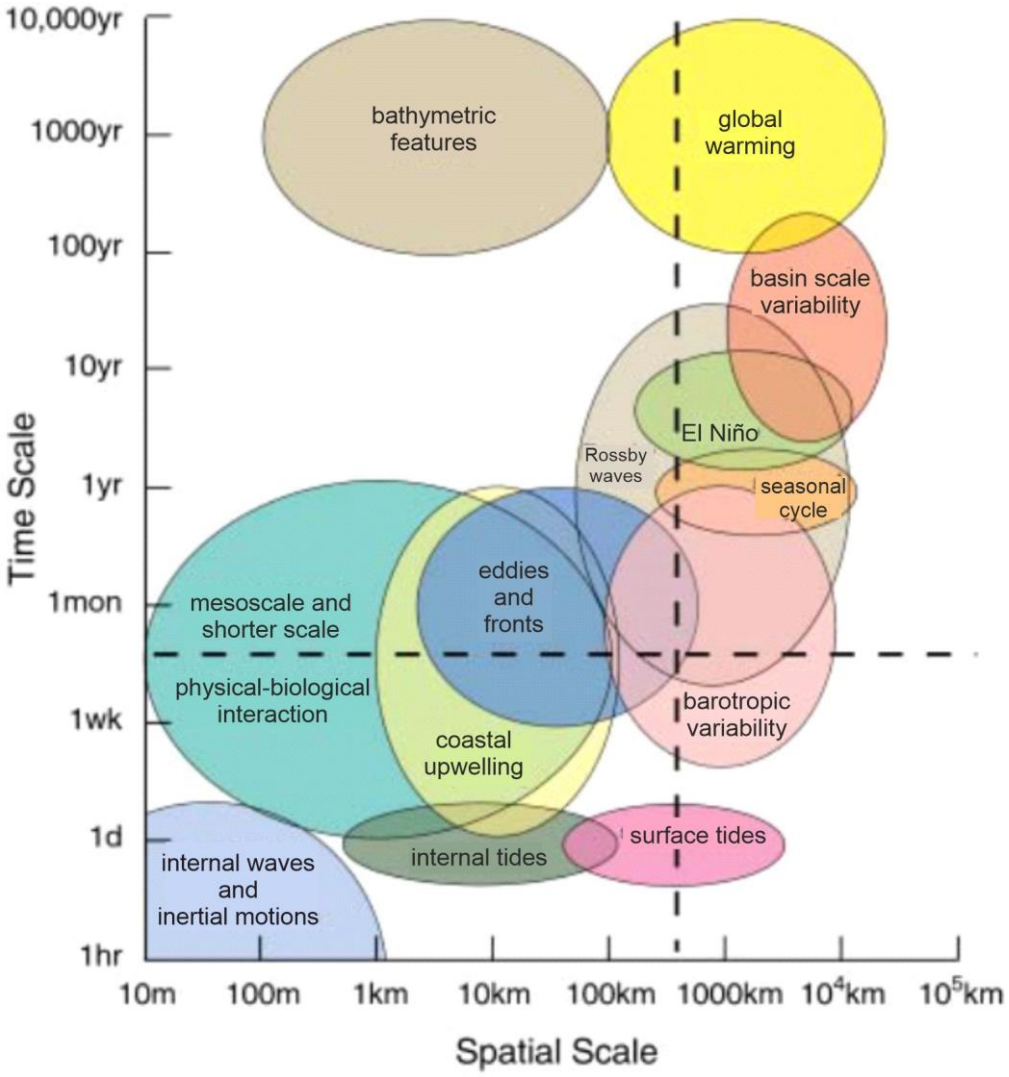

Figure 6.2. Scheme of the main spatio-temporal oceanographic processes and phenomena. Taken from Chelton (2001).

On the other hand, meso- and submeso-scale samplings allowed capturing smaller-scale processes, structures and distributions that are not possible to observe in large-scale sampling strategies. In the study site of the CVFZ and during the FLUXES II cruise (Chapter 3), we had particular interest in observing the meso- and sub-mesoscale variability of the CVF associated processes of mixing between the North and South Atlantic waters, mesoscale structures such as meanders and eddies and the impact that it had in the biogeochemical properties. In submeso-scale sampling, time is an important issue since submeso-scale processes occur in periods of few days. Therefore, it requires faster samplings trying to obtain synoptic observations of the processes and structures in the delimited study area. For instance, the coupling between the physical and biogeochemical properties during FLUXES II was determined by a Seasoar transect followed by a

biogeochemical transect that was carried out few days later. During those days, changes in the physical properties and biogeochemical distribution occurred, as was determined and explained in Chapter 3. Same mismatch occurred between the biogeochemical transects 1 and 2.

Contrary to the large-scale, only mesopelagic waters were sampled during the FLUXES II cruise in an attempt to cover faster the biogeochemical transect, but losing the bathypelagic waters. Nevertheless, the second cruise was focused primarily in the upper layers, where meso- and submeso-scale processes play an important role in the biogeochemical distribution.

3. Differences in using selected fluorescence peaks and PARAFAC components

The use of fluorescence peaks at selected wavelengths constituted the first attempts to characterize DOM, consisting on a quantitative procedure of peak intensity recording within a pre-defined region of interest (Coble, 1996). A decade later, the parallel factor analysis (PARAFAC) developed by Stedmon & Bro (2008) allowed to decompose the excitation/emission matrices (EEMs) into individual components. Some advantages and drawbacks characterize both approaches that are detailed below.

In this thesis, both classical selected peaks and PARAFAC components were used to characterize the fluorescence properties of DOM. Components were employed in the FLUXES I cruise (Chapter 2) and specific peaks in the FLUXES II cruise (Chapter 3). The ultimate reason of using different approaches was due to the time constrains of the high-resolution sampling during the occupation of the biogeochemical transects in FLUXES II, which hindered recording of EEMs.

Fluorescence peaks at selected wavelengths present the main advantage of being less time consuming and permits repeated fluorescence measurements of each peak without expending too much time. Moreover, lower exposure of the samples to UV radiation prevents photodegradation. On the contrary, this technique presents the main disadvantage of overlapping between the Ex/Em intensities of different fluorophores, particularly peaks C and M.

On the other hand, PARAFAC analysis allows to decompose each sample into individual and independent fluorophores, solving the overlapping phenomenon occurring when

measuring at fixed peaks. Furthermore, it is therefore an excellent tool for finding new fluorophores.

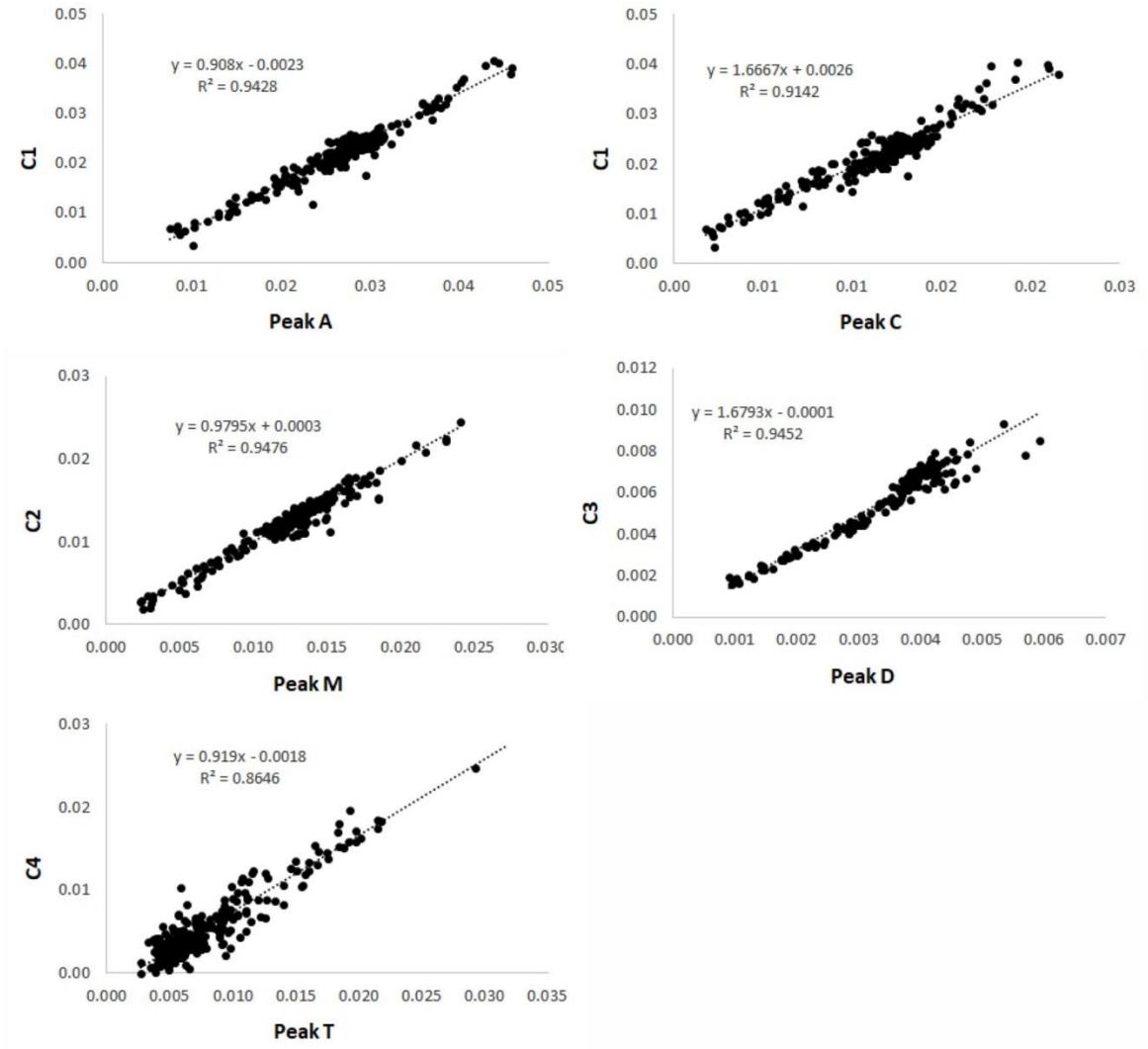

Figure 6.2. Correlation between PARAFAC components C1, C2 and C4 and the selected peaks A, C, M and T. Note that C1 is a sum of peaks A and C. Peaks B and D were not measured during the FLUXES cruises. Fluorescence intensities in Raman Units (RU).

PARAFAC components and specific peaks were very well correlated (Fig 6.3). Five components were identified during the FLUXES I cruise, being C1, C2, C4 and C5 similar to Coble's (1996) peaks A + C, peak M, peak T and peak B, respectively. C3 is similar to Stedmon's et al. (2003) peak D. The main disadvantage of the PARAFAC model is the comparison with other studies, where fluorescence spectra between the same components sometimes do not overlap exactly. In order to facilitate comparisons between PARAFAC models, the online database Openfluor was created (openfluor.lablicate.com; Murphy et al. (2014)), allowing the comparison with equivalent components include in the database.

4. Analytical challenges of δ^{13}C-DOC analysis and comparison with other methodologies

Since the first δ^{13}C-DOC measurements carried out in the late 1960's, not many studies have been reported isotopic data of bulk δ^{13}C-DOC in open ocean waters (see Table 5.6) due to the complexity of these analytical methods. Several methodologies have been developed in the last decades differing in the manner of oxidize DOC to CO_2. In this thesis, the DOC oxidation by persulfate, also named the wet oxidation (WCO-IRMS) technique was employed. A detailed description is presented in Chapter 4. The main advantages of this method are: 1) the high sample volumes allowed in the digestion vessel, which are necessary due to the low DOC concentration in seawater, and 2) the analysis performance, optimized to around 30 minutes per analysis. In studies with high amounts of samples as in the case of the FLUXES project, analysis efficiency in terms of time is essential. On the contrary, this method presents disadvantages, some of them are exclusive of this method and others are common to all the methodologies. The main drawbacks are: 1) is not appropriate for low volume samples; 2) the use of reagents, particularly the sodium persulfate produce significant corrosion in the line; 3) reagents need regular replacement; 4) halides formed during the oxidation reaction produce recurrent clogging in the copper trap; 5) the salt matrix of seawater compete for the persulfate reducing the oxidation efficiency; and 6) present relatively high blanks compared to the low carbon content of the sample (Osburn & St-Jean, 2007).

Nevertheless, the two other commonly employed methodologies also present advantages and disadvantages. For example, the HTO-IRMS technique performs high oxidation efficiency, but also presents high blanks and high maintenance of reagents (Lalonde et al., 2014). Moreover, it is designed to low volume sample injections, which could be challenging in low DOC samples when trying to concentrate sufficient CO_2. On the other hand, the UVO-IRMS technique present the lower blanks but requires several hours per sample to obtain a complete DOC oxidation (Beaupré et al., 2007; Follett et al., 2014).

5. Information extracted from the total δ^{13}C-DOC and limitations

It is well known that DOC is formed by an immense variety of different compounds, with different molecular composition, ages and reactivities (Hansell, 2013). Therefore, the bulk isotopic composition of DOC reflects an average of all the isotopic ratios of the DOC constituents (Beaupré, 2015). Since the major fraction of DOC is produced in the upper

layers of the ocean, its $\delta^{13}C$ would show mainly the isotopic composition of marine phytoplankton. However, marine phytoplankton shows a wide range of carbon fractionation (-31 to -18‰; Sharp, 2017), depending on several environmental factors and diversity of planktonic communities (Burkhardt et al., 1999; Laws et al., 1997; Rau et al., 1992). Moreover, additional carbon sources may be present in the DOC pool originating by terrestrial inputs or hydrothermal fluids (see Chapter 5) containing also a wide range of $\delta^{13}C$ values that can overlap in some degree the autochthonous DOC. So, the isotopic composition of bulk DOC precludes the distinction between the carbon sources (if not accompanied by complementary analysis) due to a significant overlap in the individual $\delta^{13}C$ values of the DOC constituents.

Previous studies of $\delta^{13}C$-DOC in coastal and estuarine areas reported a clear distinction between autochthonous photosynthetic DOC and terrestrial derived DOC, in which marine DOC end-member range between -23 to -18‰ and terrestrial DOC between -30 to -25‰ (e.g., (Barber et al., 2017; Lee et al., 2020). In the particular case of the of the CVFZ, average $\delta^{13}C$-DOC values are established around -25‰, consistent with an organic matter carbon fractionation produced by photosynthesis via C3 metabolic pathway, but this result alone does not allow to isolate between the original carbon sources or establish the relative proportion of terrestrial derived DOC. Compound specific $\delta^{13}C$ analysis goes a step further in the isotopic characterization of DOC (Broek et al., 2020; Loh et al., 2004; Williams & Gordon, 1970; Zigah et al., 2017), but in the same way, the original carbon source of each DOC fraction or component may be overlapped between the signal of several origins.

6. Relation between optical and isotopic signatures of DOC. Are they complementary?

The wide $\delta^{13}C$-DOC range obtained in the CVFZ suggests that more than one carbon source must be present in the bulk DOC, but no clear distinction can be done with isotopic data alone. As in the case of $\delta^{13}C$-DOC, the optical properties of DOM, especially the FDOM fraction serves as a tracer for the origin of DOM. There are previous works that have related the $\delta^{13}C$-DOC with the optically active fraction of DOM as complementary techniques in order to discriminate different DOC sources (Lee & Kim, 2018; Lee et al., 2020; Lu et al., 2015; Osburn & Stedmon, 2011; Ya et al., 2015), although they were applied in coastal areas as bays and estuaries, where terrestrial inputs are much more evident than in open ocean waters.

Results obtained from the FDOM analysis showed that humic-like substances of terrestrial origin (C1 and/or peak C) are present in the CVFZ, either originating from the immediate surroundings or coming from other areas transported by the water masses. The hypothesis of humic-like substances originating from atmospheric inputs of Sahara dust is postulated due to the observed band of high FDOM concentration established in the subsurface waters during the FLUXES II cruise (see Chapter 3). Moreover, the high values of C1 in the eastern transect of FLUXES I are possibly linked with terrestrial inputs from the adjacent continent (see Chapter 2). One of the likely explanations for the observed bottom nepheloid layer with high C1 signal in this transect is the connection between the surface and deep waters through the sinking particles associated with lithogenic material with DOC/POC adsorbed that contained this terrestrially derived DOC.

The multiple regression model between ^{13}C-DOC and FDOM independent of the water mass mixing showed significant regressions in the meso- and bathypelagic waters for the humic-like (C2) and protein-like (C4) substances (see Chapter 5). C2 is related to humic-like substances of marine origin, corresponding to the peak M defined by Coble (1996). It presented a negative correlation with ^{13}C-DOC, suggesting therefore depleted δ^{13}C values of humic substances.

7. Future research

Despite the efforts in deciphering DOC and suspended cycling in the study area, some questions are still unresolved, related primarily with quantification of carbon fluxes and net budgets. How significant is the lateral export of dissolved and suspended organic matter? What is the rate of organic matter photochemical degradation? What is the net carbon balance between sources and sinks? To give an answer to these questions, organic carbon fluxes and budgets have to be calculated using the inverse box model developed by Burgoa et al. (2021) in combination with the DOC, POC, CDOM and FDOM profiles for the FLUXES I cruise, allowing the quantification of the different carbon fractions (dissolved, suspended and sinking) and their final contribution to the biological pump. The model of Burgoa et al. (2021) did not accounted for the eastern transect of the FLUXES I box, precluding the quantification of the rates in relation with the inputs/outputs from the coast to the open ocean. Thus, the addition of the eastern transect to the inverse model is needed to better quantify the balances of the biogeochemical properties.

Regarding the isotopic analysis of DOC, some questions are still of interest too: what are the main loss mechanisms of DOC and how do they affect to the isotopic ratios, and how significant are the allochthonous carbon sources to the DOC pool? In order to solve these questions, future research should be focus on: 1) improve the feasibility of DOC isotopic analysis, making it more routinely and efficient; 2) expand the spatio-temporal resolution of δ^{13}C-DOC globally; 3) determine more precisely and quantitatively the allochthonous carbon sources; 4) develop the combination of isotopic data with other analytical techniques (e.g. radiocarbon dating and molecular characterization); and 5) gain a better understanding in the DOC isotopic transformations once is exported to the dark ocean.

Chapter 7: Conclusions

1. The large-scale distributions of DOC, suspended POC, CDOM and FDOM in epipelagic waters of the CVFZ are controlled by the position of the CVF, the distance from the coast and the influence of the CBGF. Conversely, the high-resolution distribution shows the tight coupling between physical and biogeochemical parameters, with the presence of mesoscale structures such as meanders and eddies explaining the short-scale biogeochemical variability.
2. Atmospheric inputs of Sahara dust are a likely relevant source of terrestrial organic matter and lithogenic particles that favors particle nucleation of sinking POC in the CVFZ.
3. DOC in the meso- and bathypelagic waters formed vertically coherent chimney-like structures that are indicative of fast DOC transport to the deep ocean through processes of adsorption/desorption onto sinking particles.
4. The distributions of DOC, suspended POC and the optically active fraction of DOM in the meso- and bathypelagic waters is controlled primarily by large-scale mineralization processes and water mass mixing from their respective formation sites to the CVFZ.
5. Organic matter mineralization in the CVFZ is mainly supported by sinking POC, since a low contribution of DOC (3.6 ± 2.1%) and suspended POC (4.5 ± 0.7%) to the local oxygen demand was observed, likely explained by the low residence time of mesopelagic waters in the CVFZ.
6. CDOM and humic-like substances are produced locally in the mesopelagic and bathypelagic waters of the CVFZ, probably originating during the degradation of sinking POC. Release of terrestrial humic-like substances transported by Sahara dust cannot be discarded. Conversely, protein-like substances are consumed in the dark ocean due to their labile nature.
7. A connection between the surface and deep waters occurred in the Mauritanian ocean margin where a column of high particle density was observed, leading to a well-developed bottom nepheloid layer (BNL). An increment in the fluorescent DOM within this BNL could be related with dissolution processes from the sinking particles (influenced by Sahara dust lithogenic particles) and/or resuspension of DOM from the anoxic sediments.
8. The carbon isotopic composition of DOC (δ^{13}C-DOC) is dictated by the isotopic composition of its individual constituents, being enriched the more labile components and depleted the more recalcitrant. Local processes of DOC mineralization did not affect significantly the isotopic composition.
9. Significant correlation between the δ^{13}C-DOC and FDOM suggested enriched isotopic values for protein-like substances and depleted values for humic-like substances.

References

Abell, J., Emerson, S., Renaud, P., 2000. Distributions of TOP, TON and TOC in the North Pacific subtropical gyre: Implications for nutrient supply in the surface ocean and remineralization in the upper thermocline. J Mar Res 58, 203–222. https://doi.org/10.1357/002224000321511142

Aiken, G.R., 1992. Chloride Interference in the Analysis of Dissolved Organic Carbon by the Wet Oxidation Method. Environ Sci Technol 26, 2435–2439. https://doi.org/10.1021/es00036a015

Alonso-González, I.J., Arístegui, J., Vilas, J.C., Hernández-Guerra, A., 2009. Lateral POC transport and consumption in surface and deep waters of the Canary Current region: A box model study. Global Biogeochem Cycles 23. https://doi.org/10.1029/2008GB003185

Álvarez, M., Álvarez-Salgado, X.A., 2009. Chemical tracer transport in the eastern boundary current system of the North Atlantic. Ciencias marinas, 35(2), 123-139.

Álvarez-Salgado, X.A., Nieto-Cid, M., & Rossel, P. E., 2023. Dissolved Organic Matter. In J. Blasco & A. Tovar-Sánchez (Eds.), Mar Anal Chem (pp. 39–102). Springer, Cham. https://doi.org/10.1007/978-3-031-14486-8_2

Álvarez-Salgado, X.A., Álvarez, M., Brea, S., Mèmery, L., Messias, M.J., 2014. Mineralization of biogenic materials in the water masses of the South Atlantic Ocean. II: Stoichiometric ratios and mineralization rates. Prog Oceanogr 123, 24–37. https://doi.org/10.1016/J.POCEAN.2013.12.009

Álvarez-Salgado, X.A., Arístegui, J., 2015. Organic matter dynamics in the Canary Current, in: Valdés, L., Déniz-González, I. (Eds.), Oceanographic and Biological Features in the Canary Current Large Marine Ecosystem. IOC-UNESCO, Paris, pp. 151–159.

Álvarez-Salgado, X.A., Doval, M.D., Pérez, F.F., 1999. Dissolved organic matter in shelf waters off the Ría de Vigo (NW Iberian upwelling system). J Mar Syst 18, 383–394. https://doi.org/10.1016/S0924-7963(97)00114-0

Álvarez-Salgado, X.A., Nieto-Cid, M., Álvarez, M., Pérez, F.F., Morin, P., Mercier, H., 2013. New insights on the mineralization of dissolved organic matter in central, intermediate, and deep water masses of the northeast North Atlantic. Limnol Oceanogr 58, 681–696. https://doi.org/10.4319/LO.2013.58.2.0681

Amon, R. M. W., & Benner, R., 1996. Bacterial utilization of different size classes of dissolved organic matter. Limnol Oceanogr, 41(1), 41–51. https://doi.org/10.4319/LO.1996.41.1.0041

Anderson, L.A., 1995. On the hydrogen and oxygen content of marine phytoplankton. Deep Sea Research Part I: Oceanog Res Pap 42, 1675–1680. https://doi.org/10.1016/0967-0637(95)00072-E

Arístegui, J., Barton, E.D., Álvarez-Salgado, X.A., Santos, A.M.P., Figueiras, F.G., Kifani, S., Hernández-León, S., Mason, E., Machú, E., Demarcq, H., 2009. Sub-regional ecosystem variability in the Canary Current upwelling. Prog Oceanogr 83, 33–48. https://doi.org/10.1016/J.POCEAN.2009.07.031

Arístegui, J., Barton, E.D., Montero, M.F., García-Muñoz, M., Escánez, J., 2003. Organic carbon distribution and water column respiration in the NW Africa-Canaries Coastal Transition Zone. Aquat Microb Ecol 33, 289–301. https://doi.org/10.3354/AME033289

Arístegui, J., Duarte, C.M., Agustí, S., Doval, M., Álvarez-Salgado, X.A., Hansell, D.A., 2002. Dissolved organic carbon support of respiration in the dark ocean. Science (1979) 298, 1967. https://doi.org/10.1126/SCIENCE.1076746

Arístegui, J., Montero, M.F., Hernández-Hernández, N., Alonso-González, I.J., Baltar, F., Calleja, M.L., Duarte, C.M., 2020. Variability in Water-Column Respiration and Its Dependence on Organic Carbon Sources in the Canary Current Upwelling Region. Front Earth Sci (Lausanne) 8, 349. https://doi.org/10.3389/FEART.2020.00349/BIBTEX

Armstrong, R. A., Lee, C., Hedges, J. I., Honjo, S., & Wakeham, S. G. (2001). A new, mechanistic model for organic carbon fluxes in the ocean based on the quantitative association of POC with ballast minerals. Deep Sea Res Part II: Top Stud Oceanogr, 49(1–3), 219–236. https://doi.org/10.1016/S0967-0645(01)00101-1

Arrieta, J., Mayol, E., Hansman, R., Herndl, G., Dittmar, T., & Duarte, C., 2015. Dilution limits dissolved organic carbon utilization in the deep ocean. Science, 348(6232). https://doi.org/10.1126/science.1258955

Azam, F., Fenchel, T., Field, J. G., Gray, J. S., Meyer-Reil, L. A., & Thingstad, F., 1983. The Ecological Role of Water-Column Microbes in the Sea. In Marine Ecology - Progr Ser (Vol. 10, pp. 257–263). https://doi.org/https://doi.org/10.7208/chicago/9780226125534-024

Baker, A.R., Croot, P.L., 2010. Atmospheric and marine controls on aerosol iron solubility in seawater. Mar Chem 120, 4–13. https://doi.org/10.1016/J.MARCHEM.2008.09.003

Baltar, F., Alvarez-Salgado, X. A., Arístegui, J., Benner, R., Hansell, D. A., Herndl, G. J., & Lønborg, C., 2021. What Is Refractory Organic Matter in the Ocean? Front Mar Sci 8, 327. https://doi.org/10.3389/FMARS.2021.642637

Barber, A., Sirois, M., Chaillou, G., & Gélinas, Y., 2017. Stable isotope analysis of dissolved organic carbon in Canada's eastern coastal waters. Limnol Oceanogr, 62(S1), S71–S84. https://doi.org/10.1002/lno.10666

Barton, E.D., 1987. Meanders, eddies and intrusions in the thermohaline front off Northwest Africa. Oceanol, 10(No3), 267–283.

Barton, E.D., 1989. The Poleward Undercurrent On The Eastern Boundary Of The Subtropical North Atlantic. In Neshyba, S., Smith, R.L. & Mooers, C.N.K. (Eds.), Poleward flows along Eastern Ocean Boundaries (pp. 82–95). Springer Verlag. https://doi.org/10.1029/CE034P0082

Bauer, J.E., 2002. Carbon isotopic composition of DOM. In Hansell, D.A. & Carlson, C.A. (Eds.), Biogeochemistry of Dissolved Organic Matter (pp. 405–453). Academic Press.

Bauer, J. E., & Bianchi, T.S., 2011. Dissolved Organic Carbon Cycling and Transformation. In Wolanski, E. & McLusky D.S. (Eds.), Treatise on Estuarine and Coastal Science (Vol. 5, p. 67). Academic Press. https://doi.org/10.1016/B978-0-12-374711-2.00502-7

Bauer, J.E., Druffel, E.R.M., Williams, P.M., Wolgast, D.M., Griffin, S., 1998a. Temporal variability in dissolved organic carbon and radiocarbon in the eastern North Pacific Ocean. J Geophys Res Oceans 103, 2867–2881. https://doi.org/10.1029/97JC02545

Bauer, J.E., Druffel, E.R.M., Wolgast, D.M., Griffin, S., Masiello, C.A., 1998b. Distributions of dissolved organic and inorganic carbon and radiocarbon in the eastern North Pacific continental margin. Deep Sea Res 2 Top Stud Oceanogr 45, 689–713. https://doi.org/10.1016/S0967-0645(97)00098-2

Beaupré, S.R., & Druffel, E.R.M., 2009. Constraining the propagation of bomb-radiocarbon through the dissolved organic carbon (DOC) pool in the northeast Pacific Ocean. Deep Sea Res Part I: Oceanogr Res Pap 56(10), 1717–1726. https://doi.org/10.1016/J.DSR.2009.05.008

Beaupré, S.R., 2015. The Carbon Isotopic Composition of Marine DOC, In: Hansell, D. & Carlson, C. (Eds.). Biogeochemistry of Marine Dissolved Organic Matter. Elsevier, pp. 335–368. https://doi.org/10.1016/B978-0-12-405940-5.00006-6

Beaupré, S.R., Druffel, E.R.M., Griffin, S., 2007. A low-blank photochemical extraction system for concentration and isotopic analyses of marine dissolved organic carbon. Limnol Oceanogr Methods 5, 174–184. https://doi.org/10.4319/lom.2007.5.174

Behrenfeld, M.J., & Falkowski, P.G., 1997. Photosynthetic rates derived from satellite-based chlorophyll concentration. Limnol and Oceanogr 42(1), 1–20. https://doi.org/10.4319/LO.1997.42.1.0001

Benner, R., & Amon, R.M.W., 2015. The Size-Reactivity Continuum of Major Bioelements in the Ocean. Ann Rev Mar Sci 7(1), 185–205. https://doi.org/10.1146/annurev-marine-010213-135126

Berner, R.A., 2003. The long-term carbon cycle, fossil fuels and atmospheric composition. Nature 426, 323–326. https://doi.org/10.1038/nature02131

Biddanda, B., & Benner, R., 1997. Carbon, nitrogen, and carbohydrate fluxes during the production of particulate and dissolved organic matter by marine phytoplankton. Limnol and Oceanogr 42(3), 506–518. https://doi.org/10.4319/LO.1997.42.3.0506

Bograd, S.J., Jacox, M.G., Hazen, E. L., Lovecchio, E., Montes, I., Pozo Buil, M., Shannon, L.J., Sydeman, W.J., & Rykaczewski, R.R., 2023. Climate Change Impacts on Eastern Boundary Upwelling Systems. Ann Rev Mar Sci 15, 303–328. https://doi.org/10.1146/ANNUREV-MARINE-032122-021945

Boisséson, E. de, Thierry, V., Mercier, H., Caniaux, G., & Desbruyères, D., 2012. Origin, formation and variability of the Subpolar Mode Water located over the Reykjanes Ridge. J Geophys Res: Oceans, 117(C12). https://doi.org/10.1029/2011JC007519

Bory, A.M., Newton, P., 2000. Transport of airborne lithogenic material down through the water column in two contrasting regions of the eastern subtropical North Atlantic Ocean. Global Biogeochem Cycles 14, 297–315. https://doi.org/10.1029/1999GB900098

Bouillon, S., Korntheuer, M., Baeyens, W., Dehairs, F., 2006. A new automated setup for stable isotope analysis of dissolved organic carbon. Limnol Oceanogr Methods 4, 216–226. https://doi.org/10.4319/lom.2006.4.216

Boutton, T., 1991. Stable carbon isotope ratios in natural materials. II. Atmospheric, terrestrial, marine and freshwater environments. In Coleman, D. & Fry, B. (Eds.), Carbon Isotope Techniques (pp. 173–185).

Boyd, P.W., Claustre, H., Levy, M., Siegel, D.A., Weber, T., 2019. Multi-faceted particle pumps drive carbon sequestration in the ocean. Nature 568:7752 568, 327–335. https://doi.org/10.1038/s41586-019-1098-2

Brand, W.A., 2004. Mass Spectrometer Hardware for Analyzing Stable Isotope Ratios, in: Handbook of Stable Isotope Analytical Techniques. Elsevier Inc., pp. 835–856. https://doi.org/10.1016/B978-044451114-0/50040-5

Bricaud, A., & Morel, A., 1981. Absorption by dissolved organic matter of the sea (yellow substance) in the UV and visible domains. Limnol Oceanogr, 26, 43–53.

Bro, R., 1997. PARAFAC. Tutorial and applications. Chemometrics and Intelligent Laboratory Systems 38, 149–171. https://doi.org/10.1016/S0169-7439(97)00032-4

Broek, T.A.B., Walker, B.D., Guilderson, T.P., Vaughn, J.S., Mason, H.E., & McCarthy, M.D., 2020. Low Molecular Weight Dissolved Organic Carbon: Aging, Compositional Changes, and Selective Utilization During Global Ocean Circulation. Glob Biogeochem Cycles, 34(6). https://doi.org/10.1029/2020GB006547

Brzezinski, M.A., 1985. The Si:C:N Ratio of marine diatoms: Interspecific variability and the effect of some environmental variables. J Phycol 21, 347–357. https://doi.org/10.1111/J.0022-3646.1985.00347.X

Buck, K.N., Lohan, M.C., Berger, C.J.M., Bruland, K.W., 2007. Dissolved iron speciation in two distinct river plumes and an estuary: Implications for riverine iron supply. Limnol Oceanogr 52, 843–855. https://doi.org/10.4319/LO.2007.52.2.0843

Burdige, D.J., 2007. Preservation of organic matter in marine sediments: Controls, mechanisms, and an imbalance in sediment organic carbon budgets? Chem Rev, 107(2), 467–485. https://doi.org/https://doi.org/10.1021/cr050347q

Burgoa, N., 2022. From large to mesoscale dynamics in the Cape Verde Frontal Zone. Dissertation thesis, University of Las Palmas de Gran Canaria, Las Palmas de Gran Canaria (Spain).

Burgoa, N., Machín, F., Rodríguez-Santana, Á., Marrero-Diáz, Á., Álvarez-Salgado, X.A., Fernández-Castro, B., Gelado-Caballero, M.D., & Arístegui, J., 2021. Cape Verde Frontal Zone in summer 2017: Lateral transports of mass, dissolved oxygen and inorganic nutrients. Ocean Sci, 17(3), 769–788. https://doi.org/10.5194/OS-17-769-2021

Burkhardt, S., Riebesell, U., Zondervan, I., 1999. Effects of growth rate, CO2 concentration, and cell size on the stable carbon isotope fractionation in marine phytoplankton. Geochim Cosmochim Acta 63, 3729–3741. https://doi.org/10.1016/S0016-7037(99)00217-3

Calleja, M.L., Al-Otaibi, N., Morán, X.A.G., 2019. Dissolved organic carbon contribution to oxygen respiration in the central Red Sea. Sci Rep 9, 1–12. https://doi.org/10.1038/s41598-019-40753-w

Campanero, R., Burgoa, N., Fernández-Castro, B., Valiente, S., Nieto-Cid, M., Martínez-Pérez, A.M., Gelado-Caballero, M.D., Hernández-Hernández, N., Marrero-Díaz, Á., Machín, F., Rodríguez-Santana, Á., Hernández-García, I., Delgado-Huertas, A., Martínez-Marrero, A., Arístegui, J., Álvarez-Salgado, X.A., 2022. High-resolution variability of dissolved and suspended organic matter in the Cape Verde Frontal Zone. Front Mar Sci 9. https://doi.org/10.3389/FMARS.2022.1006432

Capet, X., McWilliams, J.C., Molemaker, M.J., Shchepetkin, A.F., 2008. Mesoscale to Submesoscale Transition in the California Current System. Part I: Flow Structure, Eddy Flux, and Observational Tests. J Phys Oceanogr 38, 29–43. https://doi.org/10.1175/2007JPO3671.1

Carlson, C.A., Hansell, D.A., 2015. DOM Sources, Sinks, Reactivity, and Budgets. In: Hansell, D. & Carlson, C. (Eds.). Biogeochemistry of Marine Dissolved Organic Matter: Second Edition 65–126. https://doi.org/10.1016/B978-0-12-405940-5.00003-0

Carlson, C.A., Hansell, D.A., Nelson, N.B., Siegel, D.A., Smethie, W.M., Khatiwala, S., Meyers, M.M., Halewood, E., 2010. Dissolved organic carbon export and subsequent remineralization in the mesopelagic and bathypelagic realms of the North Atlantic basin. Deep Sea Research Part II: Topical Studies in Oceanography 57, 1433–1445. https://doi.org/10.1016/J.DSR2.2010.02.013

Carr, M.E., 2001. Estimation of potential productivity in Eastern Boundary Currents using remote sensing. Deep Sea Res Part II: Top Stud Oceanogr, 49(1–3), 59–80. https://doi.org/10.1016/S0967-0645(01)00094-7

Catalá, T.S., Martínez-Pérez, A.M., Nieto-Cid, M., Álvarez, M., Otero, J., Emelianov, M., Reche, I., Arístegui, J., Álvarez-Salgado, X.A., 2018. Dissolved Organic Matter (DOM) in the open Mediterranean Sea. I. Basin–wide distribution and drivers of chromophoric DOM. Prog Oceanogr 165, 35–51. https://doi.org/10.1016/J.POCEAN.2018.05.002

Catalá, T.S., Reche, I., Álvarez, M., Khatiwala, S., Guallart, E.F., Benítez-Barrios, V.M., Fuentes-Lema, A., Romera-Castillo, C., Nieto-Cid, M., Pelejero, C., Fraile-Nuez, E., Ortega-Retuerta, E., Marrasé, C., Álvarez-Salgado, X.A., 2015a. Water mass age and aging driving chromophoric dissolved organic matter in the dark global ocean. Global Biogeochem Cycles 29, 917–934. https://doi.org/10.1002/2014GB005048

Catalá, T.S., Reche, I., Fuentes-Lema, A., Romera-Castillo, C., Nieto-Cid, M., Ortega-Retuerta, E., Calvo, E., Álvarez, M., Marrasé, C., Stedmon, C.A., Álvarez-Salgado, X.A., 2015b. Turnover time of fluorescent dissolved organic matter in the dark global ocean. Nat Commun 6, 1–9. https://doi.org/10.1038/ncomms6986

Catalá, T.S., Reche, I., Ramón, C.L., López-Sanz, À., Álvarez, M., Calvo, E., Álvarez-Salgado, X.A., 2016. Chromophoric signatures of microbial by-products in the dark ocean. Geophys Res Lett 43, 7639–7648. https://doi.org/10.1002/2016GL069878

Cauwet, G., 1981. Non-Living Particulate Matter. In Duursma, E. & Dawson, R. (Eds.), Marine Organic Chemistry (Vol. 31, Issue C, pp. 71–89). Elsevier. https://doi.org/10.1016/S0422-9894(08)70326-X

Chavez, F. P., & Messié, M., 2009. A comparison of Eastern Boundary Upwelling Ecosystems. Progr Oceanogr, 83(1–4), 80–96. https://doi.org/10.1016/J.POCEAN.2009.07.032

Chavez, F.P., Messié, M., Pennington, J.T., 2010. Marine Primary Production in Relation to Climate Variability and Change. AnnRev Mar Sci, 3, 227-260. https://doi.org/10.1146/annurev.marine.010908.163917 3, 227–260.

Chelton, D.B., 2001. Report of the High-Resolution Ocean Topography Science Working Group Meeting. College of Oceanic and Atmospheric Sciences, Oregon State University.

Chen, M., Kim, J.H., Nam, S. Il, Niessen, F., Hong, W.L., Kang, M.H., Hur, J., 2016. Production of fluorescent dissolved organic matter in Arctic Ocean sediments. Scientific Reports 2016 6:1 6, 1–10. https://doi.org/10.1038/srep39213

Ciais, P., Sabine, C., Bala, G., Bopp, L., Brovkin, V., Canadell, J., & et al., 2013. Carbon and Other Biogeochemical Cycles. In Stocker, T.F., Qin, D., Plattner, G.K., Tignor, M., Allen, S.K., Boschung, J., Nauels, A., Xia,, Y., Bex, V. & Midgley, P.M. (Eds.), Climate Change 2013: The Physical Science Basis. Contribution of Working Group I to the Fifth Assessment Report of the Intergovernmental Panel on Climate Change. Cambridge University Press. https://www.ipcc.ch/report/ar5/wg1/

Coble, P.G., 1996. Characterization of marine and terrestrial DOM in seawater using excitation-emission matrix spectroscopy. Mar Chem 51, 325–346. https://doi.org/10.1016/0304-4203(95)00062-3

Coble, P.G., 2007. Marine Optical Biogeochemistry: The Chemistry of Ocean Color. Chem Rev 107, 402–418. https://doi.org/10.1021/CR050350

Colman, B., & Rotatore, C., 1995. Photosynthetic inorganic carbon uptake and accumulation in two marine diatoms. Plant, Cell & Environ, 18(8), 919–924. https://doi.org/10.1111/J.1365-3040.1995.TB00601.X

Dahlén, J., Bertilsson, S., Pettersson, C., 1996. Effects of UV-A irradiation on dissolved organic matter in humic surface waters. Environ Int 22, 501–506. https://doi.org/10.1016/0160-4120(96)00038-4

De La Rocha, C., 2006. The Biological Pump. In H. Elderfield (Ed.), The Oceans and Marine Geochemistry (Vol. 6, pp. 83–112). Elsevier.

de Troyer, I., Bouillon, S., Barker, S., Perry, C., Coorevits, K., Merckx, R., 2010. Stable isotope analysis of dissolved organic carbon in soil solutions using a catalytic combustion total organic carbon analyzer-isotope ratio mass spectrometer with a cryofocusing interface. Rapid Communications in Mass Spectrometry 24, 365–374. https://doi.org/10.1002/rcm.4403

Degens, E.T., Guillard, R.R.L., Sackett, W.M., Hellebust, J.A., 1968a. Metabolic fractionation of carbon isotopes in marine plankton—I. Temperature and respiration experiments. Deep

Sea Research and Oceanographic Abstracts 15, 1–9. https://doi.org/10.1016/0011-7471(68)90024-7

Degens, E.T., Behrendt, M., Gotthardt, B., & Reppmann, E., 1968b. Metabolic fractionation of carbon isotopes in marine plankton—II. Data on samples collected off the coasts of Peru and Ecuador. Deep-Sea Res Oceanogr Abst 15(1), 11–20. https://doi.org/10.1016/0011-7471(68)90025-9

Del Giorgio, P.A., Duarte, C.M., 2002. Respiration in the open ocean. Nature 420, 379–384. https://doi.org/10.1038/nature01165

Del Vecchio, R., Blough, N. v., 2002. Photobleaching of chromophoric dissolved organic matter in natural waters: kinetics and modeling. Mar Chem 78, 231–253. https://doi.org/10.1016/S0304-4203(02)00036-1

Del Vecchio, R., Blough, N. V., 2004. On the origin of the optical properties of humic substances. Environ Sci Technol 38, 3885–3891. https://doi.org/https://doi.org/10.1021/es049912h

DeNiro, M.J., & Epstein, S., 1977. Mechanism of Carbon Isotope Fractionation Associated with Lipid Synthesis. Science, 197(4300), 261–263. https://doi.org/10.1126/SCIENCE.327543

Descolas-Gros, C., Fontugne, M.R., 1985. Carbon fixation in marine phytoplankton: carboxylase activities and stable carbon-isotope ratios; physiological and paleoclimatological aspects. Mar Biol 87, 1–6. https://doi.org/10.1007/BF00396999

Deuser, W.G., Degens, E.T., & Guillard, R.R.L., 1968. Carbon isotope relationships between plankton and sea water. Geochim Cosmochim Acta 32(6), 657–660. https://doi.org/10.1016/0016-7037(68)90055-0

Dickson, R.R., & Brown, J., 1994. The production of North Atlantic Deep Water: Sources, rates, and pathways. J Geophys Res Oceans 99(C6), 12319–12341. https://doi.org/10.1029/94JC00530

Ding, L., Qi, Y., Shan, S., Ge, T., Luo, C., Wang, X., 2020. Radiocarbon in Dissolved Organic and Inorganic Carbon of the South China Sea. J Geophys Res Oceans 125, e2020JC016073. https://doi.org/10.1029/2020JC016073

Dittmar, T., & Koch, B.P., 2006. Thermogenic organic matter dissolved in the abyssal ocean. Mar Chem 102(3–4), 208–217. https://doi.org/10.1016/J.MARCHEM.2006.04.003

Dittmar, T., & Paeng, J., 2009. A heat-induced molecular signature in marine dissolved organic matter. Nat Geosci 2009 2:3, 2(3), 175–179. https://doi.org/10.1038/ngeo440

Dittmar, T., 2015. Reasons Behind the Long-Term Stability of Dissolved Organic Matter, In: Hansell, D. & Carlson, C. (Eds.). Biogeochemistry of Marine Dissolved Organic Matter: Second Edition. Elsevier Inc., pp. 369–388. https://doi.org/10.1016/B978-0-12-405940-5.00007-8

Dittmar, T., De Rezende, C.E., Manecki, M., Niggemann, J., Coelho Ovalle, A.R., Stubbins, A., & Bernardes, M.C., 2012. Continuous flux of dissolved black carbon from a vanished

tropical forest biome. Nat Geosci 2012 5:9, 5(9), 618–622. https://doi.org/10.1038/ngeo1541

Doval, M.D., Álvarez-Salgado, X.A., Gasol, J.M., Lorenzo, L.M., Mirón, I., Figueiras, F.G., Pedrós-Alió, C., 2001. Dissolved and suspended organic carbon in the Atlantic sector of the Southern Ocean. Stock dynamics in upper ocean waters. Mar Ecol Prog Ser 223, 27–38. https://doi.org/10.3354/MEPS223027

Doval, M.D., Hansell, D.A., 2000. Organic carbon and apparent oxygen utilization in the western South Pacific and the central Indian Oceans. Mar Chem 68, 249–264. https://doi.org/10.1016/S0304-4203(99)00081-X

Druffel, E.R.M., Griffin, S., Wang, N., Garcia, N.G., McNichol, A.P., Key, R.M., Walker, B.D., 2019. Dissolved Organic Radiocarbon in the Central Pacific Ocean. Geophys Res Lett 46, 5396–5403. https://doi.org/10.1029/2019GL083149

Druffel, E.R.M., Williams, P.M., 1990. Identification of a deep marine source of particulate organic carbon using bomb 14C. Nature 347:6289 347, 172–174. https://doi.org/10.1038/347172a0

Druffel, E.R.M., Williams, P.M., Bauer, J.E., Ertel, J.R., 1992. Cycling of dissolved and particulate organic matter in the open ocean. J Geophys Res 97, 15639–15659. https://doi.org/10.1029/92jc01511

Duarte, C.M., Dachs, J., Llabrés, M., Alonso-Laita, P., Gasol, J.M., Tovar-Sánchez, A., Sañudo-Wilhemy, S., Agustí, S., 2006. Aerosol inputs enhance new production in the subtropical northeast Atlantic. J Geophys Res Biogeosci 111. https://doi.org/10.1029/2005JG000140

Ducklow, H.W., Purdie, D.A., Williams, P.J.L.B., & Davies, J.M., 1986. Bacterioplankton: A Sink for Carbon in a Coastal Marine Plankton Community. Science, 232(4752), 871–873. https://doi.org/10.1126/SCIENCE.232.4752.865

Ducklow, H.W., Quinby, H.L., & Carlson, C.A., 1995. Bacterioplankton dynamics in the equatorial Pacific during the 1992 El Niño. Deep Sea Res Part II: Top Stud Oceanogr 42(2–3), 621–638. https://doi.org/10.1016/0967-0645(95)00022-I

Ducklow, H., & McCallister, S., 2004. The biogeochemistry of carbon dioxide in the coastal oceans. In: Robinson, R., McCarthy, J. and Rothchild B.J. (Eds.). The sea (Vol. 13). Harvard, pp. 269-315.

Ducklow, H., Steinberg, D., Buesseler, K., 2001. Upper ocean carbon export and the biological pump. Oceanogr 14, 50–58.

Eadie, B.J., Jeffrey, L.M., Sackett, W.M., 1978. Some observations on the stable carbon isotope composition of dissolved and particulate organic carbon in the marine environment. Geochim cosmochim acta 42, 126–1269.

Eglinton, T.I., Eglinton, G., Dupont, L., Sholkovitz, E.R., Montluçon, D., Reddy, C.M., 2002. Composition, age, and provenance of organic matter in NW African dust over the Atlantic Ocean. Geochemistry, Geophysics, Geosystems 3, 1–27. https://doi.org/10.1029/2001GC000269

Eglinton, T.I., Repeta, D.J., 2004. Organic matter in the contemporary ocean, treatise on geochemistry, in: Turekian, K., Holland, H. (Eds.), Treatise on Geochemistry. Elsevier, Amsterdam, pp. 145–180.

Engel, A., Szlosek, J., Abramson, L., Liu, Z., & Lee, C., 2009. Investigating the effect of ballasting by CaCO3 in Emiliania huxleyi: I. Formation, settling velocities and physical properties of aggregates. Deep Sea Res Part II: Top Stud Oceanogr 56(18), 1396–1407. https://doi.org/10.1016/J.DSR2.2008.11.027

Engelhaupt, E., Bianchi, T.S., Wetzel, R.G., Tarr, M.A., 2003. Photochemical transformations and bacterial utilization of high-molecular-weight dissolved organic carbon in a southern Louisiana tidal stream (Bayou Trepagnier). Biogeochem 62, 39–58. https://doi.org/10.1023/A:1021176531598

Esposito, M., Achterberg, E.P., Bach, L.T., Connelly, D.P., Riebesell, U., Taucher, J., 2019. Application of Stable Carbon Isotopes in a Subtropical North Atlantic MesocosmStudy: A New Approach to Assess CO2 Effects on the Marine Carbon Cycle. Front Mar Sci 6. https://doi.org/10.3389/fmars.2019.00616

Farquhar, G.D., O'Leary, M.H., Berry, J.A., 1982. On the Relationship Between Carbon Isotope Discrimination and the Intercellular Carbon Dioxide Concentration in Leaves. Functional Plant Biology 9, 121–137. https://doi.org/10.1071/PP9820121

Fasham, M.J.R., Baliño, B.M., Bowles, M.C., Anderson, R., Archer, D., Bathmann, U., et al., 2001. A new vision of ocean biochemistry after a decade of the joint global ocean flux study (JGOFS). Ambio 30, 4–30.

Federherr, E., Cerli, C., Kirkels, F.M.S.A., Kalbitz, K., Kupka, H.J., Dunsbach, R., Lange, L., Schmidt, T.C., 2014. A novel high-temperature combustion based system for stable isotope analysis of dissolved organic carbon in aqueous samples. I: development and validation. Rapid Communications in Mass Spectrometry 28, 2559–2573. https://doi.org/10.1002/rcm.7052

Feely, R.A., Sabine, C.L., Lee, K., Berelson, W., Kleypas, J., Fabry, V. J., & Millero, F.J., 2004. Impact of anthropogenic CO2 on the CaCO3 system in the oceans. Science, 305(5682), 362–366. https://doi.org/https://www.science.org/doi/abs/10.1126/science.1097329

Fernández-Castro, B., Mouriño-Carballido, B., Álvarez-Salgado, X.A., 2019. Non-redfieldian mesopelagic nutrient remineralization in the eastern North Atlantic subtropical gyre. Prog Oceanogr 171, 136–153. https://doi.org/10.1016/J.POCEAN.2018.12.001

Fichot, C.G., Sathyendranath, S., & Miller, W.L., 2008. SeaUV and SeaUVC: Algorithms for the retrieval of UV/Visible diffuse attenuation coefficients from ocean color. Remote Sens Environ 112(4), 1584–1602. https://doi.org/10.1016/J.RSE.2007.08.009

Fichot, C.G., Benner, R., 2012. The spectral slope coefficient of chromophoric dissolved organic matter (S275–295) as a tracer of terrigenous dissolved organic carbon in river-influenced ocean margins. Limnol Oceanogr 57, 1453–1466. https://doi.org/10.4319/LO.2012.57.5.1453

Field, C.B., Behrenfeld, M.J., Randerson, J.T., Falkowski, P., 1998. Primary production of the biosphere: Integrating terrestrial and oceanic components. Science (1979) 281, 237–240. https://doi.org/https://www.science.org/doi/10.1126/science.281.5374.237

Fischer, G., Karakaş, G., 2009. Sinking rates and ballast composition of particles in the Atlantic ocean: Implications for the organic carbon fluxes to the deep ocean. Biogeosciences 6, 85–102. https://doi.org/10.5194/bg-6-85-2009

Fischer, G., Reuter, C., Karakas, G., Nowald, N., Wefer, G., 2009. Offshore advection of particles within the Cape Blanc filament, Mauritania: Results from observational and modelling studies. Prog Oceanogr 83, 322–330. https://doi.org/10.1016/J.POCEAN.2009.07.023

Fischer, G., Romero, O., Merkel, U., Donner, B., Iversen, M., Nowald, N., Ratmeyer, V., Ruhland, G., Klann, M., Wefer, G., 2016. Deep ocean mass fluxes in the coastal upwelling off Mauritania from 1988 to 2012: Variability on seasonal to decadal timescales. Biogeosciences 13, 3071–3090. https://doi.org/10.5194/BG-13-3071-2016

Fischer, G., Romero, O., Toby, E., Iversen, M., Donner, B., Mollenhauer, G., Nowald, N., Ruhland, G., Klann, M., Hamady, B., Wefer, G., 2019. Changes in the Dust-Influenced Biological Carbon Pump in the Canary Current System: Implications From a Coastal and an Offshore Sediment Trap Record Off Cape Blanc, Mauritania. Global Biogeochem Cycles 33, 1100–1128. https://doi.org/10.1029/2019GB006194

Follett, C.L., Repeta, D.J., Rothman, D.H., Xu, L., Santinelli, C., 2014. Hidden cycle of dissolved organic carbon in the deep ocean. Proc Natl Acad Sci U S A 111, 16706–11. https://doi.org/10.1073/pnas.1407445111

Fréon, P., Barange, M., & Arístegui, J., 2009. Eastern Boundary Upwelling Ecosystems: Integrative and comparative approaches. Progr Oceanogr, 83(1–4), 1–14. https://doi.org/10.1016/J.POCEAN.2009.08.001

Friedlingstein, P., O'sullivan, M., Jones, M.W., Andrew, R.M., Gregor, L., Hauck, J., Le Quéré, C., Luijkx, I.T., Olsen, A., Peters, G.P., Peters, W., Pongratz, J., Schwingshackl, C., Sitch, S., Canadell, J.G., Ciais, P., Jackson, R.B., Alin, S.R., Alkama, R., Zheng, B., 2022. Global Carbon Budget 2022. Earth Syst Sci Data 14, 4811–4900. https://doi.org/10.5194/ESSD-14-4811-2022

Friedlingstein, P., O'Sullivan, M., Jones, M.W., Andrew, R.M., Hauck, J., Olsen, et al., 2020. Global Carbon Budget 2020. Earth Syst Sci Data 12, 3269–3340. https://doi.org/10.5194/essd-12-3269-2020

Gabric, A.J., Garcia, L., Van Camp, L., Nykjaer, L., Eifler, W., Schrimpf, W., 1993. Offshore export of shelf production in the Cape Blanc (Mauritania) giant filament as derived from coastal zone color scanner imagery. J Geophys Res Oceans 98, 4697–4712. https://doi.org/10.1029/92JC01714

García-Muñoz, M., Arístegui, J., Montero, M.F., & Barton, E.D., 2004. Distribution and transport of organic matter along a filament-eddy system in the Canaries - NW Africa coastal transition zone region. Prog Oceanogr, 62(2–4), 115–129. https://doi.org/10.1016/j.pocean.2004.07.005

García-Muñoz, M., Arístegui, J., Pelegrí, J. L., Antoranz, A., Ojeda, A., & Torres, M., 2005. Exchange of carbon by an upwelling filament off Cape Ghir (NW Africa). J Mar Syst 54(1-4 SPEC. ISS.), 83–95. https://doi.org/10.1016/j.jmarsys.2004.07.005

García-Reyes, M., Sydeman, W.J., Schoeman, D.S., Rykaczewski, R.R., Black, B.A., Smit, A.J., & Bograd, S.J., 2015. Under pressure: Climate change, upwelling, and eastern boundary upwelling ecosystems. Front Mar Sci 2, 109. https://doi.org/10.3389/FMARS.2015.00109

Gattuso, J.P., Frankignoulle, M., Wollast, R., 1998. Carbon and Carbonate Metabolism in Coastal Aquatic Ecosystems. Annu Rev Ecol Evol Syst 29, 405-434. https://doi.org/10.1146/annurev.ecolsys.29.1.405

Gelado-Caballero, M.D., 2015. Saharan dust inputs to the Northeast Atlantic, in: Valdés, L., Déniz-González, I. (Eds.), Oceanographic and Biological Features in the Canary Current Large Marine Ecosystem. IOC-UNESCO, Paris. IOC Tech Ser. IOC-UNESCO, Paris, pp. 53–61.

Godwin, H. (1962). Half-life of radiocarbon. Nature, 195 (4845), 984.

Goldman, J.C., & Dennett, M.R., 2000. Growth of marine bacteria in batch and continuous culture under carbon and nitrogen limitation. Limnol Oceanogr 45(4), 789–800. https://doi.org/10.4319/LO.2000.45.4.0789

Gómez-Letona, M., Arístegui, J., Hernández-Hernández, N., Álvarez-Salgado, X.A., Álvarez, M., Delgadillo, E., Pérez-Lorenzo, M., Teira, E., Hernández-León, S., Sebastián, M., 2022. Deep ocean prokaryotes and fluorescent dissolved organic matter reflect the history of the water masses across the Atlantic Ocean. Prog Oceanogr 205, 102819. https://doi.org/10.1016/J.POCEAN.2022.102819

Griffith, D.R., McNichol, A.P., Xu, L., McLaughlin, F.A., Macdonald, R.W., Brown, K.A., Eglinton, T.I., 2012. Carbon dynamics in the western Arctic Ocean: insights from full-depth carbon isotope profiles of DIC, DOC, and POC. Biogeosciences 9, 1217–1224. https://doi.org/10.5194/bg-9-1217-2012

Hansell, D.A., 2013. Recalcitrant Dissolved Organic Carbon Fractions. Ann Rev Mar Sci 5, 421–445. https://doi.org/10.1146/annurev-marine-120710-100757

Hansell, D.A., Carlson, C.A., 2001. Biogeochemistry of total organic carbon and nitrogen in the Sargasso Sea: control by convective overturn. Deep Sea Res Part II: Top Stud Oceanogr 48, 1649–1667. https://doi.org/10.1016/S0967-0645(00)00153-3

Hansell, D.A., Carlson, C.A., 2013. Localized refractory dissolved organic carbon sinks in the deep ocean. Global Biogeochem Cycles 27, 705–710. https://doi.org/10.1002/gbc.20067

Hansell, D.A., Carlson, C.A., Repeta, D.J., Schlitzer, R., 2009. Dissolved organic matter in the ocean: A controversy stimulates new insights. Oceanogr 22, 202–211. https://doi.org/10.5670/oceanog.2009.109

Hansell, D.A., Carlson, C.A., Schlitzer, R., 2012. Net removal of major marine dissolved organic carbon fractions in the subsurface ocean. Global Biogeochem Cycles 26. https://doi.org/10.1029/2011GB004069

Hansen, J., Nazarenko, L., Ruedy, R., Sato, M., Willis, J., del Genio, A., Koch, D., Lacis, A., Lo, K., Menon, S., Novakov, T., Perlwitz, J., Russell, G., Schmidt, G.A., & Tausnev, N., 2005. Climate Change: Earth's energy imbalance: Confirmation and implications. Science 308, 1431–1435. https://doi.org/DOI: 10.1126/science.1110252

Hansen, H.P., Koroleff, F., 1999. Methods of Seawater Analysis, 3rd, Completely Revised and Extended Edition, Ed. by K. Grashoff et al. Wiley, Weinheim.

Hatch, M.D., & Slack, C.R., 1966. Photosynthesis by sugar-cane leaves: A new carboxylation reaction and the pathway of sugar formation. Bioch J 101(1), 103. https://doi.org/10.1042/BJ1010103

Hayes, J.M., 1993. Factors controlling 13C contents of sedimentary organic compounds: Principles and evidence. Mar Geol 113, 111–125. https://doi.org/10.1016/0025-3227(93)90153-M

Haynes, W.M. (Ed.), 2016. CRC Handbook of Chemistry and Physics. In CRC Handbook of Chemistry and Physics (97th Edition). CRC Press. https://doi.org/10.1201/9781315380476

Hedges, J.I., 2002. Why dissolved organics matter? In Hansell, D.A & Carlosn C.A. (Eds.), Biogeochemistry of marine dissolved organic matter (pp. 1–33). Academic Press. https://cir.nii.ac.jp/crid/1572824501086070400

Hedges, J.I., Keil, R.G., 1995. Sedimentary organic matter preservation: an assessment and speculative synthesis. Mar Chem 49, 81–115. https://doi.org/10.1016/0304-4203(95)00008-F

Helmke, P., Romero, O., Fischer, G., 2005. Northwest African upwelling and its effect on offshore organic carbon export to the deep sea. Global Biogeochem Cycles 19. https://doi.org/10.1029/2004GB002265

Helms, J.R., Stubbins, A., Ritchie, J.D., Minor, E.C., Kieber, D.J., Mopper, K., 2008. Absorption spectral slopes and slope ratios as indicators of molecular weight, source, and photobleaching of chromophoric dissolved organic matter. Limnol Oceanogr 53, 955–969. https://doi.org/10.4319/LO.2008.53.3.0955

Hernández-Hernández, N., Arístegui, J., Montero, M.F., Velasco-Senovilla, E., Baltar, F., Marrero-Díaz, Á., Martínez-Marrero, A., Rodríguez-Santana, Á., 2020. Drivers of Plankton Distribution Across Mesoscale Eddies at Submesoscale Range. Front Mar Sci 7, 667. https://doi.org/10.3389/FMARS.2020.00667/BIBTEX

Herndl, G.J., Müller-Niklas, G., & Frick, J., 1993. Major role of ultraviolet-B in controlling bacterioplankton growth in the surface layer of the ocean. Nature, 361(6414), 717–719. https://doi.org/10.1038/361717a0

Hertkorn, N., Benner, R., Frommberger, M., Schmitt-Kopplin, P., Witt, M., Kaiser, K., Kettrup, A., & Hedges, J.I., 2006. Characterization of a major refractory component of marine dissolved organic matter. Geochim Cosmochim Acta 70(12), 2990–3010. https://doi.org/10.1016/J.GCA.2006.03.021

Hoefs, J., 2021. Isotope Fractionation Processes of Selected Elements. In Stable Isotope Geochemistry 9th Edition (pp. 49–265). Springer, Cham. https://doi.org/10.1007/978-3-030-77692-3_2

Hoefs, J., 1975. Geochemistry of Stable Isotopes. Angewandte Chemie International Edition in English 14, 75–79. https://doi.org/10.1002/ANIE.197500751

Holm-Hansen, O., Lorenzen, C.J., Holmes, R.W., Strickland, J.D., 1965. Fluorometric determination of chlorophyll. J Mar Sci 30, 3–15.

Holmén, K., 1992. The Global Carbon Cycle. In Butcher, S.S., Charlson, R.J., Orians, G.H. & Wolfe, G.V. (Eds.), Global Biogeochemical Cycles (Vol. 50, Issue C, pp. 239–262). Academic Press. https://doi.org/10.1016/S0074-6142(08)62694-7

Hosegood, P.J., Nightingale, P.D., Rees, A.P., Widdicombe, C.E., Woodward, E.M.S., Clark, D.R., Torres, R.J., 2017. Nutrient pumping by submesoscale circulations in the mauritanian upwelling system. Prog Oceanogr 159, 223–236. https://doi.org/10.1016/J.POCEAN.2017.10.004

Ibánhez, J.S.P., Flores Montes, M., Lefèvre, N., 2022. Evidence for enhanced primary production driving significant CO2 drawdown associated with the Atlantic ITCZ. Sci Total Environ 838, 156592. https://doi.org/10.1016/J.SCITOTENV.2022.156592

Iuculano, F., álverez-Salgado, X.A., Otero, J., Catalá, T.S., Sobrino, C., Duarte, C.M., Agustí, S., 2019. Patterns and drivers of UV absorbing chromophoric dissolved organic matter in the euphotic layer of the open ocean. Front Mar Sci 6, 320. https://doi.org/10.3389/FMARS.2019.00320/BIBTEX

Iversen, M.H., 2023. Carbon Export in the Ocean: A Biologist's Perspective. Ann Rev Mar Sci 15, 357–381. https://doi.org/10.1146/ANNUREV-MARINE-032122-035153

Iversen, M.H., Nowald, N., Ploug, H., Jackson, G.A., Fischer, G., 2010. High resolution profiles of vertical particulate organic matter export off Cape Blanc, Mauritania: Degradation processes and ballasting effects. Deep Sea Res 1 Oceanogr Res Pap 57, 771–784. https://doi.org/10.1016/j.dsr.2010.03.007

Jerusalén-Lleó, E., Nieto-Cid, M., Fuentes-Santos, I., Dittmar, T., & Álvarez-Salgado, X.A., 2023. Solid phase extraction of ocean dissolved organic matter with PPL cartridges: efficiency and selectivity. Front Mar Sci, 10, 652. https://doi.org/10.3389/FMARS.2023.1159762

Jiao, N., & Azam, F., 2011. Microbial carbon pump and its significance for carbon sequestration in the ocean. In N. Jiao, F. Azam, & S. Sanders (Eds.), Microbial Carbon Pump in the Ocean (Vol. 10, pp. 43–45).

Jiao, N., Herndl, G.J., Hansell, D.A., Benner, R., Kattner, G., Wilhelm, S.W., Kirchman, D.L., Weinbauer, M.G., Luo, T., Chen, F., Azam, F., 2010. Microbial production of recalcitrant dissolved organic matter: long-term carbon storage in the global ocean. Nat Rev Microbiol 8, 593–599. https://doi.org/10.1038/nrmicro2386

Jørgensen, L., Stedmon, C.A., Granskog, M.A., & Middelboe, M., 2014. Tracing the long-term microbial production of recalcitrant fluorescent dissolved organic matter in seawater. Geophys Res Lett, 41(7), 2481–2488. https://doi.org/10.1002/2014GL059428

Jørgensen, L., Stedmon, C.A., Kragh, T., Markager, S., Middelboe, M., Søndergaard, M., 2011. Global trends in the fluorescence characteristics and distribution of marine dissolved organic matter. Mar Chem 126, 139–148. https://doi.org/10.1016/J.MARCHEM.2011.05.002

Jurado, E., Dachs, J., Duarte, C.M., & Simó, R., 2008. Atmospheric deposition of organic and black carbon to the global oceans. Atmos Environ, 42(34), 7931–7939. https://doi.org/10.1016/J.ATMOSENV.2008.07.029

Kaiser, K., & Benner, R., 2009. Biochemical composition and size distribution of organic matter at the Pacific and Atlantic time-series stations. Marine Chemistry, 113(1–2), 63–77. https://doi.org/10.1016/J.MARCHEM.2008.12.004

Karakaş, G., Nowald, N., Blaas, M., Marchesiello, P., Frickenhaus, S., Schlitzer, R., 2006. High-resolution modeling of sediment erosion and particle transport across the northwest African shelf. J Geophys Res Oceans 111, 6025. https://doi.org/10.1029/2005JC003296

Karstensen, J., Tomczak, M., 1998. Age determination of mixed water masses using CFC and oxygen data. J Geophys Res Oceans 103, 18599–18609. https://doi.org/10.1029/98JC00889

Kawase, M., & Sarmiento, J.L., 1985. Nutrients in the Atlantic thermocline. J Geophys Res: Oceans 90, 8961–8979. https://doi.org/10.1029/JC090IC05P08961

Keeling, C.D., 1972. Industrial production of carbon dioxide from fossil fuels and limestone. Tellus A: Dyn Meteorol Oceanogr 25(2), 198. https://doi.org/10.3402/TELLUSA.V25I2.9652

Keller, K., Morel, F.M.M., 1999. A model of carbon isotopic fractionation and active carbon uptake in phytoplankton. Mar Ecol Prog Ser 182, 295–298. https://doi.org/10.3354/MEPS182295

Kempe, S., 1979. Carbon in the rock cycle. In Bolin, B., Degens, E.T., Kempe, S. & Ketner, P. (Eds.), The Global Carbon Cycle (pp. 343–377). Wiley & Sons.

Kérouel, R., Aminot, A., 1997. Fluorometric determination of ammonia in sea and estuarine waters by direct segmented flow analysis. Mar Chem 57, 265–275. https://doi.org/10.1016/S0304-4203(97)00040-6

Kim, J., Kim, G., 2016. Significant anaerobic production of fluorescent dissolved organic matter in the deep East Sea (Sea of Japan). Geophys Res Lett 43, 7609–7616. https://doi.org/10.1002/2016GL069335

Kim, T.-H., Kim, G., Lee, S.-A., Dittmar, T., 2015. Extraordinary slow degradation of dissolved organic carbon (DOC) in a cold marginal sea. Sci Rep 5, 13808. https://doi.org/10.1038/srep13808

Kinsey, J.D., Corradino, G., Ziervogel, K., Schnetzer, A., & Osburn, C.L., 2018. Formation of chromophoric dissolved organic matter by bacterial degradation of phytoplankton-derived aggregates. Front Mar Sci 4, 430. https://doi.org/10.3389/FMARS.2017.00430

Kirkels, F.M.S.A., Cerli, C., Federherr, E., Gao, J., Kalbitz, K., 2014. A novel high-temperature combustion based system for stable isotope analysis of dissolved organic carbon in aqueous samples. II: optimization and assessment of analytical performance. Rapid Commun Mass Spectrom 28, 2574–2586. https://doi.org/10.1002/rcm.7053

Kitidis, V., Stubbins, A. P., Uher, G., Upstill Goddard, R. C., Law, C. S., & Woodward, E. M. S. (2006). Variability of chromophoric organic matter in surface waters of the Atlantic Ocean. Deep Sea Res I Top Stud Oceanogr, 53(14–16), 1666–1684. https://doi.org/10.1016/J.DSR2.2006.05.009

Kitidis, V., Tilstone, G. H., Serret, P., Smyth, T. J., Torres, R., & Robinson, C., 2014. Oxygen photolysis in the Mauritanian upwelling: Implications for net community production. Limnol Oceanogr 59(2), 299–310. https://doi.org/10.4319/lo.2014.59.2.0299

Klein, B., & Tomczak, M., 1994. Identification of diapycnal mixing through optimum multiparameter analysis: 2. Evidence for unidirectional diapycnal mixing in the front between North and South Atlantic Central Water. J Geophys Res: Oceans 99(C12), 25275–25280. https://doi.org/10.1029/94JC01948

Kothawala, D.N., Murphy, K.R., Stedmon, C.A., Weyhenmeyer, G.A., Tranvik, L.J., 2013. Inner filter correction of dissolved organic matter fluorescence. Limnol Oceanogr Methods 11, 616–630. https://doi.org/10.4319/LOM.2013.11.616

Kudela, R.M., Dugdale, R.C., 2000. Nutrient regulation of phytoplankton productivity in Monterey Bay, California. Deep Sea Res II Top Stud Oceanogr 47 1023–1053. https://doi.org/10.1016/S0967-0645(99)00135-6

Kuhlbusch, T.A.J., 1998. Black Carbon and the Carbon Cycle. Science (1979) 280, 1903–1904. https://doi.org/10.1126/SCIENCE.280.5371.1903

Kumar, A., Abouchami, W., Galer, S.J.G., Singh, S.P., Fomba, K.W., Prospero, J.M., Andreae, M.O., 2018. Seasonal radiogenic isotopic variability of the African dust outflow to the tropical Atlantic Ocean and across to the Caribbean. Earth Planet Sci Lett 487, 94–105. https://doi.org/10.1016/J.EPSL.2018.01.025

Lalonde, K., Middlestead, P., Gélinas, Y., 2014. Automation of 13 C/ 12 C ratio measurement for freshwater and seawater DOC using high temperature combustion. Limnol Oceanogr Methods 12, 816–829. https://doi.org/10.4319/lom.2014.12.816

Lang, S.Q., Bernasconi, S.M., Früh-Green, G.L., 2012. Stable isotope analysis of organic carbon in small (μg C) samples and dissolved organic matter using a GasBench preparation device. Rapid Comm Mass Spectrom 26, 9–16. https://doi.org/10.1002/rcm.5287

Lang, S.Q., Butterfield, D.A., Lilley, M.D., Paul Johnson, H., Hedges, J.I., 2006. Dissolved organic carbon in ridge-axis and ridge-flank hydrothermal systems. Geochim Cosmochim Acta 70, 3830–3842. https://doi.org/10.1016/J.GCA.2006.04.031

Lang, S.Q., Früh-Green, G.L., Bernasconi, S.M., Wacker, L., 2013. Isotopic (δ13C, Δ14C) analysis of organic acids in marine samples using wet chemical oxidation. Limnol Oceanogr Methods 11, 161–175. https://doi.org/10.4319/lom.2013.11.161

Lang, S.Q., Lilley, M.D., Hedges, J.I., 2007. A method to measure the isotopic (13C) composition of dissolved organic carbon using a high temperature combustion instrument. Mar Chem 103, 318–326. https://doi.org/10.1016/J.MARCHEM.2006.10.002

Langdon, C., 2010. Determination of Dissolved Oxygen in Seawater by Winkler Titration Using The Amperometric Technique., in: Hood, E., Sabine, C., Sloyan, B. (Eds.), The GO-SHIP Repeat Hydrography Manual: A Collection of Expert Reports and Guidelines. Version 1. https://doi.org/https://doi.org/10.25607/OBP-1350

LaRowe, D.E., Dale, A.W., Amend, J.P., & Van Cappellen, P., 2012. Thermodynamic limitations on microbially catalyzed reaction rates. Geochim Cosmochim Acta 90, 96–109. https://doi.org/10.1016/J.GCA.2012.05.011

Laws, E.A., Bidigare, R.R., Popp, B.N., 1997. Effect of growth rate and CO2 concentration on carbon isotopic fractionation by the marine diatom Phaeodactylum tricornutum. Limnol Oceanogr 42, 1552–1560. https://doi.org/10.4319/LO.1997.42.7.1552

Lechtenfeld, O.J., Kattner, G., Flerus, R., McCallister, S.L., Schmitt-Kopplin, P., & Koch, B. P., 2014. Molecular transformation and degradation of refractory dissolved organic matter in the Atlantic and Southern Ocean. Geochim Cosmochim Acta 126, 321–337. https://doi.org/10.1016/J.GCA.2013.11.009

Lee, S.-A., Kim, G., 2018. Sources, fluxes, and behaviors of fluorescent dissolved organic matter (FDOM) in the Nakdong River Estuary, Korea. Biogeosciences 15, 1115–1122. https://doi.org/10.5194/bg-15-1115-2018

Lee, S.A., Kim, T.H., Kim, G., 2020. Tracing terrestrial versus marine sources of dissolved organic carbon in a coastal bay using stable carbon isotopes. Biogeosciences 17, 135–144. https://doi.org/10.5194/BG-17-135-2020

Legendre, L., Rivkin, R.B., Weinbauer, M.G., Guidi, L., Uitz, J., 2015. The microbial carbon pump concept: Potential biogeochemical significance in the globally changing ocean. Prog Oceanogr 134, 432–450. https://doi.org/10.1016/J.POCEAN.2015.01.008

Lévy, M., Ferrari, R., Franks, P.J.S., Martin, A.P., Rivière, P., 2012. Bringing physics to life at the submesoscale. Geophys Res Lett 39. https://doi.org/10.1029/2012GL052756

Loh, A.N., Bauer, J.E., Druffel, E.R.M., 2004. Variable ageing and storage of dissolved organic components in the open ocean. Nature 430, 877–881. https://doi.org/10.1038/nature02780

Lønborg, C., Álvarez-Salgado, X.A., Davidson, K., & Miller, A.E.J., 2009. Production of bioavailable and refractory dissolved organic matter by coastal heterotrophic microbial populations. Estuar Coast Shelf Sci 82(4), 682–688. https://doi.org/10.1016/J.ECSS.2009.02.026

Lønborg, C., Álvarez-Salgado, X.A., 2014. Tracing dissolved organic matter cycling in the eastern boundary of the temperate North Atlantic using absorption and fluorescence

spectroscopy. Deep Sea Res I Oceanog Res Pap 85 35–46. https://doi.org/10.1016/J.DSR.2013.11.002

Lopez, C.N., Robert, M., Galbraith, M., Bercovici, S.K., Orellana, M. v., Hansell, D.A., 2020. High Temporal Variability of Total Organic Carbon in the Deep Northeastern Pacific. Front Earth Sci (Lausanne) 8, 80. https://doi.org/10.3389/FEART.2020.00080/BIBTEX

Lovecchio, E., Gruber, N., Münnich, M., 2018. Mesoscale contribution to the long-range offshore transport of organic carbon from the Canary Upwelling System to the open North Atlantic. Biogeosciences 15, 5061–5091. https://doi.org/10.5194/BG-15-5061-2018

Lovecchio, E., Gruber, N., Münnich, M., Frenger, I., 2022. On the Processes Sustaining Biological Production in the Offshore Propagating Eddies of the Northern Canary Upwelling System. J Geophys Res Oceans 127, e2021JC017691. https://doi.org/10.1029/2021JC017691

Lovecchio, E., Gruber, N., Münnich, M., Lachkar, Z., 2017. On the long-range offshore transport of organic carbon from the Canary Upwelling System to the open North Atlantic. Biogeosciences 14, 3337–3369. https://doi.org/10.5194/BG-14-3337-2017

Lu, Y.H., Edmonds, J.W., Yamashita, Y., Zhou, B., Jaegge, A., & Baxley, M., 2015. Spatial variation in the origin and reactivity of dissolved organic matter in Oregon-Washington coastal waters. Ocean Dyn 65(1), 17–32. https://doi.org/10.1007/S10236-014-0793-7/FIGURES/7

Martínez-Marrero, A., Rodríguez-Santana, A., Hernández-Guerra, A., Fraile-Nuez, E., López-Laatzen, F., Vélez-Belchí, P., Parrilla, G., 2008. Distribution of water masses and diapycnal mixing in the Cape Verde Frontal Zone. Geophys Res Lett 35, 0–4. https://doi.org/10.1029/2008GL033229

Martínez-Pérez, A.M., Catalá, T.S., Nieto-Cid, M., Otero, J., Álvarez, M., Emelianov, M., Reche, I., Álvarez-Salgado, X.A., Arístegui, J., 2019. Dissolved organic matter (DOM) in the open Mediterranean Sea. II: Basin–wide distribution and drivers of fluorescent DOM. Prog Oceanogr 170, 93–106. https://doi.org/10.1016/J.POCEAN.2018.10.019

Martiny, A.C., Pham, C.T.A., Primeau, F.W., Vrugt, J.A., Moore, J.K., Levin, S.A., Lomas, M.W., 2013a. Strong latitudinal patterns in the elemental ratios of marine plankton and organic matter. Nat Geosci 6, 279–283. https://doi.org/10.1038/ngeo1757

Martiny, A.C., Vrugt, J.A., Primeau, F.W., Lomas, M.W., 2013b. Regional variation in the particulate organic carbon to nitrogen ratio in the surface ocean. Wiley Online Library 27, 723–731. https://doi.org/10.1002/gbc.20061

Marty, J., & Planas, D., 2008. Comparison of methods to determine algal δ13C in freshwater. Limnology and Oceanography: Methods 6(1), 51–63. https://doi.org/10.4319/LOM.2008.6.51

Masiello, C.A., Druffel, E.R.M., 1998. Black Carbon in Deep-Sea Sediments. Science (1979) 280, 1911–1913. https://doi.org/10.1126/SCIENCE.280.5371.1911

Mbaye, M.L., Gaye, A.T., Spitzy, A., Dähnke, K., Afouda, A., Gaye, B., 2016. Seasonal and spatial variation in suspended matter, organic carbon, nitrogen, and nutrient concentrations

of the Senegal River in West Africa. Limnologica 57, 1–13. https://doi.org/10.1016/J.LIMNO.2015.12.003

McCarthy, M.D., Beaupré, S.R., Walker, B.D., Voparil, I., Guilderson, T.P., Druffel, E.R.M., 2010. Chemosynthetic origin of 14C-depleted dissolved organic matter in a ridge-flank hydrothermal system. Nat Geosci 4:1 4, 32–36. https://doi.org/10.1038/ngeo1015

McCave, I.N., 1986. Local and global aspects of the bottom nepheloid layers in the world ocean. Netherlands J Sea Res 20, 167–181. https://doi.org/10.1016/0077-7579(86)90040-2

McKenna, J.H., Doering, P.H., 1995. Measurement of dissolved organic carbon by wet chemical oxidation with persulfate: influence of chloride concentration and reagent volume. Mar Chem 48, 109–114. https://doi.org/10.1016/0304-4203(94)00049-J

McNichol, A.P., Aluwihare, L.I., 2007. The power of radiocarbon in biogeochemical studies of the marine carbon cycle: Insights from studies of dissolved and particulate organic carbon (DOC and POC). Chem Rev 107, 443–466. https://doi.org/10.1021/cr050374g

Messié, M., Chavez, F.P., 2015. Seasonal regulation of primary production in eastern boundary upwelling systems. Prog Oceanogr 134, 1–18. https://doi.org/10.1016/J.POCEAN.2014.10.011

Meunier, T., Barton, E.D., Barreiro, B., Torres, R., 2012. Upwelling filaments off cap blanc: Interaction of the NW african upwelling current and the cape verde frontal zone eddy field? J Geophys Res Oceans 117, 1–18. https://doi.org/10.1029/2012JC007905

Monson, K.D., & Hayes, J.M., 1982. Carbon isotopic fractionation in the biosynthesis of bacterial fatty acids. Ozonolysis of unsaturated fatty acids as a means of determining the intramolecular distribution of carbon isotopes. Geochim Cosmochim Acta 46(2), 139–149. https://doi.org/10.1016/0016-7037(82)90241-1

Mook, W.G., Bommerson, J.C., Staverman, W.H., 1974. Carbon isotope fractionation between dissolved bicarbonate and gaseous carbon dioxide. Earth Planet Sci Lett 22, 169–176. https://doi.org/10.1016/0012-821X(74)90078-8

Muller-Karger, F.E., Varela, R., Thunell, R., Luerssen, R., Hu, C., & Walsh, J.J., 2005. The importance of continental margins in the global carbon cycle. Geophys Res Lett 32(1), 1–4. https://doi.org/10.1029/2004GL021346

Murphy, K.R., Butler, K.D., Spencer, R.G.M., Stedmon, C.A., Boehme, J.R., Aiken, G.R., 2010. Measurement of dissolved organic matter fluorescence in aquatic environments: An interlaboratory comparison. Environ Sci Technol 44, 9405–9412. https://doi.org/https://doi.org/10.1021/es102362t

Murphy, K.R., Stedmon, C.A., Graeber, D., Bro, R., 2013. Fluorescence spectroscopy and multi-way techniques. PARAFAC. Anal Methods 5, 6557–6566. https://doi.org/10.1039/C3AY41160E

Murphy, K.R., Stedmon, C.A., Wenig, P., Bro, R., 2014. OpenFluor- An online spectral library of auto-fluorescence by organic compounds in the environment. Anal Methods 6, 658–661. https://doi.org/10.1039/C3AY41935E

Nagai, T., Gruber, N., Frenzel, H., Lachkar, Z., McWilliams, J.C., Plattner, G.K., 2015. Dominant role of eddies and filaments in the offshore transport of carbon and nutrients in the California Current System. J Geophys Res Oceans 120, 5318–5341. https://doi.org/10.1002/2015JC010889

Nelson, N.B., Siegel, D.A., Carlson, C.A., & Swan, C.M., 2010. Tracing global biogeochemical cycles and meridional overturning circulation using chromophoric dissolved organic matter. Geophys Res Lett 37(3), n/a-n/a. https://doi.org/10.1029/2009GL042325

Nelson, N.B., Carlson, C.A., Steinberg, D.K., 2004. Production of chromophoric dissolved organic matter by Sargasso Sea microbes. Mar Chem 89, 273–287. https://doi.org/10.1016/J.MARCHEM.2004.02.017

Nelson, N.B., Gauglitz, J.M., 2016. Optical signatures of dissolved organic matter transformation in the global ocean. Front Mar Sci 2, 118. https://doi.org/10.3389/FMARS.2015.00118/BIBTEX

Nelson, N.B., Siegel, D.A., 2013. The Global Distribution and Dynamics of Chromophoric Dissolved Organic Matter. Ann Rev Mar Sci 5, 447–476. https://doi.org/https://doi.org/10.1146/annurev-marine-120710-100751

Nelson, N.B., Siegel, D.A., Michaels, A.F., 1998. Seasonal dynamics of colored dissolved material in the Sargasso Sea. Deep Sea Res I Oceanogr Re Pap 45, 931–957. https://doi.org/10.1016/S0967-0637(97)00106-4

Neuer, S., Freudenthal, T., Davenport, R., Llinás, O., & Rueda, M.J., 2002. Seasonality of surface water properties and particle flux along a productivity gradient off NW Africa. Deep-Sea Res II Top Stud Oceanogr 49(17), 3561–3576. https://doi.org/10.1016/S0967-0645(02)00098-X

Nieto-Cid, M., Álvarez-Salgado, X.A., Pérez, F.F., 2006. Microbial and photochemical reactivity of fluorescent dissolved organic matter in a coastal upwelling system. Limnol Oceanogr 51, 1391–1400. https://doi.org/10.4319/LO.2006.51.3.1391

Nowald, N., Fischer, G., Iversen, M.H., Wegener, A., Wefer, G., 2009. In-situ sinking speed measurements of marine snow aggregates acquired with a settling chamber mounted to the Cherokee ROV. ieeexplore.ieee.org. https://doi.org/10.1109/OCEANSE.2009.5278186

Nowald, N., Iversen, M.H., Fischer, G., Ratmeyer, V., & Wefer, G., 2015. Time series of in-situ particle properties and sediment trap fluxes in the coastal upwelling filament off Cape Blanc, Mauritania. Progr Oceanogr 137, 1–11. https://doi.org/10.1016/J.POCEAN.2014.12.015

Nowicki, M., DeVries, T., Siegel, D.A., 2022. Quantifying the Carbon Export and Sequestration Pathways of the Ocean's Biological Carbon Pump. Global Biogeochem Cycles 36, e2021GB007083. https://doi.org/10.1029/2021GB007083

O'Leary, M.H., 1981. Carbon isotope fractionation in plants. Phytochemistry 20, 553–567. https://doi.org/10.1016/0031-9422(81)85134-5

Oba, Y., Naraoka, H., 2008. Carbon and hydrogen isotopic fractionation of low molecular weight organic compounds during ultraviolet degradation. Org Geochem 39, 501–509. https://doi.org/10.1016/J.ORGGEOCHEM.2007.11.009

Ogawa, H., Amagai, Y., Koike, I., Kaiser, K., & Benner, R., 2001. Production of Refractory Dissolved Organic Matter by Bacteria. Science, 292(5518), 917–920. https://doi.org/10.1126/SCIENCE.1057627

Ohde, T., Fiedler, B., Körtzinger, A., 2015. Spatio-temporal distribution and transport of particulate matter in the eastern tropical North Atlantic observed by Argo floats. Deep Sea Res 1 Oceanogr Res Pap 102, 26–42. https://doi.org/10.1016/j.dsr.2015.04.007

Osburn, C.L., & Stedmon, C.A., 2011. Linking the chemical and optical properties of dissolved organic matter in the Baltic–North Sea transition zone to differentiate three allochthonous inputs. Mar Chem 126(1–4), 281–294. https://doi.org/10.1016/J.MARCHEM.2011.06.007

Osburn, C.L., St-Jean, G., 2007. The use of wet chemical oxidation with high-amplification isotope ratio mass spectrometry (WCO-IRMS) to measure stable isotope values of dissolved organic carbon in seawater. Limnol Oceanogr Methods 5, 296–308. https://doi.org/10.4319/lom.2007.5.296

Pan, D., Liu, Q., & Bai, Y., 2014. Review and suggestions for estimating particulate organic carbon and dissolved organic carbon inventories in the ocean using remote sensing data. Acta Oceanol Sin 33(1), 1–10. https://doi.org/10.1007/S13131-014-0419-4/METRICS

Panetta, R.J., Ibrahim, M., Gélinas, Y., 2008. Coupling a High-Temperature Catalytic Oxidation Total Organic Carbon Analyzer to an Isotope Ratio Mass Spectrometer To Measure Natural-Abundance δ 13 C-Dissolved Organic Carbon in Marine and Freshwater Samples. Anal Chem 80, 5232–5239. https://doi.org/10.1021/ac702641z

Park, R., Epstein, S., 1960. Carbon isotope fractionation during photosynthesis. Geochim. et Cosmochim. Acta Vol: 21, 110–126. https://doi.org/10.1016/S0016-7037(60)80006-3

Passow, U., & De La Rocha, C.L., 2006. Accumulation of mineral ballast on organic aggregates. Glob Biogeochem Cycles, 20(1), 1013. https://doi.org/10.1029/2005GB002579

Pastor, M. V, Vélez-Belchí, P., Hernández-Guerra, A., 2015. Water masses in the Canary Current Large Marine Ecosystem, in: Valdés, L., Déniz-González, I. (Eds.), Oceanographic and Biological Features in the Canary Current Large Marine Ecosystem. IOC-Tech Ser, Paris, pp. 73–79.

Pastor, M.V., Palter, J.B., Pelegrí, J. L., & Dunne, J.P., 2013. Physical drivers of interannual chlorophyll variability in the eastern subtropical North Atlantic. J Geophys Res Oceans, 118(8), 3871–3886. https://doi.org/10.1002/jgrc.20254

Pastor, M. V., Pelegrí, J.L., Hernández-Guerra, A., Font, J., Salat, J., Emelianov, M., 2008. Water and nutrient fluxes off Northwest Africa. Cont Shelf Res 28, 915–936. https://doi.org/10.1016/J.CSR.2008.01.011

Pauly, D., & Christensen, V., 1995. Primary production required to sustain global fisheries. Nature 374:6519, 374(6519), 255–257. https://doi.org/10.1038/374255a0

Pelegrí, J., Arístegui, J., Cana, L., González-Dávila, M., Hernández-Guerra, A., Hernández-León, S., Marrero-Díaz, A., Montero, M.F., Sangrà, P., & Santana-Casiano, M., 2005. Coupling between the open ocean and the coastal upwelling region off northwest Africa: Water recirculation and offshore pumping of organic matter. J Mar Sys 54(1-4 SPEC. ISS.), 3–37. https://doi.org/10.1016/j.jmarsys.2004.07.003

Pelegrí, J.L., Marrero-Díaz, A., Ratsimandresey, A.W., 2006. Nutrient irrigation of the North Atlantic. Prog Oceanogr 70, 366–406. https://doi.org/10.1016/J.POCEAN.2006.03.018

Pelegrí, JL., Peña-Izquierdo, J., 2015a. Eastern boundary currents off North-West Africa, in: Valdés, L., Déniz-González, I. (Eds.), Oceanographic and Biological Features in the Canary Current Large Marine Ecosystem. IOC-UNESCO, Paris, pp. 81–92.

Pelegrí, JL., Peña-Izquierdo, J., 2015b. Inorganic nutrients and dissolved oxygen in the Canary Current Large Marine Ecosystem, in: Valdés, L., Déniz-González, I. (Eds.), Oceanographic and Biological Features in the Canary Current Large Marine Ecosystem. IOC-UNESCO, Paris, pp. 133-142.

Peltzer, E.T., Fry, B., Doering, P.H., McKenna, J.H., Norrman, B., Li Zweifel, U., 1996. A comparison of methods for the measurement of dissolved organic carbon in natural waters. Mar Chem 54, 85–96. https://doi.org/10.1016/0304-4203(96)00023-0

Perez, F.F., Mourino, C., Fraga, F., Rios, A.F., 1993. Displacement of water masses and remineralization rates off the Iberian Peninsula by nutrient anomalies. J Mar Res 51, 869–892. https://doi.org/10.1357/0022240933223891

Pérez-Barrancos, C., Gelado-Caballero, M.D., Hernández-Hernández, N., Baños, I., Gómez-Letona, M., Montero, M.F., Arrieta, J.M., Arístegui, J., 2022. Uneven response of microbial communities to intense dust deposition across the coastal transition zone off Mauritania. Front Mar Sci 9. https://doi.org/10.3389/FMARS.2022.999729

Pérez-Rodríguez, P., Pelegrí, J.L., Marrero-Díaz, A., 2001. Dynamical characteristics of the Cape Verde frontal zone. Sci Mar 65, 241–250. https://doi.org/10.3989/SCIMAR.2001.65S1241

Peyton, G.R., 1993. The free-radical chemistry of persulfate-based total organic carbon analyzers. Mar Chem 41, 91–103. https://doi.org/10.1016/0304-4203(93)90108-Z

Pohlman, J.W., Bauer, J.E., Waite, W.F., Osburn, C.L., Chapman, N.R., 2010. Methane hydrate-bearing seeps as a source of aged dissolved organic carbon to the oceans. Nat Geosci 4, 37–41. https://doi.org/10.1038/ngeo1016

Pomeroy, L., Williams, P., Azam, F., & Hobbie JE., 2007. The microbial loop. Oceanogr 20, 28–33. https://www.jstor.org/stable/24860040

Poole, R., Tomczak, M., 1999. Optimum multiparameter analysis of the water mass structure in the Atlantic Ocean thermocline. Deep Sea Res 1 Oceanogr Res Pap 46, 1895–1921. https://doi.org/10.1016/S0967-0637(99)00025-4

Popp, B.N., Laws, E.A., Bidigare, R.R., Dore, J.E., Hanson, K.L., Wakeham, S.G., 1998. Effect of Phytoplankton Cell Geometry on Carbon Isotopic Fractionation. Geochim Cosmochim Acta 62, 69–77. https://doi.org/10.1016/S0016-7037(97)00333-5

Rau, G.H., Takahashi, T., Des Marais, D.J., Repeta, D.J., Martin, J.H., 1992. The relationship between δ13C of organic matter and [CO2(aq)] in ocean surface water: Data from a JGOFS site in the northeast Atlantic Ocean and a model. Geochim Cosmochim Acta 56, 1413–1419. https://doi.org/10.1016/0016-7037(92)90073-R

Raymond, P.A., Bauer, J.E., 2001. Use of 14C and 13C natural abundances for evaluating riverine, estuarine, and coastal DOC and POC sources and cycling: a review and synthesis. Org Geochem 32, 469–485. https://doi.org/10.1016/S0146-6380(00)00190-X

Redfield, A.C., Ketchum, B.H., Richards, F.A., 1963. The influence of organisms on the composition of seawater, in: Hill, M.N. (Ed.), The Sea. John Wiley, New York, pp. 12–37.

Repeta, D.J., 2015. Chemical Characterization and Cycling of Dissolved Organic Matter. Biogeochemistry of Marine Dissolved Organic Matter: Second Edition 21–63. https://doi.org/10.1016/B978-0-12-405940-5.00002-9

Ridgwell, A., & Arndt, S., 2015. Why Dissolved Organics Matter: DOC in Ancient Oceans and Past Climate Change. In D. Hansell & C. Carlson (Eds.), Biogeochemistry of Marine Dissolved Organic Matter: Second Edition (pp. 1–20). Academic Press. https://doi.org/https://doi.org/10.1016/B978-0-12-405940-5.00001-7

Riley, J.S., Sanders, R., Marsay, C., le Moigne, F.A.C., Achterberg, E.P., Poulton, A.J., 2012. The relative contribution of fast and slow sinking particles to ocean carbon export. Glob Biogeochem Cycles 26. https://doi.org/10.1029/2011GB004085

Roberts, K., Granum, E., Leegood, R.C., & Raven, J.A., 2007. C3 and C4 Pathways of Photosynthetic Carbon Assimilation in Marine Diatoms Are under Genetic, Not Environmental, Control. Plant Physiol 145(1), 230–235. https://doi.org/10.1104/PP.107.102616

Rochelle-Newall, E.J., & Fisher, T.R., 2002. Production of chromophoric dissolved organic matter fluorescence in marine and estuarine environments: an investigation into the role of phytoplankton. Mar Chem 77(1), 7–21. https://doi.org/10.1016/S0304-4203(01)00072-X

Romero, O.E., 2002. Interannual variability (1988-1991) of siliceous phytoplankton fluxes off northwest Africa. J Plank Res 24(10), 1035–1046. https://doi.org/10.1093/plankt/24.10.1035

Rotatore, C., Colman, B., & Kuzma, M., 1995. The active uptake of carbon dioxide by the marine diatoms Phaeodactylum ticornutum and Cyclotella sp. Plant, Cell & Environ 18(8), 913–918. https://doi.org/10.1111/J.1365-3040.1995.TB00600.X

Ruiz-González, C., Mestre, M., Estrada, M., Sebastián, M., Salazar, G., Agustí, S., Moreno-Ostos, E., Reche, I., Álvarez-Salgado, X.A., Morán, X.A.G., Duarte, C.M., Sala, M.M., Gasol, J.M., 2020. Major imprint of surface plankton on deep ocean prokaryotic structure and activity. Mol Ecol 29, 1820–1838. https://doi.org/10.1111/MEC.15454

Sabine, C.L., Feely, R.A., Gruber, N., Key, R.M., Lee, K., Bullister, J.L., Wanninkhof, R., Wong, C.S., Wallace, D.W.R., Tilbrook, B., Millero, F.J., Peng, T.H., Kozyr, A., Ono, T., & Rios, A.F., 2004. The oceanic sink for anthropogenic CO2. Science 305, 367–371. https://doi.org/DOI: 10.1126/science.1097403

Sánchez-Leal, R. F., Bellanco, M. J., Fernández-Salas, L. M., García-Lafuente, J., Gasser-Rubinat, M., González-Pola, C., Hernández-Molina, F. J., Pelegrí, J. L., Peliz, A., Relvas, P., Roque, D., Ruiz-Villarreal, M., Sammartino, S., & Sánchez-Garrido, J. C. (2017). The Mediterranean Overflow in the Gulf of Cadiz: A rugged journey. Sci Advan 3(11). https://doi.org/10.1126/sciadv.aao0609

Sanders, R., Henson, S.A., Koski, M., de La Rocha, C.L., Painter, S.C., Poulton, A.J., Riley, J., Salihoglu, B., Visser, A., Yool, A., Bellerby, R., Martin, A.P., 2014. The Biological Carbon Pump in the North Atlantic. Prog Oceanogr 129, 200–218. https://doi.org/10.1016/J.POCEAN.2014.05.005

Sangrà, P., 2015. Canary Islands eddies and coastal upwelling filaments off North-west Africa, in: Valdés, L., Déniz-González, I. (Eds.), Oceanographic and Biological Features in the Canary Current Large Marine Ecosystem. IOC-UNESCO, Paris, pp. 105–114.

Santana-Falcón, Y., Mason, E., Arístegui, J., 2020. Offshore transport of organic carbon by upwelling filaments in the Canary Current System. Prog Oceanogr 186, 102322. https://doi.org/10.1016/J.POCEAN.2020.102322

Sarmiento, J.L., Rooth, C.G.H., & Roether, W., 1982. The North Atlantic tritium distribution in 1972. J Geophys Res Oceans, 87(C10), 8047–8056. https://doi.org/10.1029/JC087IC10P08047

Schlitzer, R., 2017. Ocean Data View, https://odv.awi.de

Schmidt, K., Schlosser, C., Atkinson, A., Fielding, S., Venables, H.J., Waluda, C.M., Achterberg, E.P., 2016. Zooplankton Gut Passage Mobilizes Lithogenic Iron for Ocean Productivity. Curr Biol 26, 2667–2673. https://doi.org/10.1016/J.CUB.2016.07.058

Schneider, B., Schlitzer, R., Fischer, G., Nöthig, E.M., 2003. Depth-dependent elemental compositions of particulate organic matter (POM) in the ocean. Glob Biogeochem Cycles 17. https://doi.org/10.1029/2002GB001871

Seager, S., Slabaugh, M., & Hansen, M., 2021. Chemistry for Today: General, Organic, and Biochemistry (Tenth Edition). Cengage Learning.

Sharp, Z., 2017. Principles of Stable Isotope Geochemistry, 2nd Edition. Open Textbooks. https://doi.org/ https://doi.org/10.25844/h9q1-0p82

Siedler, G., Kuhl, A., & Zenk, W., 1986. The Madeira mode water. J Phys Oceanogr 17, 1561–1570. https://doi.org/https://doi.org/10.1175/1520-0485(1987)017<1561:TMMW>2.0.CO;2

Siegel, D.A., Maritorena, S., Nelson, N.B., Behrenfeld, M.J., 2005. Independence and interdependencies among global ocean color properties: Reassessing the bio-optical assumption. J Geophys Res Oceans 110, 1–14. https://doi.org/10.1029/2004JC002527

Simon, M., Grossart, H.P., Schweitzer, B., Ploug, H., 2002. Microbial ecology of organic aggregates in aquatic ecosystems. Aquatic Microb Ecol 28, 175–211. https://doi.org/10.3354/AME028175

Smith, D.C., Simon, M., Alldredge, A.L., Azam, F., 1992. Intense hydrolytic enzyme activity on marine aggregates and implications for rapid particle dissolution. Nature 359, 139–142. https://doi.org/10.1038/359139A0

Stedmon, C.A., Bro, R., 2008. Characterizing dissolved organic matter fluorescence with parallel factor analysis: a tutorial. Limnol Oceanogr Methods 6, 572–579. https://doi.org/10.4319/LOM.2008.6.572

Stedmon, C.A., Markager, S., 2005. Tracing the production and degradation of autochthonous fractions of dissolved organic matter by fluorescence analysis. Limnol Oceanogr 50, 1415–1426. https://doi.org/10.4319/LO.2005.50.5.1415

Stedmon, C.A., Markager, S., Bro, R., 2003. Tracing dissolved organic matter in aquatic environments using a new approach to fluorescence spectroscopy. Mar Chem 82, 239–254. https://doi.org/10.1016/S0304-4203(03)00072-0

Stedmon, C.A., Nelson, N.B., 2015. The Optical Properties of DOM in the Ocean. Biogeochemistry of Marine Dissolved Organic Matter: Second Edition 481–508. https://doi.org/10.1016/B978-0-12-405940-5.00010-8

St-Jean, G., 2003. Automated quantitative and isotopic (13C) analysis of dissolved inorganic carbon and dissolved organic carbon in continuous-flow using a total organic carbon analyser. Rapid Commun Mass Spectrom 17, 419–428. https://doi.org/10.1002/rcm.926

Stramma, L. (1984). Geostrophic transport in the warm water sphere of the eastern subtropical North Atlantic. Journal of Marine Research, 42, 537–558.

Stramma, L., & England, M., 1999. On the water masses and mean circulation of the South Atlantic Ocean. J Geophys Res Oceans 104, 20863–20883. https://doi.org/10.1029/1999JC900139

Stubbins, A., Niggemann, J., & Dittmar, T., 2012. Photo-lability of deep ocean dissolved black carbon. Biogeosciences, 9(5), 1661–1670. https://doi.org/10.5194/BG-9-1661-2012

Suga, T., & Talley, L.D., 1995. Antarctic Intermediate Water circulation in the tropical and subtropical South Atlantic. J Geophys Res 100, 13441. https://doi.org/10.1029/95JC00858

Swan, C.M., Siegel, D.A., Nelson, N.B., Carlson, C.A., & Nasir, E., 2009. Biogeochemical and hydrographic controls on chromophoric dissolved organic matter distribution in the Pacific Ocean. Deep-Sea Res I Oceanogr Res Pap 56(12), 2175–2192. https://doi.org/10.1016/J.DSR.2009.09.002

Swan, C.M., Nelson, N.B., Siegel, D.A., Kostadinov, T.S., 2012. The effect of surface irradiance on the absorption spectrum of chromophoric dissolved organic matter in the global ocean. Deep-Sea Res I Oceanogr Res Pap 63, 52–64. https://doi.org/10.1016/J.DSR.2012.01.008

Tanaka, T., Otosaka, S., Wakita, M., Amano, H., Togawa, O., 2010. Preliminary result of dissolved organic radiocarbon in the western North Pacific Ocean. Nucl Instrum Methods Phys Res B 268, 1219–1221. https://doi.org/10.1016/J.NIMB.2009.10.137

Tcherkez, G.G.B., Farquhar, G.D., Andrews, T.J., 2006. Despite slow catalysis and confused substrate specificity, all ribulose bisphosphate carboxylases may be nearly perfectly optimized. Proc Nati Acad Sci 103 7246–7251. https://doi.org/10.1073/PNAS.0600605103

Teng, H., Masutani, S. M., Kinoshita, C.M., & Nihous, G.C., 1996. Solubility of CO2 in the ocean and its effect on CO2 dissolution. Energy Convers Manag 37(6–8), 1029–1038. https://doi.org/10.1016/0196-8904(95)00294-4

Tomczak, M., 1999. Some historical, theoretical and applied aspects of quantitative water mass analysis. J Mar Res 57, 275–303. https://doi.org/10.1357/002224099321618227

Twardowski, M.S., Boss, E., Sullivan, J.M., & Donaghay, P.L., 2004. Modeling the spectral shape of absorption by chromophoric dissolved organic matter. Mar Chem 89, 69–88. https://doi.org/10.1016/J.MARCHEM.2004.02.008

Twardowski, M.S., Donaghay, P.L., 2002. Photobleaching of aquatic dissolved materials: Absorption removal, spectral alteration, and their interrelationship. J Geophys Res Oceans 107, 6–1. https://doi.org/10.1029/1999JC000281

UNESCO, 1985. The International System of Units (SI) in oceanography. UNESCO Tech Pap Mar Sci 45, 1-124.

UNESCO, 1986. Progress on Oceanographic Tables and Standards 1983–1986. Work and Recommendations of the UNESCO/SCOR/ICES/IAPSO Joint Panel. UNESCO Tech Pap Mar Sci 50, 1-59.

Valiente, S., Fernández-Castro, B., Campanero, R., Marrero-Díaz, A., Rodríguez-Santana, A., Gelado-Cabellero, M.D., Nieto-Cid, M., Delgado-Huertas, A., Arístegui, J., Álvarez-Salgado, X.A., 2022. Dissolved and suspended organic matter dynamics in the Cape Verde Frontal Zone (NW Africa). Prog Oceanogr 201, 102727. https://doi.org/10.1016/J.POCEAN.2021.102727

Van Camp, L., Nykjaer, L., Mittelstaedt, E., Schlittenhardt, P., 1991. Upwelling and boundary circulation off Northwest Africa as depicted by infrared and visible satellite observations. Prog Oceanogr 26, 357–402. https://doi.org/10.1016/0079-6611(91)90012-B

van der Jagt, H., Friese, C., Stuut, J.B.W., Fischer, G., Iversen, M.H., 2018. The ballasting effect of Saharan dust deposition on aggregate dynamics and carbon export: Aggregation, settling, and scavenging potential of marine snow. Limnol Oceanogr 63, 1386–1394. https://doi.org/10.1002/LNO.10779

Verdugo, P., 2011. Marine Microgels. Ann Rev Mar Sci 4, 375–400. https://doi.org/10.1146/ANNUREV-MARINE-120709-142759

Walker, B.D., Beaupré, S.R., Griffin, S., Druffel, E.R.M., 2019. UV Photochemical Oxidation and Extraction of Marine Dissolved Organic Carbon at UC Irvine: Status, Surprises, and Methodological Recommendations. Radiocarbon 61 1603–1617. https://doi.org/10.1017/rdc.2019.9

Walker, B.D., Druffel, E.R.M., Kolasinski, J., Roberts, B.J., Xu, X., Rosenheim, B.E., 2017. Stable and radiocarbon isotopic composition of dissolved organic matter in the Gulf of Mexico. Geophys Res Lett 44, 8424–8434. https://doi.org/10.1002/2017GL074155

Weber, G., 1961. Enumeration of components in complex systems by fluorescence spectrophotometry. Nature 90(4770), 27–29.

Weishaar, J.L., Aiken, G.R., Bergamaschi, B.A., Fram, M.S., Fujii, R., Mopper, K., 2003. Evaluation of specific ultraviolet absorbance as an indicator of the chemical composition and reactivity of dissolved organic carbon. Environ Sci Technol 37, 4702–4708. https://doi.org/10.1021

Weiss, R.F., 1974. Carbon dioxide in water and seawater: the solubility of a non-ideal gas. Mar Chem 2(3), 203–215. https://doi.org/10.1016/0304-4203(74)90015-2

Williams, P.M., Druffel, E.R.M., 1987. Radiocarbon in dissolved organic matter in the central North Pacific Ocean. Nature 330, 246–248. https://doi.org/10.1038/330246a0

Williams, P.M., Gordon, L.I., 1970. Carbon-13: carbon-12 ratios in dissolved and particulate organic matter in the sea. Deep-Sea Res Oceanogr Abst 17, 19–27. https://doi.org/10.1016/0011-7471(70)90085-9

Xiao, X., Yamashita, Y., Gonsior, M., Jiao, N., 2023. The efficiency of the microbial carbon pump as seen from the relationship between apparent oxygen utilization and fluorescent dissolved organic matter. Prog Oceanogr 210, 102929. https://doi.org/10.1016/J.POCEAN.2022.102929

Xu, J., Fan, X., Zhang, X., Xu, D., Mou, S., Cao, S., Zheng, Z., Miao, J., & Ye, N., 2012. Evidence of Coexistence of C3 and C4 Photosynthetic Pathways in a Green-Tide-Forming Alga, Ulva prolifera. Plos One 7. https://doi.org/10.1371/JOURNAL.PONE.0037438

Ya, C., Anderson, W., & Jaffé, R., 2015. Assessing dissolved organic matter dynamics and source strengths in a subtropical estuary: Application of stable carbon isotopes and optical properties. Cont Shelf Res, 92, 98–107. https://doi.org/10.1016/J.CSR.2014.10.005

Yamashita, Y., & Tanoue, E., 2003. Chemical characterization of protein-like fluorophores in DOM in relation to aromatic amino acids. Mar Chem 82(3–4), 255–271. https://doi.org/10.1016/S0304-4203(03)00073-2

Yamashita, Y., Tanoue, E., 2008. Production of bio-refractory fluorescent dissolved organic matter in the ocean interior. Nat Geosci 1, 579–582. https://doi.org/10.1038/ngeo279

Young, J.N., Bruggeman, J., Rickaby, R.E.M., Erez, J., Conte, M., 2013. Evidence for changes in carbon isotopic fractionation by phytoplankton between 1960 and 2010. Global Biogeochem Cycles 27, 505–515. https://doi.org/10.1002/GBC.20045

Yu, K., Gan, Y., Zhou, A., Han, L., Liu, Y., 2015. A persulfate oxidation method for stable isotope analysis of dissolved organic carbon and the influence of inorganic ions on the results. Int J Mass Spectrom 392, 63–68. https://doi.org/10.1016/j.ijms.2015.09.006

Zeebe, R.E., & Caldeira, K., 2008. Close mass balance of long-term carbon fluxes from ice-core CO2 and ocean chemistry records. Nat Geosci 1, 312–315. https://doi.org/10.1038/ngeo185

Zenk, W., Klein, B., Schroder, M., 1991. Cape Verde Frontal Zone. Deep Sea Research Part A. Oceanogr Res Pap 38, S505–S530. https://doi.org/10.1016/S0198-0149(12)80022-7

Zhang, Xianrong, Sun, Z., Fan, D., Xu, C., Wang, L., Zhang, Xilin, Geng, W., Luan, X., 2019. Compositional characteristics and sources of DIC and DOC in seawater of the Okinawa Trough, East China Sea. Cont Shelf Res 174, 108–117. https://doi.org/10.1016/J.CSR.2018.12.014

Zigah, P.K., McNichol, A.P., Xu, L., Johnson, C., Santinelli, C., Karl, D.M., Repeta, D.J., 2017. Allochthonous sources and dynamic cycling of ocean dissolved organic carbon revealed by carbon isotopes. Geophys Res Lett 44, 2407–2415. https://doi.org/10.1002/2016GL071348

Ziolkowski, L.A., Druffel, E.R.M., 2010. Aged black carbon identified in marine dissolved organic carbon. Geophys Res Lett 37. https://doi.org/10.1029/2010GL043963